Modélisation géologique et hydrogéochimique de réservoirs souterrains à géométrie complexe

Pauline Collon

Modélisation géologique et hydrogéochimique de réservoirs souterrains à géométrie complexe

Mémoire présenté pour obtenir
l' Habilitation à Diriger des Recherches
Spécialité Géosciences

Présenté et soutenu publiquement le 01 Décembre 2016
à l'Université de Lorraine
par

Pauline COLLON

Maître de Conférences

Composition du jury :

Rapporteurs :	Alain DASSARGUES	Professeur à l'Université de Liège
	Frédérick DELAY	Professeur à l'Université de Strasbourg
	Mickaele LE RAVALEC	Chef du Département Géoressources à l'IFPEN
Examinateurs :	Guillaume CAUMON	Professeur à l'Université de Lorraine
	Philippe RENARD	Professeur à l'Université de Neuchâtel
	Sophie VIOLETTE	Maître de Conférence à l'ENS-Paris UPMC
Invité :	Michel BUES	Professeur à l'Université de Lorraine

GeoRessources - UMR 7359
Université de Lorraine - ENSG / CNRS / CREGU
2 rue du Doyen Marcel Roubault, TSA 70605
Vandoeuvre-lès-Nancy, F-54518 France

Résumé

La modélisation numérique des réservoirs souterrains est un outil essentiel à la compréhension de leur organisation, de leur fonctionnement et à la prévision des impacts des activités anthropiques sur leur évolution. Certains réservoirs se caractérisent par des géométries complexes qui vont directement influencer la connectivité hydrodynamique en leur sein, et plus largement l'hétérogénéité des propriétés du milieu et tous les processus physiques qui s'y déroulent. C'est le cas des bassins miniers ennoyés, des karsts, des chenaux, ou des dépôts salifères. L'objectif de mes travaux est de définir de nouvelles méthodologies de modélisation numérique adaptées à ces réservoirs à géométrie complexe et ce, en fonction de l'échelle spatiale et du processus physique d'intérêt.

Dans une première partie, l'accent est mis sur le lien entre la stratégie de modélisation retenue et le phénomène étudié lorsque deux processus principaux, ou plus, entrent en jeu. Ceci est principalement illustré à travers des travaux menés sur la gestion de l'après-mine lorrain. La deuxième partie est consacrée à l'analyse et à la caractérisation des objets géologiques à géométrie complexe, et notamment des systèmes karstiques et chenalisés. La troisième partie s'intéresse aux méthodes de simulation stochastiques de ces milieux : l'objectif n'est pas de trouver *la* solution unique, mais d'identifier *une/des* solutions honorant les données disponibles et rendant compte de la réalité, de sa complexité et des incertitudes qui lui sont associées. Le dernier chapitre dresse enfin une rapide conclusion et présente les perspectives de ces travaux à court et moyen termes.

Abstract

Numerical modelling of subsurface reservoirs is crucial to better understand their organization, their response and to improve our capacity in forecasting the impacts of human activity on their becoming. Some reservoirs are characterized by complex geometries that directly control their hydrodynamic connectivity, and more globally their petrophysical heterogeneity and the physical processes that occur in them. It is particularly the case of flooded mines, karsts, channelized systems and salt deposits. The goal of my works is to find new methodologies dedicated to the modelling of reservoirs characterized by a complex geometry, and this, depending on the spatial scale and the main physical process of interest.

In a first part, I focus on the link between the adopted modelling strategy and the main phenomena of interest when two processes, or more, are involved. It is mainly illustrated with works made on the post-mining management. The second part is dedicated to the analysis and characterization of geological objects with a complex geometry, notably karstic and channelized systems. The third part deals with stochastic simulations of these reservoirs: the aim is not to find *the* exact theoretical solution but to find *a set of* solutions that account for the observed reality, its complexity and the associated uncertainties. The last chapter presents a brief conclusion and proposes some short and long term perspectives of these works.

Remerciements

Écrire son HDR est globalement perçu comme un passage obligé et plutôt contraignant de la carrière d'un enseignant-chercheur. Mais je crois qu'en ce qui me concerne la rédaction de ces remerciements a longtemps constitué une perspective enthousiasmante qui "adoucissait" l'exercice, voire l'aurait presque motivé à elle seule... ;-) Si pour ma thèse je m'étais auto-contrainte à rester très "consensuelle", j'ai ici une deuxième chance (et dernière ?) d'enfin "me lâcher" et de remercier comme il le faut tous ceux qui le méritent : ça va être long !

Bien sûr je commence par mon équipe d'aujourd'hui : le **RING**. Plus que des collègues, nombreux sont parmi vous ceux qui sont devenus de vrais amis. Je fais partie de ces gens qui vont à leur travail avec plaisir, et sont même impatients d'y retourner après une absence prolongée. C'est une chance incroyable que de connaître une telle ambiance de travail alors merci à tous, sincèrement.

Merci à Guillaume C. : avant tout pour m'avoir fait confiance il y a 9 ans alors que je n'avais pas franchement le profil idéal de l'emploi ; pour avoir cru en moi souvent plus que moi-même ; et pour avoir aujourd'hui accepté d'être mon "parrain scientifique". Être à la hauteur de cette confiance a toujours constitué un vrai moteur pour moi.

Merci à tous les doctorants avec qui j'ai travaillé et avec qui je travaille, cette HDR vous doit beaucoup :

- à Guillaume Rongier : pour avoir été le premier à se lancer sur une thèse dont j'étais le pilote principal ; parce que travailler avec toi a toujours été un plaisir et que tu es pour une large part dans les travaux présentés ici : un "incommensurable merci" ;-). J'espère que nous aurons l'occasion de continuer à travailler ensembles et que tu trouveras rapidement un poste où exploiter tous tes talents ;
- à Romain Merland et Guillaume Reichart : pour m'avoir fait confiance en temps que co-pilote de vos thèses respectives. Vous m'avez beaucoup appris, j'espère vous avoir apporté tout autant ;
- à Marion Parquer : pour avoir pris la relève de tes prédécesseurs et osé défricher de nouveaux horizons. J'espère te transmettre mon goût pour la recherche

et t'accompagner du mieux possible durant ta thèse. Avec ton entraînement équestre, sûre que tu vas passer les obstacles avec brio ;-) ;

- à Lorraine Dewaide : pour m'avoir sollicité depuis la Belgique ; me donner l'occasion de voir le côté "terrain" des choses que je modélise et me permettre de garder un pied dans l'hydrogéologie de mes premiers "amours". C'est toujours un plaisir de venir à Namur et de t'accueillir à Nancy.

Merci à tous les étudiants de master qui ont travaillé avec moi et ont donc contribué, à leur mesure, à ces travaux (dans l'ordre anté-chronologique) : Pauline M., Margot DB., Pierre A., Damien, Clément B., Guillaume R. (encore lui ;-)), Cécile V. (qui n'a pas eu peur de quitter ses montagnes suisses pour travailler 6 mois en Lorraine), Gaétan, Fifi (on te retrouve après), Jean-Baptiste, Mayouma, Claire Ch., Marion B., et Aurélie L. ; merci à Wendy S.-L., avec qui j'ai travaillé sur le BHL dans le cadre de son stage de fin d'étude au BRGM ; ainsi qu'à tous les étudiants que j'ai encadré en projet 2A ou 3A.

Merci à mes collègues "permanents" du RING :

- Paul, mon alter-ego du bureau d'à côté : ton arrivée dans l'équipe m'a gratifié d'un grand ami, j'espère que notre route côte à côte sera longue ;
- Christine, "pas tout à fait RING" mais tout comme. Merci d'avoir été ma prof d'info à Geol, de m'avoir fait aimer la programmation, de m'avoir montré ce que c'était qu'une prof' passionnée qui motive ses étudiants. Merci d'être aujourd'hui une amie, un peu une grande soeur de boulot, merci pour les soirées filles, les discussions chiffons, livres, ciné... c'est génial, je souhaite à tout le monde de croiser une "Christine" dans sa vie ;
- Judith, mi-RING mi-GORE, toujours de bon conseil, dommage que ton EdT surchargé ne nous permette pas de te voir plus ;
- Fifi, sur qui on peut toujours compter et qui en plus maîtrise les barbecues comme personne ; j'en profite aussi pour remercier toute ta petite famille qui fait un peu partie du RING aussi ;-) Que de bons moments en votre compagnie, j'espère que ça continuera longtemps ! Voilà... ;-)
- Fatima, une secrétaire comme ça, ça ne court pas les rues, crois-moi : top efficacité, toujours le sourire au lèvres ;
- Christophe, qui a toujours la solution aux problèmes de codes, même si au début ça parait toujours compliqué ;-)
- Pierre et Jean-Jacques, les "ex-permanents", qui nous ont ouvert le chemin et ont supporté nos impertinences sans broncher (ou juste un peu) ;-)

Merci à tous les "non-permanents" du RING, ceux d'hier, d'aujourd'hui et les futurs :

- les "happy fews" avec qui j'ai partagé mon bureau : Jeanne bien sûr, collègue de bureau, de couture, de ciné, de Jane Austen... ; Flo Lallier, évidemment, toujours fourmillant d'idées et d'enthousiasme, et avec qui j'aurai passé une soirée mémorable in London ; et Paulin (DR), parce que tu étais la première "autre", et que tu as supporté mes bavardages pendant la phase critique de rédaction de ta thèse (et qu'Harvard ça pète ;-)) ;
- tous les doctorants qui n'ont pas travaillé directement avec moi ni partagé mon bureau, mais avec qui nous avons eu pleins d'échanges scientifiques lors des

séminaires, et avec qui j'ai passé de très bonnes soirées et/ou avec qui ont a bien grimpé/couru/ sport du moment/ cinéphilé, dans l'ordre alphabétique (pas de jaloux) : Antoine M., le jeune vieux des soirées à thèmes tip top (attention, France Inter te guette ;-)) ; Arnaud ; Benjamin ; Charline (Girl Power ;-)) ; Gaby (yes, Turkey !) ; Jérémy ; Jon et son avocat ; Julien R. ; Luc B. ; Marc-O ; Margaux R. (qui a gentiment exercé ses talents de relectrice sur cette HDR) ; Modeste ; Nico C. (t'en es as combien d'abonnés ? ;-)) ; Olivier R., le québécois ; Pablo, notre Carlos préféré qui danse la salsa comme personne ; Pierre A. ; Théophile ; Thomas V. ; Vincent H. ;

- Gogo, qu'on ne sait plus dans quelle catégorie mettre, vu que t'es un peu partout, alors j'en fait une juste pour toi :-), j'espère que nous pourrons collaborer longtemps sur ces thématiques de "transport réactif" ;
- Sophie R., qui a pris la relève de Fatima avec brillo ! Ce n'était pas facile et tu l'as fait, d'ailleurs on se demande s'il n'y a pas un truc cosmique entre vous : même efficacité, même sourire ;
- tous ceux qui sont passés par l'équipe et ont apporté leur bonne humeur et leur sympathie : Andrea (karsts is my life ;-)) ; Marianne ; Julien Cl. ; Anton.

Après le RING, cercle rapproché, je tiens à remercier **tous mes collègues de Géol** qui font que mon quotidien d'enseignante me plait tant : EC, chercheurs, directeurs, et tout le personnel administratif et technique qui nous permet d'exercer dans des conditions qu'on n'a pas partout : merci ! Impossible de les citer tous mais je ne pouvais pas ne pas faire une "spéciale dédicace" à Julien Ch., collègue de terrain, de course, d'escalade, de soirées... et de ce défi "HDR" : ça nous aura bien motivés ! Du coup j'en profite pour saluer les autres participants du défi : Yves, l'heureux vainqueur qui ne voulait même pas participer au départ, Benoît qui a fini le premier son manuscrit mais aura pâti de délais administratifs (pour la peine je t'offre un 2e paragraphe plus loin ;-)), et PH, allez courage, accroche toi, nous on y croit pour toi.

Je remercie également tous **les collègues *extérieurs*** avec qui j'ai/ai eu grand plaisir à collaborer ponctuellement ou sur des projets plus longs : Philippe Renard et toute l'équipe de Neuchâtel, si sympathiques et dynamiques qu'on s'y sent comme "à la maison" ; Vincent Hallet, Isabelle B., Lorraine et tous les collègues de Namur, qui m'ont fait découvrir Han-sur-Lesse et Furfooz ; Alexandre P. et Jean-Claude R., qui nous ont permis de monter un (super) stage de terrain en Turquie et fait découvrir la tectonique salifère à Sivas ; mes collègues du BRGM : Virginie Hamm, Laurent Vaute et Robert Fabriol, avec qui j'ai eu plaisir à travailler durant plusieurs années sur la thématique de l'après-mine ; Bruno Lévy, le grand spécialiste des maillages et du L_pCVT, qui m'a aussi fait découvrir Claude Ponti ; Chiaki Oguchi, qui m'a tellement bien accueillie en 2006 au Japon ; et tous les autres collègues avec qui j'échange régulièrement en conférences, réunions, etc.

Il y a le laboratoire d'aujourd'hui, mais il y a aussi ceux "d'avant" : le **GEGENA** à Reims, le **CEVH** à l'ENGEES Strasbourg, et bien entendu le **LaEGO** à Nancy, mon

tout premier labo. Merci à chaque directeur d'avoir cru en moi et de m'avoir intégrée avec une égale gentillesse dans leurs équipes respectives. Chacune a été l'occasion de nouvelles rencontres, toujours enrichissantes. Et certaines ont, là encore, particulièrement compté pour moi :

- Céline T. (maintenant S.), ma jumelle de recrutement, marraine de ma fille aînée, rien que pour te rencontrer, Reims ça valait le détour ! ;-)
- Olivier C., 16 ans maintenant qu'on se connait ! Tout premier collègue de bureau à l'époque du LaEGO, la vie passe et l'amitié reste. J'en profite donc pour te remercier à nouveau (puisque tu étais déjà là en 2003 ! ;-)) et y joindre cette fois Claire qui prend son rôle de marraine si à cœur.

Ils m'ont plongé dedans quand j'étais petite : **Michel Buès** et **Robert Fabriol** m'ont encadré durant ma thèse et appris "les bases". Merci Michel de m'avoir fait entrer dans cet univers, de m'avoir toujours permis de garder un pied à Géol et dans l'hydrogéologie et d'accepter aujourd'hui de participer à mon jury d'HDR en tant qu'invité. Merci à toi Robert d'avoir été le moteur de mes tous premiers travaux sur le Bassin Ferrifère Lorrain et de m'avoir toujours encouragée par la suite en me donnant d'avisés conseils. Ta bienveillance a toujours été d'un grand réconfort.

Bien entendu je remercie également tous les **membres de ce jury d'HDR** que je n'aurais pas encore cité par ailleurs. Alain Dassargues, Frédéric Delay, Mickaële Le Ravalec et Sophie Violette. Trouver des collègues avec qui je n'avais jamais travaillé (ni mon équipe) et qui ne soit pas trop éloignés pour autant de mes sujets de recherche n'a pas été chose aisée. Vous avez gentiment accepté de relire ce document un peu touffu qui touche à beaucoup de domaines et d'y porter un regard de professionnels. Merci à vous.

Il n'ont pas directement été impliqués dans mon travail mais **ma famille et mes proches** ont toujours été là pour moi, je les en remercie :

- la team Geol Girl Elo-Nono-Mary et tous les géoliens qui répondent présents dès que je les sollicite pour X raison professionnelle (ou personnelle) ;
- mes frères et leurs familles respectives ;
- Benoît, qui supporte mes bavardages et m'encourage même à continuer, qui a fait ce chemin d'HDR en même temps que moi et qui partage mon goût pour le surimi et pour tellement d'autres choses ; merci *d'être*, tout simplement ;
- et bien sûr mes parents, merci, un immense merci pour votre soutien sans faille à mes côtés, la confiance que vous m'accordez et l'amour que vous m'avez donné et continuez à me donner.

Je remercie enfin le lecteur qui sera parvenu à la fin de tout ceci et sera triste de ne pas voir son nom : j'ai essayé de n'oublier personne mais ce n'est pas toujours évident.

Je dédie cette HDR à mes deux filles, Néva et Lila,
qui illuminent ma vie de leurs sourires, de leurs rires et de leur tendresse.
Je vous aime...

Sommaire

Première partie

Notice Individuelle

1 Curriculum Vitæ

1.1 Information Administratives

Informations biographiques :	Pauline COLLON Née le 12 Novembre 1978, à Paris (37 ans). Nationalité Française. 2 enfants (7 et 9 ans).
Situation professionnelle :	Maître de conférences à l'Université de Lorraine. École Nationale Supérieure de Géologie (ENSG). GéoRessources - UMR 7359. Section CNU : 35 - Structure et évolution de la terre et des autres planètes
Coordonnées :	GéoRessources – Equipe RING, ENSG, 2 rue du doyen Marcel Roubault, TSA 70605, 54518 Vandoeuvre-Lès-Nancy, Cedex, France. Tel : +33 (0)3 83 59 64 20. E-mail : pauline.collon@ensg.univ-lorraine.fr

1.2 Diplômes et expérience professionnelle

Diplômes

2003 : **Doctorat** de l'Institut National Polytechnique de Lorraine (INPL), spécialité "Géotechnique - Hydrosystèmes - Génie des Procédés".

2000 : **DEA** de l'INPL : "Protection Aménagement et Exploitation du Sol et du Sous-Sol", mention TB.

2000 : **Ingénieur** de l'Ecole Nationale Supérieure de Géologie de Nancy (ENSG). Option Aménagement des Eaux.

Fonctions occupées

2007- ... :	**Maître de conférences** (CNU35)	CRPG puis GeoRessources (depuis jan. 2012), Ecole Nat. Sup. de Géologie (ENSG) - Université de Lorraine (UL)
2005-07 :	**Maître de conférences** (CNU35)	Gr. d'Etude des Géomat. et des Env. Naturels et Anthropiques (GEGENA), Université de Reims Champagne Ardennes (URCA)
2004-05 :	**Maître de conférences contractuel du Ministère de l'Agriculture**	Centre d'Ecologie Végétale et d'Hydrologie (CEVH), Ecole Nat. du Génie de l'Eau et de l'Environnement de Strasbourg (ENGEES)
2003-04 :	**Ingénieur de recherche** *(4 mois)*	Ecole Nat. Sup. de Géologie (ENSG), Institut Nat. Polytechnique de Lorraine (INPL)
2000-03 :	**Doctorante - Chercheur contractuel**	Laboratoire Env. Géoméca. et Ouvrages (LaEGO), Institut Nat. Polytechnique de Lorraine (INPL)
2000 :	**Ingénieur stagiaire** *(6 mois)*	BRGM
1999 :	**Ingénieur stagiaire** *(2 mois)*	GESTER (Bureau d'étude Environnement & dépollution, auj. ARCADIS)

1.3 Activités

Thème de recherche - Domaines de compétences

Thème de recherche : Modélisation géologique et hydrogéochimique à grande échelle de réservoirs à géométrie complexe : systèmes karstiques, chenaux, bassins miniers, bassins en contexte de tectonique salifère.
Domaines de compétences : Géologie Numérique, Hydrogéologie, Géostatistiques, Hydrologie, Programmation, Systèmes d'information géographiques (SIG), Interactions fluides-roche.

Distinctions - PEDR

2005 : 1er prix de thèse scientifique de la Région Lorraine.
2015-19 : Titulaire de la PEDR

Activités d'enseignement et d'encadrement scientifique

$\sim$ 240h/an : Géomodélisation, Programmation (C++ et Python), Hydrologie de surface, Hydrogéologie, SIG, Géostatistiques, Cartographie de terrain.
Responsabilités pédagogiques : 3 UE (Niv. L3) + 1 Parcours Secondaire (72h - Niv. M1).
Co-directions de Thèses : 3 soutenues, 2 en cours.
(Co-)Encadrement de : 14 stages M2 ; 12 projets de recherche 3A ENSG ; 10 stages M1.

Activités de publication (septembre 2016)

Publications dans des revues avec comité de lecture : 12(+1) internationales + 1 nationale.
Communications dans des conférences internationales : 19 orales + 5 posters
Communications dans des conférences nationales : 9 orales + 3 posters.
Communications au GOCAD/RING meeting : 18 orales + 8 posters.
Nombre de rapports, mémoires, chapitres d'ouvrage : 6.
ORCID ID : 0000-0001-8505-4961. Scopus ID : 10840524800

Activités éditoriales & Sociétés savantes

2016-... : *Associate Editor* du journal *Computers & Geosciences*
2013-... : Membre de l'*Editorial Advisory Board* du journal *Computers & Geosciences*
2014 : Éditrice invitée d'un numéro spécial dans le journal *Mathematical Geosciences*

Membre de Comités Scientifiques (avec review d'articles et responsabilité de session) :
2014 : First EuroKarst Conference, 5-9 Sept. 2016, Neuchâtel, Switzerland
2011 : 9th Conference on Limestone Hydrogeology, 1-3 Sept. 2011, Besançon, France

Sociétés savantes : Membre permanent de l'IAMG ; Membre de l'IAH.

Activités annexes à caractère administratif

2015-... : Membre titulaire nommée au Conseil National des Universités CNU35
2012-... : Membre élue au Conseil de Collégium L-INP de l'UL
2012-... : Membre désignée au Conseil de la Vie Etudiante de l'ENSG
2010-... : Membre désignée à la Commission Enseignement
2009-14 : Membre élue à la Commission des Enseignants de l'ENSG
2009-14 : Membre élue au Conseil de l'ENSG

2 Activités pédagogiques et administratives

En tant qu'enseignant-chercheur, l'enseignement occupe une place très importante dans mes fonctions. L'accompagnement pédagogique est pour moi essentiel et constitue une source première de motivation et d'enthousiasme dans mon travail. Presque tous les étudiants dont j'ai co-dirigé les travaux scientifiques en thèse ou master ont d'abord été mes élèves : depuis toujours, mes enseignements et ma recherche se sont nourris mutuellement. C'est pourquoi j'ai choisi de commencer ce dossier par la présentation de mes activités pédagogiques.

2.1 Expériences d'enseignements

J'enseigne dans le Supérieur depuis le début de ma thèse, en 2000. D'abord enseignante vacataire, puis contractuelle et enfin titulaire, j'ai eu l'occasion d'enseigner dans des structures très variées (BTS, Université, Ecoles d'ingénieur) et à tous les niveaux (du L1 au M2) (Tab. I.1). Dans la majeure partie des formations que je donne, j'enseigne en français. Cependant, de 2010 à 2015 dans le cadre du master international *Subterranean Reservoirs of Energy : Hydrodynamics - Geology - Modelling* (SRE-HGM), j'ai enseigné la géomodélisation en anglais à un public international (18h CM).

Chaque structure a ses propres modes de fonctionnement qui se traduisent "sur le terrain" en différences de moyens humains et financiers. Chaque niveau et type de formation a ses propres objectifs pédagogiques, qu'il convient de relier à la diversité de provenance et aux motivations personnelles des étudiants. C'est pourquoi je revendique cette variété d'expériences comme un point fort de mon parcours d'enseignante.

Tableau I.1 : Structures et Niveaux dans lesquelles j'ai enseigné depuis 2000.

Années	**Structure**	**Niveau***	**Statut**
2007-auj.	École Nat. Sup. de Géologie (ENSG)	1A, 2A, 3A Ing. + M1 international	McF
2005-2009	Lycée Loritz : BTS Géologie Appliquée	2A BTS	McF (Vacations)
2005 - 2007	Univ. de Reims Champ.-Ardennes (URCA)	L1, L2, L3, M2	McF
	École Nat. Sup. de Géologie (ENSG)	3A Ing.	McF (Vacations)
fév.2004 - aou.2005	École Nat. du Génie de l'Eau et de l'Env. de Strasbourg (ENGEES)	1A Ing. + M1	McF Contractuel
2000-2003	École Nat. Sup. de Géologie (ENSG)	1A, 2A Ing.	Vacataire

*1A, 2A et 3A Ing. désignent les années de formation dans le cycle Ingénieur qui recrute après 2 ans de classes préparatoires. Ce sont donc des équivalents aux niveaux L3, M1 et M2 dans le système international. 2A BTS désigne la deuxième année de BTS et équivaut à un niveau L2.

2.2 Nature des enseignements et projet pédagogique

Mes enseignements (en moyenne 240h eq. TD/an) sont à l'image de ma formation initiale et de ma recherche : pluri-disciplinaires et évoluant au fil des années, des structures d'accueil, des formations concernées et des besoins. Il est ainsi difficile d'en donner une image fixe en terme de volume annuel. Ils peuvent néanmoins se rassembler autour de quatre thématiques majeures : Géologie Numérique, Hydrogéologie, Systèmes d'Information Géographique (SIG) et Géologie Générale (Tab. I.2).

En plus de ces enseignements, j'ai monté, avec l'appui du directeur de l'ENSG Jean-Marc-Montel, une UE nommée "Mardis de Géol" lors de la réforme des enseignements de l'ENSG de 2009. Cette UE a ceci de particulier qu'elle s'étale sur les 3 semestres de Tronc Commun de la formation Ingénieur (eq. S5, S6, S7) et consiste en une série de conférences (2h /semaine) à but d'ouverture sur le monde professionnel. Chaque semestre a sa spécificité. Le premier semestre porte sur les "Frontières de la Recherche et Développement" et fait essentiellement intervenir des chercheurs français et étrangers. Elle a pour objectif de montrer aux étudiants la diversité des géosciences et de les sensibiliser à la recherche. J'ai été organisatrice de ces conférences de 2009 à 2011 avant d'en transmettre la responsabilité à des collègues. Le deuxième semestre porte sur "Les métiers des Géosciences" et fait essentiellement intervenir des industriels. J'en suis la responsable depuis 2009 et je m'appuie pour cela fortement sur le réseau des anciens élèves de l'ENSG. Je contacte et accueille ainsi chaque année une dizaine d'entreprises recrutant des ingénieurs ENSG. C'est une occasion unique pour les étudiants de découvrir les futurs métiers qu'ils pourront exercer, de commencer un réseau et de se construire un projet professionnel. C'est une responsabilité gourmande en temps et en énergie mais qu'il me tient à cœur de maintenir même si elle n'apparait pas dans un relevé de "service". Le troisième semestre concerne les "Fonctions dans l'Entreprise". Elle est gérée depuis sa mise en place par Jean-Marc Montel, directeur de l'ENSG.

Enfin, je participe également tous les ans à l'évaluation des stages industriels de 2ème et 3ème année Ingénieur ENSG et des stages de fin d'étude Technicien des élèves du BTS de Géologie Appliquée.

L'enseignement est une aventure humaine passionnante qui doit sans cesse se réinventer pour s'adapter à une population étudiante évoluant avec les générations. C'est avec cette philosophie que je construis mes cours. Pour cela, je n'hésite pas à suivre régulièrement des formations : MOOC "Gestion de Projet", formation UL "Concevoir un questionnaire à choix multiple", "Utilisation des boîtiers de vote électronique dans l'enseignement" et récemment "Être un enseignant motivant pour ses étudiants".

Ainsi, en pratique, je suis une grande utilisatrice des plateformes numériques (Arche) et j'intègre depuis 2 ans les boitiers de vote électronique à des fins d'autoévaluation, pour rythmer des séances de travaux dirigés ou pour la vérification des connaissances. De manière générale, j'accorde une grande importance au travail

Tableau I.2 : Résumé des matières enseignées depuis 2000.

	Matière	Formation*	Volume (eq. TD)	Période
Géologie numérique et programmation	Programmation Orientée Objet : C++	2A ENSG	24h	2007-...
	Introduction à la Programmation : le langage Python	1A ENSG	6 à 24h	2007-...
	Géomodélisation	1A ENSG + M1	20 à 30h	2007-...
	Simulation Objet et Simulation Multi-points	3A ENSG	4.5h	2014-...
	Géostatistiques	2A ENSG	12h	2008-10
	Modélisation 3D des objets miniers	3A ENSG	10h	2008-10
Hydrologie / Hydrogéologie	Hydrologie et Hydrogéologie	1A ENSG	17.5h	2009-...
	Statistiques appliquées à l'hydrologie	2A et 3A ENSG	16.5h	2007-...
	Projet d'hydrologie de surface	3A ENSG	12h	2005-...
	Hydrogéologie et Hydrologie de surface	2A BTS GA	52h	2005-09
	Hydrologie de surface	L1 URCA	32h	2005-07
	Hydrogéologie	M1 URCA	6h	2005-07
	La Modélisation en Hydrogéologie	M2 URCA	7.5h	2005-07
	Hydrologie de surface	1A + M2 ENGEES	58h	2004-05
	TP Hydrodynamique et Hydrogéologie	2A ENSG	32h	2002-03
	TD Hydrogéologie	1A ENSG	26h	2001-02
Systèmes d'Information Géographique (SIG)	Introduction à la géomatique et aux SIG avec le logiciel ArcGIS	1A ENSG + M2	24 à 39h	2007-...
	Géomatique théorique : géodésie, géodésie spatiale, GPS, ...	M1 URCA	27h	2005-07
	Apprentissage d'un logiciel SIG : MAPINFO©	M2 URCA	36h	2005-07
	Introduction à la Géomatique sous Mapinfo	1A ENGEES	8h	2004-05
	Aménagement foncier	1A ENGEES	8h	2004-05
Géologie générale	Stage "Cartographie de terrain"	1A ENSG	36h	2011-15
	Géologie de terrain, Cartographie, Initiation à la pétrologie sédimentaire	L1 URCA	44h	2005-07
	Géologie appliquée (géothermie, hydrogéologie, exploitation minière)	L1 URCA	35h	2005-07
	Préparation aux concours de l'IUFM (Univers et étoiles, Structure de la Terre, Géodynamique interne et externe, Les grandes étapes de l'évolution)	L3 URCA	20h	2005-07
	Préparation au CAPES (leçons sur les barrages et le génie civil)	URCA	2.5h	2005-07
	Stage terrain dans le Doubs	1A ENGEES	21h	2004-05

*ENSG : Ecole Nationale Supérieure de Géologie ; BTS GA : BTS Géologie Appliquée du Lycée Loritz ;
URCA : Université de Reims-Champagne-Ardennes ;
ENGEES : Ecole Nationale du Génie de l'Eau et de l'Environnement de Strasbourg.

par projet, que j'intègre dans une majorité de mes modules. En effet, il permet un investissement plus grand des étudiants et stimule leur motivation. Réalisé en équipe, il favorise l'entraide et la discussion, mais permet également aux élèves d'être confrontés aux difficultés managériales d'un travail en groupe, central dans le monde professionnel d'aujourd'hui. Enfin, les projets sont souvent l'occasion de réaliser des *ponts* entre différentes matières. La formation ne se résume alors plus à une juxtaposition de connaissances et de compétences indépendantes mais devient un ensemble cohérent qui permet à chaque individu de se projeter dans son projet professionnel et personnel.

Dans les prochaines années, je compte profiter des infrastructures de captation vidéo mises en place à l'université pour créer des séquences filmées courtes permettant d'expliquer, de développer et/ou d'approfondir certains points des enseignements qui sont parfois rapidement traités en cours.

2.3 Responsabilités pédagogiques et administratives

Parce que le partage des responsabilités pédagogiques et administratives est essentiel au bon fonctionnement des structures, je m'implique et me suis impliquée à différents niveaux.

Responsabilités Pédagogiques

- Initiatrice et Responsable de l'UE "Mardis de Géol" qui fait intervenir chaque semaine des professionnels de l'industrie pour présenter aux étudiants les "métiers de la géologie" (Semestre 5 en 2009-11 + Semestre 6 de 2009 à auj.).
- Responsable de différents modules d'enseignements :
  - Parcours Secondaire (UE de 72h – S8) "Programmation C++ et éléments finis"
  - Module de Tronc Commun (UE de 24h - S6) "SIG- Télédétection- Cartographie" (entre 4 et 8 intervenants selon les années)
  - Module de Tronc Commun (UE de 24h - S6) "Géomodélisation"
  - Module de "Geomodelling" dans le Master International *Subterranean Reservoirs of Energy* (SRE) (UE 24h – enseignée en anglais – M1)
- 2014-2015 : En raison du ½ CRCT du Pr. Caumon, j'ai partagé avec lui la responsabilité du Parcours de 3e année Ingénieur "Géologie Numérique" (18 étudiants).

Dans le cadre de mes fonctions de maître de conférences à l'Université de Reims Champagne Ardennes (URCA ; 2005-07), j'ai été :

- Co-responsable de 4 modules d'enseignement de Licence :
  - GEOL22 : "L'eau à la surface de la Terre"
  - GEOL23 : "Les métiers de la géologie"
  - SEN62 : "Sciences Naturelles 2"
  - SEN63 : "Sciences Naturelles 3"

- Responsable de 2 modules d'enseignement de Master :
  - Géomatique 1 : "Introduction à la géomatique"
  - Géomatique 3 : "Apprentissage d'un logiciel de SIG : MapInfo"

Participation à des jurys

- **Jurys de thèse, à l'étranger, en tant que rapporteur :**
  - 2013 : "*Multiple Scenario Generation of Subsurface Models*" par Knud Cordua, soutenue le 18 décembre 2013 à la Technical University of Denmark (DTU, Copenhague, Danemark).
  - 2011 : "*Etude hydogéologique et dimensionnement par modélisation du "Système-Traçage" du réseau karstique de Han-sur-Lesse (Massif de Boine - Belgique)*" par Isabelle Bonniver, soutenue en septembre 2011 à la FUNDP Namur (aujourd'hui Université de Namur) (Namur, Belgique).
- **Jurys de thèse à l'Université de Lorraine en tant que co-directrice :**
  - 2016 : "*Connectivité de corps sédimentaires chenalisés : stratégies d'analyse et de simulation en modélisation de subsurface*" par Guillaume Rongier, soutenue le 15 mars 2016.
  - 2015 : "*Modélisation thermo-hydrodynamique d'un réservoir minier profond ennoyé - Le cas du Bassin Houiller Lorrain*" par Guillaume Reichart, soutenue le 1er juin 2015.
  - 2013 : "*Génération de grilles de type volumes finis : adaptation à un modèle structural, pétrophysique et dynamique*" par Romain Merland, soutenue le 18 avril 2013.
- **Jurys de master** : Depuis ma prise de fonction à l'ENSG en 2007, je participe tous les ans au jury du master (M2) *Géosciences : Planètes, Ressources, Environnement* (GPRE) , Spécialité *Géosciences Pétrolières et Ingénierie des Réservoirs* (GPIR), Parcours *Géologie Numérique*. Ce parcours diplôme depuis 2007 entre 6 et 15 étudiants chaque année.

- **Autres jurys** :
  - Stages de Fin d'Etudes "Ingénieur" (4 à 6 mois) à l'ENSG (depuis 2007) : stages d'ingénierie et/ou de recherche en milieu professionnel (soutenance orale et rapport écrit).
  - Stages "Pratique de l'Ingénierie" (8 à 12 semaines) à l'ENSG (depuis 2007) et à l'ENGEES(2004-05) : stages réalisés entre la 2ème et la 3ème année de formation Ingénieur dans diverses structures - entreprises, bureaux d'études et administration - (soutenance orale et rapport écrit).
  - Oraux du concours d'entrée 2004 à l'ENGEES : épreuve de TIPE (Travaux d'Initiative Personnelle Encadrés).

Responsabilités Administratives

- Depuis nov. 2015 : Membre nommée au Conseil National des Universités (CNU35).

Cette charge importante comprend l'évaluation de dossiers et la participation aux réunions concernant :
  - les demandes de qualification aux fonctions de maître de conférences
  - les demandes d'avancement de grade (passages Hors Classe)
  - les demandes de Congé pour Recherches ou Conversions Thématiques (CRCT)
  - les demandes de Prime d'Encadrement Doctoral et de Recherche (PEDR)
  - à partir de 2017 : le suivi de carrière des Enseignants-Chercheurs.
- 2012-... : Membre élue au Conseil de Collégium L-INP de l'UL.
  En tant qu'élue au Conseil de Collegium L-INP de l'Université de Lorraine (UL), j'ai mis en place et je maintiens un blog pour transmettre les informations et comptes-rendus de conseil à mes pairs[1].
  Cette fonction m'a également amenée à évaluer au niveau local des dossiers de demande d'avancement de grade pour les maîtres de conférences (passage Hors Classe).
- 2012-... : Membre nommée au Conseil de la Vie Etudiante ENSG
- 2010-... : Membre nommée à la Commission Enseignement ENSG
- 2009-14 : Membre élue à la Commission des Enseignants ENSG
- 2009-14 : Membre élue au Conseil de l'ENSG

J'ai également participé aux **Comités de Sélection** pour les recrutements suivants :
- 2014 : poste de Maître de Conférences en "Géosciences : hydrogéologie de la zone saturée, modélisation" à l'Université de Reims Champagne-Ardennes (N°36MCF 4200)
- 2012 : poste de Maître de Conférences en "Géologie Numérique - Géophysique" à l'ENSG (N° 35MCF 0468)

3 Présentation synthétique des activités de recherche

3.1 Contexte de la recherche

Depuis l'obtention de mon doctorat en octobre 2003, j'ai successivement occupé différents postes d'enseignant-chercheur. J'ai tout d'abord été pendant 18 mois Maître de conférences contractuelle à l'Ecole Nationale du Génie de l'Eau et de l'Environnement de Strasbourg (ENGEES), rattachée au Centre d'Ecologie Végétale et d'Hydrologie (CEVH, aujourd'hui intégré au LHyGeS). Puis, à la rentrée 2005, j'ai été nommée maître de conférences à l'Université de Reims Champagne Ardennes (URCA) au sein du laboratoire GEGENA. J'ai enfin intégré Nancy Université (depuis Université de Lorraine) et le CRPG à la rentrée 2007 sur mutation. En 2012, une restructuration profonde des Sciences de la Terre à Nancy au sein du jeune Observatoire des sciences de l'univers (OSU) OTELo a conduit mon équipe à rejoindre la nouvelle unité de recherche "GeoRessources – UMR7359" résultant du regroupement de personnels issus

[1] https ://interecolesingenieursudl.wordpress.com/

de 4 laboratoires. Toutes ces expériences ont influencé à leur mesure l'orientation de mes activités de recherche.

L'originalité de mon travail repose sur le développement de nouvelles méthodologies adaptées aux réservoirs souterrains à géométrie complexe tels que les bassins miniers ennoyés, les karsts, ou les chenaux. Quel que soit l'objet d'étude, l'enjeu est de reproduire un ou plusieurs processus naturels (e.g., hydrogéochimie des bassins miniers) et/ou des géométries d'objets géologiques complexes (e.g., karsts, chenaux) en s'appuyant avant tout sur les données de terrain ou de laboratoire et en honorant des concepts théoriques. L'objectif n'est pas de trouver *la* solution unique, mais de trouver *une/des* solutions rendant compte de la réalité, de sa complexité et des incertitudes qui lui sont associées. Mes activités de recherches se situent donc à la croisée de plusieurs disciplines : géologie numérique, géomodélisation, hydrogéologie/hydrogéochimie et géostatistique.

Depuis 2007, mes activités de recherche s'inscrivent pour l'essentiel dans le cadre de l'équipe de recherche RING (Research for Integrative Numerical Geology) associée au Consortium RING-Gocad [2] qui assure le financement d'une dizaine de stages Master et de 2 à 3 thèses par an. Ce consortium nous permet également de financer sur fonds propres 2 ingénieurs de recherche et 1 secrétaire, tous en CDI. Dans ce cadre, nous organisons chaque année un meeting annuel à destination de nos sponsors et partenaires académiques et industriels, à la suite duquel se tient le *steering commitee* où nous présentons budget et projet pour l'année à venir. Nous rédigeons également annuellement un rapport d'activité. De ce fait, je m'implique aujourd'hui essentiellement dans le développement de cette structure de recherche et participe à un nombre plus réduit de projets "classiques" (types ANR, INSU, . . .). Voici la liste des principaux projets extérieurs au Consortium RING-Gocad dans lesquels je suis/j'ai été impliquée et qui ont obtenu le financement demandé :

- Un "Projet Exploratoire Premier Soutien" (PEPS) Mirabelle 2015 (2015-2016) porté par Jean Cauzid (Maître de Conférences GeoRessources - UL) et visant à intégrer des données spectroscopiques de terrain dans des géomodèles 3D. Ces travaux, en collaboration avec des archéologues visent à mieux définir les minéralisations de la Grande Région (Warndt, Château-Lambert, Stolzembourg). Suite à ce travail, une ANR "Ressources minérales et territoires (ReMiT)" vient d'être déposée.

- Le projet GEOTREF (2015-2019) (Plate-forme pluridisciplinaire d'innovation et de démonstration pour l'exploration et le développement de la GEOThermie haute énergie dans les REservoirs Fracturés) : c'est un projet rassemblant 4 partenaires industriels et 8 partenaires académiques entrant dans le cadre des Investissements d'Avenir de l'ADEME. Le projet vise à améliorer la compréhension du fonctionnement des réservoirs géothermiques fracturés. J'interviens dans une partie (Tâche 7) visant à développer des nouvelles méthodologies pour la modélisation du transport réactif dans ce contexte. J'ai été la repré-

[2] http ://ring.georessources.univ-lorraine.fr/

sentante de mon équipe lors du montage de ce projet (montage du dossier, répartition des moyens, . . .).

- Le Labex Ressources 21 (2011-2019) (Ressources stratégiques pour le 21ème siècle) : comme tous les chercheurs de notre laboratoire, je suis impliquée dans le Labex Ressources21. Plus particulièrement, j'interviens dans l'axe «Modéliser la géométrie, le transport et les processus physico-chimiques en 3D aux échelles régionales". Dans ce cadre j'ai co-écrit un projet de Post-doc défendu en 2015 devant les commissions locales. Il doit être réalisé par Gautier Laurent en 2 phases, l'une de 3 mois de juin à septembre 2015, la seconde de 9 mois de septembre 2016 à juin 2017.

- Le projet ProMine (2009-2013) (Nano-particle products from new mineral resources in Europe) : j'ai été impliquée dans le volet "géomodélisation" de ce projet partiellement financé par l'Europe. Le porteur était Jean-Jacques Royer, ingénieur de recherche CNRS dans notre équipe.

- Le GISOS (1999-2013) : Groupement d'intérêt scientifique sur l'Impact et la Sécurité des Ouvrages Souterrains (GISOS) rassemblant le BRGM, l'INPL, l'INERIS et l'Ecole des Mines de Paris. C'est dans ce cadre que j'ai réalisé mes travaux de thèse, puis que j'ai continué à développer des recherches en collaboration sur la thématique de l'Après-Mine en Lorraine et de ses impacts sur la qualité de l'eau.

À ces principaux programmes de recherche, s'ajoute une participation ponctuelle aux différents programmes dans lesquels étaient impliqué le laboratoire GEGENA (Reims) où j'ai travaillé plus brièvement (2005-2007) :

- le programme Transpoll / AQUAL rattaché au PIREN Seine
- le projet BQR 2006 "Comportement dilatométrique des pierres de construction des monuments de Paris soumises à des solutions salines : expérimentation et modélisation" porté par ma collègue Céline Thomachot-Schneider.

3.2 Encadrement doctoral et scientifique

Mes travaux de recherche ont pour partie été menés dans le cadre de cinq thèses de doctorat où je suis intervenue en tant qu'encadrante, dont deux en cours, et de 14 stages de master. Ils se sont déroulés dans le cadre de projets soutenus par le Consortium RING-Gocad qui regroupe de nombreux industriels et universitaires, par l'institut Carnot ICEEL et le BRGM, et par la région Lorraine. Les résultats de ces travaux ont été diffusés grâce à 12 articles dans des revues à comités de lecture, plus 1 en cours d'évaluation, 35 conférences ou séminaires nationaux et internationaux, plus une participation annuelle au RING (/Gocad) Meeting organisé chaque mois de septembre par notre équipe à Nancy. Par ailleurs, je suis titulaire de la Prime d'Encadrement Doctoral et de Recherche (PEDR) pour la période 2015-2019.

Co-directions de thèses

- *4 à l'Université de Lorraine (3 soutenues + 1 en cours), dont 1 en cotutelle avec la Suisse*
- *1 en Belgique*

Je suis/ai été impliquée dans l'encadrement de 4 thèses de doctorat à l'Université de Lorraine, tous officiellement validés par des ACT (Tab. I.3). L'une d'elle a été réalisée dans le cadre d'une co-tutelle avec l'Université de Neuchâtel (Suisse) et soutenue par Guillaume Rongier en mars et avril 2016 à Nancy et Neuchâtel.

Tableau I.3 : Co-directions de thèses à l'Université de Lorraine (avec ACT).

Année	Etudiant	Sujet	%encadrement (co-encadrant)	Devenir après diplôme
2014-...	Marion Parquer	Simulation et calage d'objets sédimentaires à partir de données de surface et de subsurface	50% (G. Caumon)	
2013-2016	Guillaume Rongier*	Connectivité de corps sédimentaires chenalisés : stratégies d'analyse et de simulation en modélisation de subsurface	33% (J. Sausse, P. Renard)	Post-doc (MIT Haystack Obs.)
2010-2015	Guillaume Reichart	Modélisation thermo-hydrodynamique d'un réservoir minier profond ennoyé - Le cas du Bassin Houiller Lorrain.	30% (M. Buès, L. Vaute)	GEODERIS
2010-2013	Romain Merland	Génération de grilles de type volumes finis : adaptation à un modèle structural, pétrophysique et dynamique.	30% (G. Caumon, B. Lévy)	PARADIGM

*La thèse de Guillaume Rongier a été réalisée en cotutelle entre l'Université de Lorraine et l'Université de Neuchâtel, Suisse. Il a donc un double diplôme et a réalisé un séjour de 1 à 2 mois/an en Suisse.

Par ailleurs je suis également co-encadrante de Lorraine Dewaide, doctorante à l'Université de Namur (Belgique) (Tab. I.4). Lorraine réalise sa thèse avec le statut d'assistante d'enseignement, statut n'existant pas en France. Il s'agit d'un financement accordé par l'Université pour réaliser une thèse en 6 ans avec une charge d'enseignement associée de 192h eq TD environ par an. Ce co-encadrement est officiellement déclaré auprès de l'Université de Namur mais il n'y a pas de % officiellement associé. J'indique un ratio 30%/70% car Lorraine est essentiellement basée à Namur et n'effectue que des séjours réguliers à Nancy.

Tableau I.4 : Co-direction de thèses à l'étranger.

Année	Etudiant	Sujet	%encadrement (co-encadrant)	Université d'inscription
2012-...	Lorraine Dewaide	Karstification et comportement hydrogéologique des mudmounds waulsortien (Belgique)	30% (V. Hallet)	Université de Namur (Belgique)

Encadrements de Master 2 et équivalent

- ▷ *14 étudiants de M2*
- ▷ *12 étudiants en Projet de Recherche de 3e année Ingénieur*

L'expérimentation de la recherche en laboratoire est un point important de la formation des ingénieurs ENSG. En 3ème année (Tab. I.5), chaque élève ingénieur doit réaliser un projet de Recherche en laboratoire. Cela représente une charge d'environ 120h, plus deux mois pleins pour les étudiants inscrits dans un double cursus Master.

Tableau I.5 : Encadrements de projets de recherche de 3ème année ENSG

Année	**Etudiant**	**Sujet**	**%encadrement (co-encadrant*)**
2012-13	Aurore Plougoulen	Modélisation 3D du système karstique de Han-sur-Lesse	100%
	Matthieu Baïsset	Modélisation 3D du système karstique de Foussoubie	100%
	Eva Leriche	Interpolation de données pluviométriques sur le basin versant de Serre-Ponçon	100%
	Elsa Mondon	Construction d'un modèle numérique de la nappe de la Crau	100%
	Marion Michou		
2011-12	Yolande Corneil	Construction d'un modèle numérique de la nappe de la Crau	100%
	Emilie Tridon		
2010-11	Marie Salillas	Construction d'un modèle géologique 3D du bassin houiller lorrain en vue de son exploitation géothermique	80% *(G. Reichart)*
	Adeline Moignard		
	Claire Moynot	Effet sur la chimie de l'eau des fluctuations du niveau de l'eau dans les mines ennoyées (Bassin Ferrifère Lorrain, France)	100%
	Emilie Gueret	Caractérisation de la géométrie 3D de karsts	100%
2009-10	Rémi Vigouroux	Caractérisation de la géométrie 3D de karsts	80% (V. Henrion)

*Les co-encadrants en italique sont des doctorants que je co-dirige.

Les stages de master, plus longs, permettent d'aborder des sujets plus ambitieux (Tab. I.6). Ainsi, leurs résultats sont présentés oralement ou sous forme de poster à l'occasion du congrès annuel RING (anciennement Gocad) qui rassemble une audience internationale d'environ 100 personnes. Cela s'accompagne de l'écriture d'un article de 10 à 20 pages en anglais, publié dans les actes du congrès. Pour les doctorants, les masters et projets 3A sont aussi une occasion de tester leur capacités d'encadrement de travaux de recherche.

Tableau I.6 : Encadrements de M2. (O) indique une présentation orale et (P) un poster au congrès annuel RING/Gocad (audience internationale). Le symbole ^{t} désigne les étudiants ayant ensuite entrepris une thèse.

Année	**Etudiant**	**Sujet**	**%encadrement (co-encadrant*)**
		Depuis 2007 en tant que MCF dans l'équipe RING	
2015-16	^{t}Pauline Mourlanette	Prise en compte d'informations géologiques dans la simulation de systèmes karstiques par L-Systems (P)	50% (*G. Rongier*, P. Anquez)
	^{t}Margot De Baecque	Analyse de données sismiques présentant des systèmes chenalisés (P)	30% (*M. Parquer*, G. Caumon)
2014-15	^{t}Pierre Anquez	Simulation de karsts à l'aide de systèmes de Lindenmayer (O)	50% (*G.Rongier*)
	Damien Lavandier	Reconstruction 3D de conduits karstiques (P)	70% (*G.Rongier*)
2012-13	^{t}Clément Barthélemy	Simulation stochastique de karsts anastomosés (O)	100%
2011-12	^{t}Guillaume Rongier	Simulation stochastique de conduits karstiques contrainte aux connaissances géologiques (O)	100%
2010-11	^{t}Gaétan Bardy	Simulation stochastique de systèmes karstiques : conditionnement aux données (O)	80% (J. Pellerin)
2009-10	^{t}François Bonneau	Simulation stochastique de systèmes karstiques (O)	50% (V. Henrion)
2007-08	Jean-Baptiste Mathieu	Hydrogeological developments for Gocad streamline simulator (P)	50% (C. Antoine)
		2000-2003 en tant que doctorante au LAEGO	
2003-04	Mayouma Loumouamou	Modélisation hydrochimique du Bassin Sud de Briey-Longwy	50% (M. Buès, R. Fabriol)
2002-03	Claire Chargueron	Caractérisation de la dispersion au sein de colonnes. Expérimentation et interprétation	70% (M. Buès, R. Fabriol)
	Marion Blaise	Contribution à la compréhension de l'origine de la sulfatation de l'eau des réservoirs miniers ennoyés dans le bassin ferrifère lorrain : aspects chimiques et spatiaux du mécanisme réactionne	70% (M. Buès, R. Fabriol)
2000-01	Aurélie Labastie	Oxydation de la pyrite : Mise en place d'un dispositif expérimental	70% (M. Buès, R. Fabriol)

*Les co-encadrants en italique sont des doctorants que je co-dirige.

Encadrement de stages de M1 et équivalent

- ▷ *3 étudiants de M1*
- ▷ *8 étudiants en Projet de Recherche de 2e année Ingénieur*

Tableau I.7 : Encadrements de M1

Année	Univ.	Etudiant	Sujet	%encadrement (co-encadrant*)
2005-06	URCA	Sophie Hincelin	Évolution des relations nappe-rivière dans le bassin versant de la Vesle	100%
		Cédric Lambert	Étude des interactions nappe - rivière dans le bassin versant de la Vesle : réalisation d'un transec	100%
2002-03	ENSG	Aurélien Osnowycz	Comportement physico-chimique des intercalaires marneux de la formation ferrifère de Lorraine ; Essai de lessivage sous contrainte	60% (R. Fabriol)

En 2ème année (niveau M1) un stage d'initiation à la recherche, qui représente une charge d'au moins 60h de travail, est proposé à tous les étudiants ingénieurs de l'ENSG (Tab. I.8).

Tableau I.8 : Encadrements de projets de recherche de 2ème année ENSG

Année	Etudiant	Sujet	%encadrement (co-encadrant*)
2014-15	Thomas Monin	Automatisation du découpage de MNT	100%
2013-14	Maxim Torgonskiy	Calcul de bassins versants et application à la comparaison d'images	50%(G. Caumon)
2011-12	Aurore Plougoulen	Modélisation 3D du système karstique de Han-sur-Lesse	100%
	Lilas Vivin	Incertitudes sur les datations magnétostratigraphiques de sédiments d'Asie Centrale	33% (J. Charreau, F. Lallier)
	Victor Jullien		
2007-08	Nicolas Laurent	Modélisation de l'ennoyage des mines de fer lorraines à l'aide d'EPANET	100%
	Martin Pujol	Modélisation environnementale avec le logiciel Gocad	75% (C. Antoine)
	Bastien Decle		

Dans le cadre de mes fonctions à l'ENGEES, j'ai également été tutrice du stage de Licence Professionnelle Eau et Environnement de Denis Montanach (mai à août 2005) chez Ginger Environnement.

3.3 Rayonnement scientifique, Valorisation, Transfert

Congrès internationaux

- ▷ 24 communications (orales ou posters) dans des congrès internationaux
- ▷ 26 communications (orales ou posters) au RING Meeting (international)
- ▷ 12 communications (orales ou posters) dans des congrès nationaux

Membre des comités scientifiques et Organisation de Sessions :

- ▷ 9th Conference on Limestone Hydrogeology, 1-3 September 2011, Besançon, France : Organisation de la Session “Karst Network Analysis and Modelling”
- ▷ First EuroKarst Conference, 5-9 September 2016, Neuchâtel, Switzerland : Sélection des résumés, révision des articles et Chairwoman de la Session "Spatial data analysis and numerical modeling".

Par ailleurs, en tant que membre actif du groupe de recherche sponsorisé par le Consortium RING-Gocad, je participe chaque année à l’organisation du RING Meeting (anciennement Gocad Meeting) rassemblant à Nancy une centaine de scientifiques et industriels de tous pays, spécialistes de la géologie numérique et de la géomodélisation. Cet événement est l’occasion de présenter les avancées de notre équipe mais aussi de proposer aux partenaires industriels et académiques une vitrine pour leurs propres travaux. Le meeting propose 2 jours de congrès puis 2 jours de "trainings", qui sont des formations destinées à faciliter la prise en main par nos partenaires des outils que nous développons.

Activités éditoriales et Expertise d’articles

Je suis membre depuis juillet 2013 de l’*Editorial Advisory Board* du journal *Computers & Geosciences*. Àce titre, je participe chaque année à l’élection du "*Best Paper Award*" de *Computers & Geosciences* et j’ai également été juge pour le prix "*IAMG’s Computers and Geosciences Scholarship Award*" 2014 de l’IAMG (*International Association for Mathematical Geosciences*).

En septembre 2016, le nouveau bureau éditorial du journal *Computers & Geosciences* m’a sollicitée pour devenir *Associate Editor*.

Avec mon collègue Guillaume Caumon, j’ai été Éditrice Invitée d’un numéro spécial du journal *Mathematical Geosciences* consacré à la modélisation structurale 3D et paru en Novembre 2014. Àcette occasion nous avons du gérer l’appel à articles pour ce numéro spécial, nous avons traité environ 25 propositions d’articles, géré 13 articles soumis et organisé ce numéro comportant au final 6 articles (2 articles soumis dans le cadre du numéro spécial ont été publiés dans un numéro "normal" du journal).

En parallèle de ce gros travail d’édition, je suis régulièrement sollicitée pour la review d’articles par les journaux de rang A suivants : *Mathematical Geosciences*, *Computers & Geosciences*, *Hydrogeology Journal* et *Journal of Hydrology*.

Membre de Sociétés Savantes

- Membre permanent de l'*International Association of Mathematical Geosciences* (IAMG)
- Membre de l'*International Association of Hydrogeology* (IAH) - Comité Français d'Hydrogéologie (CFH)

Expertise de projets de recherche

En 2011, j'ai été engagée en qualité d'experte scientifique pour évaluer des projets DIM et SESAME déposés auprès de l'Unité Développement de la région Ile de France.

Collaborations à l'international

Mes activités de recherche sont essentiellement réalisées dans le cadre du Consortium de recherche RING-Gocad qui finance notre équipe de recherche RING - *Research for Integrative Numerical Geology*. En 2016, ce consortium comprenait 14 industries et 143 universités de tous pays [3]. Àce titre, nous entretenons des relations avec de nombreuses universités de tous pays. Néanmoins les liens sont plus forts avec certaines d'entre elles, ce qui se traduit par des séjours de nos étudiants là-bas, ou des visites de chercheurs. J'ai choisi de mettre ici l'accent sur les collaborations les plus importantes (en termes de pérennité et d'implications) :

- Suisse : Je travaille régulièrement avec Philippe Renard, professeur à l'Université de Neuchâtel (Suisse), et cette collaboration s'est concrétisée en 2012 par le lancement d'une thèse en cotutelle réalisée par G. Rongier et soutenue le 15 mars 2016.

- Belgique : De même je collabore fortement avec l'Université de Namur (Belgique) puisque je suis officiellement co-encadrante de la thèse de Lorraine Dewaide dont le promoteur dans cette université est le professeur V. Hallet.

- Turquie : Enfin, dans le cadre d'un projet de recherche commun avec l'Université de Pau et des pays de l'Adour (UPPA) portant sur la modélisation en contexte salifère, j'ai co-encadré un stage de terrain pour les étudiants de Master de l'ENSG en avril 2014 à Sivas, Turquie. Ce stage a été réalisé en partenariat avec les Professeurs Kaan Kavak et Haluk Temiz de l'Université de Sivas (Sivas Cumhuriyet Universitesi, Turquie). Àcette occasion, j'ai donné une formation sur la géomodélisation aux collègues turcs. J'ai également réalisé le modèle 3D d'un mini bassin, travail présenté à plusieurs congrès et qui a donné lieu à une publication dans le journal *Interpretation*.

Séminaires invités et Vulgarisation

J'ai réalisé plusieurs conférences sur invitation dans le cadre de séminaires d'Ecoles Doctorales :

- École Doctorale RP2E, 23 janvier 2003, Nancy : "Evolution chimique de l'eau lors de l'ennoyage des mines de fer lorraines"

[3] http ://ring.georessources.univ-lorraine.fr/consortium/members

- Ecole doctorale Envitam , janvier 2010, Namur, Belgique : "From numerical modeling of geological objects to environmental simulation by reactor networks"

Grâce au prix de thèse de la Région Lorraine obtenu en 2005, j'ai réalisé une série de conférences invitées au Japon en août 2006 "*Evolution of the quality of water in the abandoned mines of the lorrain iron basin. From laboratory experiments to in situ modelling*" :

- 2 août 2006 : Université de Saitama
- 7 août 2006 : Université de Tsukuba
- 9 août 2006 : Université d'Osaka

Dans le cadre des opérations liées à la célébration du centenaire de l'ENSG en 2008, j'ai également participé à une émission télévisée diffusée sur France 3 Lorraine : "Heureux qui communiquent. . . les sciences".

3.4 Liste complète des publications

Publications dans des revues à comité de lecture [4]

Les étudiants que je supervise sont soulignés

Articles publiés : ***12 Revues internationales (+ 1 éditorial), 1 Revue nationale.***

Collon P., Pichat A., Kergaravat C., Botella A., Caumon G., Ringenbach J.C., Callot J.P. (2016), 3D modelling from outcrop data in a salt tectonic context : Example from the Inceyol minibasin, Sivas Basin, Turkey. *Interpretation*, 4(3) :pp. SM17–SM31.

Rongier G., **Collon P.**, Renard P., Straubhaar J., Sausse J. (2016), Comparing connected structures in ensemble of random fields. *Advances in Water Resources*, 96 :pp. 145–169.

Collon P., Steckiewicz-Laurent W., Pellerin J., Gautier L., Caumon G., Reichart G., Vaute L. (2015), 3D geomodelling combining implicit surfaces and Voronoi-based remeshing : A case study in the Lorraine Coal Basin (France). *Computers & Geosciences*, 77 :pp. 29–43.

Dewaide L., Baele J.M., **Collon-Drouaillet P.**, Quinif Y., Rochez G., Vandycke S., Hallet V. (2014), Karstification in dolomitized Waulsortian mudmounds (Belgium). *Geologica Belgica*, 17(1) :pp. 43–51.

Merland R., Caumon G., Lévy B., **Collon-Drouaillet P.** (2014), Voronoi Grids Conforming to 3D Structural Features. *Computational Geosciences*, 18(3-4) :pp. 373–383.

Rongier G., **Collon P.** (2014), Conduits Karstiques en 3D : une méthode de simulation stochastique. *Karstologia*, 63(1) :pp. 58–60.

Rongier G., **Collon-Drouaillet P.**, Filipponi M. (2014), Simulation of 3D karst conduits with an object-distance based method integrating geological knowledge. *Geomorphology*, 217 :pp. 152–164.

[4] ORCID ID : 0000-0001-8505-4961. Scopus ID : 10840524800

Collon-Drouaillet P., Henrion V., Pellerin J. (2012), An algorithm for 3D simulation of branchwork karst networks using Horton parameters and A* Application to a synthetic case. *Geological Society, London, Special Publications*, 370(1) :pp. 295–306.

Caumon G., **Collon-Drouaillet P.**, Le Carlier de Veslud C., Viseur S., Sausse J. (2009), Surface-Based 3D Modeling of Geological Structures. *Mathematical Geosciences*, 41(8) :pp. 927–945.

Hamm V., **Collon-Drouaillet P.**, Fabriol R. (2008), Two modelling approaches to water-quality simulation in a flooded iron-ore mine (Saizerais, Lorraine, France) : A semi-distributed chemical reactor model and a physically based distributed reactive transport pipe network model. *Journal of Contaminant Hydrology*, 96(1-4) :pp. 97–112.

Collon P., Fabriol R., Buès M. (2006), Modelling the evolution of water quality in abandoned mines of the Lorraine Iron Basin. *Journal of Hydrology*, 328(3-4) :pp. 620–634.

Collon P., Fabriol R., Buès M. (2005), Evolution of water quality in the abandoned iron mines of Lorraine : towards a semi-distributed modelling approach. *Comptes Rendus Geosciences*, 337(16) :pp. 1492–1499.

Collon P., Fabriol R., Buès M. (2004), Ennoyage des mines de fer lorraines : impact sur la qualité de l'eau. *Comptes Rendus Geoscience*, 336(10) :pp. 889–899.

Numéro Spécial : 1
Caumon G., **Collon-Drouaillet P.** (2014), Special Issue on Three-Dimensional Structural Modeling. *Mathematical Geosciences*, 46(8) :pp. 905–908.

Article(s) en révision : *3 Revues internationales*

Collon P., Bernasconi D., Vuilleumier C., Renard P. (2016), Statistical metrics for the characterization of karst network geometry and topology *Geomorphology*, Acc. with revisions.

Rongier G., **Collon P**., Renard P. (2016). A geostatistical approach to the simulation of stacked channels. *Marine and Petroleum Geology*, Acc. with revisions.

Rongier G., **Collon P**., Renard P. (2016). Stochastic simulation of channelized sedimentary bodies using a constrained L-system. *Computers & Geosciences*, Submitted.

Conférences

Les étudiants que je supervise sont soulignés
$^{(o)}$ *présentation orale, * présentateur,* $^{(p)}$ *poster,* $^{(a)}$ *avec actes publiés (>2p),* $^{(\#)}$ *présentation invitée*

Internationales : *19 orales, 5 posters, dont 6 avec actes (> 2p.).*

$^{(o)}$ **Collon P.***, Rongier G., Anquez P., Mourlanette P. (2016), Karst simulation with Lindenmayer-systems and ODSIM. In : *EuroKarst 2016*, Neuchâtel, Suisse.

$^{(o)}$ **Collon P.***, Bernasconi D., Vuilleumier C., Renard P. (2016), Geometry and topology of karstic networks : a statistical analysis. In : *EuroKarst 2016*, Neuchâtel, Suisse.

$^{(o)}$ Parquer M.*, **Collon P.**, Caumon G. (2016a), Stochastic simulation of channel migration conditioned to subsurface data. In : *Geostats2016*, Valencia, Spain.

$^{(o,a)}$ Parquer M.*, **Collon P.**, Caumon G. (2016b), Conditioning channel backward migration modeling to seismic data. In : *78th EAGE Conference & Exhibition 2016*, June, 5p, Vienna, Austria.

$^{(o)}$ **Collon P.***, Pichat A., Kergaravat C., Botella A., Caumon G., Favreau O., Fuss G., Godefroy G., Lerat M., Mazuyer A. (2015), 3D modelling in salt tectonic context : the Crocodile mini-basin in Sivas (Turkey). In : *EGU General Assembly 2015*, vol. 17, pp. 12313-12313, Vienna, Austria.

$^{(p)}$ Rongier G.*, **Collon P.**, Renard P., Ruiu J. (2015a), Channel simulation using L-system, potential fields and NURBS. In : *EAGE - Petroleum Geostatistics 2015*, Biarritz, France.

$^{(p)}$ Rongier G.*, **Collon P.**, Renard P., Straubhaar J., Sausse J. (2015b), Quality analysis of geostatistical simulations through their connected structures. In : *EAGE - Petroleum Geostatistics 2015*, Biarritz, France.

$^{(p)}$ Rongier G.*, **Collon P.**, Renard P., Straubhaar J., Sausse J. (2014a), Exploring multiple-point realization quality through connected geobodies. In : *AAPG 2014 Annual Convention & Exhibition*, Houston, Texas, USA.

$^{(o)}$ Rongier G.*, **Collon-Drouaillet P.**, Filipponi M. (2014b), Incorporation of geomorphological information into the stochastic simulation of karst conduits. In : *GeoEnv 2014, 10th conference on Geostatistics for Environmental Applications*, Presses des Mines.

$^{(p)}$ Rongier G.*, **Collon-Drouaillet P.**, Renard P., Straubhaar J., Sausse J. (2014c), Assessment of multiple point simulation quality focusing on connected geobodies. In : *GeoEnv 2014, 10th conference on Geostatistics for Environmental Applications*, Presses des Mines.

$^{(o)}$ Renard P.*, Bernasconi D., Borghi A., **Collon-Drouaillet P.**, Vuilleumier C. (2013), Karst network geometry and topology : automatic classification of network geometry. In : *15th IAMG Conference*, Madrid, Spain.

$^{(o)}$ Royer J.J.*, Mejia-Herrera P., Caumon G., **Collon-Drouaillet P.** (2013), 3&4D Geomodeling Applied to Mineral Exploration. In : *12th SGA Biennial Meeting*, Uppsala.

$^{(o)}$ Dewaide L.*, **Collon-Drouaillet P.**, Quinif Y., Rochez G., Vandycke S., Hallet (2012), Karstification des mudmounds waulsortiens de Furfooz (Dinant, belgium). In : *Ghost-rock karst symposium*, Han-sur-Lesse, Belgium.

$^{(o)}$ Vuilleumier C., **Collon-Drouaillet P.*** (2012), Statistic Analysis of Karst Geometry. In : *GeoEnv 2012, 9th Conference on Geostatistics for Environmental Applications,Valencia, Spain*, pp. 325-326.

$^{(o,a)}$ **Collon-Drouaillet P.***, Pellerin J., Bardy G. (2011), Modeling karstic networks : introduction of speleogenetic hypothesis in stochastic simulations. In : *H2Karst - 9th Conference on Limestone Hydrogeology*, pp. 103-106.

$^{(o,a)}$ Merland R.*, Levy B., Caumon G., **Collon-Drouaillet P.** (2011), Building centroidal Vo-

ronoi tessellations for flow simulation in reservoirs using flow information. In : *SPE Reservoir Simulation Symposium*, pp. 141018-141029.

$^{(o,a)}$ Reichart G.*, Vaute L., **Collon-Drouaillet P.**, Buès M., Guillaume R., Vaute L. (2011), Modelling heat and salinity related convective processes in deep mining flooded wells. In : R.T. Rüde, A. Freund, C. Wolkersdorfer (Eds.), *Mine Water : Managing the Challenges.*, pp. 183-187.

$^{(p)}$ **Collon-Drouaillet P.***, Henrion V., Pellerin J. (2010), Constrained Stochastic Simulation of 3D Branchwork Karsts. In : *International Conference "Advances in Carbonate Exploration and Reservoir Analysis", Geological Society of London*, London, UK.

$^{(o,a)}$ Vaute L.*, le Pape P., **Collon-Drouaillet P.**, Fabriol R. (2010), Modelling the long-term evolution of groundwater's quality in a flooded iron-ore mine using a reactive transport pipe network model. In : C. Wolkersdorfer, A. Freund (Eds.), *International Mine Water Association Symposium – Mine Water and Innovative Thinking*, pp. 317–320, CBU Press, Sydney, Nova Scotia.

$^{(o)}$ Hamm V.*, **Collon-Drouaillet P.**, Fabriol R. (2008), Modelling the sulphate concentration of a flooded iron-ore mine with a network of chemical reactors (NCR) and a pipe network model (PNM). In : *Post-Mining 2008*, Nancy, France.

$^{(o)}$ **Collon P.***, Fabriol R., Buès M. (2005), A semi-distributed modelling of the evolution of groundwater quality in flooded mines in the Lorraine Iron Basin. In : *Post-Mining 2005*, Nancy, France.

$^{(o)}$ **Collon P.***, Fabriol R., Buès M. (2003), Predicting sulphate concentrations changes in the reservoir of a flooded iron mine. In : *SUITMA 2003*, Nancy, France.

$^{(o,a)}$ **Collon P.***, Fabriol R., Buès M. (2002a), Modelling changes in sulphate concentrations in discharge water from the abandoned iron mine of Saizerais. In : R. Ciccu (Ed.), *7th International Symposium on Environmental Issues and Waste Management in Energy and Mineral Production (SWEMP)*, pp. 917-924, Digita univ.

$^{(o,a)}$ **Collon P.***, Fabriol R., Buès M. (2002b), Chemical evolution of groundwater due to iron mine flooding in a non-acidic producing environment. In : R. Ciccu (Ed.), *7th International Symposium on Environmental Issues and Waste Management in Energy and Mineral Production (SWEMP)*, pp. 761-768, Digita univ.

Nationales : *9 orales, 3 posters.*

$^{(o)}$ **Collon-Drouaillet P.***, Pellerin J., Steckiewicz-Laurent W., Vaute L. (2014a), Les anciennes mines lorraines de charbon, réservoir géothermique du futur ? Modélisation 3D du bassin houiller lorrain. In : *Réunion des Sciences de la Terre 2014 (RST2014)*, Pau, France.

$^{(p)}$ **Collon-Drouaillet P.***, Pichat A., Kergaravat C., Botella A., Caumon G., Favreau O., Fuss G., Godefroy G., Lerat M., Mazuyer A., Parquer M., Charreau J., Callot J.p., Ringenbach J.c. (2014b), Modélisation 3D en contexte de Tectonique salifère : le mini-bassin du « Crocodile » à Sivas (Turquie). In : *Réunion des Sciences de la Terre 2014 (RST2014)*, Pau, France.

$^{(o)}$ **Collon-Drouaillet P.***, Rongier G., Le Mesnil M., Dewaide L., Hallet V. (2014c), Modélisation géométrique des systèmes karstiques : des réseaux aux conduits. In : *Réunion des Sciences de la Terre 2014 (RST2014)*, Pau, France.

$^{(\#o)}$ **Collon-Drouaillet P.** (2010), From numerical modeling of geological objects to environmental simulation by reactor networks. In : *Séminaire de l'école doctorale Envitam*, Namur, Belgique.

$^{(o)}$ **Collon-Drouaillet P.**, Fabriol R., Hamm V., Vaute L., Buès M. (2008), Etude et modélisation du drainage minier neutre dans le bassin ferrifère lorrain (BFL). In : *Réunion des Sciences de la Terre 2008 (RST 2008)*, Nancy, France.

$^{(o)}$ **Collon P.**, Fabriol R., Buès M. (2004), Evolution de la qualité de l'eau dans les mines abandonnées du bassin ferrifère lorrain. De l'expérimentation en laboratoire à la modélisation in situ. In : *Journées du PNRH (Programme Nationale de Recherche en Hydrologie)*, Bordeaux, France.

$^{(o)}$ **Collon P.**, Fabriol R., Buès M. (2003a), Evolution de la qualité de l'eau dans les mines abandonnées du bassin ferrifère lorrain. De l'expérimentation en laboratoire à la modélisation in situ. In : *Journée "Transferts Réactifs en Milieu Poreux"*, Nancy, France.

$^{(o)}$ **Collon P.**, Fabriol R., Buès M. (2003b), Variabilité minéralogique des intercalaires marneux du bassin ferrifère lorrain. Conséquences sur la qualité de l'eau dans la mine. In : *Après-Mine 2003*, Nancy, France.

$^{(o)}$ **Collon P.**, Fabriol R., Buès M. (2003c), Evolution chimique de l'eau d'une mine ennoyée en contexte de drainage minier neutre. In : *Colloque "Le Fil de l'eau"*, Nancy, France.

$^{(\#o)}$ **Collon P.**, Fabriol R., Buès M. (2003d), Evolution chimique de l'eau lors de l'ennoyage des mines de fer lorraines. In : *Séminaire de l'Ecole Doctorale RP2E*, Nancy, France.

$^{(o)}$ **Collon P.**, Fabriol R., Buès M. (2002a), Minéralisation de l'eau lors de l'ennoyage des mines de fer lorraines. In : *Journée du Réseau Génie Civil et Urbain (RGCU)*.

$^{(o)}$ **Collon P.**, Fabriol R., Buès M. (2002b), Minéralisation de l'eau lors de l'ennoyage des mines de fer de Lorraine. In : *Séminaire de l'Ecole Doctorale RP2E*.

Publications aux congrès RING (/Gocad)

Les étudiants que je supervise sont soulignés
$^{(o)}$ *présentation orale, * présentateur,* $^{(p)}$ *poster*

18 orales, 8 posters

Conférences annuelles à audience internationale mais restreinte aux sponsors (15 industries + 130 universités)

Toutes les présentations sont accompagnées d'actes en anglais (>2p., articles non soumis à relecture externe).

$^{(o)}$ **Collon P.***, Bernasconi D., Vuilleumier C., Renard P. (2016), What statistical metrics to characterize karst network geometry and topology ?. In : *2016 RING Meeting*, 29p., Nancy, France.

$^{(p)}$ De Baecque M.*, Parquer M., **Collon P.**, Caumon G. (2016), Morphological study of channelized systems Geometrical approach. In : *2016 RING Meeting*, 9p., Nancy, France.

$^{(o)}$ Laurent G.*, **Collon P.**, Golfier F., Royer J.J., Gruzdeva Y. (2016). A streamline-based approach to reactive transport simulation for in-situ bio-leaching of copper. In : *2016 RING Meeting*, 6p., Nancy, France.

$^{(p)}$ Mourlanette P.*, Anquez P.*, Rongier G., **Collon P.** (2016), Integration of geological knowledge in karstic network simulations with L-systems. In : *2016 RING Meeting*, 12p., Nancy, France.

$^{(o)}$ Parquer M.*, **Collon P.**, Caumon G. (2016), Reconstruction of channelized systems through a conditioned backward-migration method. In : *2016 RING Meeting*, 19p., Nancy, France.

$^{(o)}$ Anquez P.*, Rongier G., **Collon P.** (2015), Stochastic simulations of karst networks with Lindenmayer systems. In : *35thGocad Meeting*, 16p., Nancy, France.

$^{(p)}$ Lavandier D.*, Rongier G., **Collon P.** (2015), 3D reconstruction of karstic conduit from sparse laser data Case study : the Ox Bel ' Ha system , Yucatan , Mexico. In : *35thGocad Meeting*, 14p., Nancy, France.

$^{(o)}$ Parquer M.*, **Collon P.**, Caumon G., Rongier G. (2015), Toward more genetics concepts and data integration in channel simulation Channelized systems characterization. In : *35thGocad Meeting*, 16p., Nancy, France.

$^{(o)}$ Rongier G.*, **Collon P.**, Renard P. (2015a), A new application of L-systems to model channel system architecture and connectivity Using L-system for channel generation. In : *35thGocad Meeting*, 15p., Nancy, France.

$^{(p)}$ Rongier G.*, **Collon P.**, Renard P., Ruiu J. (2015b), Channel simulation using L-system, potential fields and NURBS. In : *35thGocad Meeting*, 5p., Nancy, France.

$^{(p)}$ Rongier G.*, **Collon P.**, Renard P., Straubhaar J., Sausse J. (2015b), Quality analysis of geostatistical simulations through their connected structures Indicators reflecting realization quality. In : *35thGocad Meeting*, 6p., Nancy, France.

$^{(o)}$ **Collon-Drouaillet P.***, Pichat A., Favreau O., Fuss G., Godefroy G., Lerat M., Mazuyer A., Parquer M., Caumon G., Charreau J., Callot J.p., Ringenbach J.c. (2014), 3D modelling in salt tectonic context : the Crocodile minibasin in Sivas (Turkey). In : *34th Gocad Meeting*, 1p., Nancy, France.

$^{(p)}$ Le Mesnil M.*, **Collon-Drouaillet P.**, Dewaide L., Mejia-Herrera P., Rongier G., Hallet V. (2014), Karst conduit generation : the Furfooz area case study (Belgium). In : *34th Gocad Meeting*, Section 2, 19p., Nancy, France.

$^{(o)}$ Rongier G.*, **Collon-Drouaillet P.**, Renard P. (2014), Channel axis simulation based on Lindenmayer systems. In : *34th Gocad Meeting*, 27 p., Nancy, France.

$^{(o)}$ Barthélémy C.*, **Collon-Drouaillet P.** (2013), Simulation of Anastomotic Karst Networks. In : *33rd Gocad Meeting*, Table 1, 13p., Nancy, France.

$^{(o)}$ Rongier G.*, **Collon-Drouaillet P.**, Renard P., Straubhaar J., Sausse J. (2013), Reproduc-

tion assessment of connected geobodies in multiple-point simulation. In : *33rd Gocad Meeting*, 32p., Nancy, France.

(o) Steckiewicz-Laurent W., **Collon-Drouaillet P.***, Pellerin J., Laurent G., Reichart G., Vaute L. (2013), Implicit modelling and variational remeshing tools : Application to the abandoned coal mines of Lorraine . In : *33rd Gocad Meeting*, 16p., Nancy, France.

(o) Rongier G., **Collon-Drouaillet P.*** (2012), Karst conduit generation : how to constrain ODSIM with geological knowledge ? In : *32nd Gocad Meeting*, 16p., Nancy, France.

(o) Vuilleumier C., **Collon-Drouaillet P.*** (2012), Statistical Analysis of Karst Geometry. In : *32nd Gocad Meeting*, 14p., Nancy, France.

(o) Bardy G.*, **Collon-Drouaillet P.**, Pellerin J. (2011), Stochastic simulation of karstic systems : data conditioning. In : *31st Gocad Meeting*, 11p., Nancy, France.

(o) **Collon-Drouaillet P.***, Pellerin J. (2011), Constrained stochastic simulation of 3D branchwork karsts. In : *31st Gocad Meeting*, 10p., Nancy, France.

(o) Bonneau F.*, Henrion V., **Collon-Drouaillet P.** (2010), Genetic-like modeling of karst network. In : *30th Gocad Meeting*, 20p., Nancy, France.

(o) Merland R.*, Lévy B., Caumon G., **Collon-Drouaillet P.** (2010), Building centroidal Voronoi tessellations for flow simulation in reservoirs using flow information. In : *30th Gocad Meeting*, 13p., Nancy, France.

(p) Vigouroux R., **Collon-Drouaillet P.***, Henrion V. (2010), New parameters for the characterization of karst geometry. In : *30th Gocad Meeting*, 10p., Nancy, France.

(o) **Collon-Drouaillet P.***, Royer J.J., Caumon G. (2008), 3D Reactive Transport Modelling : Coupling the GOCAD Streamline Simulator to the Geochemical PHREEQC Model. In : *28th Gocad Meeting*, 11p., Nancy, France.

(p) Mathieu J.B.*, **Collon P.**, Caumon G., Royer J.J. (2008), GOCAD StreamLab revisited for Hydrogeology applications. In : *28th Gocad Meeting*, 15p., Nancy, France.

Autres

Chapitres d'ouvrage

Royer J.J., Mejia-Herrera P., Caumon G., **Collon P.** (2015), *3D and 4D Geomodelling Applied to Mineral Resources Exploration - An Introduction*, chap. 4, pp. 73–89. Mineral resources reviews, Springer.

Caumon G., **Collon-Drouaillet P.** (2014), Editorial of the Special Issue on Three-Dimensional Structural Modeling. *Mathematical Geosciences*, 46(8) :pp. 905–908.

Rapports, mémoires

Collon P. (2003), *Évolution de la qualité de l'eau dans les mines abandonnées du bassin ferrifère lorrain. De l'expérimentation en laboratoire à la modélisation in situ*. Ph.D. thesis, Institut National Polytechnique de Lorraine.

Collon P. (2001), *Lessivage en colonne des intercalaires marneux de la formation ferrifère lorraine*. Tech. rep., BRGM-GISOS. LG.PC.SOS.PSI.RPRE.01.0465.A.

Collon P. (2001), *Étude minéralogique des intercalaires marneux de la formation ferrifère de Lorraine - Zone Nord du bassin de Briey*. Tech. rep., BRGM-GISOS. LG.PC.SOS.PSI.RPRE.01.0361.A.

Collon P. (2000), *Simulation de l'évolution de la concentration en sulfate dans l'eau de la mine de fer de Saizerais (Lorraine)*. Tech. rep., Mémoire de DEA Protection, Aménagement et Exploitation du Sol et du Sous-Sol (PAE3S), Institut National Polytechnique de Lorraine.

Ce rapport a également été publié sous forme de rapport "GISOS" sous les références suivantes :
Collon P., Fabriol R., Vaute L. (2000), *Simulation de l'évolution de la concentration en sulfate dans l'eau de la mine de fer de Saizerais (Lorraine)*. Tech. rep., BRGM/RP-50456-FR.

Distinctions

Janvier 2005 : 1^{er} prix de thèse scientifique 2004 de la Région Lorraine.

Réalisation d'un cycle conférences invitées au Japon (2006)
Collon P. (2006), Evolution of the quality of water in the abandoned mines of the lorrain iron basin. From laboratory experiments to in situ modelling.

- 2 août 2006 : Université de Saitama
- 7 août 2006 : Université de Tsukuba
- 9 août 2006 : Université d'Osaka

Grand public / vulgarisation

2008 : Heureux qui communiquent... les sciences. *Émission télévisée, France 3 Région Lorraine.*

Deuxième partie

Synthèse des activités de recherche

1

Introduction

Un *modèle* peut se définir comme une "*représentation schématique d'un processus ou d'une démarche raisonnée*" *(Larousse)*. Ainsi, la *modélisation* est un terme général qui rassemble aussi bien des conceptualisations de processus physiques (schémas, équations) que des reproductions de ces mêmes phénomènes au moyen de maquettes (modèles analogiques) ou de codes numériques (modèles numériques). La complexité des phénomènes physiques, couplée à la méconnaissance du milieu étudié et/ou des paramètres qui régissent son comportement, implique une nécessaire simplification de la réalité modélisée : c'est le rasoir d'Ockham ou principe de parcimonie[1]. Cette simplification peut se faire à différents niveaux, non exclusifs les uns des autres :

- la simplification physique privilégie les processus physiques dominants (p. ex., en ignorant certains processus d'interaction chimique eau-roche dans le cadre d'une étude hydrogéologique) ;
- la simplification géométrique ou spatiale consiste à faire abstraction de certaines structures (p. ex., en assimilant le milieu géologique à un réservoir homogène à grande échelle, ou en représentant par une double porosité une roche granitique fortement fracturée) et à adapter la paramétrisation du milieu à l'échelle de travail (p. ex., dans la définition des propriétés du milieu souvent considéré comme homogène) ;
- la simplification temporelle permet de ne s'intéresser qu'à un ensemble d'instants donnés, voire de ne considérer que le résultat final d'un processus continu sans chercher à reproduire l'intégralité des étapes qui l'ont généré.

Hydrogéologue de formation, mes travaux de recherche s'inscrivent dans le cadre de la modélisation numérique et se concentrent sur les objets géologiques que je

[1] "*Pluralitas non est ponenda sine necessitate* - Les multiples ne doivent pas être utilisés sans nécessité" [Ockham, XIV^{e} siècle]

qualifierais de "géométriquement complexes". Loin d'être un jugement de valeur, ce qualificatif sert surtout à les distinguer d'un milieu poreux considéré comme homogène à grande échelle et qui est le postulat de nombreux travaux en hydrogéologie ou en mécanique des milieux continus. En effet, ce qui distingue les bassins miniers, les karsts, les chenaux ou encore les objets issus de la tectonique salifère, c'est leur géométrie particulière, qui va fortement influencer la connectivité hydrodynamique en leur sein, et plus largement l'hétérogénéité des propriétés du milieu et tous les processus physiques qui s'y déroulent (p. ex., Hamm et al., 2008; Brouyère et al., 2009; Renard and Allard, 2013). L'objectif de mes travaux est donc de définir des méthodologies de modélisation numérique adaptées à ces réservoirs à géométrie complexe et ce, en fonction de l'échelle spatiale et du processus physique d'intérêt.

Bien que l'objet étudié soit ainsi central dans le processus de modélisation, les outils et les démarches scientifiques adoptées sont transverses. C'est pourquoi j'ai choisi d'organiser la présente synthèse, non par objet géologique d'intérêt, mais par approche méthodologique. Ce choix vise également à élargir le spectre des recherches présentées et des perspectives qu'elles ouvrent au-delà des objets géologiques abordés. Ainsi, l'accent est tout d'abord mis sur le lien entre la stratégie de modélisation retenue et le phénomène étudié lorsque deux processus principaux, ou plus, entrent en jeu (Chapitre 2). Quel que soit le cadre de l'étude, les données de terrain ou de laboratoire sont à chaque fois au cœur de la démarche de modélisation. Dans certains contextes, le processus physique observé est fortement dépendant de la géométrie des structures géologiques ou anthropiques, qui va notamment gouverner la connectivité statique et dynamique. Le chapitre 3 est ainsi consacré à l'analyse et à la caractérisation des objets géologiques à géométrie complexe. Par ailleurs, le caractère parcellaire, la dispersion et les différences de résolution des données empêchent généralement de les interpréter de manière univoque. De ce fait, lors de la reconstruction 3D de milieux géologiques, l'objectif n'est pas de trouver *la* solution unique, mais d'identifier *une/des* solutions honorant les données disponibles et rendant compte de la réalité, de sa complexité et des incertitudes qui lui sont associées. Cet aspect est l'objet du chapitre 4, consacré aux méthodes de simulation stochastique qui ont été développées pour la modélisation géométrique d'objets géologiques dits *connectés*. Enfin, le chapitre 5 dresse une rapide conclusion et présente les perspectives de ces travaux à court et moyen termes.

2

Une stratégie de simulation adaptée au processus d'intérêt

Le sous-sol n'est pas constitué de matériaux inertes : l'eau et les fluides qui y circulent interagissent chimiquement, thermiquement et mécaniquement avec cette matrice poreuse. Ainsi, la composition chimique d'une eau minérale reflète les terrains traversés par les eaux météoriques jusqu'à leur émergence à la source captée (figure II.1). De ce fait, tout changement de l'environnement géologique va impacter non seulement les circulations de fluides souterrains mais également leur composition

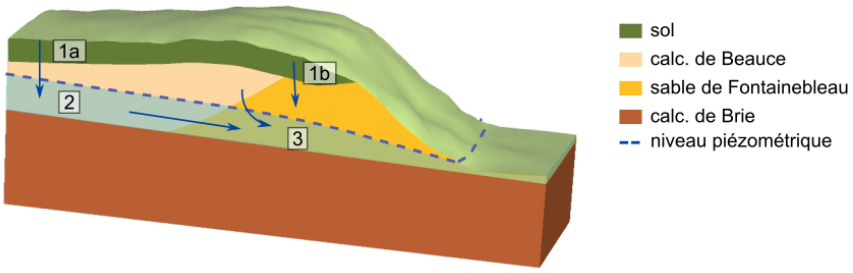

	cond	pH	Eh	Ca	Mg	Na	K	HCO3	Cl	SO4	SiO2	Al	Fe
1a	430	7.8	480	**66**	0.9	7.5	2.2	100	45.4	33.1	1.5	0.04	0.19
1b	**120**	4.7	495	7	0.5	5.7	1.9	-	8.5	22.8	3.1	**3.94**	**0.26**
2	630	6.5	425	**115**	3.9	7.7	3.6	260	19	12	**14**	0.01	0.11
3	490	6.2	415	88	3.2	6.4	0.3	244	13.5	5.8	10.2	-	0.13

Figure II.1 : Principes de l'équilibre eau-roche dans le milieu souterrain : la composition de l'eau reflète les sols et les roches qu'elle a traversés. 1a- sol calcaire, 1b- sol sableux, 2- nappe dans le calcaire de Beauce, 3- nappe dans les sables de Fontainebleau. *Données de M. Thiry.*

chimique. Les fluides vont également altérer ou précipiter des phases minérales, marquant ainsi le milieu géologique par leur passage.

La modélisation 3D du transport réactif est un défi scientifique avec de nombreux champs d'applications, aussi bien dans la gestion des ressources naturelles que dans l'ingénierie de l'environnement. De nombreux scientifiques développent des techniques de plus en plus avancées pour simuler le plus rigoureusement possible le transport réactif en milieu poreux. MacQuarrie and Mayer (2005); Steefel et al. (2005, 2015) proposent des revues complètes des techniques existantes. La majorité d'entre elles utilisent une approche "spatialisée" qui implique le calcul des flux et des concentrations en éléments chimiques dans chaque maille de l'objet modélisé. Cette approche nécessite de grands temps de calcul qui conduisent le plus souvent les modélisateurs à simplifier la chimie ou l'hétérogénéité de leurs systèmes. Des interactions fluides-roches et des espèces chimiques secondaires mais importantes peuvent ainsi être négligées. Par ailleurs, certains contextes géométriques, comme la présence de nombreux drains souterrains interconnectés, peuvent fortement complexifier les écoulements souterrains. Si les questionnements pratiques portent sur la chimie de l'eau à l'échelle des bassins versants, il peut alors être judicieux de développer des démarches de modélisation alternatives, fonctions du processus physique de prime intérêt.

2.1 Réacteurs en réseaux : la chimie au cœur du modèle

Lorsque l'intérêt porte sur la composition chimique du fluide en sortie d'un système souterrain, les réacteurs en réseaux permettent d'intégrer une cinétique chimique complète dans un modèle numérique en simplifiant fortement le processus de transport, c'est-à-dire en s'affranchissant partiellement de la spatialisation du phénomène. J'ai développé et démontré l'intérêt de cette approche dans l'étude du Bassin Ferrifère Lorrain (BFL).

Les méthodes d'exploitation minière ont la particularité de modifier profondément les caractéristiques du sous-sol (figure II.2) :

- d'un point de vue structural et hydrologique : puisqu'elles transforment un milieu initialement poreux en un réseau complexe de galeries souterraines (où la perméabilité est infinie) entrecoupées de piliers et d'intercalaires (milieux poreux à faible perméabilité) ;
- d'un point de vue géochimique : puisque le milieu initialement réducteur et isolé devient un milieu oxydant et ouvert ;
- d'un point de vue mécanique : puisque le creusement des galeries modifie les contraintes supportées par les roches.

Ces phénomènes doivent être pris en compte pour comprendre et modéliser l'évolution de la composition des roches, des gaz et des fluides dans ce type de milieu, que ce soit pendant l'exploitation ou lors de "l'après-mine".

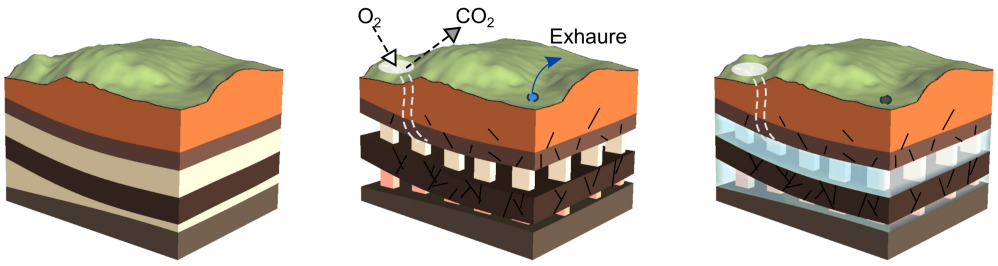

(a) Avant l'exploitation (b) Pendant l'exploitation (c) Après l'exploitation

Figure II.2 : Impact d'une exploitation minière sur le sous-sol : (a) à l'état initial le milieu est caractérisé par un état d'équilibre chimique, thermique et mécanique ; (b) pendant l'exploitation l'ouverture des galeries associée aux pompages d'exhaure entraîne l'apparition de conditions oxydantes et d'inter-connections hydrauliques entre les différents niveaux auparavant isolés ; (c) après l'arrêt de l'exploitation, la cessation de l'exhaure s'accompagne d'un ennoyage rapide des niveaux exploités, entraînant la mise en solution de certaines phases minérales néo-formées. L'eau peut alors avoir une forte charge acide et/ou polluante.

Mes travaux de DEA puis de thèse avaient pour objectifs (i) d'affiner la compréhension des mécanismes contrôlant l'évolution chimique de l'eau pendant et après l'ennoyage des réservoirs miniers lorrains et (ii) de fournir les éléments de base d'un simulateur hydro-chimique pour l'élaboration d'un modèle de gestion de la ressource en eau. La partie expérimentale a consisté en une étude minéralogique précise d'échantillons du bassin ferrifère lorrain (BFL), des essais en réacteurs fermés, des expériences de lessivage de roche en colonne et des expériences de traçage. Ceci a permis de caractériser les matériaux rocheux et d'identifier les réactions chimiques dominantes. Les résultats expérimentaux ont servi à construire un modèle chimique cinétique regroupant des réactions de dissolution/précipitation de minéraux, des réactions de complexation des ions dans l'eau, les réactions de dissolution/dégazage de l'O_2 et du CO_2 et des réactions d'échanges cationiques. Au final, le modèle comprend 50 réactions et 12 éléments chimiques et explique les observations ponctuelles faites dans le réservoir minier (Collon et al., 2004). Ces travaux ont permis de proposer des schémas réactionnels simples et validés par l'expérimentation, replacés dans un scénario en deux phases pour expliquer le drainage minier neutre observé dans le BFL (figure II.3). La première phase correspond à l'ouverture de la mine et à son exploitation qui place le milieu en conditions oxydantes. La seconde phase correspond à l'ennoyage des travaux miniers et implique la dissolution des minéraux néoformés lors de la précédente phase. Bien que développés sur un cas d'étude spécifique, ces schémas réactionnels constituent une des seules références publiées sur le drainage minier neutre (p. ex., Pettit et al., 1999; Kirby and Cravotta, 2005; Heikkinen et al., 2009), la plupart des études s'intéressant au drainage minier acide.

Pour reproduire l'évolution de la concentration de l'eau en sortie du réservoir

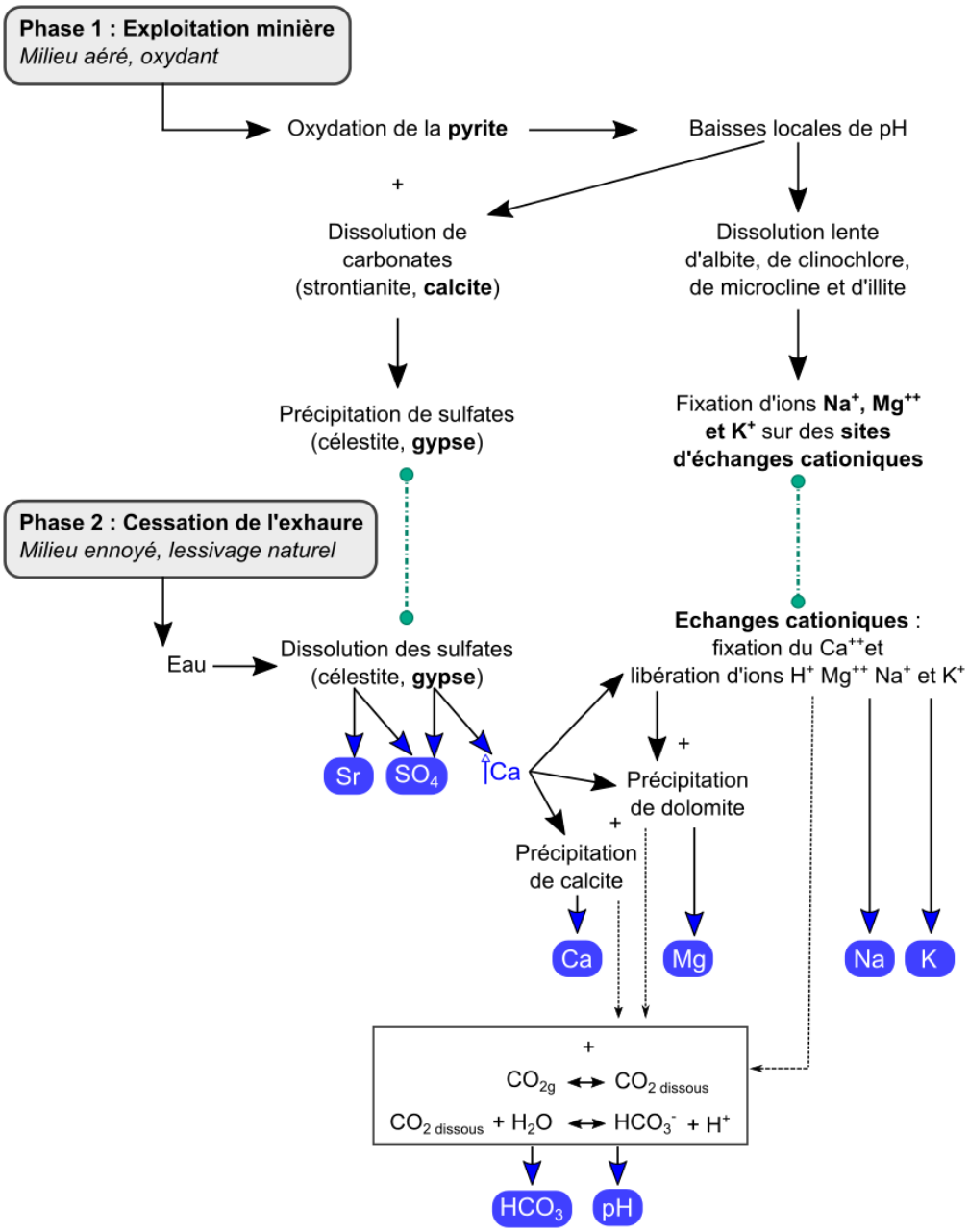

Figure II.3 : Schéma illustrant les deux phases de réactions chimiques expliquant l'évolution de la composition chimique de l'eau dans le cadre du drainage minier neutre qui s'opère dans le bassin ferrifère lorrain. En bleu sont indiqués les éléments en solution caractéristiques de la composition de l'eau souterraine.

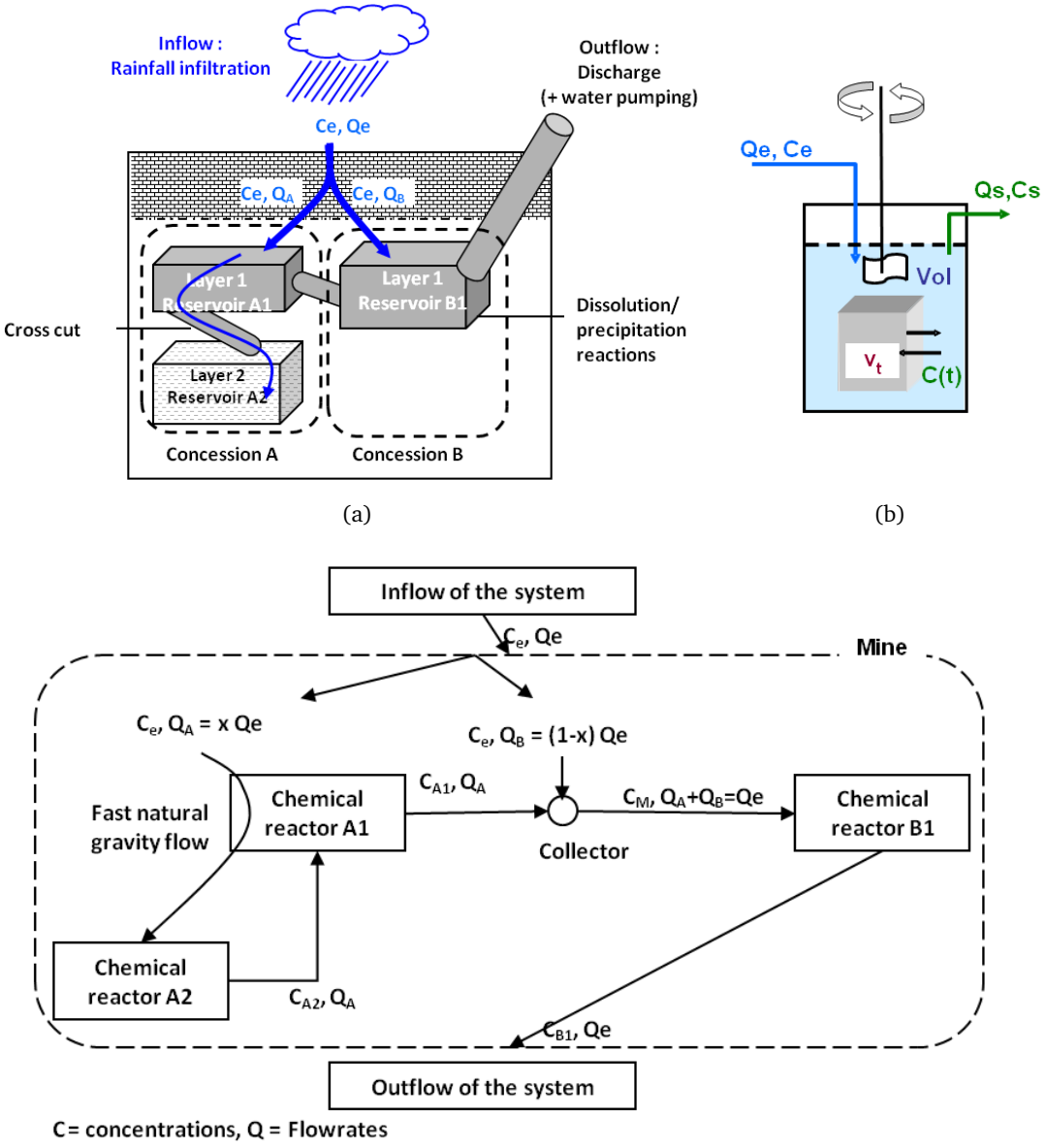

Figure II.4 : Principe de modélisation des réservoirs miniers selon l'approche de réacteurs en réseaux (Collon et al., 2006) : (a) modèle conceptuel d'une mine ; (b) schéma d'un réacteur ; (c) modèle de réacteurs en réseaux correspondant.

minier, nous avons ensuite proposé d'intégrer ce modèle chimique détaillé dans un *mélangeur parfait*, qui constitue un réacteur chimique, et d'assembler différents réacteurs en réseaux. Cette approche s'inspire de la méthode d'assemblage de réacteurs chimiques décrite par Villermaux (1993) et déjà utilisée pour modéliser le transport en milieu poreux (Jauzein et al., 1989). De manière générale, elle consiste à représenter le milieu comme un système géochimique et hydrodynamique intégré. Chaque réacteur est la représentation conceptuelle d'une entité individuelle de la totalité du système (figure II.4b). Lorsque l'eau circule dans les réservoirs, elle réagit avec les minéraux de la roche et change de composition. Un réacteur est donc défini par

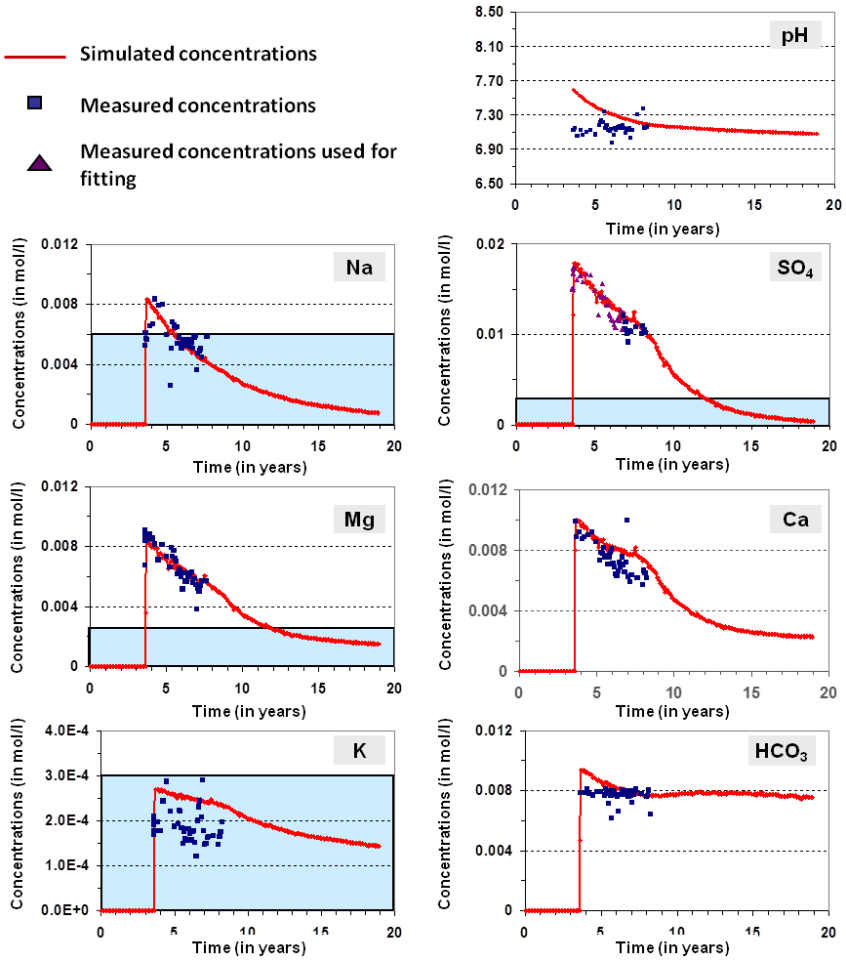

Figure II.5 : Concentrations mesurées et concentrations simulées par le modèle de réacteurs en réseaux au point de débordement du bassin sud du BFL (modifié d'après Collon et al. (2006)). La zone bleu correspond à la concentration maximale autorisée pour l'alimentation en eau potable. Elle n'est pas indiquée pour le Ca et le HCO_3 car dans ces deux cas la norme est toujours respectée.

l'équation suivante :

$$Q_s C_{s,i} = Q_e C_{e,i} + Vol_t v_{t,i} - d\frac{Vol_t C_{t,i}}{dt}$$

où Q_e , $C_{e,i}$, Q_s et $C_{s,i}$ désignent les débits et concentrations de l'élément i en entrée et sortie, Vol_t et $C_{t,i}$ le volume d'eau et la concentration en i dans le réacteur à l'instant t, et $v_{t,i}$ la vitesse de production d'un élément chimique i dans la solution due aux interactions avec la roche.

Dans cette approche, le transport de fluide se limite donc à un simple échange de matière (débit, concentration) entre différents réacteurs qui symbolisent chacun une zone entière du réservoir (figure II.4c). Il s'agit donc d'une simplification spatiale, en partie justifiée par la difficulté à modéliser correctement le transport de fluide à l'échelle d'un bassin pluri-kilométrique dans ce milieu particulier que sont les mines. La particularité des mines ennoyées est en effet de juxtaposer des drains (galeries ouvertes), une matrice rocheuse (piliers, toit et mur des formations) et des zones effondrées (liées au foudroyage). Bien que simplificatrice, cette technique des réacteurs en réseaux a permis de reproduire l'évolution des concentrations des éléments majeurs de l'eau au point de débordement de la zone Sud du bassin ferrifère lorrain, ennoyée depuis 1998 (figure II.5). Il a ainsi été démontré qu'une décroissance naturelle de la concentration des éléments polluants dans l'eau s'opérait. Nous avons également estimé le temps nécessaire pour que la composition de l'eau redevienne conforme aux normes pour l'alimentation en eau potable (Collon, 2003; Collon et al., 2006).

Par la suite, j'ai poursuivi ces travaux, en collaboration avec mes collègues du BRGM, et tenté de raffiner la spatialisation en assemblant un plus grand nombre de réacteurs pour générer un modèle semi-distribué. À partir des cartes d'exploitation et des altitudes des formations exploitées, le bassin minier Sud a été divisé en plusieurs réservoirs alors supposés homogènes. Bien qu'encourageants, les résultats obtenus ont démontré la nécessité de préciser l'organisation spatiale des flux d'eau pour reproduire les concentrations dans les différents puits de contrôle disponibles dans ce cas d'étude (Collon et al., 2005). C'est pourquoi nous avons développé une approche alternative et complémentaire simplifiant la chimie pour préciser l'organisation spatiale du système : l'approche par réseaux de tubes.

2.2 Réseaux de tubes : vers la spatialisation

Peu de travaux avaient été entrepris pour modéliser l'après-mine, et la plupart d'entre eux s'attachaient alors à reproduire l'hydrodynamique de l'ennoyage des travaux miniers (Sherwood and Younger, 1994; Adams and Younger, 1997). Pour pouvoir décrire spatialement la mine, nous avons donc développé, avec Virginie Hamm et Robert Fabriol (BRGM), une approche par *réseaux de tubes* en utilisant le code EPANET2 (Rossman, 2000). Ce code, mis à disposition par l'USGS, a été initialement conçu pour modéliser/gérer les réseaux d'approvisionnement en eau potable des villes. Nous y avons d'abord introduit la possibilité d'interactions chimiques au niveau de chaque

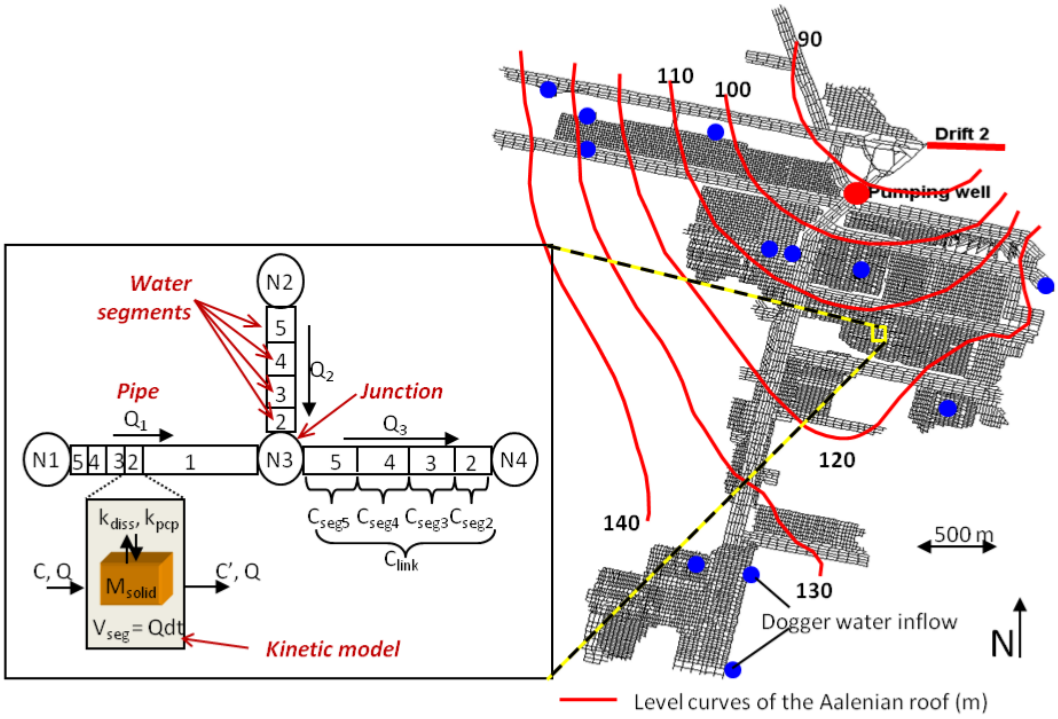

Figure II.6 : Modélisation de la mine de Saizerais (Lorraine, France) par réseaux de tubes (modifié d'après Hamm et al. (2008)).

tube du réseau. Dans cette approche, l'eau est contenue intégralement et ne circule que par les tubes, qui représentent les galeries du système. Le modèle considère les tubes comme saturés, il est impossible de ce fait de modéliser la période d'ennoyage du réservoir minier, ce qui était possible avec les réacteurs en réseaux.

Pour tester cette méthodologie nous avons utilisé la mine de Saizerais comme cas d'étude (Hamm et al., 2008). Son extension spatiale limitée (6 km^2), la disponibilité de plans miniers détaillés et de chroniques de suivi de la composition chimique de son eau depuis 20 ans en faisait en effet un sujet de choix. L'intégralité des plans miniers a été digitalisée, aboutissant à un réseau de 19 075 tubes et 10 470 noeuds (figure II.6). Pour obtenir un modèle de réseaux de tubes robuste, nous avons en revanche simplifié le modèle chimique en utilisant un modèle équivalent de dissolution-précipitation du sulfate, élément posant problème pour la potabilité de l'eau. Pour établir ce modèle chimique simplifié, deux modèles de réacteurs en réseaux de la même mine de Saizerais ont été utilisés : l'un avec une chimie complète, permettant de calibrer les paramètres physiques des réservoirs (surfaces d'échange, ...), l'autre avec une réaction simplifiée permettant de calibrer les paramètres cinétiques équivalents à la version complète.

Dans ce travail nous avons pu ainsi démontrer l'intérêt et la complémentarité des deux techniques (Hamm et al., 2008) :

- l'approche par réacteurs en réseaux permet une compréhension fine de la

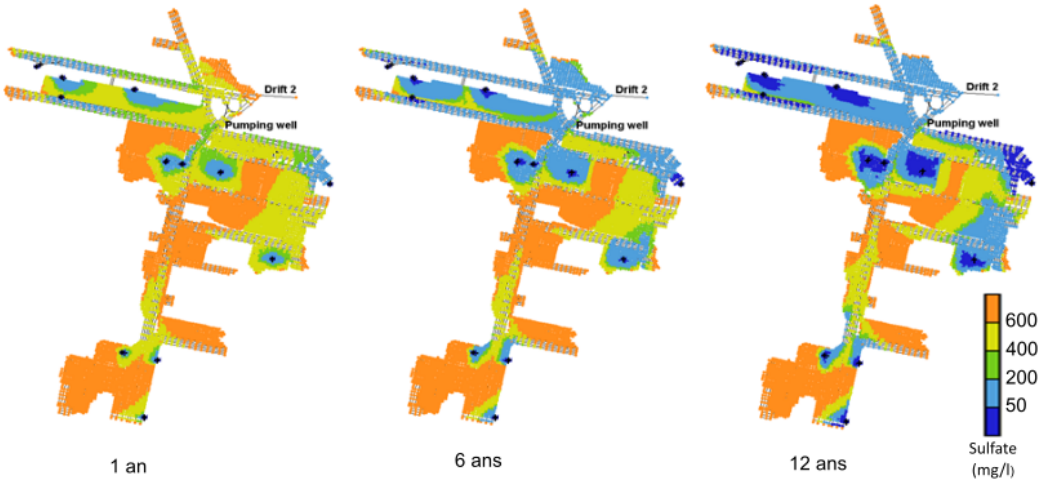

Figure II.7 : Simulation de l'évolution de la concentration en sulfate dans la mine de Saizerais par réseaux de tubes (modifié d'après Hamm et al. (2008)).

chimie du réservoir et intègre la phase d'ennoyage du réservoir minier ;

- l'approche par réseaux de tubes permet, elle, de mieux comprendre l'impact des circulations d'eau sur l'évolution des concentrations dans l'espace et d'estimer plus finement les différentes vitesses de renouvellement des volumes d'eau selon leur localisation (figure II.7).

Bien que l'approche par réseaux de tubes paraisse être, dans le cas de Saizerais, une solution intéressante pour la modélisation spatialisée en système minier, elle nécessite une connaissance complète des plans miniers et un travail colossal de digitalisation. Elle devient alors impossible à mettre en place à l'échelle d'un bassin minier entier comme le bassin Sud lorrain (plus de 139 km² de surface exploitée (Collon, 2003)). Ceci nous a finalement conduit, avec Laurent Vaute et Robert Fabriol à développer une approche mixte. Celle-ci utilise le modèle de réseaux de tubes développé avec EPANET 2, mais intégre les réactions chimiques au niveau de réservoirs (*tanks*) qui représentent des domaines miniers.

Après une étude plus détaillée des circulations fluides dans le système, un nouveau modèle semi-distribué a ainsi pu être développé, dans le cadre du stage de Pierre Le Pape, sur le bassin minier Sud (Vaute et al., 2010). Trente-trois unités fonctionnelles, c'est-à-dire des zones de mine ennoyées considérées comme indépendantes des réservoirs voisins, ont été définies (figure II.8). Chaque zone est en effet isolée par des failles ou des zones inexploitées de la mine qui constituent ici des barrières hydrauliques. Elles sont par ailleurs connectées entre elles par quelques galeries minières. Chaque unité fonctionnelle comporte un réacteur chimique qui correspond aux zones effondrées de l'unité - où se produisent les réactions chimiques - et un tube sans chimie qui représente les zones de galeries - où l'eau en contact avec la formation ferrifère ne réagit que très peu. Le modèle chimique utilisé ici est identique au modèle simplifié que nous avions développé pour Saizerais (Hamm et al., 2008).

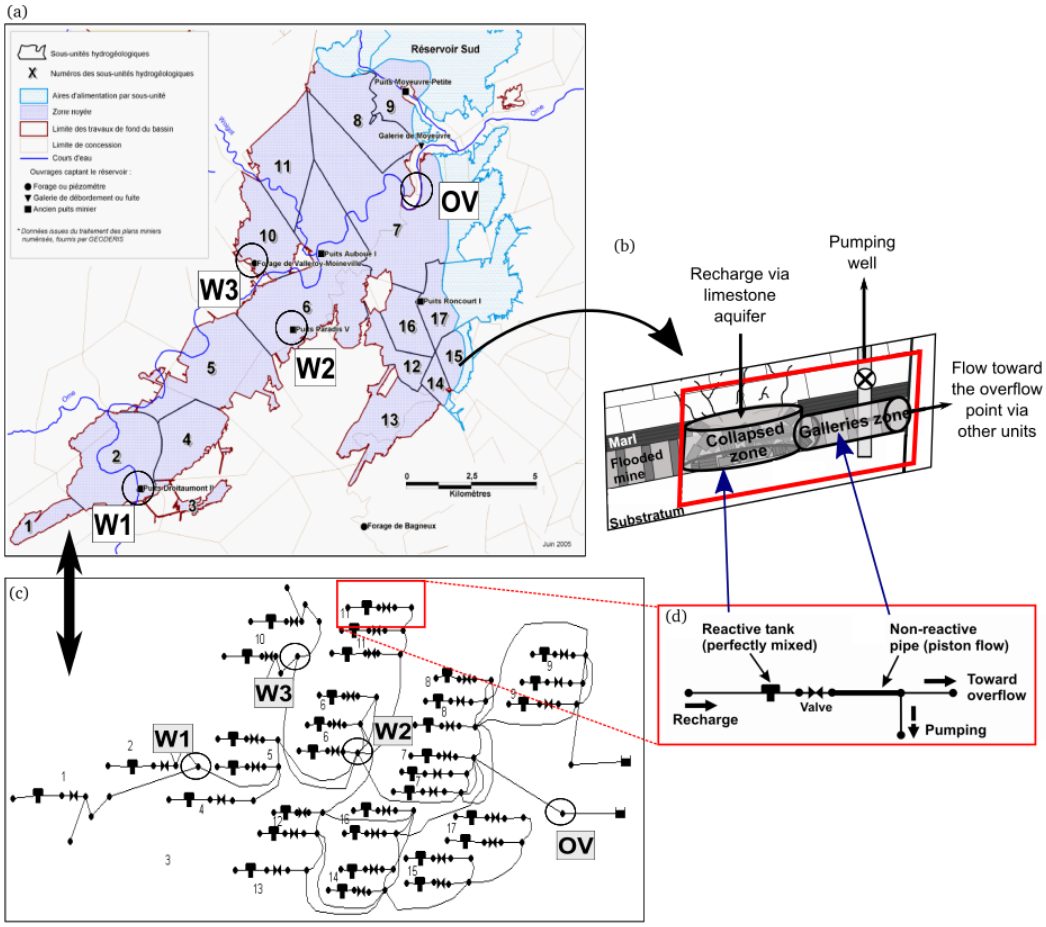

Figure II.8 : Modélisation semi-spatialisée de la partie Sud du bassin ferrifère lorrain (modifié d'après Vaute et al. (2010)) : (a) division du bassin en unités fonctionnelles (certaines zones possèdent des unités superposées) ; (b) schéma d'une unité fonctionelle et (d) son équivalent dans le modèle EPANET ; (c) Représentation du réseau EPANET correspondant à l'image (a).

Cette approche, plus détaillée et conforme à la réalité des connections hydrauliques, a alors permis une meilleure reproduction des concentrations en sulfate observées aux 3 puits disponibles et au point de débordement du bassin (figure II.9).

2.3 Approches spatialisées : un juste équilibre entre simplification physique et géométrique

2.3.1 Approche par lignes de courant

Une autre façon de simplifier le couplage entre transport et réactions chimiques est d'utiliser une approche par lignes de courant.

Le principe de la simulation d'écoulement sur lignes de courant est de découpler

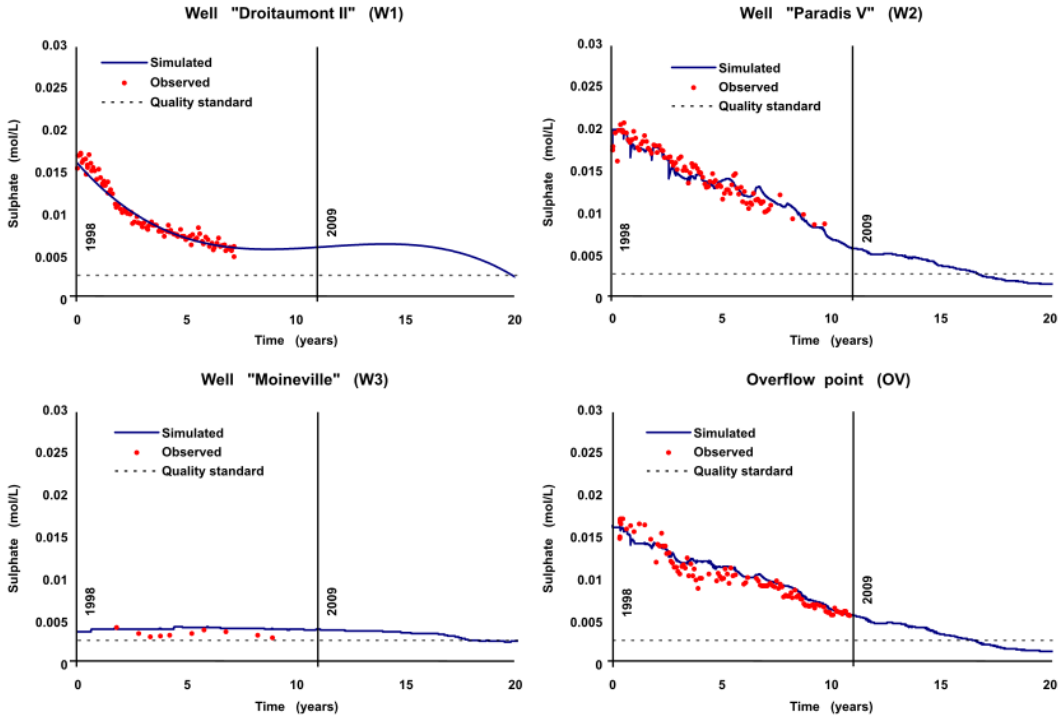

Figure II.9 : Concentrations simulées aux points de contrôle du bassin Sud (modifié d'après Vaute et al. (2010)).

un problème complexe tridimensionnel en un ensemble de sous-problèmes dont certains sont traités de manière unidimensionnelle. En effet, les champs de pression et de vitesse sont tout d'abord calculés sur la grille tridimensionnelle. Un certain nombre de lignes de courant sont alors calculées dans la grille et les propriétés sont transférées sur ces lignes, caractérisées par un "temps de vol". Les équations de transport sont alors résolues le long de ces lignes de courant avec de courts pas de temps, et les propriétés résultantes sont transférées à leur tour sur la grille 3D ainsi mise à jour.

Cette méthode a été développée pour modéliser efficacement le transport dans les systèmes très hétérogènes où l'advection domine (Batycky, 1997; Batycky et al., 1997; Crane and Blunt, 1999; Voillemont and Royer, 2002; Voillemont, 2003; Fetel et al., 2004). Elle a ensuite été étendue pour mieux tenir compte de la diffusion et de la dispersion (Obi and Blunt, 2004) et également adaptée aux réservoirs fracturés (Donato et al., 2004). Les plus récents développements permettent de simuler des écoulements diphasiques non-isothermes dans des réservoirs d'hydrocarbures (Siavashi et al., 2014).

Nous avons appliqué cette technique aux calculs géochimiques en couplant le code PhreeqC (Parkhurst and Appelo, 1999) au simulateur d'écoulement par volumes finis et lignes de courant *StreamLab* (Fetel et al., 2004; Fetel, 2007) dans le géomodeleur Gocad (Collon-Drouaillet et al., 2008). De larges fonctionnalités sont en effet offertes

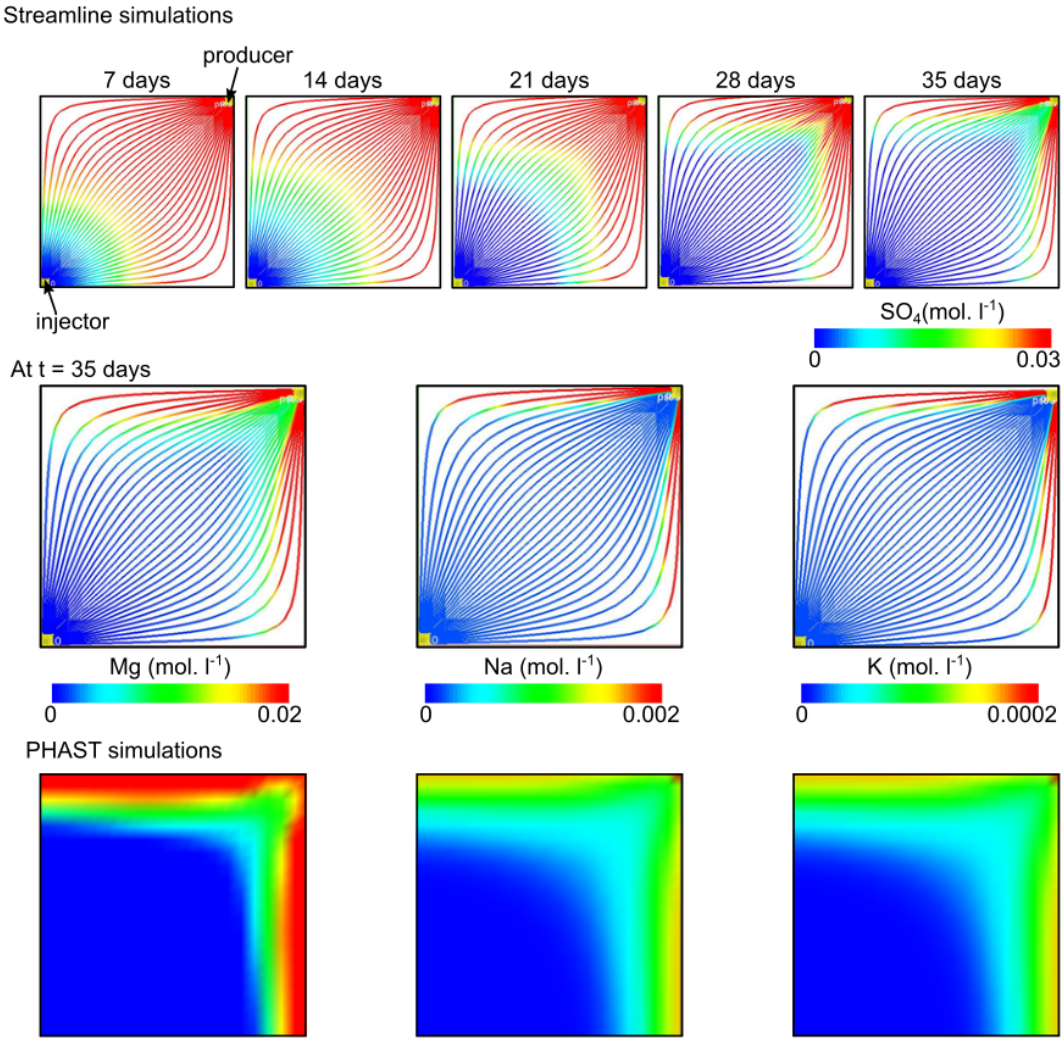

Figure II.10 : Concentrations en S, Mg, Na, et K modélisées avec le simulateur par lignes de courant (modifié d'après Collon-Drouaillet et al. (2008)). Pour pouvoir comparer avec le logiciel PHAST (en bas), le cas synthétique présenté ici correspond à une grille cartésienne de 20 x 20 x 1 cellules représentant un domaine de 200 m x 200 m x 25 m. Le milieu est homogène isotrope et correspond à une roche de composition identique aux travers-bancs du bassin ferrifère lorrain, riches en gypse, dans lesquels on injecte une eau à l'équilibre avec les calcaires du Dogger sus-jacents.

par le module de transport 1D de PhreeqC qui intègre les processus i) de diffusion, ii) d'advection, iii) d'advection et de dispersion et iv) d'advection et de dispersion avec diffusion dans des zones "d'eau morte". Tous ces processus peuvent y être combinés avec les réactions - cinétiques ou à l'équilibre - de la base de données de PhreeqC. De manière complémentaire, les milieux construits avec le géomodeleur Gocad peuvent avoir des géométries complexes. Plis, failles, biseaux sédimentaires, etc. sont autant de structures géologiques difficiles à générer (voire impossibles) avec les outils de modélisation actuellement couplés avec PhreeqC, comme le logiciel PHAST (Parkhurst et al., 2010). PHAST utilise en effet des grilles cartésiennes pour résoudre les équations d'écoulement et de transport par différences finies. Par ailleurs, les outils géostatistiques disponibles dans le géomodeleur facilitent la génération de milieux hétérogènes. Les outils permettant la visualisation de la composition chimique des roches et des fluides en 3D ont également été développés.

Bien que testée avec succès sur des cas théoriques simples (figure II.10), la méthodologie proposée dans ces travaux nécessite encore d'être perfectionnée pour permettre une application à des systèmes géologiques à géométrie complexe ou présentant des propriétés anisotropes (Collon-Drouaillet et al., 2008). Des cas d'application en contexte de circulation de fluides minéralisateurs sont envisagés dans le cadre du Labex RESSOURCES21. Dans l'immédiat, c'est dans le cadre du projet

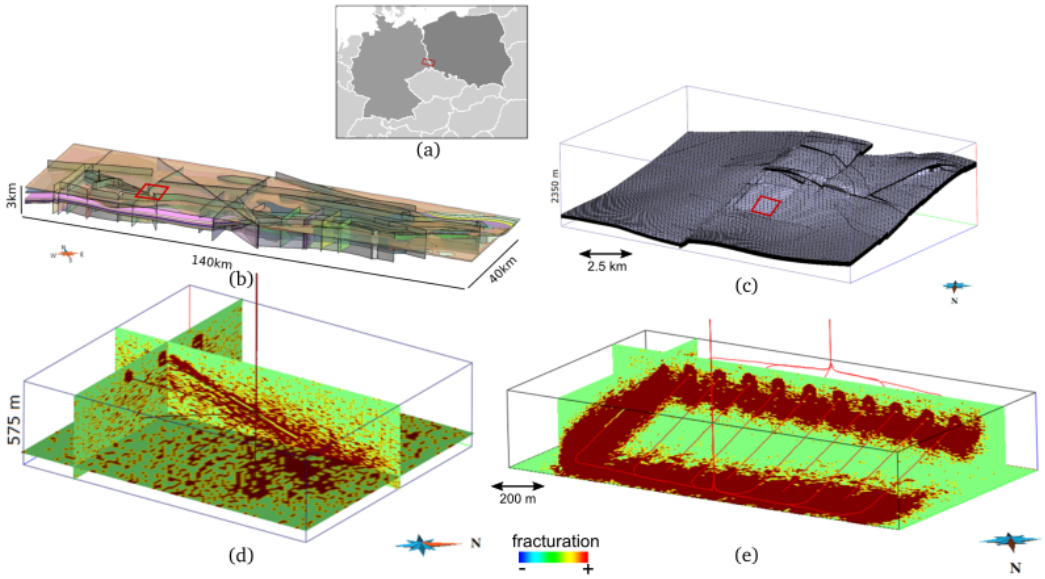

Figure II.11 : Modèles géologiques développés pour l'extraction de cuivre par bio-lixiviation in situ (modifié d'après Laurent et al. (2016)) : (a) localisation de l'aire d'investigation ; (b) modèle structural de la zone A avec un exemple de zone cible (rectangle rouge) ; (c) grille stratigraphique de la zone cible B avec la localisation des puits (rectangle rouge) ; (d) et (e) exemples de positionnement des puits (respectivement designs radial et rectangulaire) et de la fracturation hydraulique correspondante calculée selon les critères développés par Royer (2014).

européen BIOMORE que les premières applications sont envisagées (post-doctorat de Gautier Laurent). Ce projet vise à estimer l'efficacité d'une bio-lixiviation in-situ pour exploiter les métaux dans des zones minéralisées profondes tout en limitant l'impact sur l'environnement. Le projet se focalise actuellement sur la formation du Zechstein dans les dépôts du Kupferschiefer (Kucha and Pawlikowski, 1986; Kutschke et al., 2015). Le procédé de bio-lixiviation est testé à l'échelle du laboratoire et mis à l'épreuve dans la mine de Rudna, en Pologne. En parallèle de ces expérimentations, développer des simulateurs numériques adaptés est indispensable pour identifier le design des puits permettant une récupération optimale de la ressource. C'est dans cet objectif que des travaux de modélisation du transport réactif ont été engagés. Si pour le moment l'accent a surtout été mis sur la définition du modèle chimique (Laurent et al., 2016), la prochaine étape consistera à réaliser une simulation couplée sur les modèles géologiques correspondant aux différents scénarios d'exploitation (figure II.11(d) et II.11(e)).

2.3.2 Modèles thermo-hydrodynamiques à petite échelle

Les interactions eau-roche ne se limitent pas aux processus chimiques. Dans le cadre de l'étude des réservoirs géothermiques, un autre phénomène physique domine : les échanges de chaleur entre le fluide en circulation et la matrice rocheuse. Nous avons étudié ce couplage thermo-hydrodynamique dans le cadre de la thèse de Guillaume Reichart (Reichart, 2015), réalisée en collaboration avec Laurent Vaute du BRGM et Michel Buès de l'équipe Hydrogéomécanique multiéchelle du laboratoire GeoRessources.

Avec une température allant jusqu'à 59°C à 1200m de profondeur, les anciennes mines lorraines de charbon, aujourd'hui ennoyées, sont envisagées comme une potentielle ressource d'énergie géothermique basse-température. Néanmoins, avant de mettre en place ce "détournement géothermique" des anciennes mines, la faisabilité du projet doit être soigneusement étudiée. Les réseaux de galeries existants facilitent en effet la circulation des fluides mais peuvent aussi générer des courts-circuits diminuant le rendement de l'installation. Il est donc essentiel de bien caractériser la géométrie tridimensionnelle du système dans le modèle d'écoulement final. Une modélisation préliminaire avaient permis d'identifier la mine de Merlebach comme le site le plus favorable à l'exploitation (Hamm and Bazargan Sabet, 2010). Pour mieux comprendre le fonctionnement de ce réservoir particulier, deux approches ont été mises en œuvre : i) une approche décrivant finement les mécanismes thermo-hydrodynamiques à l'échelle d'un puits ; ii) une approche uniquement hydrodynamique à l'échelle d'un étage minier.

Sur les trois puits suivis durant 5 ans sur la zone d'étude (2009 à 2013), le puits Vouters 2 présente un comportement thermo-hydrochimique particulier (Reichart, 2015). La colonne d'eau y est en effet divisée en 5 zones. Les 3 premières zones, distinctes les premières années par leur conductivité électrique et la température mesurée, se sont progressivement homogénéisées au cours des ans. Seuls quelques

"sauts" de température permettaient encore de les distinguer en 2013. La zone 2 se démarque néanmoins par un gradient de température d'intensité variable selon les années, permettant la transition entre les zones 1 et 3. La zone 4, homogène, est caractérisée par une augmentation nette de la salinité et de la température en son sommet. La zone 5, la plus profonde (entre 1050 m et 1272 m de profondeur), présente des profils de température et conductivité en escalier, très différents de ce qui a été observé par ailleurs (figure II.12(a)). Le fait de s'intéresser uniquement à un puits minier permet de décrire finement les processus physiques en jeu tout en ayant une discrétisation spatiale détaillée. Différentes modélisations ont été réalisées sous COMSOL Multiphysics afin de reproduire les diverses observations de terrain. En particulier, l'escalier thermohalin a pu être reproduit en simulant une colonne d'eau hydrauliquement isolée aux parois de laquelle on applique les gradients de salinité et de température croissants vers le bas qui ont été observés dans cette tranche d'eau (figure II.12(b)). En effet, dans ces conditions apparaissent rapidement des cellules

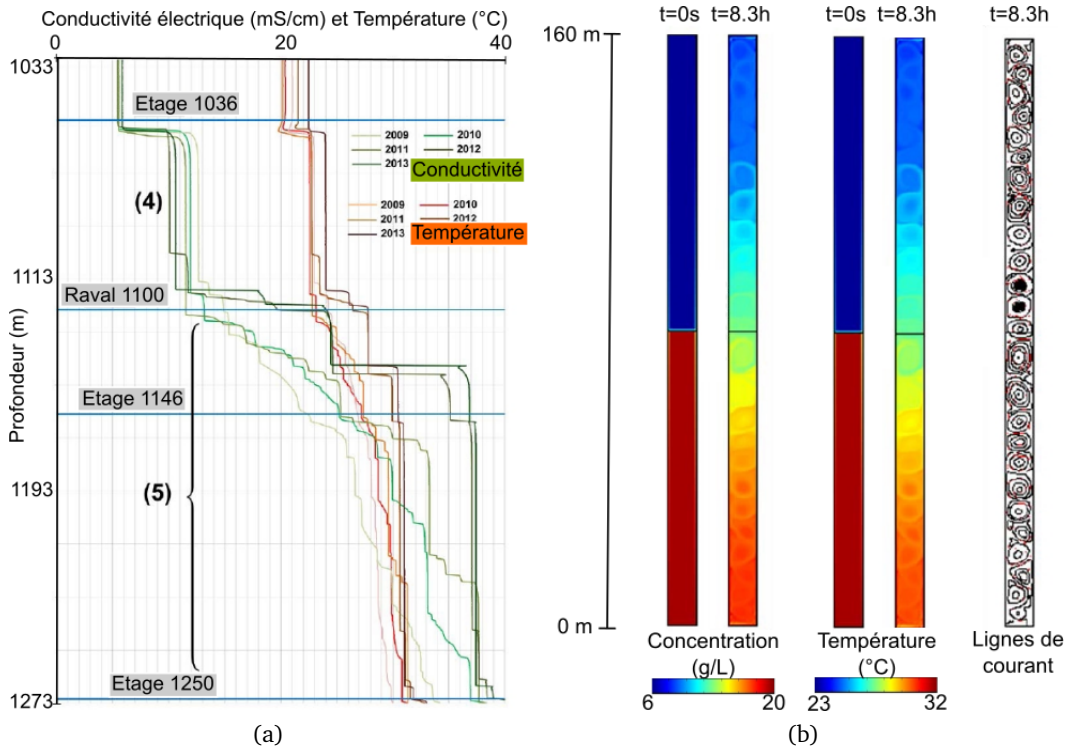

Figure II.12 : Étude du comportement thermosolutal du puits minier Vouters 2 (modifié d'après Reichart (2015)) : (a) mesures de Conductivité et Température de 2009 à 2013 ; (b) résultats de la simulation de la zone 5 : convection thermosolutale naturelle induite par des gradients de température et salinité croissants vers le bas imposés aux parois dans une colonne d'eau hydrauliquement isolée.

de convection circulaires, au sein desquelles la concentration et la température de l'eau sont homogénéisées. Différentes valeurs de gradients ont été testées, montrant un impact sur la taille et le nombre de cellules (cas de la concentration) et sur les vitesses en jeu (cas de la température). Dans les parties moins profondes de la mine, la modélisation a confirmé l'existence d'une convection inter-étages importante.

2.3.3 Changement d'échelle et génération de maillage sous contraintes

Dans le cas des réservoirs houillers lorrains, après l'étude fine des processus opérant dans les puits miniers, il était envisagé de modéliser le comportement thermo-hydrodynamique de la mine de Merlebach (2.5 km x 7.5 km x 1500 m de haut). À cet effet, un géomodèle 3D complet du secteur a été construit pour décrire finement la géométrie du réservoir minier (Collon et al., 2015) (voir aussi section 3.1). Cependant, comme dit précédemment, l'une des grandes limites à l'utilisation directe de modèles couplés à des échelles pluri-kilométriques est le grand temps de calcul inhérent à une description fine de la géométrie et des propriétés du domaine étudié. De ce fait, une alternative couramment utilisée consiste à construire une grille de plus faible résolution, la grille réservoir, de manière à limiter les temps de calcul. La difficulté réside alors dans l'estimation de la propriété équivalente dans les cellules grossières à l'effet cumulé d'un ensemble de cellules plus fines, et ce notamment pour les propriétés non additives comme la perméabilité ou la transmissibilité. Cette étape de mise à l'échelle des propriétés est classiquement nommée *upscaling*.

L'upscaling est un problème complexe qui a fait l'objet de nombreux travaux et synthèses (Christie, 1996; Wen and Gómez-Hernández, 1996; Renard and de Marsily, 1997) et est toujours d'actualité (Ampomah et al., 2015; Christensen et al., 2015). Dans le cadre de sa thèse, Guillaume Reichart a choisi d'implémenter la méthode de renormalisation étendue aux 3 dimensions proposée par Karim and Krabbenhoft (2010) (figure II.13). Cette renormalisation a permis de réduire le nombre de mailles du géomodèle pour obtenir une représentation 3D du milieu compatible avec les exigences du simulateur d'écoulement MARTHE[1] retenu par les partenaires du projet. Une simulation d'écoulement a ainsi pu être réalisée sur le modèle mis à l'échelle et a permis de reproduire l'historique d'ennoyage du réservoir minier (Reichart, 2015). Cependant, ces résultats sont préliminaires et demanderaient à être confrontés à des données supplémentaires de terrain et à ceux d'autres méthodes pour pouvoir confirmer leur pertinence. Par ailleurs, ces travaux ont mis en lumière les limites de l'approche de mise à l'échelle qui avait été choisie : difficultés à traiter des structures ne traversant pas le bloc de calcul de part en part (p. ex, raccordement d'une galerie à un puits), et surtout difficultés à traiter les structures 3D non-alignées avec les directions d'écoulement principales (bande remontante, veine exploitée en semi-dressant, etc.). L'indépendance entre le maillage utilisé pour la discrétisation des équations et les directions des structures géologiques dominant l'écoulement est donc apparue comme un verrou méthodologique.

[1] http://www.brgm.fr/production-scientifique/logiciels-scientifiques/marthe-logiciel-modelisation-ecoulements

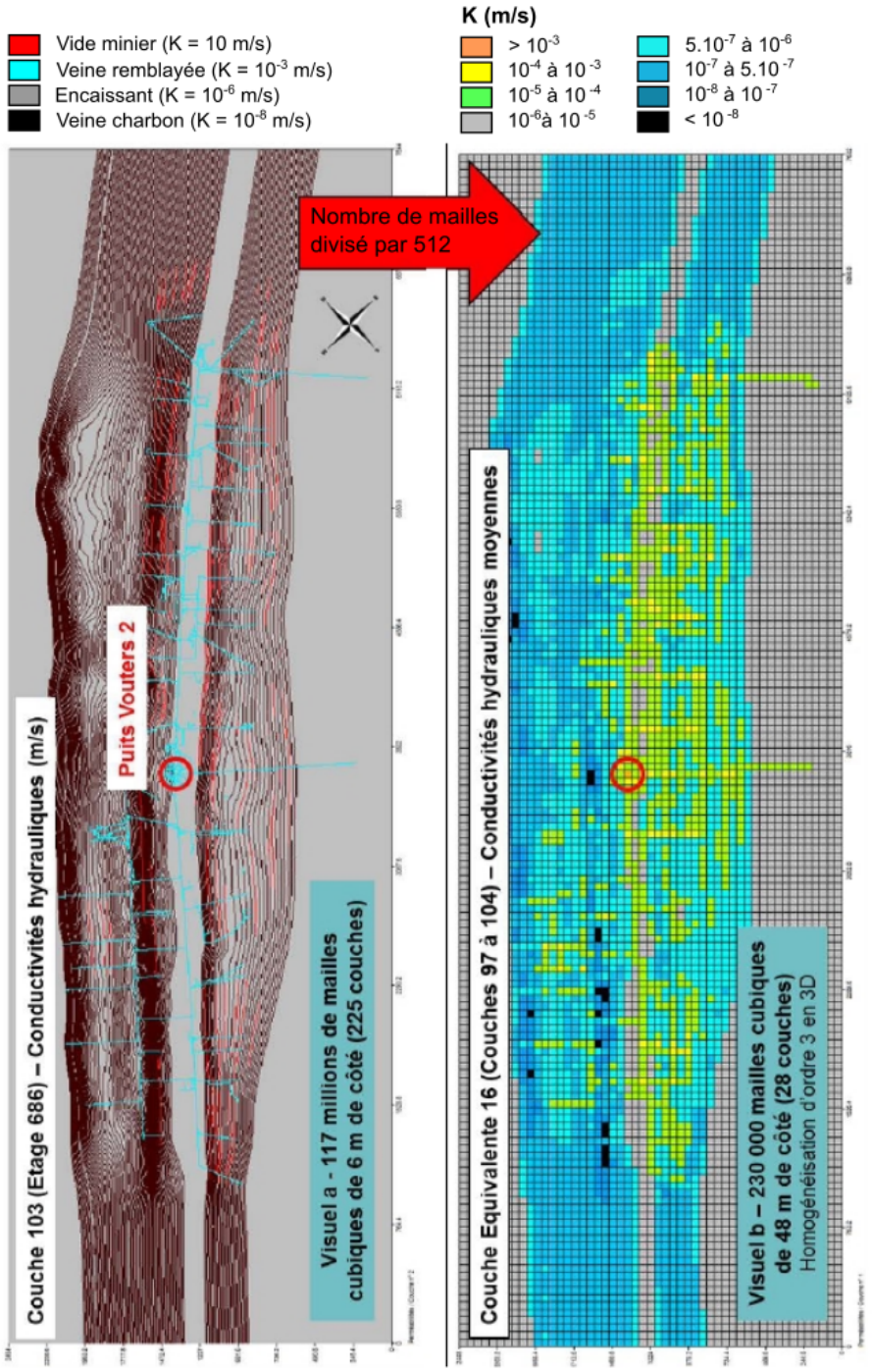

Figure II.13 : Mise à l'échelle d'un bloc de 8 couches contenant l'étage minier 686 (2.5 km x 7.5 km) (modifié d'après Reichart (2015)).

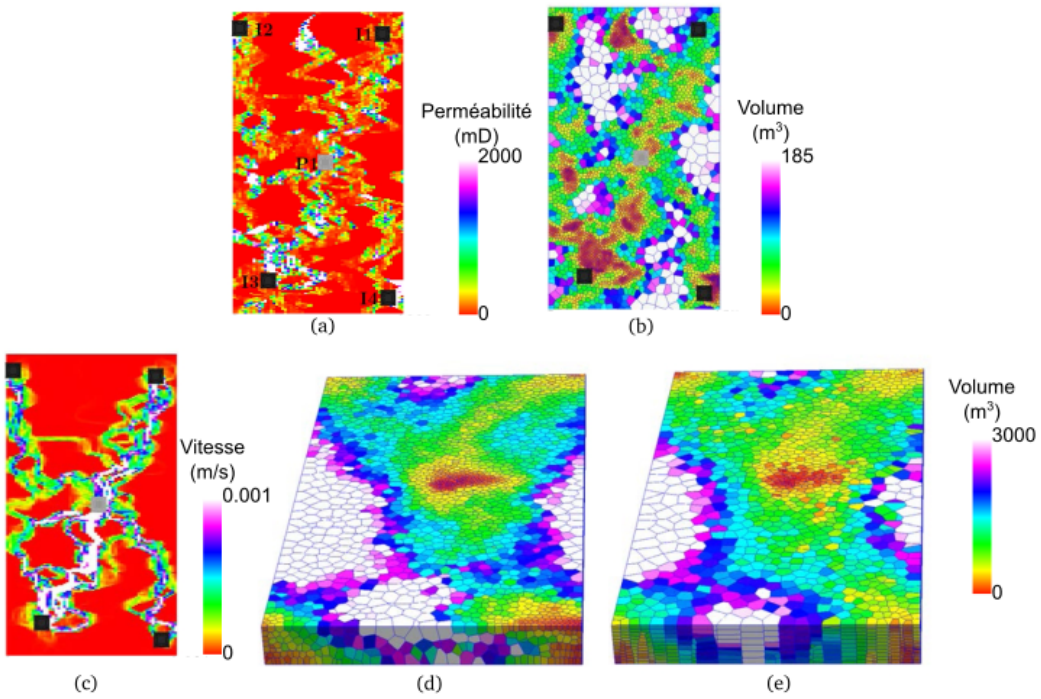

Figure II.14 : Exemples de maillages générés pour la simulation d'écoulement (modifié d'après Merland (2013)) : (a) perméabilité de la couche 61 du modèle de référence SPE10 (Christie and Blunt, 2001), comprenant quatre puits injecteurs en noir et un puits producteur au centre en gris ; (b) exemple 2D de maillage raffiné selon la perméabilité ; (d) et (e) exemples 3D (modèle SPE10) de maillages raffinés selon la norme de la vitesse présentée en (c). En (d) les cellules sont isotropes, en (e) le maillage est anisotrope avec un aplatissement vertical d'un facteur 10 et un raccourcissement dans la direction de l'écoulement d'un facteur 2.

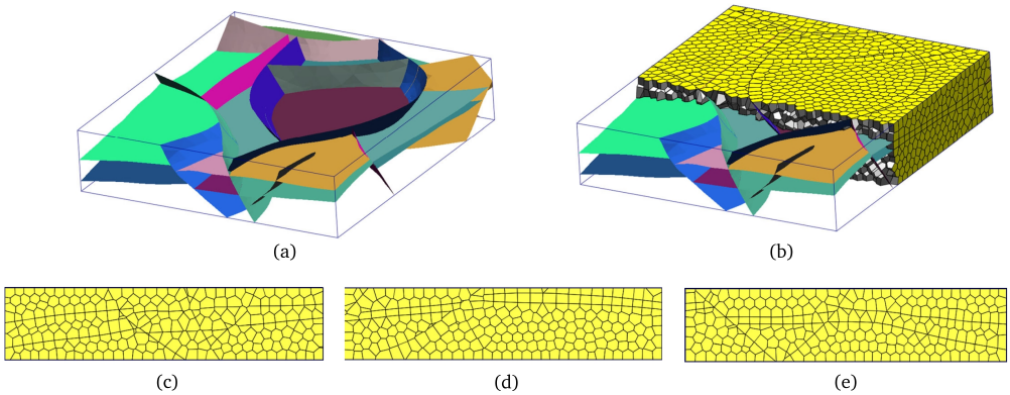

Figure II.15 : Génération d'un maillage de 10 000 cellules conforme aux failles et horizons (modifié d'après Merland et al. (2014)) : (a) modèle de graben (fourni par Total) ; (b) vue 3D de la grille générée ; (c), (d) et (e) respectivement, vues depuis le Sud, le Nord et l'Ouest.

Ce genre de problématique a motivé les travaux de thèse de Romain Merland (Merland, 2013), lancés en collaboration avec Bruno Lévy (Inria - Équipe Alice) et Guillaume Caumon (GeoRessources - Équipe RING). Notre objectif était de développer de nouvelles méthodes de génération de grilles réservoirs respectant un certain nombre de contraintes pour améliorer la pertinence et la précision de la simulation d'écoulement. Nous avons choisi d'utiliser des grilles non structurées de Voronoï car elles offrent la flexibilité nécessaire pour respecter des contraintes géométriques en 3D[2]. Dans ces travaux, différentes contraintes ont été considérées : maximisation de la qualité des cellules en positionnant les points de Voronoï près des barycentres des cellules ; raffinement local du maillage en fonction d'un champ de densité ρ (figure II.14) ; contrôle de l'anisotropie des cellules qui peuvent être déformées selon le vecteur vitesse (figure II.14(e)) ou un gradient stratigraphique (valeur temps) ; orientation des faces des cellules orthogonalement au vecteur vitesse ; conformité aux interfaces géologiques, c'est-à-dire aux failles et aux horizons d'un modèle structural (figure II.15) ; alignement des points de Voronoï le long des puits. Tandis que dans les travaux existants les contraintes sont généralement encodées et appliquées séparément, l'approche proposée par Merland et al. (2011) permet de les appliquer simultanément et en 3D (figure II.16). Ceci est réalisé grâce à un encodage des contraintes dans une fonction objectif commune qui est minimisée. L'optimisation globale employée à cet effet se base sur des algorithmes de construction de diagrammes de Voronoï barycentriques (*CVT* pour *Centroidal Voronoï Tesselation*) utilisant une norme L_p (Lévy and Liu, 2010).

À noter que dans cette démarche plusieurs contraintes s'appuient sur un calcul

[2] Le diagramme de Voronoï d'un ensemble de points X plongé dans un domaine Ω fini ou infini est l'ensemble $V_i{}_{i=N}^{N}$ défini, pour une fonction de distance d donnée (généralement la norme Euclidienne), par :

$$V_i = y \in \Omega \mid d(y, x_i) \leq d(y, x_j), pour j \neq i$$

préalable d'écoulement monophasique (optimisation de la taille ou de l'anisotropie des cellules) (Merland et al., 2010). Il a été réalisé avec le simulateur Streamlab de Gocad, que j'avais déjà utilisé pour l'approche par lignes de courant. On retrouve d'ailleurs un peu ici la philosophie des lignes de courant : un premier calcul est réalisé qui ne tient pas compte des phénomènes complexes (comme l'aspect multi-phasique de l'écoulement, un couplage avec le transport ou la thermique, ...), avant de procéder à un remaillage plus grossier du système qui, par simplification spatiale, permet d'avoir les ressources en calcul nécessaires pour effectuer des simulations couplées des processus d'intérêt.

Si les critères géométriques, développés pour apprécier la qualité des grilles générées, ont démontré une amélioration géométrique systématique, l'amélioration en terme de résultats de simulation d'écoulement n'a pas été à la hauteur de nos attentes (Merland et al., 2014). Ces résultats sont peut-être liés à la méthodologie de calcul des propriétés équivalentes (changement d'échelle de la transmissibilité) et/ou au schéma de discrétisation associé (discrétisation de type Two Point Flux Approximation - TPFA). Ils nécessiteraient des travaux en collaboration avec des spécialistes de mécanique des fluides pour être précisés.

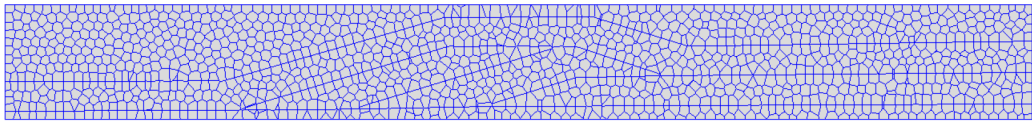

(a)

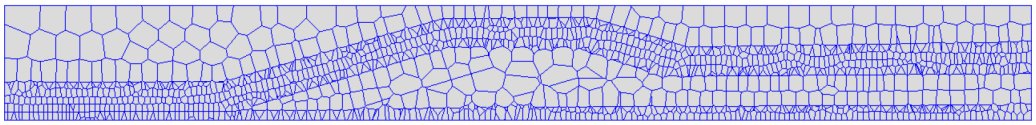

(b)

Figure II.16 : Exemples de grilles réservoirs (10 000 cellules) (Merland, 2013) : (a) grille générée avec une contrainte de conformité aux éléments structuraux seule ; (b) grille générée avec une fonction objectif combinant plusieurs contraintes (conformité aux éléments structuraux, taille de cellules fonction du champ de perméabilité, orientation des faces de cellule selon le vecteur vitesse).

3

Caractérisation et analyse d'objets géologiques à géométrie complexe

Comme nous venons de le voir, certains questionnements scientifiques nécessitent une description spatiale des paramètres et des processus. Dans ce cas, il est nécessaire de caractériser géométriquement le milieu étudié. Sa représentation numérique sert alors de support spatial à la simulation du processus d'intérêt. La géomodélisation vise à créer des représentations géométriques tridimensionnelles du sous-sol à partir des données de sub-surface.

3.1 Modélisation structurale 3D

Les défis de la géomodélisation sont nombreux et incluent la capacité à reconstruire rapidement des géométries complexes à partir de données plus ou moins éparses et aux résolutions variées : données d'affleurement, interprétations cartographiques, données de puits, données sismiques... Différentes approches sont possibles : approches surfaciques utilisant des surfaces paramétriques (p. ex. Gjoystdal et al., 1985; Fisher and Wales, 1992; de Kemp and Sprague, 2003) ou polygonales (p. ex. Mallet, 1988, 2002; Jessell, 2001) ou approches volumiques utilisant des grilles régulières ou non, structurées ou non, ou encore des modèles par frontières (p. ex. Gjoystdal et al., 1985; Johnson and Jones, 1988; Hoffman et al., 2003). Dans son article, Caumon (2010) dresse une revue détaillée de l'état des lieux en géomodélisation. Les surfaces ont longtemps été un objet privilégié en géomodélisation de par le faible coût mémoire associé à leur manipulation. Néanmoins, les progrès techniques ont permis l'essor des approches volumiques depuis quelques années. Il serait cependant malheureux d'opposer deux approches avant tout complémentaires. Ainsi, nos récentes études de cas ont démontré que la réussite de certaines reconstructions 3D dépendait finalement de notre capacité à combiner les techniques existantes.

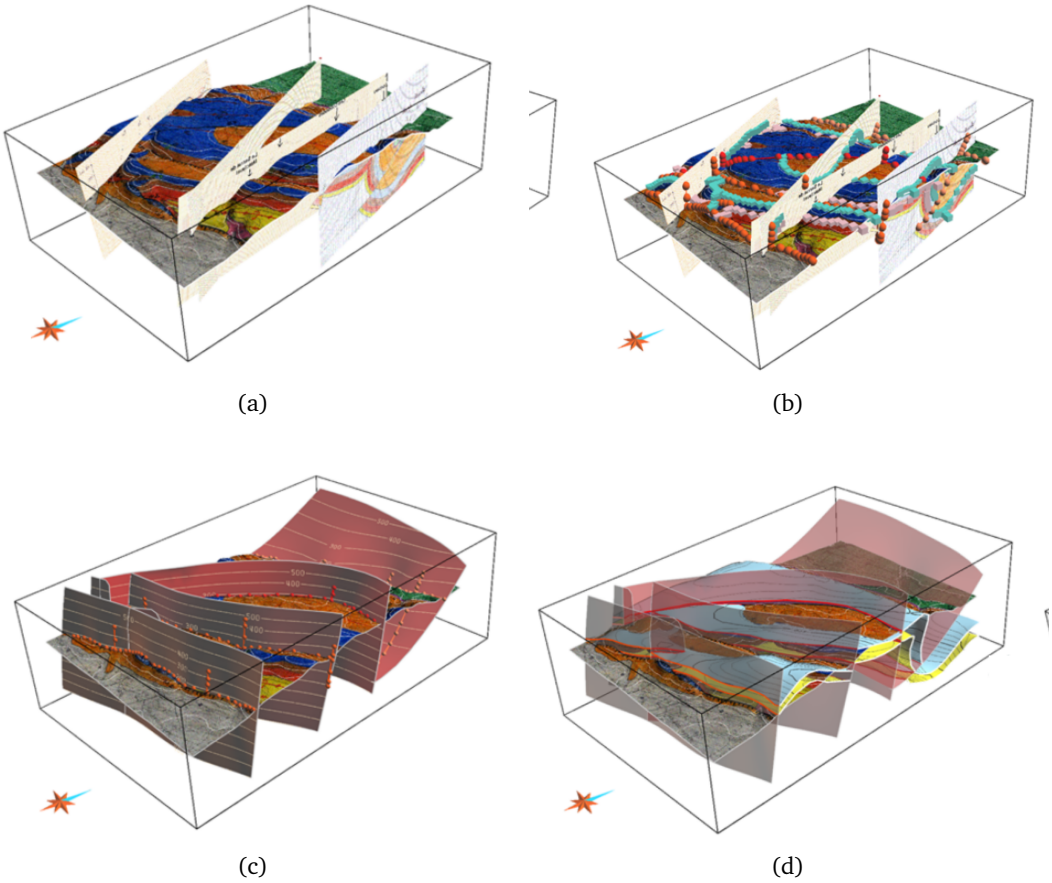

(a) (b)

(c) (d)

Figure II.17 : Étapes classiques de construction d'un modèle structural surfacique à partir de données de terrain (Caumon et al., 2009) : (a) géoréférencement des données (cartes et coupes) ; (b) digitalisation des interfaces structurales : les courbes avec des nœuds sphériques correspondent aux failles, celles avec des nœuds cubiques correspondent à des horizons stratigraphiques ; (c) création du réseau de failles ; (d) modélisation des horizons stratigraphiques : les horizons sont recoupés par les failles (en transparence).

La modélisation structurale surfacique consiste à représenter les différentes formations géologiques par les interfaces qui les délimitent : horizons et failles. Classiquement, la construction d'une interface géologique consiste à la représenter explicitement par une surface triangulée ; c'est l'*approche explicite*. Un milieu géologique comprenant plusieurs interfaces est modélisé itérativement, généralement en considérant les interfaces par ordre inverse de leur apparition. Par exemple, on construit le réseau de failles avant de chercher à modéliser les horizons faillés (figure II.17). Au cours de ce processus, le modélisateur doit veiller scrupuleusement au maintien de la cohérence géologique et numérique du système. Au cœur des formations que nous dispensons aux élèves de l'ENSG, ces principes ont fait l'objet d'une publication à vocation didactique que j'ai co-signée (Caumon et al., 2009).

Pour construire explicitement une surface géologique triangulée, deux approches

principales peuvent être distinguées : i) la triangulation directe des points et ii) la construction par méthode indirecte. Trianguler directement à partir des points de données est une solution particulièrement bien adaptée aux nuages de points denses et surtout régulièrement distribués puisque chaque point constitue un nœud du maillage final. Cette méthode est donc utilisée couramment pour la construction de surfaces topographiques à partir de Modèles Numériques de Terrain (MNT) (figure II.18(a)). Lorsque les points de données sont peu nombreux, irrégulièrement répartis, et bruités, l'approche indirecte est plus appropriée. Elle consiste à construire une surface initiale, puis à la déformer sous contraintes de manière à minimiser sa distance aux points de données (figure II.18(b) et (c)). Différentes méthodes d'interpolation existent (p. ex Haecker, 1992; Kaven et al., 2009). Dans mes travaux j'utilise l'interpolation lisse discrète (*Discrete Smooth Interpolation* ou *DSI*) implé-

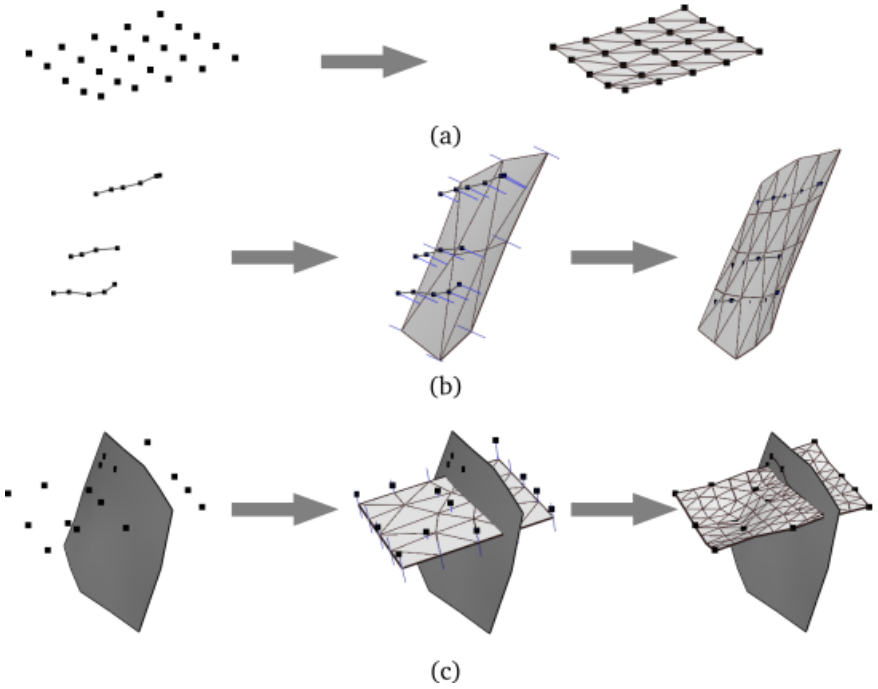

Figure II.18 : Construction d'une surface triangulée (modifié d'après Collon et al. (2015)) : (a) triangulation directe d'un nuage de points régulièrement échantillonnés : chaque point constitue un sommet du maillage ; (b) approche indirecte : une surface de départ est construite. Des contraintes sont appliquées aux bords (déplacements contraints selon un axe normal au bord de la surface) et vers les points de données (traits bleus). La surface est ensuite interpolée pour honorer les contraintes tout en minimisant sa rugosité ; (c) deuxième exemple d'approche indirecte : construction d'un horizon faillé. Après interpolation de la surface pour honorer les points de données (image centrale), la surface est coupée par la faille et de nouvelles contraintes "bords contre surface" sont imposées sur les lignes d'incision pour maintenir le contact entre l'horizon et la faille après ré-interpolation.

mentée dans le géomodeleur Gocad-Skua (Mallet, 1992). Cette méthode minimise une somme pondérée de la rugosité surfacique et de la distance aux données au sens des moindres carrés (Mallet, 1989, 1997). Certaines données peuvent être honorées exactement en les introduisant comme nœuds de contrôle du maillage (p. ex. des marqueurs de puits), tandis que d'autres données, considérées comme moins fiables, sont uniquement honorées à un degré choisi par l'utilisateur (p. ex. isobathes, courbes interprétatives extraites de coupes géologiques). Chaque contrainte visant à déformer la surface est associée à une direction particulière. Une des difficultés de l'approche de modélisation indirecte, et qui reste actuellement un problème ouvert géré à la main par les modélisateurs, est donc liée à la définition de directions de projections compatibles entre elles et avec les discontinuités (failles, etc.) (p. ex. Mallet, 1997; Sprague and de Kemp, 2005).

Par ailleurs, cette technique atteint ses limites lors de certaines configurations géométriques, notamment pour représenter rapidement et de façon cohérente les empilements stratigraphiques. En considérant les horizons géologiques comme des équipotentielles d'un champ scalaire $f(x, y, z)$, les approches implicites facilitent cette tâche (figure II.19). Rendues possibles par les capacités croissantes des ordinateurs, elles se développent depuis une dizaine d'années (p. ex. Carr et al., 2001; Chilès et al., 2004; Frank et al., 2007). Les défis scientifiques et techniques consistent à intégrer une large variété de données de terrain et de concepts géologiques dans le processus d'interpolation du champ scalaire. Dans ce contexte, l'équipe RING développe son propre outil de modélisation implicite (p. ex. Moyen et al., 2004; Frank et al., 2007; Caumon et al., 2009, 2013). Nous avons mis en application ces différentes approches de modélisation pour proposer un géomodèle 3D de deux sites d'intérêt : la concession minière de Merlebach (France) et le mini-bassin d'Inceyol à Sivas (Turquie).

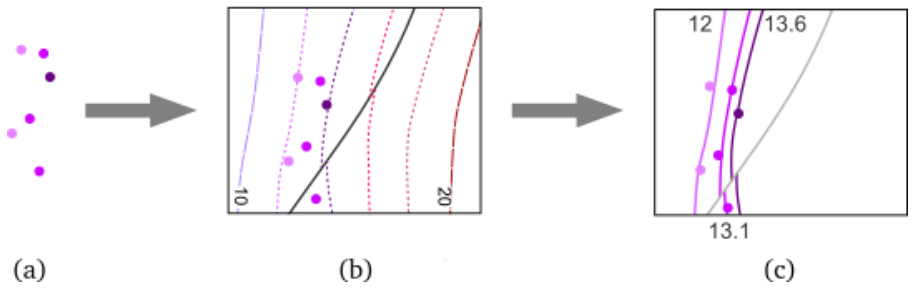

Figure II.19 : Principe de construction d'un ensemble de surfaces stratigraphiques par méthode implicite : (a) une valeur scalaire, qui peut être assimilée à un âge relatif, est attachée à chaque point de donnée ; (b) le champ scalaire correspondant est interpolé dans l'espace de manière à honorer les valeurs imposées aux points de données. D'autres contraintes peuvent également être intégrées (gradient constant, direction axiale, ...) ; (c) les horizons correspondent aux surfaces d'isovaleur du champ scalaire. Ils peuvent être extraits sous la forme de surfaces triangulées puis être remaillés (modifié d'après Collon et al. (2015)).

3.1.1 Bassin minier

Le premier cas d'étude concernait la mine de Merlebach dans le bassin houiller lorrain (Collon et al., 2015). S'inscrivant en amont de la thèse de Guillaume Reichart évoquée plus tôt, ces travaux ont été amorcés dans le cadre de projets de 3ème année ingénieur, puis du stage de fin d'étude de Wendy Steckiewicz-Laurent au BRGM. La construction du géomodèle nécessitait une remise en cohérence de toutes les données cartographiques et géologiques acquises sur le site depuis une centaine d'années. Le défi consistait à représenter un ensemble de 71 couches de charbon sub-verticales, très fines et très proches les unes des autres mais également à en distinguer les parties exploitées et non-exploitées. Il convenait également d'intégrer les horizons discordants sus-jacents, les failles et les infrastructures minières pour générer finalement un modèle volumique complet de la concession minière discriminant les différents milieux. Dans un premier temps, un modèle structural surfacique, plus large que la zone d'intérêt, a été construit par approche explicite (figure II.20(a)) : la surface topographique a été reconstruite par triangulation directe des points du modèle numérique de terrain, tandis que les 13 failles du secteur et le mur de la formation permienne ont été modélisés par approche indirecte. Les 71 couches de charbon, sub-verticales, espacées de 5 à 10 m et recoupées par les failles et la formation permienne sus-jacente, ont ensuite été modélisées par une approche implicite (figure II.20(b) et (c)). Les surfaces extraites de ce modèle implicite ont alors été remaillées grâce à une technologie nouvelle basée sur une analyse des diagrammes de Voronoï restreints et développée spécifiquement pour les modèles géologiques dans le cadre de la thèse de Jeanne Pellerin au sein de l'équipe RING (Pellerin et al., 2014). Sur ces surfaces sont enfin distinguées les parties exploitées, qui ont fait l'objet d'un remplissage par du sable et ont donc une très grande perméabilité, et des parties non-exploitées, peu perméables. Les infrastructures minières, qui constituent des drains, ont été modélisées comme objets de type "courbes". Le modèle géométrique final, indépendant de la discrétisation volumique choisie, permet donc de distinguer : les drains que constituent les infrastructures, les failles, les parties exploitées et non-exploitées des 71 veines de charbon, la formation gréseuse encaissante du charbon et la couverture permienne (figure II.20(d)). Il est disponible au téléchargement[1]. Ce modèle a été ensuite discrétisé en grille volumique (figure II.20(e)) pour servir de base à la construction du modèle hydrogéologique spatialisé requis pour la thèse de Guillaume Reichart (Reichart, 2015) (section 2.3.3).

3.1.2 Mini-bassin en contexte de tectonique salifère

Le deuxième cas d'étude portait sur un mini-bassin en contexte de tectonique salifère (Collon et al., 2016b). Il a été réalisé dans le cadre d'une collaboration avec des collègues de l'Université de Pau et des Pays de l'Adour, de l'entreprise Total et de la Cumhuriyet Universitesi de Sivas, Turquie. La principale difficulté résultait de la

[1] http://www.ring-team.org/ring_dl/public/models/3D_Surface_Model_MerlebachMine_Collon_etal_2014.zip

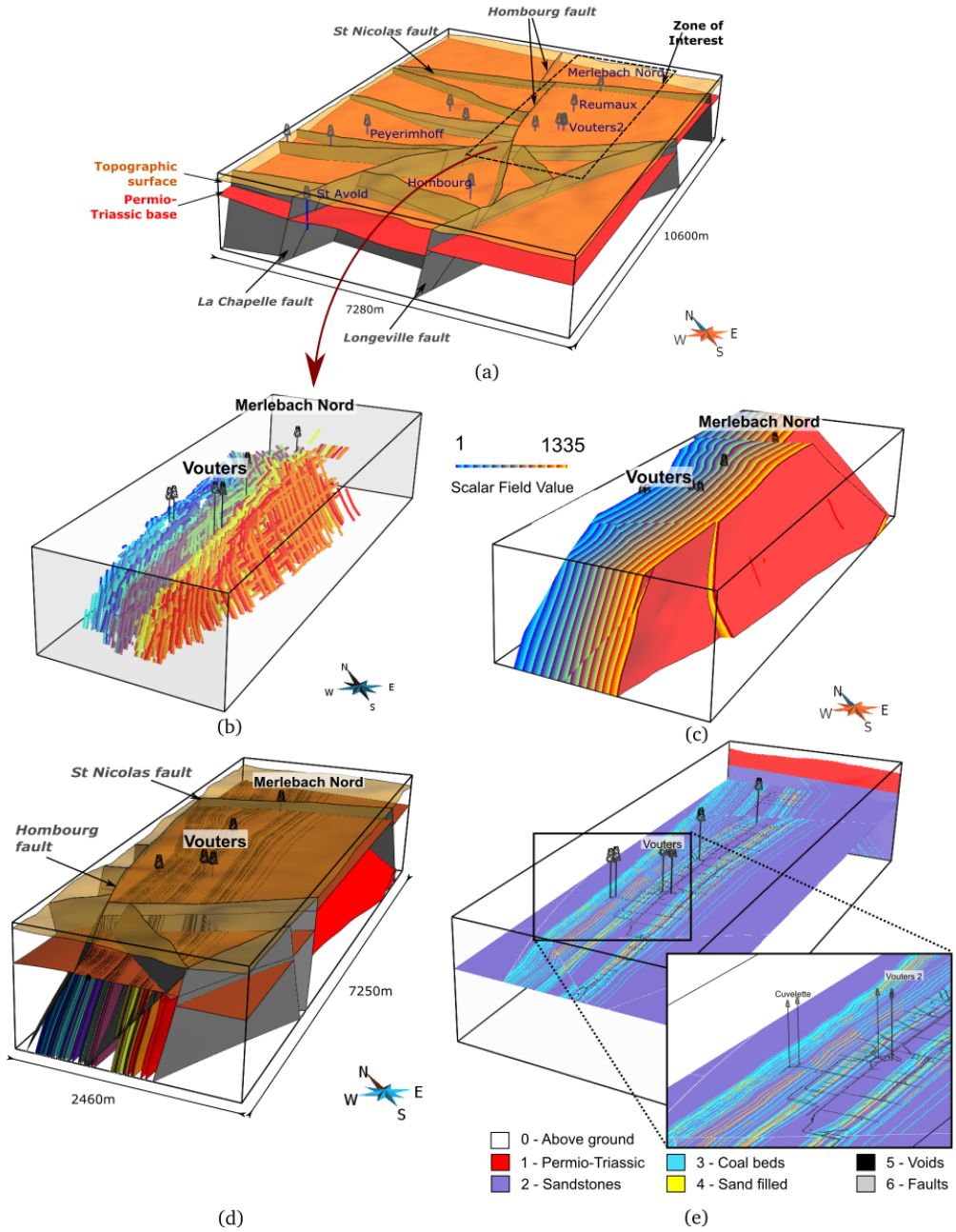

Figure II.20 : Modélisation de la concession minière de Merlebach, dans le bassin houiller lorrain (modifié d'après Collon et al. (2015)) : (a) modèle structural surfacique de la zone d'intérêt élargie ; (b) lignes représentant les différentes couches de charbon digitalisées à partir des coupes et plans de mines ; (c) champ scalaire 3D interpolé correspondant ; (d) Modèle structural surfacique final de la mine de Merlebach ; (e) modèle discrétisé pour la simulation d'écoulement.

combinaison d'une géométrie très tortueuse de la surface de sel à représenter avec un remplissage sédimentaire plissé du mini-bassin et des données de terrain disponibles uniquement à l'affleurement. Comme nous l'avons évoqué précédemment, la construction de modèles 3D s'appuie essentiellement sur des techniques d'interpolation et/ou d'extrapolation qui ont généralement tendance à lisser les surfaces entre les données. Cependant, la déformation et la migration du sel, qui se comporte comme un fluide visqueux à l'échelle de temps géologique, ne génère pas des surfaces minimales mais au contraire des formes complexes qu'on ne rencontre pas ailleurs

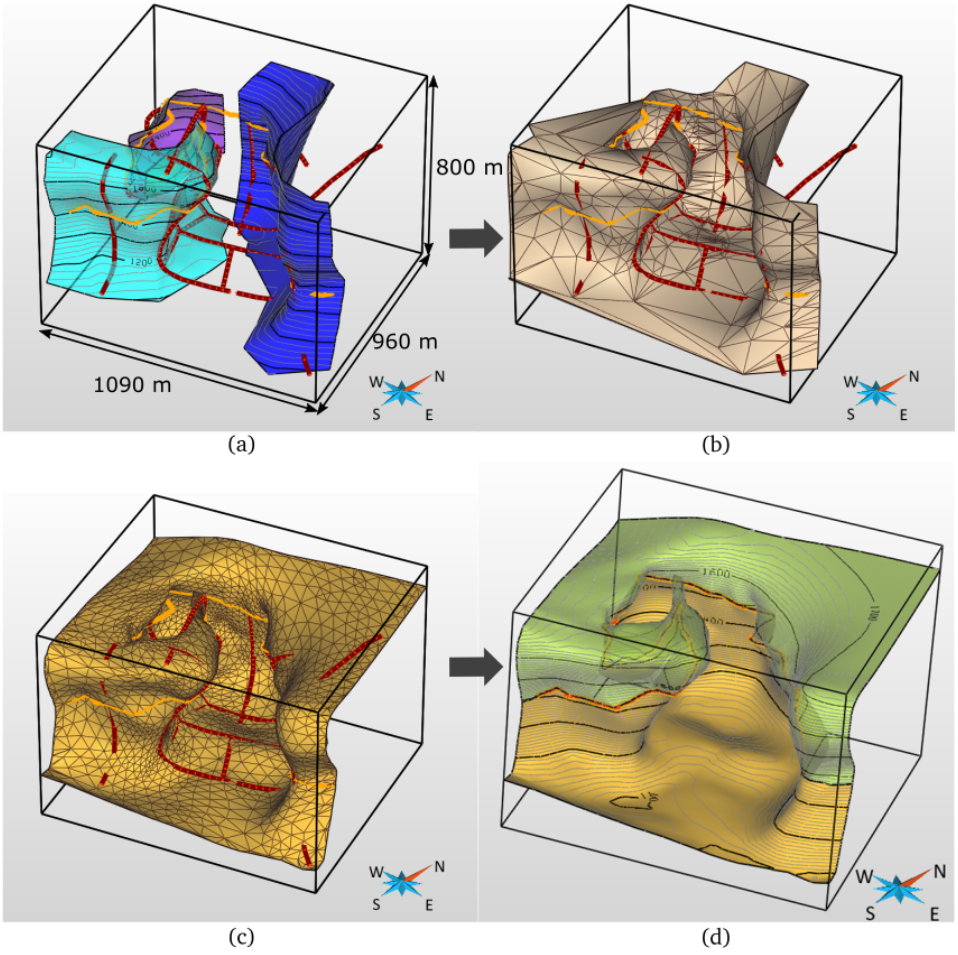

Figure II.21 : Modélisation de la surface de sel du mini-bassin d'Inceyol (modifié d'après Collon et al. (2016b)) : (a) construction de la surface par morceaux : chaque partie est construite indépendamment par une approche explicite indirecte ; (b) de petites surfaces sont créées par triangulation directe entre les bords, puis toutes les parties connexes sont fusionnées pour générer une surface unique ; (c) le maillage est nettoyé et raffiné manuellement de manière à générer une surface finale lisse qui honore les données du modèle ; (d) surface finale du toit de la couche de sel : en vert est représentée la partie située au-dessus de la surface topographique, en jaune la partie située en-dessous.

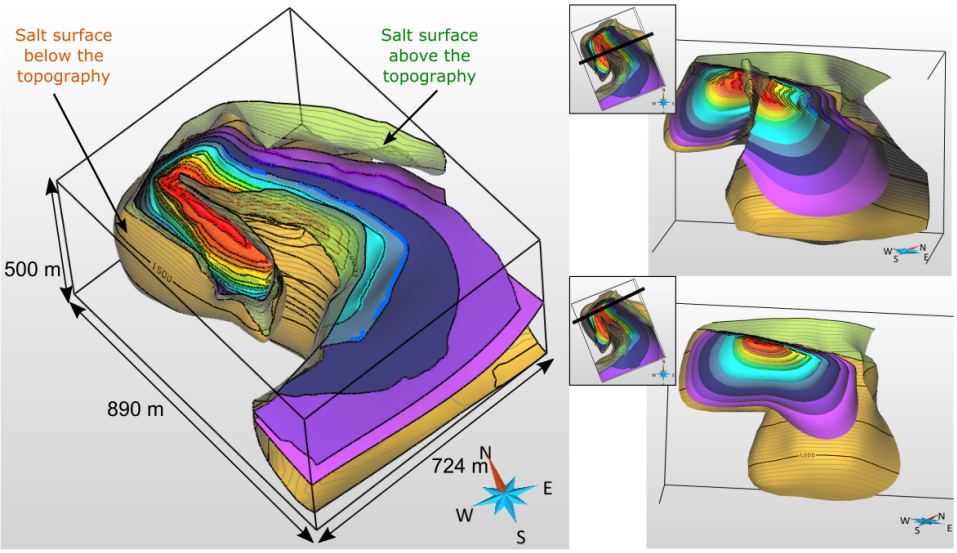

Figure II.22 : Modèle final du mini-bassin d'Inceyol (modifié d'après Collon et al. (2016b)). Vue d'ensemble à gauche. La surface jaune représente le toit de la couche de sel. À droite, deux coupes verticales sont présentées. On y voit la structure en synclinal refermé percé au Sud par un diapir central autour duquel deux synclinaux très serrés se sont individualisés.

(Giles and Lawton, 2002; Jackson and Harrison, 2006; Fossen, 2010). Ceci explique probablement en partie l'absence de cadre théorique pour la modélisation de ce type d'environnement. De ce fait l'extrapolation des géométries salifères constitue un véritable défi lorsque les données sont parcellaires (p. ex. en l'bsence de données sismiques 3D) et peu d'exemples ont été aujourd'hui publiés (Trocmé et al., 2011; Caumon et al., 2013).

La démarche adoptée pour le mini-bassin d'Inceyol a consisté à reconstruire tout d'abord la surface supérieure du sel. Pour cela, nous avons procédé par morceaux, chacun d'eux étant obtenu par une approche explicite indirecte (figure II.21). Après découpage puis connexion des différentes parties ainsi générées, le maillage de la surface triangulée obtenue a été nettoyé et raffiné manuellement. Le remplissage sédimentaire du mini-bassin a été modélisé par une approche implicite. Le calcul d'un champ scalaire 3D nécessite la construction préalable d'un maillage volumique de la zone d'intérêt. Dans le cas du mini-bassin d'Inceyol, ce maillage devait être conforme au sel pour permettre de déconnecter les différentes parties du mini-bassin lors de l'interpolation. Pour contrer les problèmes induits par les parties pincées de la surface du sel lors de la génération du maillage, un modèle alternatif remplaçant la partie pincée du sel par une faille (assimilable à une suture) a donc été généré. Le volume d'intérêt a alors pu être maillé avec les outils développés dans le cadre de la thèse d'Arnaud Botella (Botella et al., 2016). Le champ scalaire a ensuite été calculé dans ce domaine maillé par une interpolation lisse discrète contrainte notamment par les limites stratigraphiques observées à l'affleurement, les pendages mesurés sur le terrain et la relation de conformité observée sur la partie externe du mini-bassin

entre le remplissage sédimentaire et la surface salifère. Les surfaces correspondant aux limites stratigraphiques observées à l'affleurement ont ainsi pu être extraites pour proposer un modèle final correspondant à l'interprétation géologique du secteur (figure II.22).

En plus de démontrer la faisabilité d'un tel modèle 3D, ce travail a aussi permis de comparer différentes techniques de modélisation. Certaines n'ont pas donné de résultats satisfaisants, mais des améliorations potentielles ont été proposées et les progrès méthodologiques continus les rendront probablement performantes prochainement. Pour permettre aux collègues intéressés de tester d'autres approches, nous avons donc choisi de publier également les données utilisées dans ce projet[2]. Ce travail a par ailleurs permis aux géologues de mieux appréhender la géométrie 3D correspondant à leur interprétation des données d'affleurement, et, ponctuellement, de la corriger. Le modèle 3D résultant (visible en 3D en ligne[3]) peut désormais servir à des calculs de volumes, des simulations de réponses gravimétriques ou autres calculs numériques.

3.2 Analyse statistique de corps géologiques connectés

En mettant l'accent sur les interfaces que sont les horizons géologiques et les failles, la modélisation peut tendre à représenter les structures géologiques comme une succession de couches sédimentaires, potentiellement faillées et déformées, mais caractérisées par des propriétés pétrophysiques plus ou moins homogènes, simulables par des approches géostatistiques classiques dites "deux points". Pourtant certains objets géologiques ont une géométrie très particulière qui va fortement impacter les propriétés pétrophysiques et gouverner les écoulements souterrains. C'est le cas des systèmes chenalisés - fluviatiles et turbiditiques - et des (paléo)karsts.

Éléments géométriques allongés et tortueux, souvent sièges privilégiés de la circulation de fluides du fait de leur grande perméabilité, ces structures géologiques naturelles ont un rôle drainant qui rappelle les réseaux de galeries minières. Cependant, alors que les mines sont le résultat d'une activité anthropique notifiée sur des plans, la géométrie des karsts et des systèmes chenalisés n'est connue que de manière parcellaire. Reconstituer ces milieux nécessite donc tout d'abord de bien comprendre et caractériser leur architecture.

3.2.1 Réseaux karstiques

La caractérisation des systèmes karstiques n'est pas une problématique récente (p. ex. Curl, 1966; Howard, 1971; Williams and Williams, 1972) et s'est développée en parallèle d'études des systèmes fluviatiles actuels (p. ex. Horton, 1945; Scheidegger, 1966; Woldenberg, 1966; Scheidegger, 1967; Smart, 1969; Howard et al., 1970). Cependant, les moyens techniques alors disponibles ont limité ces travaux aux projections cartographiques, donc à un report en 2 dimensions d'un objet géologique

[2] http://www.ring-team.org/ring_dl/public/models/Sivas_onLine_Data.zip
[3] http://www.ring-team.org/model_3d_html/Sivas.html

Tableau II.1 : Classification des systèmes karstiques. Le nombre d'étoiles indique l'abondance relative de chaque type dans chacune des catégories (modifié par Bonneau et al. (2010) d'après Palmer (2003)).

Cave Pattern		 curvilinear branchwork	 rectilinear branchwork	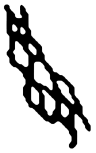 anastomotic maze	 network maze	 spongework pattern	 ramiform pattern
Water source	Doline	⋆⋆⋆	⋆⋆⋆	⋆⋆	⋆		
	Sinking Stream	⋆⋆	⋆⋆	⋆⋆⋆	⋆⋆	⋆	
	Uniform Seepage			⋆⋆⋆	⋆⋆		
	Mixing Sources				⋆⋆	⋆⋆⋆	⋆⋆
	Hypogenic			⋆	⋆⋆	⋆⋆	⋆⋆⋆
Dom. struct.	Bedding Planes	⋆⋆⋆		⋆⋆⋆		⋆⋆	⋆⋆⋆
	Fractures		⋆⋆⋆		⋆⋆⋆		⋆⋆⋆
	Matrix Porosity					⋆⋆⋆	⋆⋆

pourtant organisé en 3 dimensions (Howard, 1971). Depuis une dizaine d'années, l'émergence de nouvelles technologies d'investigation facilite l'acquisition, le stockage et le partage de données 3D. De ce fait, on assiste à un renouveau d'intérêt pour la caractérisation des systèmes karstiques (Pardo-Iguzquiza et al., 2011; Piccini, 2011; Fournillon et al., 2012). Néanmoins, la plupart de ces études mettent l'accent sur la géométrie des conduits karstiques, et sont généralement illustrées par des applications à un, parfois deux réseaux réels.

J'ai choisi d'aborder cette thématique peu après mon arrivée dans l'équipe RING de GeoRessources, en 2009. L'idée était alors de mettre l'accent sur l'analyse de la topologie des réseaux karstiques, en espérant identifier un lien avec la classification morphologique établie par Palmer (1991) (tableau II.1). Pour cela, les métriques retenues devaient être testées sur une base de données la plus large possible de réseaux. Après de premiers tests théoriques sur des plans 2D dans le cadre d'un projet de 3ème année ingénieur (Vigouroux et al., 2010), nous sommes rapidement passés au développement de codes numériques pour automatiser le traitement de données 3D dans le cadre d'un stage de master (Vuilleumier and Collon-Drouaillet, 2012). Dans cette approche, le karst est assimilé à un graphe, dont chaque nœud correspond à une station de mesure et chaque segment à une visée entre 2 stations.

Nous avons parallèlement contacté de nombreux spéléologues pour constituer une base de données de réseaux 2D et 3D. Ces premiers travaux ont montré la difficulté de définir des critères quantitatifs de classification des systèmes karstiques qui établiraient un lien clair entre topologie du réseau karstique et spéléogenèse. Ils ont également permis d'identifier les métriques pertinentes, et celles qui ne le sont pas, pour décrire un réseau karstique. Par exemple, la tortuosité s'est avérée être un paramètre plus influencé par l'échantillonnage du milieu souterrain que le reflet d'une réelle caractéristique géométrique du système.

En travaillant en collaboration avec nos collègues du Centre d'Hydrologie et de Géothermie de l'université de Neuchâtel (CHYN), nous avons complété ce travail et entrepris de tester de nouveaux paramètres issus de la théorie des graphes. En effet, depuis une dizaine d'années de nombreux travaux se sont intéressés à l'analyse topologique de réseaux. Beaucoup de métriques ont été proposées qui n'avaient jamais été utilisées sur des systèmes naturels comme les réseaux karstiques (Ravasz and Barabasi, 2002; Boccaletti et al., 2006; Costa et al., 2007). Nous en avons sélectionné plusieurs pour proposer une caractérisation des réseaux karstiques intégrant la géométrie et la topologie (figure II.23). Pour diminuer les temps de calcul et s'af-

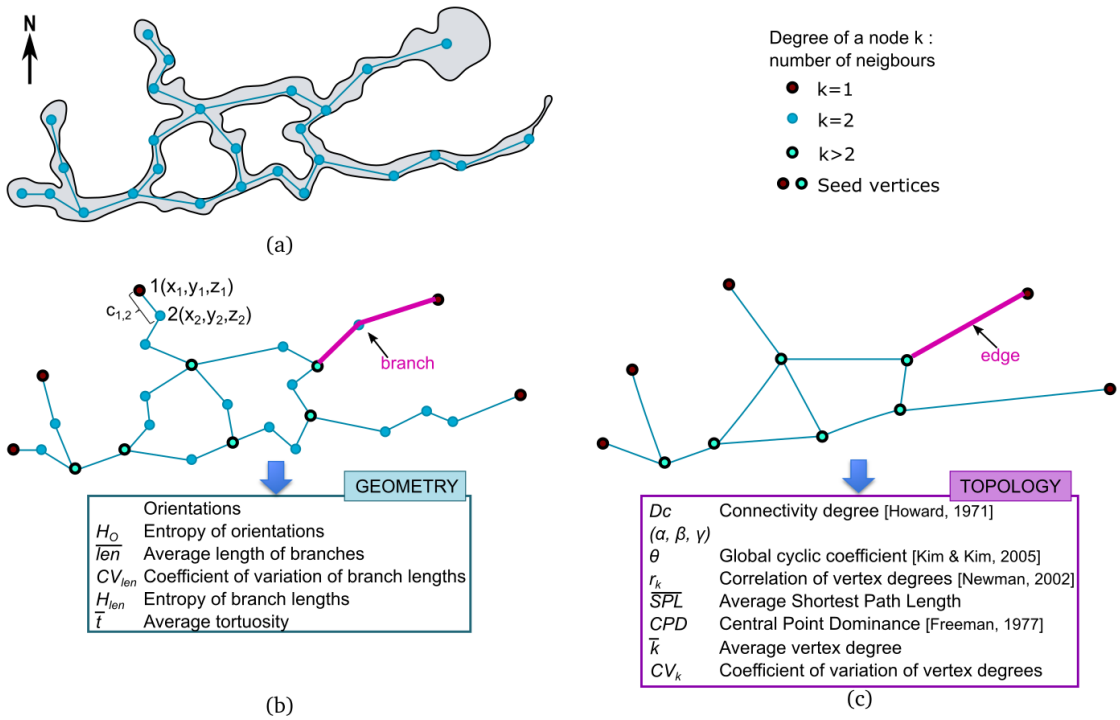

Figure II.23 : Représentation du réseau karstique sous forme de graphe : (a) plan du système karstique ; (b) graphe complet ; (c) graphe réduit correspondant (modifié d'après Collon et al. (Subm.)). Chaque graphe permet de calculer des métriques caractérisant la géométrie ou la topologie du réseau.

Tableau II.2 : Valeurs extrêmes mesurées sur les 34 réseaux karstiques naturels analysés (données extraites de Collon et al. (Subm.)

		Min	Max
H_O	Entropy of orientations	0.745	0.997
$\overline{len}$	Average length of branches	8.4 m	332 m
CV_{len}	Coefficient of variation of branch lengths	0.9 %	2.6 %
H_{len}	Entropy of of branch lengths	0.042	0.335
$\overline{t}$	Average tortuosity	1.12	1.54
$\overline{k}$	Average node degree	1.75	2.6
CV_k	Coefficient of variation of degrees	31 %	60 %
D_C	Connectivity degree	-4.3 %	60.5 %
Θ	Global cyclic coefficient	0	0.12
r_k	Correlation of vertex degrees	0.44	0.88
$\overline{SPL}$	Average shortest path length	2.32	55.8
CPD	Central point dominance	0.02	0.57

franchir au possible du biais lié à l'échantillonnage, un graphe réduit du réseau est utilisé pour plusieurs paramètres. Cette approche a été appliquée à 31 réseaux karstiques 3D et 3 réseaux 2D. Les résultats permettent de discuter de la pertinence des métriques proposées, d'aider à une perception plus intuitive de la signification des valeurs mesurées et surtout de fournir une base de données de valeurs "réalistes" correspondant aux systèmes karstiques naturels (tableau II.2).

Les métriques retenues dans ces études peuvent avoir deux types d'utilisation : (i) elles peuvent être intégrées comme variables de contrôle dans les processus de simulation ; ou (ii) elles peuvent servir à mettre au point un dispositif de validation du "réalisme" des réseaux simulés. Cette dernière perspective fait actuellement l'objet de travaux communs avec nos collègues neuchâtelois (Renard et al., 2013).

3.2.2 Systèmes chenalisés

Cette dernière application a également motivé les travaux de caractérisation des systèmes chenalisés que nous avons menés dans le cadre de la thèse de Guillaume Rongier (Rongier, 2016), réalisée en cotutelle avec Philippe Renard à l'Université de Neuchâtel. De nombreuses techniques de simulation sont en effet développées pour modéliser géométriquement les environnements fluviatiles et turbiditiques qui constituent d'importants réservoirs souterrains. Face à une donnée de terrain lacunaire, qui explique d'ailleurs ce recours à la simulation, la difficulté est de disposer d'indicateurs clairs permettant de comparer les différentes réalisations. La plupart des comparaisons se font d'un point de vue statistique (p. ex. Boisvert et al., 2010; Tan et al., 2014). Or l'approche statistique ne permet pas de rendre pleinement compte de la connectivité des systèmes modélisés. Partant du principe que ces simulations sont essentiellement motivées par l'influence des chenaux sur les écoulements de

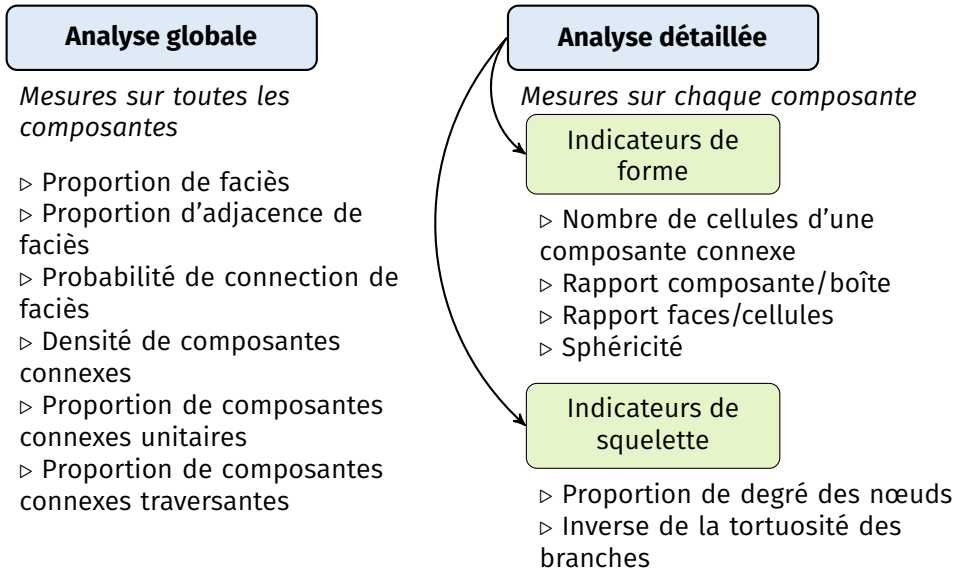

Figure II.24 : Indicateurs utilisés pour la comparaison de réalisations (Rongier, 2016).

fluides, nous avons choisi de traiter cette question en s'appuyant sur les notions de composantes connexes déjà abordées par Deutsch (1998) et De Iaco (2013). Nous avons ainsi proposé un ensemble de 12 indicateurs permettant de rendre compte de la connectivité statique des objets géologiques (Rongier et al., 2013; Rongier, 2016; Rongier et al., 2016b) (figure II.24).

Pour permettre une comparaison rapide des résultats, nous proposons de calculer une dissemblance entre les réalisations grâce à une combinaison de distances euclidiennes et de divergences de Jensen-Shannon. La visualisation de ces dissemblances est facilitée par le recours au positionnement multidimensionnel (*MultiDimensional Scaling ou MDS*) (Cox and Cox, 1994), qui permet une projection optimisée des dissemblances entre réalisations dans un espace 2D (figure II.25). Néanmoins, cette représentation étant biaisée par la réduction du nombre de dimensions, nous proposons également d'utiliser une carte de chaleur (*heatmap*) pour visualiser directement les dissemblances. La carte de chaleur est une représentation directe de la matrice de dissemblance où les valeurs sont remplacées par des couleurs afin de faciliter son interprétation (figure II.26). Représentation MDS et carte de chaleur permettent donc une comparaison globale des réalisations. Pour mieux comprendre les dissemblances observées, il convient ensuite de revenir aux indicateurs pour parfaire l'analyse (Rongier et al., 2015c; Rongier, 2016; Rongier et al., 2016b).

Nous avons réalisé deux applications de cette méthodologie. Tout d'abord, pour tester la démarche, 4 ensembles de 100 réalisations chacun, simulées selon 4 méthodes différentes de simulation stochastique (approche objet, simulation séquentielle d'indicatrices, et deux méthodes de simulation multipoints) ont été utilisés (Rongier et al., 2016b). Les réalisations n'étant pas de mêmes dimensions que l'image de

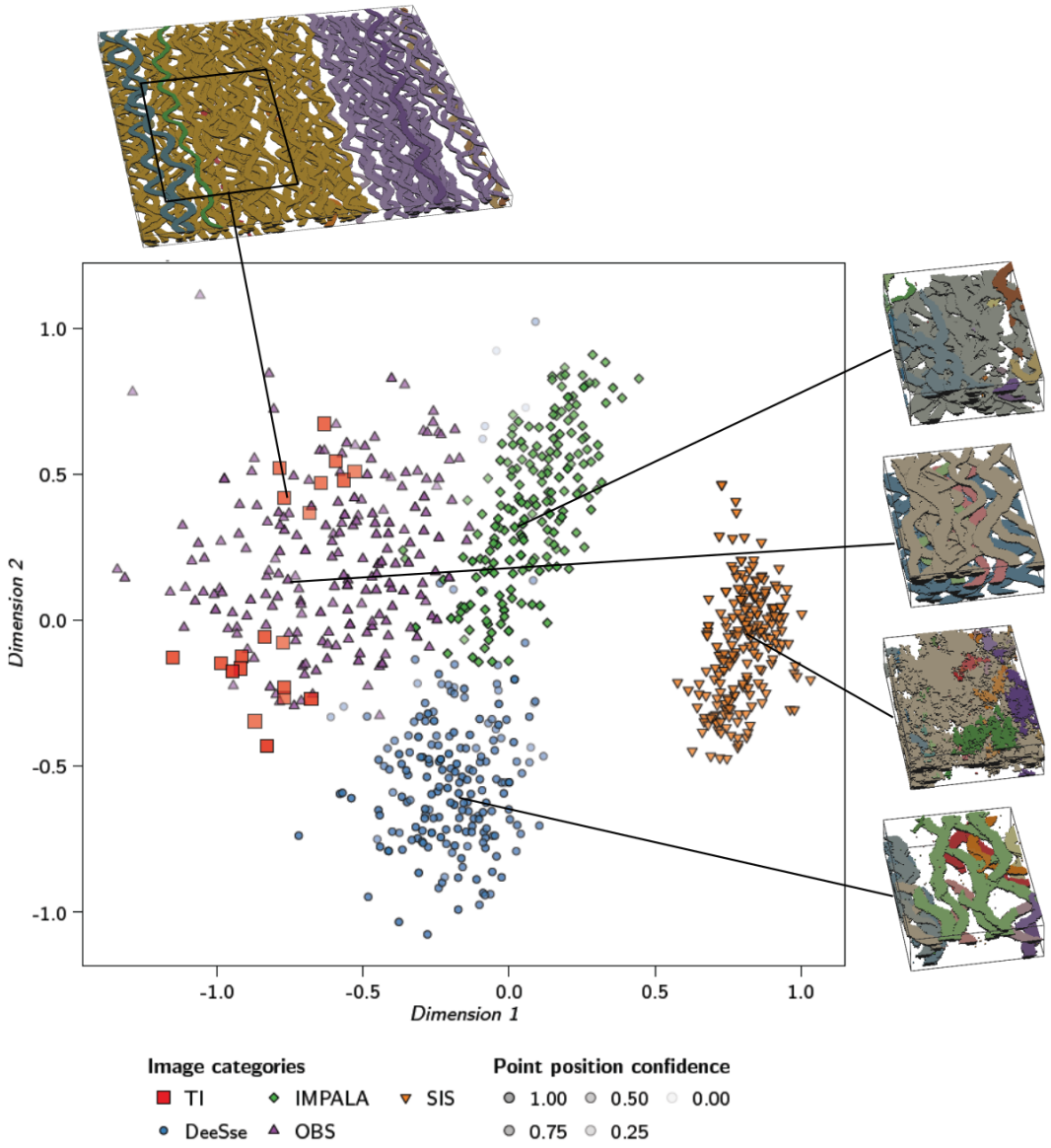

Figure II.25 : Exemple d'application du MDS à un ensemble de réalisations provenant de différentes méthodes (modifié d'après Rongier et al. (2016b)). La comparaison est faite sur des échantillons des réalisations de manière à s'affranchir du biais lié à la différence de dimension entre les réalisations. On remarque que les réalisations de chaque méthode forment des groupes clairement distincts traduisant des différences de connectivité.

référence, l'étude a démontré que les coefficients correctifs de dimensions mis au point étaient insuffisants et qu'il convenait d'échantillonner image de référence et réalisations de manière à éviter tout biais de taille lors de la comparaison. Par la suite, 3 ensembles de 100 réalisations de systèmes chenalisés simulés stochastiquement par systèmes de Lindenmayer (cf. section 4.1) avec une organisation spatiale différente, ont été comparés. Dans les deux études, la démarche que nous proposons a montré son potentiel pour comparer rapidement, et surtout objectivement, plusieurs centaines de réalisations. Elle permet en effet d'expliciter par des critères quantitatifs les différences géométriques qui résultent de chaque méthode de simulation, et les différences de connectivité statique qui en découlent.

De nombreuses perspectives existent à ces travaux. Travailler sur d'autres cas d'études et/ou sur des systèmes réels, p. ex. imagés par sismique, serait une première étape. Il conviendrait également de développer d'autres indicateurs, de mieux exploiter les informations de faciès et d'étudier la connectivité dynamique de ces systèmes.

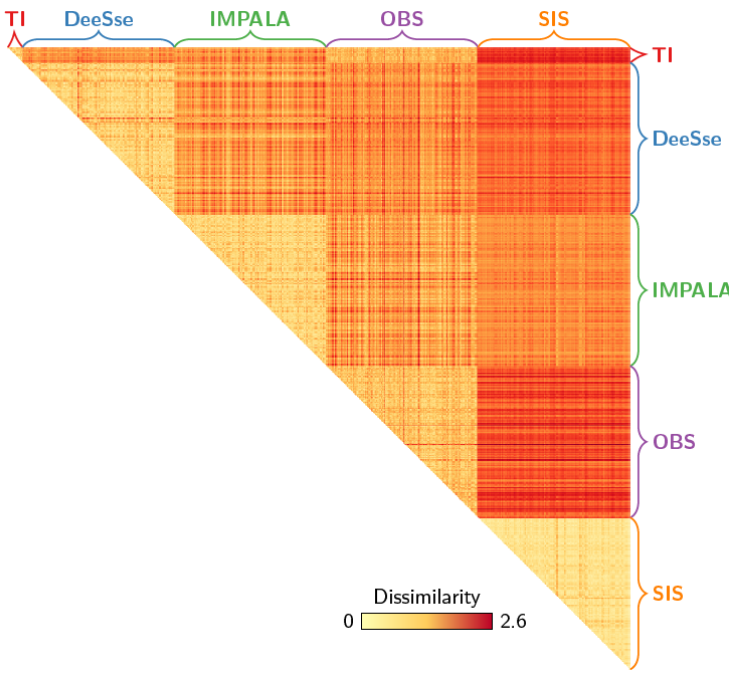

Figure II.26 : Représentation par carte de chaleur de la matrice des dissemblances calculées sur les échantillons de réalisations provenant de différentes méthodes (Rongier et al., 2016b).

4

La gestion des incertitudes dans la représentation géométrique des corps géologiques complexes

Modéliser la subsurface est complexe car les données disponibles sont lacunaires et ne permettent pas d'interprétation univoque. De ce fait, de nombreuses incertitudes sont associées aux modèles du sous-sol et la simulation stochastique est un moyen d'en rendre compte. Partant du principe que les observations disponibles sont l'enregistrement d'un état final du système, la simulation stochastique s'attache, en règle générale, à s'affranchir de la dimension temporelle en simulant directement cet état final. Autrement dit, elles ne reproduisent pas les processus physiques de mise en place du milieu observé, mais uniquement la géométrie résultante de ces processus. L'idée est alors de ne pas privilégier une représentation particulière, mais de tenter de générer un ensemble de possibles. Mes travaux ont pour objectif principal de définir de nouvelles méthodes de simulation stochastique intégrant la spécificité des corps géologiques à géométrie complexe. À cet effet, nous cherchons avant tout à nous appuyer sur : i) les données de terrain - de couverture spatiale et de résolutions variées selon leurs natures, et ii) les concepts géologiques.

Jusqu'à présent focalisés sur deux types d'objets géologiques - les karsts et les chenaux -, nos travaux ont considéré deux échelles d'observation : i) la *grande échelle* - kilométrique à pluri-kilométrique - , à laquelle les structures sont assimilables à des réseaux ou graphes filaires ; et ii) l'*échelle locale* - métrique à pluri-métrique -, à laquelle les structures sont assimilables à des conduits dont on va caractériser la forme, le volume et les propriétés de surface.

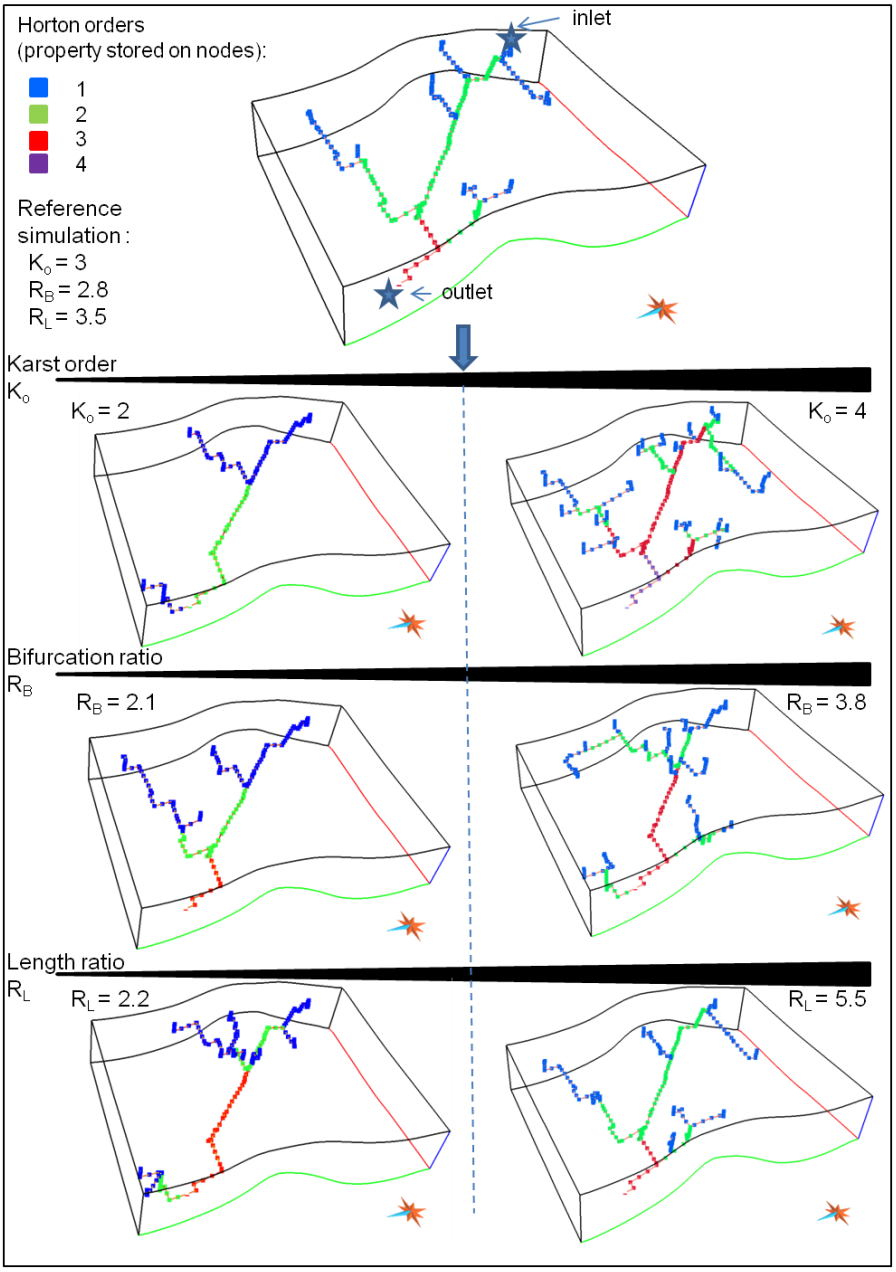

Figure II.27 : Simulation de réseaux karstiques arborescents à topologie contrôlée (Collon-Drouaillet et al., 2012). L'ordre global du système K_O contrôle la complexité hiérarchique du réseau. Le nombre global de conduits augmente avec le ratio de bifurcation R_B. Une plus grande valeur du ratio des longueurs R_L génère des conduits secondaires plus longs.

4.1 À l'échelle kilométrique : simuler des réseaux

4.1.1 Systèmes karstiques

Depuis 2009, nous avons exploré plusieurs pistes avec pour objectif de mettre au point une méthodologie simulant des réseaux karstiques :

- qui respecteraient les données de terrain, p. ex. qui passeraient par les points d'observation du karst (pertes, dolines, etc.) ;
- qui respecteraient les informations géologiques et spéléogénétiques, telles que les surfaces d'inception : zones préférentielles de développement du karst qui peuvent être d'origine tectonique (fractures, failles), sédimentaires (horizon séparant deux formations sédimentaires) ou hydrogéologique (paléo-piézométrie) ;
- dont on pourrait contrôler la topologie.

Dans un premier temps, nous sommes partis de l'analogie avec les systèmes fluviatiles et de la classification morpho-topologique des karsts proposée par Palmer

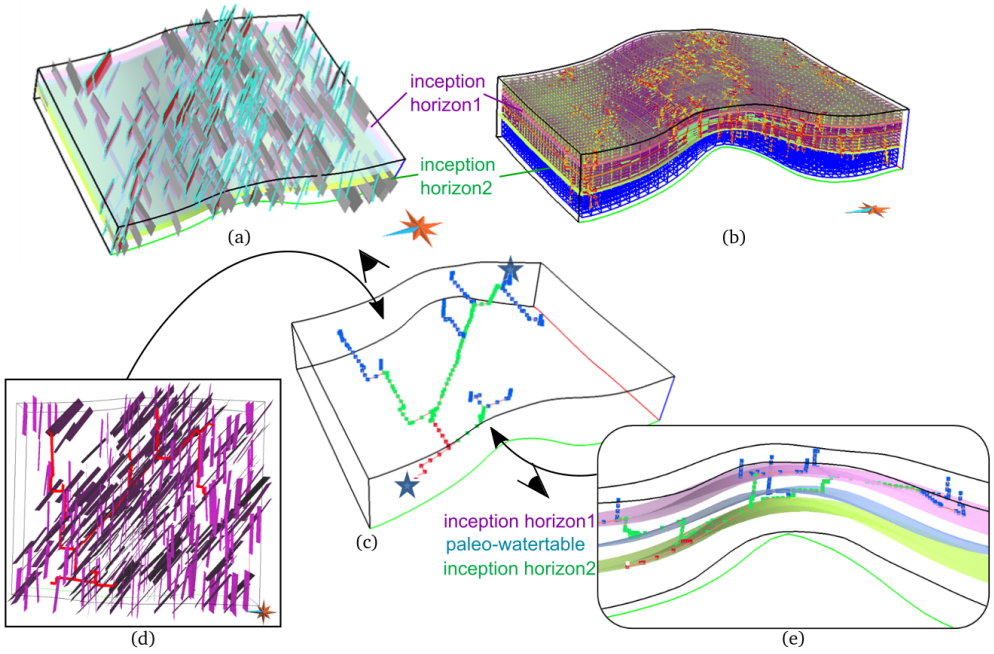

Figure II.28 : Simulation de réseau karstique arborescent : prise en compte des informations géologiques (modifié d'après Collon-Drouaillet et al. (2012)) : (a) le milieu initial est constitué de 3 couches sédimentaires séparées par des horizons d'inception. Dans les 2 niveaux calcaires supérieurs, 2 familles de fractures ont été simulées ; (b) graphe de connectivité correspondant, sur lequel on distingue nettement l'influence des fractures, des horizons d'inception et d'un niveau paléo-piézométrique ; (c) réseau karstique simulé avec $K_O = 3$, $R_B = 2.8$ et $R_L = 3.5$; (d) vue de dessus et (e) vue de côté superposées aux surfaces d'inception.

(1991). Nous avons alors utilisé la classification de Strahler (Strahler, 1952) et les ratios correspondants de Horton (Horton, 1945) pour simuler stochastiquement des réseaux karstiques arborescents à topologie contrôlée (Collon-Drouaillet et al., 2012). L'algorithme permet de générer des réseaux arborescents à topologie contrôlée à partir d'un ratio de bifurcation R_B, d'un ratio des longueurs R_L et d'un ordre global du réseau K_O (figure II.27).

Les informations apportées par la connaissance du milieu géologique traversé sont intégrées dans le calcul du chemin reliant deux points comme initialement proposé par Henrion et al. (2007, 2008) et Pellerin et al. (2008). Le milieu géologique est, en effet, tout d'abord discrétisé sous forme d'un graphe de connectivité (Vitel and Mallet, 2005; Vitel, 2007) (figure II.28b). Un chemin de moindre coût est ensuite calculé à travers ce graphe en utilisant l'algorithme $\mathcal{A}\star$ (Hart et al., 1968). Un point critique de cette démarche était alors la définition de coûts adéquats pour éviter tout biais dû à l'irrégularité de la discrétisation spatiale (Collon-Drouaillet et al., 2012). La méthode proposée permet ainsi d'intégrer la présence de surfaces d'inception, d'origine sédimentaire, tectonique ou hydrogéologique (figure II.28b). Les points d'entrée et de sortie du réseau karstique peuvent être définis aléatoirement par un processus de Poisson ou imposés par les observations de terrain (Bonneau et al., 2010; Bardy et al., 2011).

Si cette méthode s'avère efficace pour générer des réseaux arborescents à topologie contrôlée, les travaux parallèles que nous avons menés sur les réseaux karstiques réels ont démontré que très peu de réseaux sont purement arborescents (Vigouroux et al., 2010; Vuilleumier and Collon-Drouaillet, 2012). Dans les réseaux naturels, des reconnections apparaissent fréquemment et constituent des boucles ou cycles

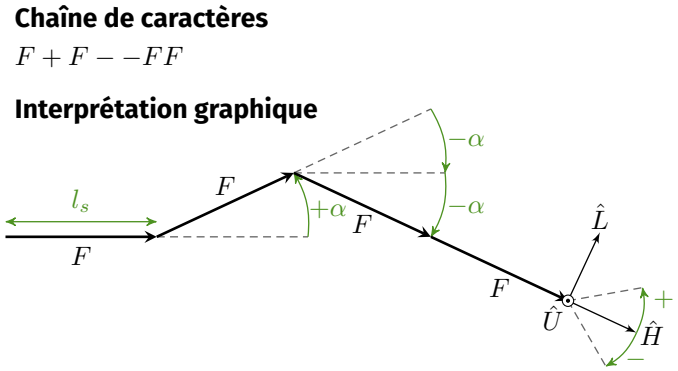

Figure II.29 : Système de Lindenmayer (L-système) : Exemple de chaîne de caractères et de son interprétation géométrique (Rongier, 2016). l_s représente la longueur d'un segment et α l'angle entre deux segments successifs. Dans cet exemple, le caractère F correspond à un mouvement de longueur l_s et au dessin d'un segment entre la position actuelle et l'ancienne. Les caractères $+$ et $-$ correspondent à une rotation, respectivement vers la droite et vers la gauche, d'un angle α. Les vecteurs $\hat{H}$, $\hat{L}$ et $\hat{U}$ sont représentés dans la position courante $\vec{P}$. Ils contrôlent le déplacement à venir.

(*loops*). Après avoir exploré les possibilités de générer de tels réseaux par des modèles booléens lors du master de Clément Barthélémy (Barthélémy and Collon-Drouaillet, 2013), nous avons décidé de développer une méthode de simulation basée sur le système de Lindenmayer - ou *L-système* (Lindenmayer, 1968; Prusinkiewicz, 1986; Prusinkiewicz and Lindenmayer, 1996).

Le L-système est une grammaire formelle parallèle (par opposition aux grammaires séquentielles) initialement développée pour la simulation des plantes et très utilisée en biologie (p. ex., Mvech and Prusinkiewicz, 1996; Streit et al., 2005). Il utilise un ensemble de symboles (ou alphabet) et de règles pour reproduire un processus de croissance. Il repose sur la notion de réécriture : à chaque étape les symboles agencés en une chaîne de caractères vont être remplacés suivant les différentes règles de réécriture du système pour produire une nouvelle chaîne de caractères. Par exemple, supposons un L-système simple composé de deux lettres a et b, d'un axiome (état initial) $\omega : a$, et de deux règles de production :

$$\begin{aligned} p_1 &: a \longrightarrow ba \\ p_2 &: b \longrightarrow a \end{aligned}$$

alors l'évolution du système sur 4 étapes donne :

$$\begin{aligned} 0 &: a \\ 1 &: ba \\ 2 &: aba \\ 3 &: baaba \\ 4 &: ababaaba \end{aligned}$$

Au-delà de ce simple exemple, la puissance du L-système est de pouvoir intégrer de la stochasticité et des informations "environnementales" dans les règles de production. Il est possible en effet de faire dépendre ces règles de paramètres représentant l'état du système ou du voisinage des caractères. Elles peuvent également être sélectionnées selon une règle probabiliste. Chaque symbole est associé à une interprétation graphique en deux ou trois dimensions permettant de représenter le résultat de la simulation (figure II.29). Là encore, l'interprétation graphique peut intégrer un caractère stochastique, p. ex. en tirant les longueurs des segments dessinés ou les angles de rotation dans des lois de distribution.

En s'appuyant sur les développements réalisés pour la simulation de chenaux dans le cadre de la thèse de Guillaume Rongier (section 4.1.2), nous avons adapté l'approche pour simuler des karsts de différentes topologies, de purement arborescents à purement anastomosés et qui honorent les données d'observation du karst (figure II.30). Ce premier travail a été réalisé lors du stage de master de Pierre Anquez (Anquez et al., 2015). Pendant celui de Pauline Mourlanette, nous avons intégré le conditionnement aux points de données (Mourlanette et al., 2016). L'algorithme se décompose en 3 étapes :

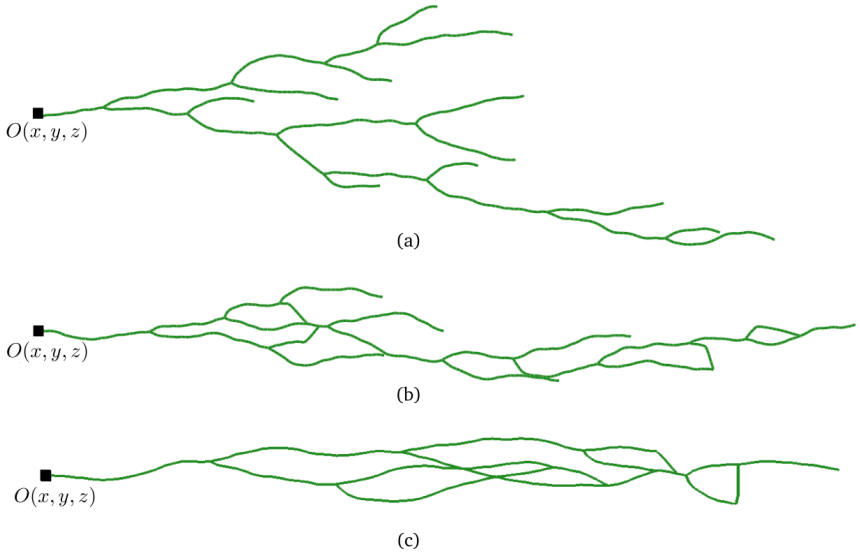

Figure II.30 : Trois exemples de réseaux simulés avec l'approche L-système (modifié d'après Anquez et al. (2015)). En entrée l'utilisateur indique le nombre de cycle souhaités n_l (ou un ratio dans la version 2016) : (a) $n_l = 0$, réseau purement arborescent, (b) $n_l = 8$, réseau mixte (c) $n_l = 10$, réseau anatomosé.

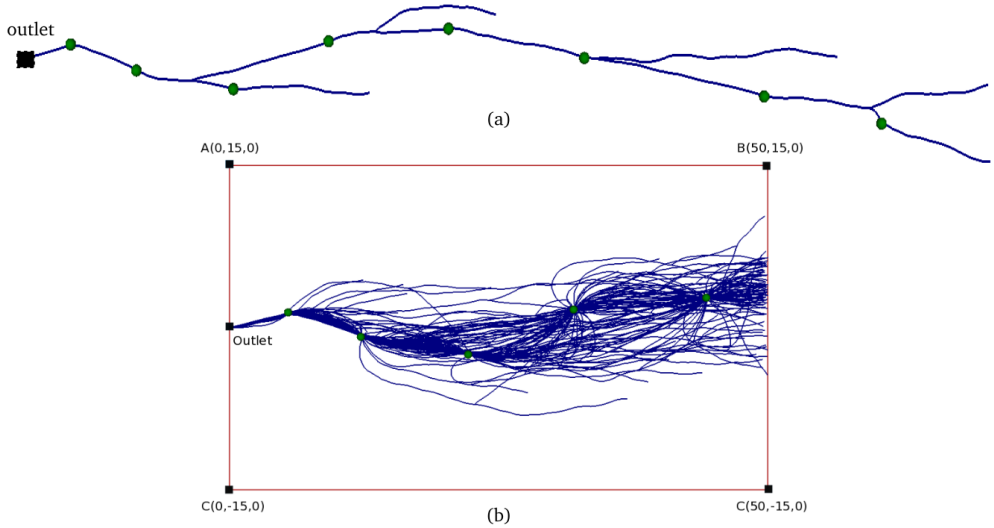

Figure II.31 : Introduction du conditionnement aux données dures dans la simulation de réseaux karstiques (modifié d'après Mourlanette et al. (2016)) : (a) résultat de la simulation d'un conduit purement arborescent conditionné aux données (points verts) ; (b) résultat de la simulation de 50 réseaux karstiques conditionnés aux données dures (points verts) et limité à une zone d'intérêt 2D (cadre rouge).

- Génération d'un système arborescent, avec attraction par les données. Certains conduits sont placés en "attente" pour permettre plus tard la génération de cycles.
- Conditionnement aux données non honorées à l'issue de la première étape.
- Génération des cycles à partir des conduits placés en "attente".

Les résultats sont encourageants mais les travaux demandent encore a être approfondis (figure II.31) et à être testés sur des données réelles. Un jeu de données du Val d'Orléans, mis à disposition par notre collègue Stéphane Binet de l'Institut des Sciences de la Terre d'Orléans, pourra être utilisé à cet effet. La prochaine étape doit également permettre d'intégrer les informations géologiques (fracturation, surface d'inception).

4.1.2 Systèmes chenalisés turbiditiques et fluviatiles

La continuité longitudinale des chenaux a un impact majeur sur la connectivité statique de ces structures. Or les méthodes stochastiques *basées cellule* (*cell-based methods*), qui, en remplissant les cellules d'une grille, conditionnent facilement aux données, ont des difficultés à reproduire la forme particulière de ces corps géologiques (section 3.2.2) (p. ex., Strebelle, 2002; Liu and Journel, 2004; Journel and Zhang, 2006). À l'inverse, les méthodes stochastiques *basées objet* (*object-based methods*), qui reposent sur une description géométrique de l'objet géologique à représenter, reproduisent facilement des chenaux mais conditionnent plus difficilement aux données (p. ex., Wietzerbin, 1994; Deutsch and Wang, 1996; Holden et al., 1998; Deutsch and Tran, 2002; Viseur, 2001; Pyrcz et al., 2009).

C'est pourquoi nous avons travaillé à adapter le L-système pour simuler stochastiquement des chenaux dans le cadre de la thèse de Guillaume Rongier (2016). Un alphabet et un ensemble de règles de production ont été spécifiquement développées pour simuler la morphologie de cet objet géologique, et reproduire aussi bien des chenaux rectilignes que sinueux. Des contraintes attractives et répulsives ont été intégrées dans le procédé pour influencer la croissance du chenal et honorer ainsi les données disponibles : interprétation de corps sédimentaires au niveau des puits, connectivité entre les puits, cube de proportion de faciès ou confinement des chenaux (figure II.32). La méthodologie ainsi proposée préserve la continuité des chenaux tout en ayant la flexibilité nécessaire pour conditionner aux données. Ceci a été démontré par une application à plusieurs cas synthétiques, intégrant plus ou moins de données d'entrées (Rongier et al., 2014b, 2015b; Rongier, 2016; Rongier et al., Subm.). À chaque fois, les contraintes sont honorées et ce parfois au détriment de la morphologie du chenal. La continuité des chenaux est, elle, toujours préservée, ce qui est justement un facteur de premier ordre influençant la connectivité statique du système.

L'agencement spatial des chenaux entre eux est également un élément de contrôle important. De ce fait, nous avons ensuite axé nos recherches sur la simulation de systèmes chenalisés complets en intégrant la migration et la rétro-migration des

chenaux. Les travaux existants dans le domaine s'appuient essentiellement sur des modèles physiques lourds à paramétrer (p. ex. Lopez, 2003; Pyrcz et al., 2009). Nous avons choisi là encore d'aborder ces questions par une approche descriptive du phénomène (Rongier et al., 2015a; Rongier, 2016). Le point de départ de cette méthode est un chenal, soit simulé stochastiquement par la méthode précédente basée L-système, soit interprété sur une image sismique de qualité (Ruiu et al., 2015). Deux méthodes sont alors proposées pour reproduire l'évolution du chenal : la première utilise une simulation gaussienne séquentielle (*Sequential Gaussian Simulation* ou SGS (Deutsch and Journel, 1992)), la deuxième une simulation multipoints d'échantillonnage direct (*Multiple Point Simulation* ou MPS (Mariethoz et al., 2010)) et une image d'entraînement. Le phénomène d'avulsion, qui consiste en un changement de lit brutal, est intégré à la simulation par le biais d'un tirage aléatoire le long du chenal et la génération d'un nouveau bras par L-système. La méthodologie ainsi développée

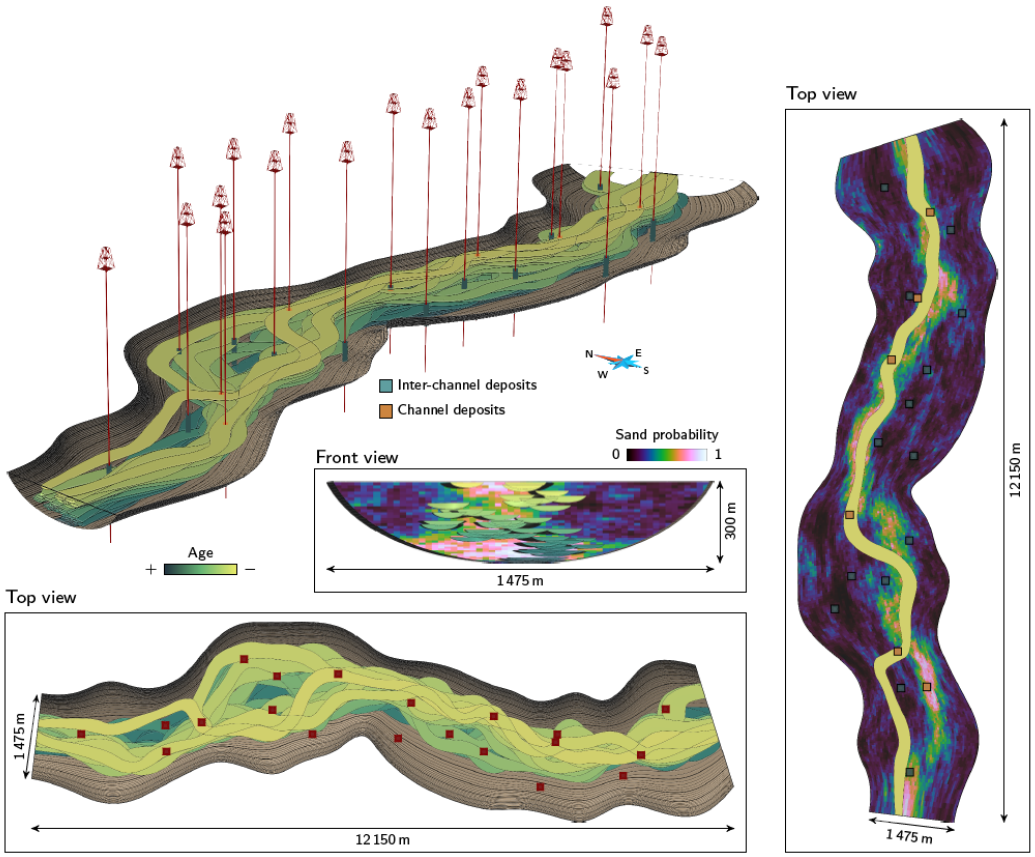

Figure II.32 : Exemple de réalisation de chenaux turbiditiques dans un chenal principal (Rongier et al., Subm.). Les chenaux sont conditionnés par un cube de probabilité de sable, par le chenal principal dont ils ne doivent pas dépasser les bords et par des données de puits : 14 puits imposent des faciès "non-chenaux" et 6 puits imposent le passage du chenal. Sur la droite est présenté le plus haut chenal de l'empilement.

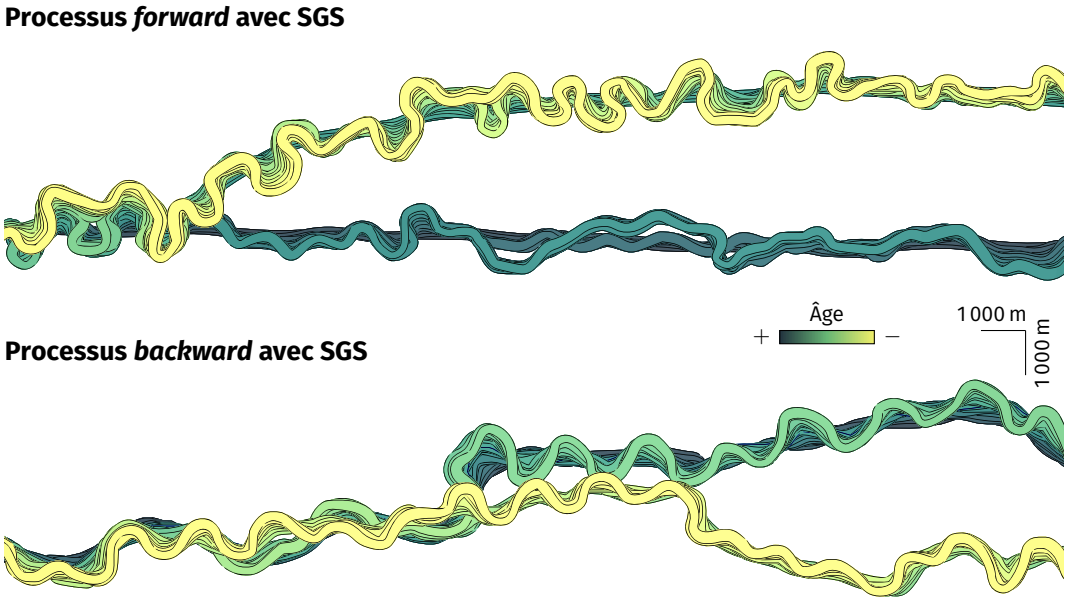

Figure II.33 : Exemples de réalisations avec une migration basée sur une simulation gaussienne séquentielle (Rongier, 2016). Le processus *forward* implique de commencer la simulation de la migration par le plus jeune des chenaux, c'est-à-dire celui en bas de séquence. Le processus *backward* implique de commencer la simulation de la migration par le plus vieux des chenaux, c'est-à-dire celui en haut de séquence. Cette dernière se justifie par le fait que ce chenal en haut de séquence est souvent observable sur les données sismiques.

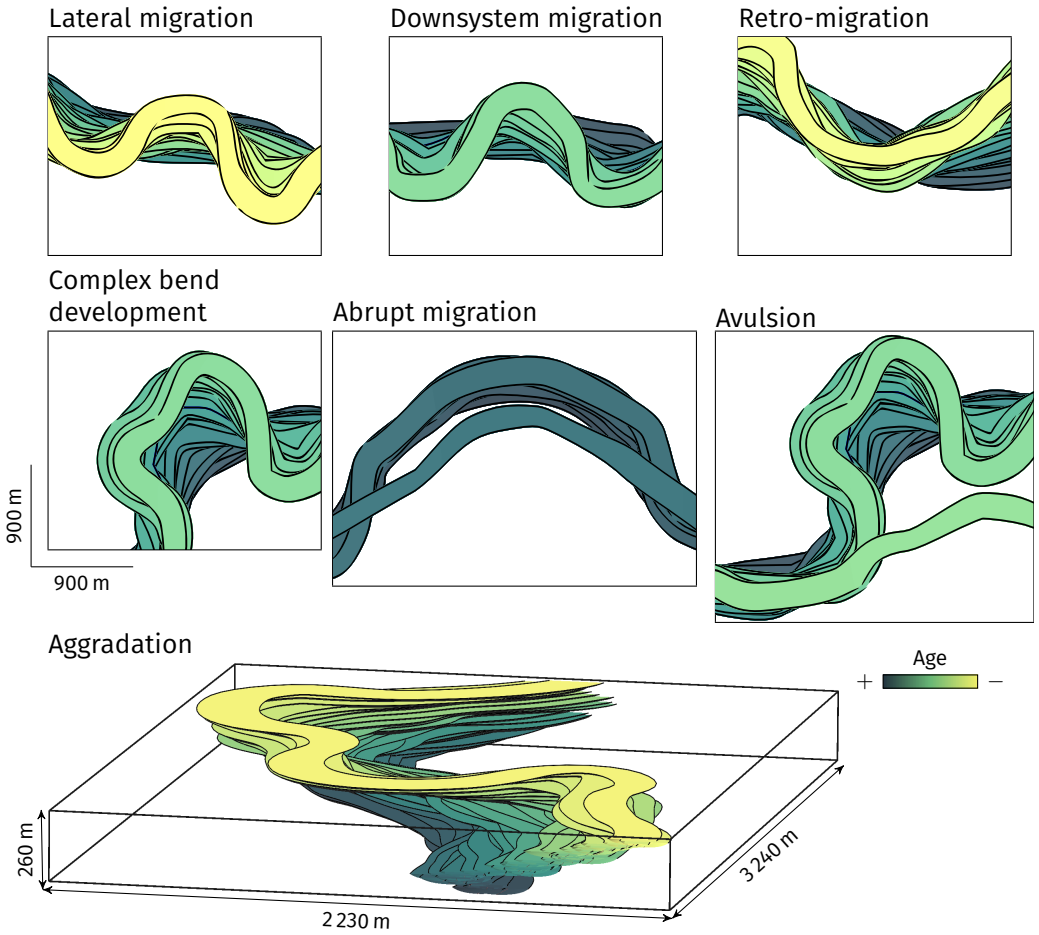

Figure II.34 : Zooms sur quelques parties des chenaux du processus *backward* de la figure II.33 illustrant différents aspects de l'évolution d'un chenal reproduits par la méthode : migration latérale, avale, rétro-migration locale, développement de méandres complexes, migrations brusques, avulsion et aggradation (Rongier, 2016).

permet de reproduire les différentes géométries observées dans des systèmes turbiditiques (figures II.33 et II.34). De plus, elle peut être réalisée en *forward*, c'est-à-dire en partant du chenal ancien et en simulant sa migration au cours du temps, mais aussi en *backward*, c'est-à-dire en simulant la rétro-migration d'un chenal à partir de son état final. Bien que contre-intuitive, cette dernière technique présente un intérêt pratique : le dernier chenal, caractérisé par des faciès d'abandon, est souvent rempli d'argiles, ce qui le fait ressortir sur les images sismiques (figure II.35). La rétro-migration du dernier chenal permet donc de partir de l'enregistrement sédimentaire, c'est-à-dire de l'état final du système, pour reconstruire les paléo-systèmes.

Appliquées à un cas synthétique, ces méthodologies ont montré leur potentiel. Il convient désormais de les appliquer à des cas pratiques et de les compléter pour intégrer encore plus d'informations géologiques. C'est l'ambition des travaux que nous menons actuellement dans le cadre de la thèse de Marion Parquer, réalisée dans l'équipe RING en co-encadrement avec Guillaume Caumon. L'accent est mis sur la combinaison entre des méthodes déterministes, utilisées là où les informations sismiques ou satellites permettent une interprétation sans ambiguïté, et des méthodes stochastiques là où peu d'informations sont disponibles.

Afin de définir un processus de rétro-migration plus proche des concepts géologiques, une étude statistique de la migration du fleuve Mississipi a été réalisée (Parquer et al., 2016a). Elle a mis en avant l'absence de corrélation entre courbure et am-

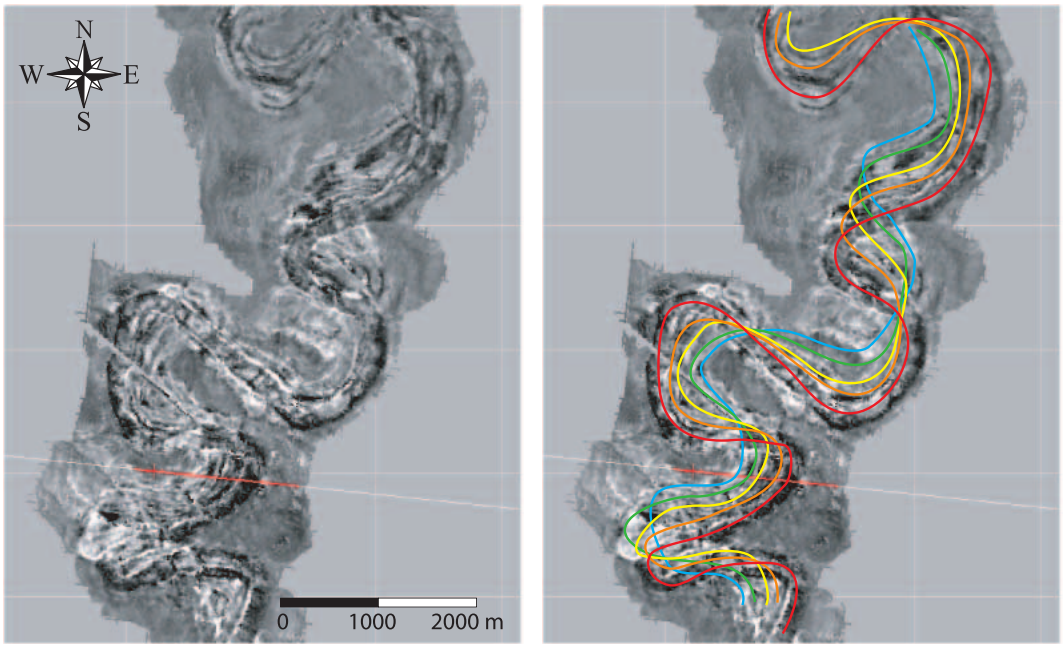

Figure II.35 : Exemple d'image sismique d'un système turbiditique d'Afrique de l'Ouest (Labourdette and Bez, 2010) : le dernier chenal et quelques unes de ses positions antérieures sont nettement identifiables et permettent une interprétation des plus récents évènements.

plitude de migration à l'échelle du fleuve. À l'échelle de chacun des demi-méandres, une corrélation peut cependant apparaître dont la valeur et le signe changent selon le demi-méandre étudié. Ces observations sont intégrées dans la nouvelle méthodologie de rétro-migration des chenaux que nous proposons : les déplacements sont stochastiquement simulés par demi-méandres et dissociés en deux composantes - avale et latérale.

L'autre contribution de ces travaux est d'intégrer les méandres d'abandon dans le processus de rétro-migration (Parquer et al., 2015, 2016a,b). Ces objets souvent identifiables sur les images sismiques sont en effet des éléments issus d'une évolution discrète et brutale du chenal, et donc non reproductibles par un processus continu. Nous proposons d'utiliser une distribution d'âge relatif pour chaque méandre d'abandon observé et digitalisé. Chaque méandre d'abandon est intégré itérativement lors du processus de rétro-migration dès que son âge relatif est atteint. L'opération consiste à segmenter le chenal aux points les plus proches des extrémités du méandre concerné, puis à connecter ces points aux extrémités du méandre d'abandon. Des processus d'attraction et de répulsion influencent avant cela la migration du chenal pour faciliter le processus d'intégration.

Cette méthode a été testée sur des données synthétiques et sur des images satellites. Elle fournit de bons résultats comme le montre la figure II.36. L'intégration des méandres d'abandon permet notamment à la rétro-migration d'un chenal de balayer l'étendue de la ceinture chenalisante et de reproduire plus fidèlement le processus de reprise de la rivière dans la plaine de débordement. À l'heure actuelle, certaines limites apparaissent dans la méthode puisque tous les méandres d'abandon ne sont pas systématiquement intégrés dans les différentes réalisations. Les travaux engagés cette année viseront à gérer ces configurations particulières, mais aussi à intégrer les données de puits. L'application à des données sismiques, auxquelles nous n'avons pas accès pour le moment, constitue également un de nos objectifs.

4.2 À l'échelle pluri-métrique : simuler des conduits

Alors que l'influence de la géométrie des réseaux drainants sur la connectivité statique d'un système à grande échelle semble assez intuitive, peu de travaux s'intéressent aux plus petites échelles d'hétérogénéités, et notamment à la simulation de conduits karstiques (Labourdette et al., 2007; Boggus and Crawfis, 2009). Pourtant la taille et le volume des conduits, données d'entrée des simulateurs d'écoulements, sont directement fonctions de leur géométrie. L'exploration des systèmes karstiques est un travail dangereux et complexe réalisé par les spéléogologues dans un objectif de cartographie et non pas d'analyse statistique. Dans le meilleur des cas, 4 mesures sont prises à chaque station : une distance au toit (*Up*), une distance au fond (*Down*), une distance au mur de droite (*Right*) et une à celui de gauche (*Left*). À partir de ces données, la galerie est alors approximée en une ellipse et chaque ellipse est reliée à la suivante par une interpolation linéaire. C'est à partir de cette approximation géométrique que sont généralement estimés les volumes. Pourtant, dans le cas des systèmes karstiques, les variations de morphologie sont importantes et des élargissements ou

(a) Image satellite (Google Earth 36°12'34.31"N 123°00'01.02"E)

(b) Identification de 24 méandres d'abandon et de leurs âges relatifs respectifs

(c) Réalisation 1 de rétro-migration stochastique conditionnant 17 méandres d'abandon (30 étapes temporelles)

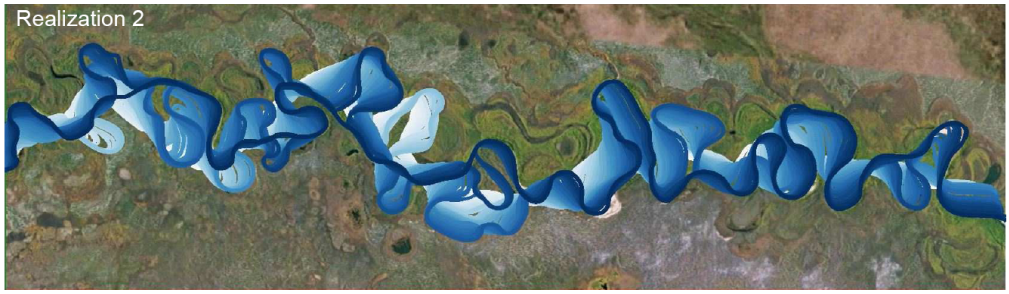

(d) Réalisation 2 de rétro-migration stochastique conditionnant 14 méandres d'abandon (30 étapes temporelles)

Figure II.36 : Simulation de rétro-migration sur la rivière Tangnara (Russie) (Parquer et al., 2016a).

rétrécissements brutaux peuvent avoir un impact non-négligeable sur la circulation des fluides (Morales et al., 2010). C'est pourquoi, en parallèle de la simulation et de la caractérisation des réseaux karstiques, nous avons également travaillé sur la reproduction de la géométrie des conduits karstiques.

Dans un premier temps, partant de la méthode "distance aux objets" (ODSIM pour *Object-based SImulation Method*) proposée par Henrion et al. (2010), nous avons proposé une adaptation spécifique aux conduits karstiques (Rongier and Collon, 2014; Rongier et al., 2014a). La méthode ODSIM propose de simuler des enveloppes tridimensionnelles d'objets géologiques quelconques en combinant un champ de distance euclidienne à un squelette avec un champ aléatoire. Il en résulte des enveloppes à base globalement circulaire alors que les géométries karstiques, fortement influencées par la géologie locale, ont des formes lenticulaires, en trou de serrure ou allongées selon un plan de fracture. C'est cette influence de la géologie locale que nous avons prise en compte dans la méthode e-ODSIM (*enhanced-ODSIM*) développée dans le cadre du stage de master de Guillaume Rongier (figure II.37).

Tout d'abord l'influence de plans d'inception lithostratigraphiques (p. ex., plans de stratification) ou tectoniques (failles, fractures) (Lowe and Lowe D., 1992; Filipponi et al., 2009) est intégrée par l'utilisation d'un champ de propagation généré par *fast marching* (Sethian, 1999). Le squelette est considéré comme source du champ propagé, et les éléments géologiques favorisant la genèse des conduits karstiques sont considérés comme des zones de forte vitesse. L'influence des niveaux piézométriques et paléo-piézométriques est intégrée directement ou indirectement au champ de vitesse, par un élargissement des valeurs de haute vitesse autour de ces couches (génération "d'encoches") ou par l'intermédiaire de niveaux d'attraction (génération des formes en "trou de serrure"). Ensuite, l'utilisation de régions lors de la simulation du champ aléatoire par simulation gaussienne séquentielle permet de générer des degrés de perturbation différents selon les zones concernées : p. ex. la base du conduit karstique peut ainsi être lissée par rapport au toit, ce qui traduit l'altération liée au ruissellement d'eau en fond de conduit. Grâce à un échantilloneur de Gibbs, il est également possible d'honorer des données renseignant sur la présence ou l'absence de karst le long de puits (Henrion et al., 2010).

La méthode e-ODSIM permet ainsi de reproduire une plus grande variété de géométries karstiques et, surtout, de les simuler en cohérence avec les informations géologiques (Rongier and Collon, 2014; Rongier et al., 2014a). Les paramètres restent difficiles à inférer mais l'application au karst de Furfooz (Belgique) a démontré la capacité de cette méthode à simuler des conduits réels (Le Mesnil et al., 2014). Par ailleurs, des calculs préliminaires comparant les volumes ainsi simulés aux volumes estimés à partir d'ellipses confirment les différences d'estimation de volume drainant. Des analyses plus poussées restent à conduire pour évaluer plus rigoureusement la plus-value d'une telle approche dans la gestion des incertitudes pour la simulation d'écoulements.

Depuis quelques années l'émergence des techniques d'acquisition LIDAR donne un nouvel intérêt au développement de techniques de simulation géométrique de

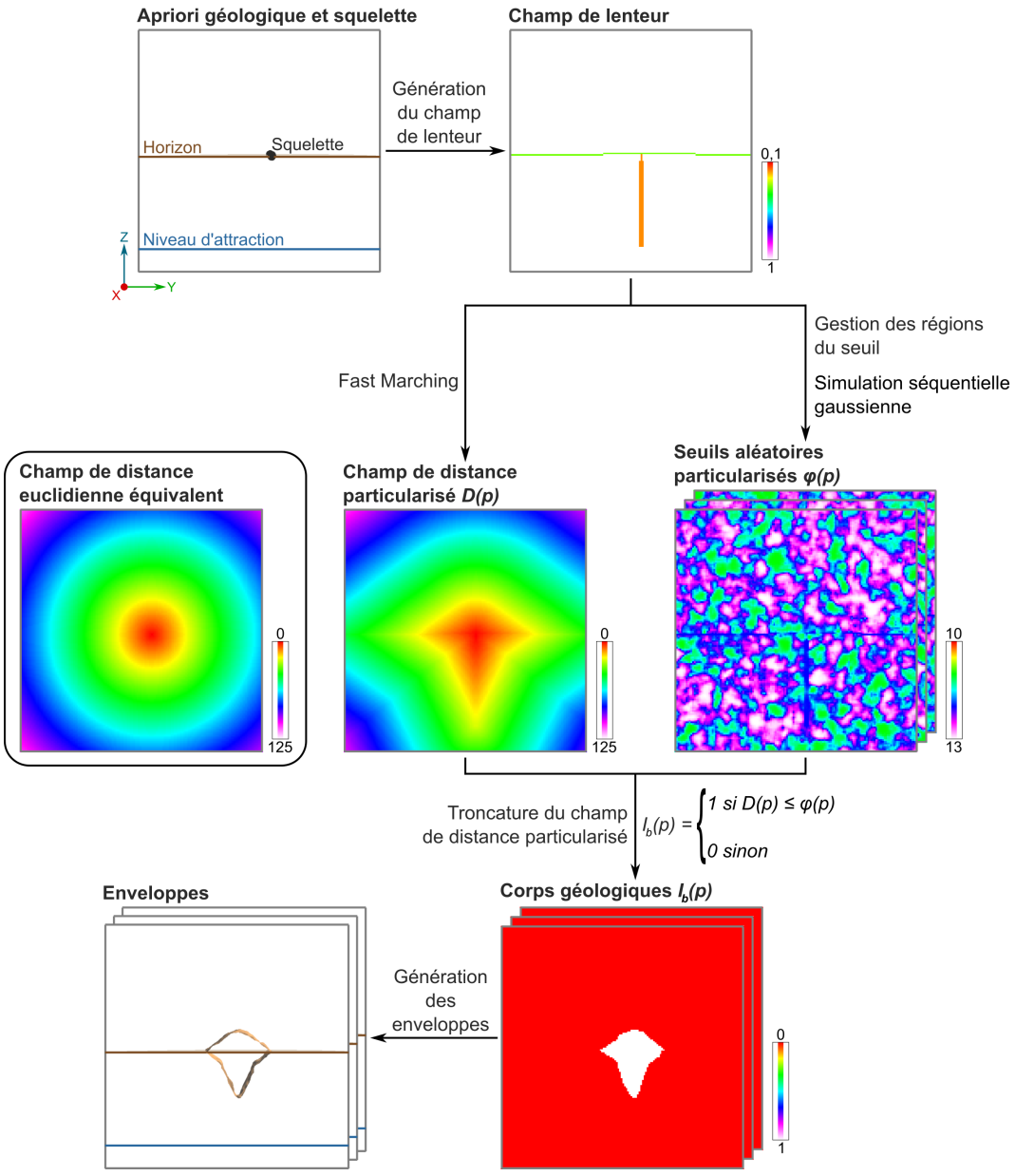

Figure II.37 : Étapes de génération des enveloppes produisant plusieurs représentations possibles d'un conduit karstique (Rongier and Collon, 2014). Le champ de lenteur correspond à l'inverse du champ de vitesse. Le champ de propagation affiche clairement la forme en trou de serrure du conduit, là où le champ de distance euclidienne affiche une forme purement circulaire. Les étapes sont présentées à l'aide de sections 2D pour plus de clarté mais les enveloppes sont générées directement en 3D.

conduits. En effet, si auparavant seules des mesures *Up-Down-Right-Left* étaient à espérer, des avancées récentes ont permis une exploration plus "volumique" des conduits. C'est le cas du système laser optique proposé par Schiller and Renard (2016) et appliqué au karst d'Ox Bel'Ha (Yucatan, Mexique). Il permet d'obtenir des sections régulières du conduit karstique et possède l'avantage de pouvoir opérer sous l'eau (figure II.39). Ainsi, en 3 plongées de 50 minutes, 800 mètres de conduits karstiques ont pu être enregistrés en une succession de sections distantes les unes des autres d'environ 3 mètres. Ces technologies fournissent donc de nouveaux types de données et requièrent de nouveaux développements méthodologiques, parmi lesquels la reconstruction en 3D du conduit échantillonné. Nous avons commencé à aborder ces questions récemment par le biais du master de Damien Lavandier (Lavandier et al., 2015). Deux approches ont été testées.

La première se base sur la méthode e-ODSIM présentée plus haut et utilise l'échantillonneur de Gibbs pour honorer les données (figure II.40(a)). Pour être opération-

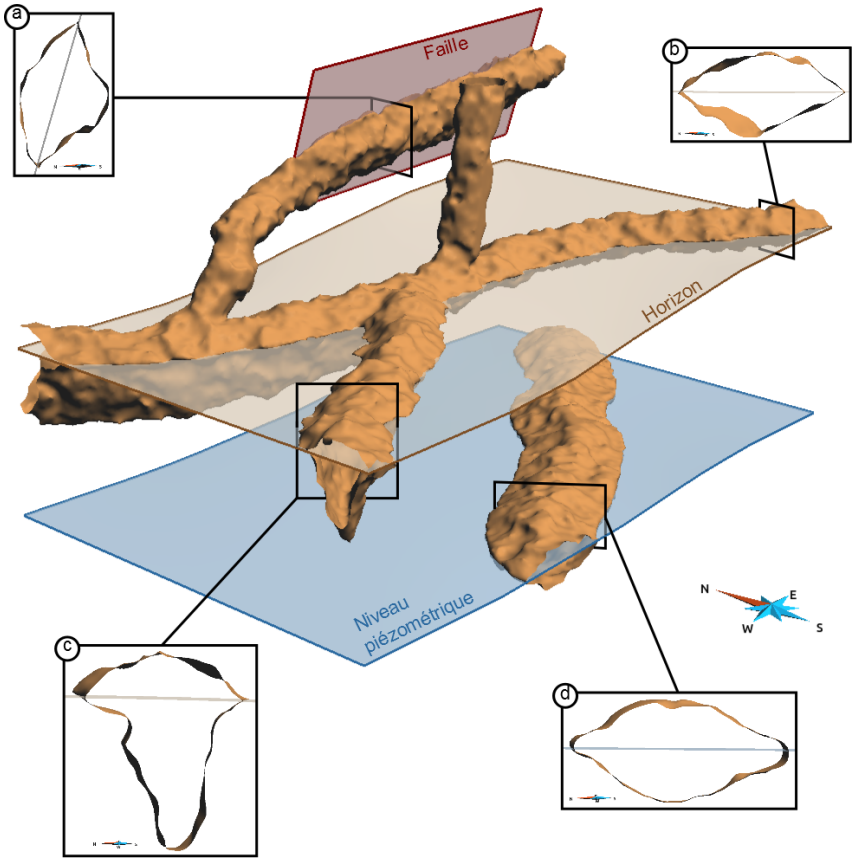

Figure II.38 : Conduit simulé à partir d'un plan d'inception stratigraphique (horizon), d'un plan d'inception tectonique (faille) et d'un niveau d'attraction superposé au niveau piézométrique. Tous ces éléments sont pris en compte dans la morphologie des conduits simulés (Rongier and Collon, 2014).

nelle, elle a été complétée d'un outil dédié qui permet de créer un nuage de points de conditionnement à partir des points de l'enveloppe relevés sur chaque section échantillonnée. Les résultats se sont avérés satisfaisants puisque les réseaux simulés honoraient les données tout en montrant une variabilité intéressante pour la gestion des incertitudes entre les sections échantillonnées. Cependant, comme la méthode utilise une grille pour calculer le champ de distance, les hautes résolutions nécessaires à ce niveau de détail rendent les calculs très longs et la méthode lourde à utiliser.

La deuxième approche consiste à interpoler itérativement une surface paramétrique (plus précisément une NURBS - *Non Uniform Rational B-Splines*) pour l'ajuster progressivement aux données (figure II.40(b)). Cette approche, bien que prometteuse, n'a pas donné les résultats escomptés puisque des artefacts apparaissaient rapidement lors du raffinement de la surface. Par ailleurs, elle est également apparue coûteuse en temps de calcul. La reconstruction de conduits 3D à partir de données denses apparaît donc comme un champ de recherche encore très riche en perspectives que nous envisageons donc de poursuivre dans les prochaines années. Elle trouve ses applications dans le cadre des conduits karstiques mais aussi dans celui de galeries souterraines d'origine anthropique, et à une autre échelle, dans la reconstruction de milieux poreux.

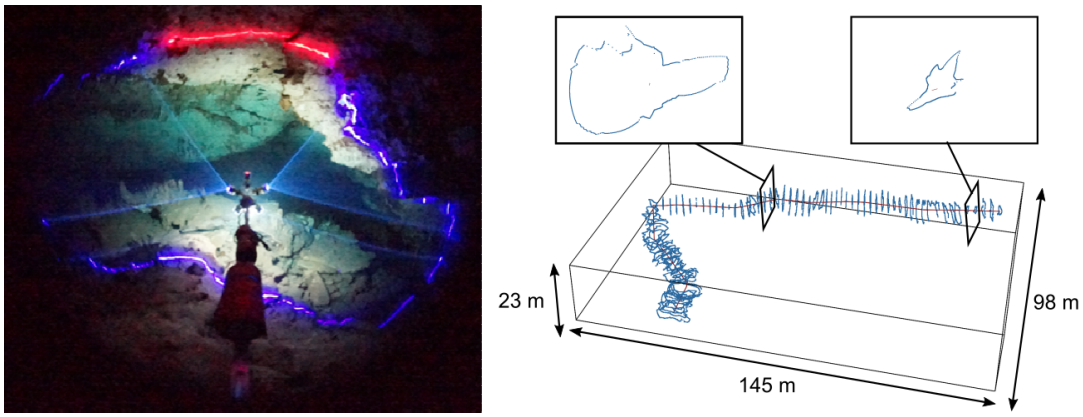

(a) (b)

Figure II.39 : Système d'acquisition par laser optique : (a) exemple de mise en œuvre du dispositif pour l'acquisition d'une section ; (b) ensemble de données résultant de l'exploration d'un tunnel (85 sections) (Schiller and Renard, 2016).

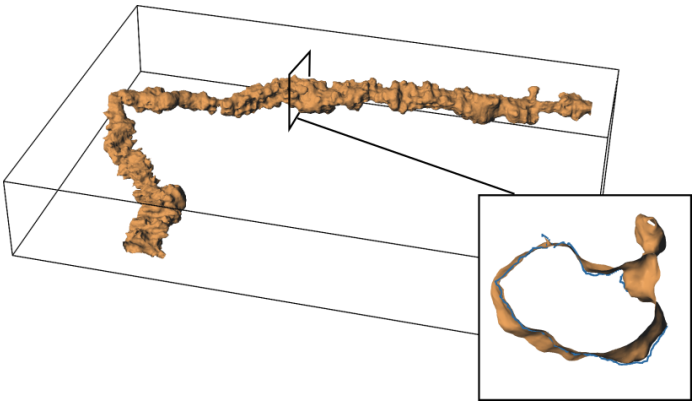

(a)

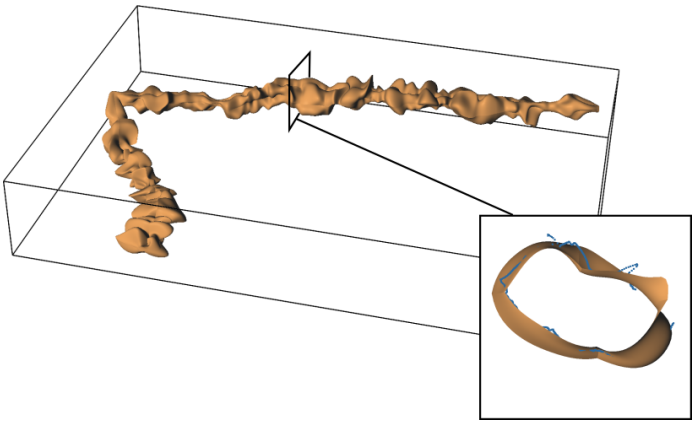

(b)

Figure II.40 : Résultats de la reconstruction 3D du conduit karstique exploré par laser optique présenté en figure II.39 (modifié d'après Lavandier et al. (2015)) : (a) réalisation obtenue avec la méthode ODSIM utilisant l'échantillonneur de Gibbs et la complétion automatique de données ; (b) réalisation avec l'approche basée sur l'interpolation itérative de surface paramétrique.

5

Conclusions et Perspectives

Certains objets souterrains, de par leur géométrie et leurs propriétés pétrophysiques spécifiques, ont une influence majeure sur les écoulements souterrains. C'est le cas des karsts, des galeries minières et des systèmes chenalisés turbiditiques et fluviatiles. Il convient dès lors de développer des stratégies de modélisation adaptées aux processus physiques dominants et/ou d'intérêt. Les travaux que j'ai menés depuis 15 ans avec de nombreux collègues et étudiants ont tous contribué à proposer des solutions innovantes à ces questions à travers une démarche combinant plusieurs disciplines : hydrogéologie, hydrogéochimie, géologie, géomodélisation, géostatistique et géologie numérique. C'est dans cette même direction que je compte articuler mes recherches futures, autour de plusieurs projets déjà engagés ou à venir.

Modélisation des systèmes chenalisés fluviatiles et turbiditiques

La modélisation des systèmes chenalisés fluviatiles et turbiditiques doit être poursuivie afin d'intégrer un maximum d'informations géologiques dans un processus de simulation combinant déterminisme, lorsque les informations de terrain le permettent, et stochasticité, dans les zones peu explorées. L'enjeu est de générer des modèles cohérents sans avoir recours à une description physique complète des processus.

Les travaux réalisés sur le L-système ont permis de proposer une méthode de simulation de chenaux qui honore à la fois les données de puits et les données sismiques tout en conservant la continuité longitudinale et la forme des structures (Rongier, 2016). La reproduction de l'organisation spatiale des chenaux a également été amorcée. Si les résultats sont déjà très satisfaisants en terme de géométrie, un des défis principaux sera de générer des ensembles complets de chenaux emboités et conditionnés, dans leur globalité, aux données de puits et de sismique.

Les travaux réalisés dans le cadre de la thèse de Marion Parquer sont un premier pas en ce sens. Ils permettent désormais d'intégrer l'abandon de méandre, processus

discontinu et parfois identifiable sur les données sismiques. Cependant, la datation relative de chaque méandre d'abandon n'est pas chose aisée et va nécessiter de nouveaux développements. Plus spécifiquement, un des défis à court terme va consister à définir des groupes cohérents de méandres d'abandon dans lesquels les âges relatifs peuvent être clairement établis, tandis que les âges relatifs entre deux groupes seront plus soumis à l'incertitude. Intégrer l'avulsion, pas uniquement de manière stochastique, mais en tenant également compte des contraintes liées au respect des observations de méandres d'abandon, est une autre piste que nous voulons rapidement explorer.

Dans cette démarche il est indispensable de s'appuyer sur des cas d'études réels et non pas synthétiques. C'est dans cet objectif que nous avons fait la récente acquisition de blocs sismiques 3D au large de l'Australie et que nous essayons de mettre en place des collaborations académiques ou industrielles. En plus de constituer un jeu de données d'entraînement, l'analyse statistique de données réelles devrait permettre de mieux contraindre les paramètres de simulation et de (rétro)-migration des chenaux.

Un point clé consiste aussi à définir des métriques pertinentes pour juger de la validité ou du réalisme d'un modèle. Les travaux déjà réalisés (Rongier et al., 2016b) permettent de comparer des réalisations selon des critères géométriques rendant compte d'une connectivité statique. Il serait intéressant de compléter cette approche en définissant des paramètres dynamiques pour caractériser la vraisemblance, au sens bayesien, des réalisations.

Enfin, à plus long terme, des stratégies spécifiques pour simuler les écoulements à travers les milieux générés devront être développées. Elles seront nécessaires pour mieux appréhender les effets de ces structures sur la connectivité souterraine. Elles pourront également permettre la mise en place d'approches inverses et ainsi réduire les incertitudes. Ceci passera par la définition de propriétés pétrophysiques adaptées aux spécificités de ces environnements, nécessitera l'établissement de stratégies de maillage, et éventuellement de changement d'échelle, permettant de mieux rendre compte des effets de ces hétérogénéités sur le transport de fluides.

Étude des réseaux karstiques

En ce qui concerne les systèmes karstiques, les perspectives sont tout aussi nombreuses. Mes recherches dans ce domaine ont en effet été principalement réalisées par le biais d'encadrement de masters (stages de 3 mois). Les nombreuses pistes défrichées ont encore besoin d'être approfondies pour amener à des résultats plus solides scientifiquement. Dans un premier temps, je pense poursuivre le développement d'une méthode basée sur le L-système entamée lors des masters de Pierre Anquez et Pauline Mourlanette (Anquez et al., 2015; Mourlanette et al., 2016). Il s'agit de parvenir à une méthode de simulation à topologie contrôlée et honorant les données d'observation du karst (présence/absence de karst mais aussi données de traçage). Il conviendra donc rapidement d'y intégrer les informations géologiques qui influencent le développement des karsts : plans d'inceptions stratigraphiques (horizons) et tectoniques (fractures et failles).

Tout comme pour les systèmes chenalisés, j'envisage d'utiliser des cas réels pour appliquer ces méthodes. Dans ce cadre, la collaboration actuelle avec l'Université de Namur nous permet déjà de disposer de données intéressantes sur les systèmes d'Han-sur-Lesse (Bonniver, 2011) et de Furfooz (Dewaide et al., 2014), tous deux en Belgique.

Actuellement la méthode basée L-système fonctionne le long de plans stratigraphiques. L'étendre, ou en développer une autre, pour simuler des réseaux dans un espace 3D complet est également indispensable. La dimension verticale de ces réseaux est en effet très variable selon les cas. Comme l'a montré l'analyse statistique de réseaux réels, certains sont clairement organisés le longs de plans sub-horizontaux reliés entre eux par quelques conduits verticaux, ils sont donc "2.5 D". À l'inverse, d'autres réseaux sont nettement développés dans les trois directions de l'espace et contrairement aux systèmes chenalisés, ne suivent pas nécessairement un gradient hydraulique : siphons, cul-de-sac, ... sont observés sur de nombreuses cartographies souterraines. Ces organisations spatiales différentes sont souvent le reflet d'un type de spéléogenèse, voire de la combinaison de plusieurs. Il est donc important de continuer les travaux d'analyse de systèmes naturels, en lien plus étroit avec les spéléologues, de manière à identifier les paramètres clés reliant une géométrie et un environnement géologique.

Par ailleurs les essais de traçage, s'ils fournissent en premier ordre une information sur les connexions hydrauliques, peuvent aussi être exploités pour aider au dimensionnement de conduits karstiques inexplorables par l'homme (Dewaide et al., 2016). Ces informations sont particulièrement intéressantes et permettraient de contraindre différemment la simulation.

Les paléo-karsts sont également un sujet d'intérêt. Par bien des points les développements prévus pour les karsts "de surface" peuvent directement s'appliquer au paléo-karst. Cependant, les données de traçage sont remplacées par des essais de puits et des informations sur la connectivité dynamique. Aucune cartographie humaine n'est disponible, elle est remplacée par des informations sismiques. Des réflexions devront donc être engagées pour mieux comprendre les particularités de ces environnements profonds et adapter nos méthodologies aux données disponibles dans ces contextes.

Enfin, comme pour les systèmes chenalisés, simuler les écoulements dans les réseaux générés est une étape indispensable vers une meilleure gestion des incertitudes : elle permet une sélection des représentations, voire une optimisation des paramètres de simulation, dans le cadre d'une approche inverse comme récemment suggéré par Borghi et al. (2016).

Reconstruction de géométries 3D d'objets géologiques

Abordée à travers la modélisation des conduits karstiques et le cas d'application du mini-bassin salifère d'Inceyol (Sivas, Turquie) (Collon et al., 2016b), la reconstruction de géométries 3D d'objets géologiques est une des voies de recherche que je souhaite explorer plus avant. À travers des applications pratiques, ce sont des verrous

méthodologiques particulièrement intéressants qui ont en effet été identifiés.

Très développées dans les domaines de l'informatique, les méthodes de reconstruction de géométries 3D s'appuient généralement sur des nuages de points relativement denses et répartis de manière homogène. Or en géologie les campagnes de terrain se traduisent plutôt par un échantillonnage hétérogène des structures, contraint par les qualités d'affleurement de surface et la résolution des technologies employées pour explorer la sub-surface. Il s'agit donc de compenser le sous-échantillonnage par des concepts géologiques pour parvenir à une reconstruction cohérente des structures, qui intègre les incertitudes associées. Dans le cadre de la tectonique salifère, le problème est d'autant plus intéressant que la déformation et la migration du sel ne conduit pas à la génération de surfaces minimales mais produit des géométries très variées (Giles and Lawton, 2002; Jackson and Harrison, 2006; Fossen, 2010). Plus particulièrement, les sutures de sel se traduisent géométriquement par une fusion locale des surfaces frontières du volume créant une contrainte topologique forte (surfaces non-variétées) que les approches actuelles ne permettent pas de gérer automatiquement. De même, les séquences halocinétiques également observées dans ces environnements sont des non-conformités délicates à intégrer dans un processus automatisé, puisqu'elles sont locales et qu'elles évoluent latéralement, et progressivement, vers des structures conformes.

Par ailleurs, l'interprétation géologique passe souvent par des coupes 2D. Outre les points d'échantillonnage, les lignes sont donc souvent un support important d'information géologique. Aujourd'hui, ces lignes sont généralement discrétisées pour être intégrées sous forme de contraintes ponctuelles dans la reconstruction de la surface. Il est pourtant pertinent de tenir compte de la relation topologique établie entre les points d'une même ligne (Caumon et al., 2013) mais également d'intégrer les relations entre plusieurs lignes, et de faciliter la prise en compte de la segmentation d'un même objet. Il conviendrait également de mieux exploiter les informations sismiques pour contraindre l'interpolation, idéalement par une utilisation directe des valeurs d'attributs sismiques. Ces perspectives sont l'objet d'une thèse qui devrait démarrer en janvier 2017.

D'autres applications pourraient profiter directement des développements induits par de tels travaux. Tout d'abord la reconstruction de conduits karstiques, telle qu'abordée dans le cas des acquisitions optiques laser à Ox-Bel'Ha (Yucatan, Mexique) (Schiller and Renard, 2016). Dans ce cas, la spécificité consiste principalement à gérer un ensemble de données concentrées sur des sections parallèles les unes aux autres tout en intégrant les incertitudes existant entre les sections échantillonnées.

Une deuxième application concerne le projet "ReMIT" porté par Jean Cauzid (GeoRessources) et faisant suite au projet PEPS Mirabelle 2015. Ce projet non financé par l'ANR en 2016 sera de nouveau présenté en 2017. Il porte sur les interactions entre les sociétés humaines et les caractères physico-chimiques d'un environnement dominé par l'exploitation passée de ressources minérales, et intègre en effet un volet "modélisation 3D". Dans ce volet, d'anciennes galeries minières devront être reconstruites en 3D, parfois à partir de données Lidar, parfois à partir d'informations plus proches des techniques spéléologiques. Elles serviront alors de support géométrique

au positionnement d'échantillonnages spectroscopiques et analytiques. Des méthodes d'extrapolation des teneurs en éléments chimiques permettront, nous l'espérons, de mieux comprendre et définir les origines métallogéniques des minéralisations observées.

Enfin, des travaux sur la reconstruction 3D de milieu poreux à partir d'images FIB-SEM sont également prévus dans le cadre du projet INTER Carnot "MultiEC-Hydrocox" porté par Fabrice Golfier (GeoRessources) et qui vise au développement d'outils de caractérisation multi-échelle du comportement hydrodynamique des milieux faiblement perméables.

Bibliographie

Adams, R. and Younger, P. (1997). Simulation of ground water rebound in abandoned mines using physically based modelling approach. In *6th international mine water association congress*, pages 353–362. Bled. *(Cited page 37)*

Ampomah, W., Balch, R. S., and Grigg, R. B. (2015). Analysis of Upscaling Algorithms in Heterogeneous Reservoirs with Different Recovery Processes. In *SPE Production and Operations Symposium*. Society of Petroleum Engineers. *(Cited page 46)*

Anquez, P., Rongier, G., and Collon, P. (2015). Stochastic simulations of karst networks with Lindenmayer systems. In *35thGocad Meeting*, pages 1–16, Nancy, France. *(Cited pages 71, 72, and 86)*

Bardy, G., Collon-Drouaillet, P., and Pellerin, J. (2011). Stochastic simulation of karstic systems : data conditioning. In *31st Gocad Meeting*, pages 1–11, Nancy, France. *(Cited page 70)*

Barthélémy, C. and Collon-Drouaillet, P. (2013). Simulation of Anastomotic Karst Networks. In *33rd Gocad Meeting*, pages 1–13, Nancy, France. *(Cited page 71)*

Batycky, R. (1997). *A three-dimensional two phase field scale streamline simulator*. PhD thesis, Stanford University. *(Cited page 41)*

Batycky, R. P., Blunt, M., and Thiele, M. (1997). A 3D field-scale streamline-based reservoir simulator. *SPE Annual Technical Conference and Exhibition*, 12(4) :246–254. *(Cited page 41)*

Boccaletti, S., Latora, V., Moreno, Y., Chavez, M., and Hwang, D. (2006). Complex networks : Structure and dynamics. *Physics Reports*, 424(4-5) :175–308. *(Cited page 61)*

Boggus, M. and Crawfis, R. (2009). Explicit Generation of 3D Models of Solution Caves for Virtual Environments. *Computer Science and Engineering*. *(Cited page 78)*

Boisvert, J. B., Pyrcz, M. J., and Deutsch, C. V. (2010). Multiple Point Metrics to Assess Categorical Variable Models. *Natural Resources Research*, 19(3) :165–175. *(Cited page 62)*

Bonneau, F., Henrion, V., and Collon-Drouaillet, P. (2010). Genetic-like modeling of karst network. In *30th Gocad Meeting*, pages 1–20, Nancy, France. *(Cited pages 60 and 70)*

Bonniver, I. (2011). *Etude hydogéologique et dimensionnement par modélisation du "Système-Traçage" du réseau karstique de Han-sur-Lesse (Massif de Boine - Belgique)*. PhD thesis, FUNDP Namur. *(Cited page 87)*

Borghi, A., Renard, P., and Cornaton, F. (2016). Can one identify karst conduit networks geometry and properties from hydraulic and tracer test data ? *Advances in Water Resources*, 90 :99–115. *(Cited page 87)*

Botella, A., Lévy, B., and Caumon, G. (2016). Indirect unstructured hex-dominant mesh generation using tetrahedra recombination. *Computational Geosciences*, 20(3) :437–451. *(Cited page 58)*

Brouyère, S., Orban, P., Wildemeersch, S., Couturier, J., Gardin, N., and Dassargues, A. (2009). The Hybrid Finite Element Mixing Cell Method : A New Flexible Method for Modelling Mine Ground Water Problems. *Mine Water Environment*, 28 :102–114. *(Cited page 30)*

Carr, J. C., Beatson, R. K., Cherrie, J. B., Mitchell, T. J., Fright, W. R., McCallum, B. C., and Evans, T. R. (2001). Reconstruction and representation of 3D objects with radial basis functions. In *SIGGRAPH '01 : Proceedings of the 28th annual conference on Computer graphics and interactive techniques*, pages 67–76, New York, NY, USA. ACM. *(Cited page 54)*

Caumon, G. (2010). Towards stochastic time-varying geological modeling. *Mathematical Geosciences*, 42(5) :555–569. *(Cited page 51)*

Caumon, G., Collon-Drouaillet, P., Le Carlier de Veslud, C., Viseur, S., and Sausse, J. (2009). Surface-Based 3D Modeling of Geological Structures. *Mathematical Geosciences*, 41(8) :927–945. *(Cited pages 52 and 54)*

Caumon, G., Gray, G., Antoine, C., and Titeux, M.-O. (2013). Three-Dimensional Implicit Stratigraphic Model Building From Remote Sensing Data on Tetrahedral Meshes : Theory and Application to a Regional Model of La Popa Basin, NE Mexico. *IEEE Transactions on Geoscience and Remote Sensing*, 51(3) :1613–1621. *(Cited pages 54, 58, and 88)*

Chilès, J.-P., Aug, C., Guillen, A., and Lees, T. (2004). Modelling the Geometry of Geological Units and its Uncertainty in 3D From Structural Data : The Potential-Field Method. In *Orebody Modelling and Strategic Mine Planning*, pages 313–320. *(Cited page 54)*

Christensen, M. l. C., Villa, U., and Vassilevski, P. (2015). Multilevel Techniques Lead to Accurate Numerical Upscaling and Scalable Robust Solvers for Reservoir Simulation. In *SPE Reservoir Simulation Symposium*. Society of Petroleum Engineers. *(Cited page 46)*

Christie, M. (1996). Upscaling for Reservoir Simulation. *Journal of Petroleum Technology*, 48(11) :1004–1010. *(Cited page 46)*

Christie, M. and Blunt, M. (2001). Tenth SPE Comparative Solution Project : A Comparison of Upscaling Techniques. In *SPE Reservoir Simulation Symposium*. Society of Petroleum Engineers. *(Cited page 48)*

Collon, P. (2003). *Évolution de la qualité de l'eau dans les mines abandonnées du bassin ferrifère lorrain. De l'expérimentation en laboratoire à la modélisation in situ*. PhD thesis, Institut National Polytechnique de Lorraine. *(Cited pages 37 and 39)*

Collon, P., Bernasconi, D., Vuilleumier, C., and Renard, P. (Subm.). Statistical metrics for the characterization of karst network geometry and topology. *Geomorphology*. *(Cited pages 61 and 62)*

Collon, P., Fabriol, R., and Buès, M. (2004). Ennoyage des mines de fer lorraines : impact sur la qualité de l'eau. *Comptes Rendus Geoscience*, 336(10) :889–899. *(Cited page 33)*

Collon, P., Fabriol, R., and Buès, M. (2005). Evolution of water quality in the abandoned iron mines of Lorraine : towards a semi-distributed modelling approach. *Comptes Rendus Geosciences*, 337(16) :1492–1499. *(Cited page 37)*

Collon, P., Fabriol, R., and Buès, M. (2006). Modelling the evolution of water quality in abandoned mines of the Lorraine Iron Basin. *Journal of Hydrology*, 328(3-4) :620–634. *(Cited pages 35, 36, and 37)*

Collon, P., Pichat, A., Kergaravat, C., Botella, A., Caumon, G., Ringenbach, J.-c., and Callot, J.-P. (2016b). 3D modelling from outcrop data in a salt tectonic context : Example from the Inceyol mini-basin, Sivas Basin, Turkey. *Interpretation*, 4(3) :SM17–SM31. *(Cited pages 55, 57, 58, and 87)*

Collon, P., Steckiewicz-Laurent, W., Pellerin, J., Gautier, L., Caumon, G., Reichart, G., and Vaute, L. (2015). 3D geomodelling combining implicit surfaces and Voronoi-based remeshing : A case study in the Lorraine Coal Basin (France). *Computers & Geosciences*, 77(0) :29–43. *(Cited pages 46, 53, 54, 55, and 56)*

Collon-Drouaillet, P., Henrion, V., and Pellerin, J. (2012). An algorithm for 3D simulation of branchwork karst networks using Horton parameters and A* Application to a synthetic case. *Geological Society, London, Special Publications*, 370(1) :295–306. *(Cited pages 68, 69, and 70)*

Collon-Drouaillet, P., Royer, J.-J., and Caumon, G. (2008). 3D Reactive Transport Modelling : Coupling the GOCAD Streamline Simulator to the Geochemical PHREEQC Model. In *28th Gocad Meeting*, pages 1–11, Nancy, France. *(Cited pages 41, 42, and 43)*

Costa, L. F. d. F., Rodrigues, F. A., Travieso, G., and Villas Boas, P. R. (2007). Characterization of complex networks : A survey of measurements. *Advances in Physics*, 56(1) :167–242. *(Cited page 61)*

Cox, T. F. and Cox, M. A. A. (1994). *Multidimensional scaling*. Chapman and Hall, London. *(Cited page 63)*

Crane, M. and Blunt, M. (1999). Streamline-based simulation of solute transport. *Water Resources Research*, 35 (10) :55–63. *(Cited page 41)*

Curl, R. L. (1966). Caves as a measure of karst. *The Journal of Geology*, 74(5) :798–830. *(Cited page 59)*

De Iaco, S. (2013). On the use of different metrics for assessing complex pattern reproductions. *Journal of Applied Statistics*, 40(4) :808–822. *(Cited page 63)*

de Kemp, E. and Sprague, K. (2003). Interpretive Tools for 3-D Structural Geological Modeling Part I : Bézier-Based Curves, Ribbons and Grip Frames. *GeoInformatica*, 7(1) :55–71. *(Cited page 51)*

Deutsch, C. V. (1998). Fortran programs for calculating connectivity of three-dimensional numerical models and for ranking multiple realizations. *Computers & Geosciences*, 24(1) :69–76. *(Cited page 63)*

Deutsch, C. V. and Journel, A. G. (1992). *GSLIB : Geostatistical Software Library and User's Guide*. Oxford University Press, New York. *(Cited page 74)*

Deutsch, C. V. and Tran, T. T. (2002). FLUVSIM : a program for object-based stochastic modeling of fluvial depositional systems. *Computers & Geosciences*, 28(4) :525–535. *(Cited page 73)*

Deutsch, C. V. and Wang, L. (1996). Hierarchical object-based stochastic modeling of fluvial reservoirs. *Mathematical Geology*, 28(7) :857–880. *(Cited page 73)*

Dewaide, L., Baele, J.-M., Collon-Drouaillet, P., Quinif, Y., Rochez, G., Vandycke, S., and Hallet, V. (2014). Karstification in dolomitized Waulsortian mudmounds (Belgium). *Geologica Belgica*, 17(1) :43–51. *(Cited page 87)*

Dewaide, L., Bonniver, I., Rochez, G., and Hallet, V. (2016). Solute transport in heterogeneous karst systems : Dimensioning and estimation of the transport parameters via multi-sampling tracer-tests modelling using the OTIS (One-dimensional Transport with Inflow and Storage) program. *Journal of Hydrology*, 534 :567–578. *(Cited page 87)*

Donato, G. D., Blunt, M. J. M., and Di Donato, G. (2004). Streamline-based dual-porosity simulation of reactive transport and flow in fractured reservoirs. *Water Resources Research*, 40(4) :W042031–W0420312. *(Cited page 41)*

Fetel, E. (2007). *Quantification des incertitudes liées aux simulations d'écoulement dans un réservoir pétrolier à l'aide de surfaces de réponse non linéaires*. PhD thesis, Institut National Polytechnique de Lorraine. *(Cited page 41)*

Fetel, E., Voillemont, J. C., Vesuld, C. L. C. D., and Gocad, J. J. R. (2004). Oil-Reservoir Streamline Simulation in GOcad. In *24th Gocad Meeting*, pages 1–13, Nancy, France. *(Cited page 41)*

Filipponi, M., Jeannin, P. P.-Y., and Tacher, L. (2009). Evidence of inception horizons in karst conduit networks. *Geomorphology*, 106(1-2) :86–99. *(Cited page 80)*

Fisher, T. R. and Wales, R. Q. (1992). Three Dimensional Solid Modeling of Geo-Objects Using Non-Uniform Rational B-Splines (NURBS). In *Three-Dimensional Modeling with Geoscientific Information Systems*, pages 85–105. Springer Netherlands, Dordrecht. *(Cited page 51)*

Fossen, H. (2010). *Structural Geology*. Cambridge University Press. *(Cited pages 58 and 88)*

Fournillon, A., Abelard, S., Viseur, S., Arfib, B., and Borgomano, J. (2012). Characterization of karstic networks by automatic extraction of geometrical and topological parameters : comparison between observations and stochastic simulations. *Geological Society, London, Special Publications*, 370(1996) :247–264. *(Cited page 60)*

Frank, T., Tertois, A.-L., and Mallet, J.-L. (2007). 3D-reconstruction of complex geological interfaces from irregularly distributed and noisy point data. *Computers and Geosciences*, 33(7) :932–943. *(Cited page 54)*

Freeman, L. C. (1977). A set of measures of centrality based on betweenness. *Sociometry*, 40(1) :35–41. *(Not cited)*

Giles, K. A. and Lawton, T. F. (2002). Halokinetic sequence stratigraphy adjacent to the El Papalote diapir, northeastern Mexico. *AAPG bulletin*, 86(5) :823–840. *(Cited pages 58 and 88)*

Gjoystdal, H., Reinhardsen, J. E., and Astebol, K. (1985). Computer representation of 3-D geological structures using a new "solid modeling" technique. *Geophysical Prospecting*, 33(8) :1195–1211. *(Cited page 51)*

Haecker, M. A. (1992). Convergent gridding : a new approach to surface reconstruction. *Geobyte*, 7(3) :48–53. *(Cited page 53)*

Hamm, V. and Bazargan Sabet, B. (2010). Modelling of fluid flow and heat transfer to assess the geothermal potential of a flooded coal mine in Lorraine, France. *Geothermics*, 39(2) :177–186. *(Cited page 44)*

Hamm, V., Collon-Drouaillet, P., and Fabriol, R. (2008). Two modelling approaches to water-quality simulation in a flooded iron-ore mine (Saizerais, Lorraine, France) : A semi-distributed chemical reactor model and a physically based distributed reactive transport pipe network model. *Journal of Contaminant Hydrology*, 96(1-4) :97–112. *(Cited pages 30, 38, and 39)*

Hart, P. E., Nilsson, N. J., and Raphael, B. (1968). A Formal Basis for the Heuristic Determination of Minimum Cost Paths in Graphs. *IEEE Trans. Syst. Sci. and Cybernetics*, SSC-4(2) :100–107. *(Cited page 70)*

Heikkinen, P. M., Räisänen, M. L., and Johnson, R. H. (2009). Geochemical Characterisation of Seepage and Drainage Water Quality from Two Sulphide Mine Tailings Impoundments : Acid Mine Drainage versus Neutral Mine Drainage. *Mine Water and the Environment*, 28(1) :30–49. *(Cited page 33)*

Henrion, V., Caumon, G., and Cherpeau, N. (2010). ODSIM : An Object-Distance Simulation method for Conditioning Complex Natural Structures. *Mathematical Geosciences*, 42(8) :911–924. *(Cited page 80)*

Henrion, V., Caumon, G., Vitel, S., and Kedzierski, P. (2007). Stochastic Simulation of Cave systems in Reservoir Modeling. In *27th Gocad Meeting*, pages 1–11. *(Cited page 70)*

Henrion, V., Pellerin, J., and Caumon, G. (2008). A stochastic methodology for 3d cave system modeling. In Ltd, G., editor, *8th Geostatistics Congress*, pages 525–533, Santiago, Chili. *(Cited page 70)*

Hoffman, K., Neave, J., and Klein, R. (2003). Streamlining the WorkFlow From Structure Model to Reservoir Grid. In *SPE Annual Technical Conference and Exhibition*. Society of Petroleum Engineers. *(Cited page 51)*

Holden, L., Hauge, R., Skare, O., and Skorstad, A. (1998). Modeling of Fluvial Reservoirs with Object Models. *Mathematical Geology*, 30(5) :473–496. *(Cited page 73)*

Horton, R. E. (1945). Erosional development of streams and their drainage basins ; hydrophysical approach to quantitative morphology. *Bulletin Geological Society of America*, 56 :275–370. *(Cited pages 59 and 70)*

Howard, A. D. (1971). Quantitative Mesures of Caves Patterns. *Caves and Karst*, 13(1) :1–7. *(Cited pages 59 and 60)*

Howard, A. D., Keetch, M. E., and Vincent, C. L. (1970). Topological and geometrical properties of braided patterns. *Water Ressources Research*, 6(6) :1674–1688. *(Cited page 59)*

Jackson, M. P. A. and Harrison, J. C. (2006). An allochthonous salt canopy on Axel Heiberg Island, Sverdrup Basin, Arctic Canada. *Geology*, 34(12) :1045–1048. *(Cited pages 58 and 88)*

Jauzein, M., Andre, C., Margrita, R., Sardin, M., and Schweich, D. (1989). A flexible computer code for modelling transport in porous media : impact. *Geoderma*, 44(2-3) :95 – 113. *(Cited page 36)*

Jessell, M. (2001). Three-dimensional geological modelling of potential-field data. *Computers and Geosciences*, 27(4) :455–465. *(Cited page 51)*

Johnson, C. and Jones, T. (1988). Putting Geology Into Reservoir Simulations : A Three-Dimensional Modeling Approach. In *SPE Annual Technical Conference and Exhibition*. Society of Petroleum Engineers. *(Cited page 51)*

Journel, A. and Zhang, T. (2006). The necessity of a multiple-point prior model. *Mathematical Geology*, 38(5) :591–610. *(Cited page 73)*

Karim, M. R. and Krabbenhoft, K. (2010). New Renormalization Schemes for Conductivity Upscaling in Heterogeneous Media. *Transport in Porous Media*, 85(3) :677–690. *(Cited page 46)*

Kaven, J., Mazzeo, R., and Pollard, D. (2009). Constraining surface interpolations using elastic plate bending solutions with applications to geologic folding. *Mathematical Geosciences*, 41(1) :1–14. *(Cited page 53)*

Kim, H.-J. and Kim, J. M. (2005). Cyclic Topology in Complex Networks. *Physical review. E, Statistical, nonlinear, and soft matter physics*, 72(3 Pt 2) :2–5. *(Not cited)*

Kirby, C. S. and Cravotta, C. A. (2005). Net alkalinity and net acidity 2 : Practical considerations. *Applied Geochemistry*, 20(10) :1941–1964. *(Cited page 33)*

Kucha, H. and Pawlikowski, M. (1986). Two-brine model of the genesis of stratabound Zechstein deposits (Kupferschiefer type), Poland. *Mineralium Deposita*, 21(1). *(Cited page 44)*

Kutschke, S., Guézennec, A., Hedrich, S., Schippers, A., Borg, G., Kamradt, A., Gouin, J., Giebner, F., Schopf, S., Schlömann, M., Rahfeld, A., Gutzmer, J., D'Hugues, P., Pollmann, K., Dirlich, S., and Bodénan, F. (2015). Bioleaching of Kupferschiefer blackshale – A review including perspectives of the Ecometals project. *Minerals Engineering*, 75 :116–125. *(Cited page 44)*

Labourdette, R. and Bez, M. (2010). Element migration in turbidite systems : Random or systematic depositional processes ? *AAPG Bulletin*, 94(3) :345–368. *(Cited page 77)*

Labourdette, R., Lascu, I., Mylroie, J., and Roth, M. (2007). Process-Like Modeling of Flank-Margin Caves : From Genesis to Burial Evolution. *Journal of Sedimentary Research*, 77(11) :965–979. *(Cited page 78)*

Laurent, G., Collon, P., Golfier, F., Royer, J.-J., and Gruzdeva, Y. (2016). A streamline-based approach to reactive transport simulation for in-situ bio-leaching of copper. In *2016 RING Meeting*, pages 337–342, Nancy, France. *(Cited pages 43 and 44)*

Lavandier, D., Rongier, G., and Collon, P. (2015). 3D reconstruction of karstic conduit from sparse laser data Case study : the Ox Bel ' Ha system , Yucatan , Mexico. In *35thGocad Meeting*, pages 1–14, Nancy, France. *(Cited pages 82 and 84)*

Le Mesnil, M., Collon-Drouaillet, P., Dewaide, L., Mejia-Herrera, P., Rongier, G., and Hallet, V. (2014). Karst conduit generation : the Furfooz area case study (Belgium). In *34th Gocad Meeting*, pages 1–19, Nancy, France. *(Cited page 80)*

Lévy, B. and Liu, Y. (2010). Lp Centroidal Voronoi Tessellation and its applications. In *ACM SIGGRAPH 2010 papers on - SIGGRAPH '10*, pages 29(4),1–11, New York, New York, USA. ACM Press. *(Cited page 49)*

Lindenmayer, A. (1968). Mathematical models for cellular interactions in development I. Filaments with one-sided inputs. *Journal of Theoretical Biology*, 18(3) :280–299. *(Cited page 71)*

Liu, Y. and Journel, A. (2004). Improving sequential simulations with a structured path guided by information content. *Mathematical Geology*, 36(8) :945–964. *(Cited page 73)*

Lopez, S. (2003). *Modélisation de réservoirs chenalisés méandriformes : une approche génétique et stochastique*. PhD thesis, Ecole Nationale Supérieure des Mines de Paris. *(Cited page 74)*

Lowe, D. and Lowe D. (1992). *The origin of limestone caverns : an inception horizon hypothesis.* PhD thesis, Manchester Polytechnic, United Kingdom. *(Cited page 80)*

MacQuarrie, K. T. and Mayer, K. U. (2005). Reactive transport modeling in fractured rock : A state-of-the-science review. *Earth-Science Reviews*, 72(3) :189–227. *(Cited page 32)*

Mallet, J.-L. (1988). Three dimensional graphic display of disconnected bodies. *Mathematical geology*, 122 :977–990. *(Cited page 51)*

Mallet, J.-L. (1989). Discrete Smooth Interpolation in Geometric Modeling. *ACM Transactions on Graphics*, 8(2) :121–144. *(Cited page 54)*

Mallet, J.-L. (1992). Discrete Smooth Interpolation. *Computer-Aided Design*, 24(4) :263–270. *(Cited page 54)*

Mallet, J.-L. (1997). Discrete Modelling for natural objects. *Mathematical geology*, 29(2) :199–219. *(Cited page 54)*

Mallet, J.-L. (2002). *Geomodeling*. Applied Geostatistics. Oxford University Press, New York, NY. *(Cited page 51)*

Mariethoz, G., Renard, P., and Straubhaar, J. (2010). The Direct Sampling method to perform multiple-point geostatistical simulations. *Water Resources Research*, 46(11) :W11536–14. *(Cited page 74)*

Merland, R. (2013). *Génération de grilles de type volumes finis : adaptation à un modèle structural, pétrophysique et dynamique*. PhD thesis, Université de Lorraine. *(Cited pages 48, 49, and 50)*

Merland, R., Caumon, G., Lévy, B., and Collon-Drouaillet, P. (2014). Voronoi Grids Conforming to 3D Structural Features. *Computational Geosciences*, 18(3-4) :373–383. *(Cited pages 49 and 50)*

Merland, R., Lévy, B., Caumon, G., and Collon-Drouaillet, P. (2010). Building centroidal Voronoi tessellations for flow simulation in reservoirs using flow information. In *30th Gocad Meeting*, pages 1–13, Nancy, France. *(Cited page 50)*

Merland, R., Levy, B., Caumon, G., and Collon-Drouaillet, P. (2011). Building centroidal Voronoi tessellations for flow simulation in reservoirs using flow information. In *SPE Reservoir Simulation Symposium*, pages 141018–11p. *(Cited page 49)*

Morales, T., Uriarte, J. A., Olazar, M., Antigüedad, I., and Angulo, B. (2010). Solute transport modelling in karst conduits with slow zones during different hydrologic conditions. *Journal of Hydrology*, 390(3-4) :182 – 189. *(Cited page 80)*

Mourlanette, P., Anquez, P., Rongier, G., and Collon, P. (2016). Integration of geological knowledge in karstic network simulations with L-systems. In *2016 RING Meeting*, pages 241–252, Nancy, France. *(Cited pages 71, 72, and 86)*

Moyen, R., Mallet, J.-L., Frank, T., Leflon, B., and Royer, J.-J. (2004). 3D-Parameterization of the 3D geological space - The GeoChron model. In *European Conference on the Mathematics of Oil Recovery (ECMOR IX)*, page 8. *(Cited page 54)*

Mvech, R. and Prusinkiewicz, P. (1996). Visual models of plants interacting with their environment. In *Proceedings of the 23rd annual conference on Computer graphics and interactive techniques*, pages 397–410. *(Cited page 71)*

Newman, M. E. J. (2002). Assortative mixing in networks. *Physical review letters*, 89(20) :208701. *(Not cited)*

Obi, E. and Blunt, M. (2004). Streamline-based simulation of advective-dispersive solute transport. *Advances in Water Resources*, 27(9) :913–924. *(Cited page 41)*

Palmer, A. (1991). Origin and morphology of limestone caves. *Geological Society of America Bulleetin*, 103 :1–21. *(Cited pages 60 and 69)*

Palmer, A. N. (2003). Speleogenesis in Carbonate Rocks. *Speleogenesis and Evolution of Karst Aquifer, The virtual Scientific Journal*, 1(1) :11. *(Cited page 60)*

Pardo-Iguzquiza, E., Duran-Valsero, J., and Rodriguez-Galiano, V. (2011). Morphometric analysis of three-dimensional networks of karst conduits. *Geomorphology*, 132(1-2) :17–28. *(Cited page 60)*

Parkhurst, D. and Appelo, C. (1999). User Guide to PHREEQC (Version 2) : A computer program for speciation, batch-reaction, one-dimensional transport, and inverse geochemical calculations. Technical report, U.S. Geological Survey Water-Resources Investigations. *(Cited page 41)*

Parkhurst, D., Kipp, K., and Charlton, S. (2010). PHAST Version 2—A program for simulating groundwater flow, solute transport, and multicomponent geochemical reactions. *U.S. Geological Survey Techniques and Methods*, 6(A35) :1–235. *(Cited page 43)*

Parquer, M., Collon, P., and Caumon, G. (2016a). Conditioning channel backward migration modeling to seismic data. In *78th EAGE Conference & Exhibition 2016*, pages 1–5, Vienna, Austria. *(Cited pages 77, 78, and 79)*

Parquer, M., Collon, P., and Caumon, G. (2016b). Stochastic simulation of channel migration conditioned to subsurface data. In *Geostats2016*, Valencia, Spain. *(Cited page 78)*

Parquer, M., Collon, P., Caumon, G., and Rongier, G. (2015). Toward more genetics concepts and data integration in channel simulation Channelized systems characterization. In *35thGocad Meeting*, pages 1–16, Nancy, France. *(Cited page 78)*

Pellerin, J., Henrion, V., and Caumon, G. (2008). Stochastic simulation of cave systems with ODSIM. In *28th Gocad Meeting*, pages 1–12. *(Cited page 70)*

Pellerin, J., Lévy, B., Caumon, G., and Botella, A. (2014). Automatic surface remeshing of 3D structural models at specified resolution : A method based on Voronoi diagrams. *Computers & Geosciences*, 62 :103–116. *(Cited page 55)*

Pettit, C., Scharer, J., Chambers, D., Halbert, B., Kirkaldy, J., and Bolduc, L. (1999). Neutral mine drainage. In *Proceedings of Mining and the Environment*, pages 829–838, Sudbury, Canada. *(Cited page 33)*

Piccini, L. (2011). Recent Developments on morphometric analysis of karst caves. *Acta Carsologica*, 40(1) :43–52. *(Cited page 60)*

Prusinkiewicz, P. (1986). Graphical applications of L-systems. In *Proceedings of graphics interface*, volume 86, pages 247–253. *(Cited page 71)*

Prusinkiewicz, P. and Lindenmayer, A. (1996). *The Algorithmic Beauty of Plants*. Springer-Verlag, New York, NY, USA. *(Cited page 71)*

Pyrcz, M. J., Boisvert, J. B., and Deutsch, C. V. (2009). ALLUVSIM : A program for event-based stochastic modeling of fluvial depositional systems. *Computers & Geosciences*, 35(8) :1671–1685. *(Cited pages 73 and 74)*

Ravasz, E. and Barabasi, A.-L. (2002). Hierarchical Organization in Complex Networks. *Physical Review E*, 67(2) :026112. *(Cited page 61)*

Reichart, G. (2015). *Modélisation thermo-hydrodynamique d'un réservoir minier profond ennoyé - Le cas du Bassin Houiller Lorrain*. PhD thesis, Université de Lorraine. *(Cited pages 44, 45, 46, 47, and 55)*

Renard, P. and Allard, D. (2013). Connectivity metrics for subsurface flow and transport. *Advances in Water Resources*, 51 :168–196. *(Cited page 30)*

Renard, P., Bernasconi, D., Borghi, A., Collon-Drouaillet, P., and Vuilleumier, C. (2013). Karst network geometry and topology : automatic classification of network geometry. In *15th IAMG Conference*, pages 1–1, Madrid, Spain. *(Cited page 62)*

Renard, P. and de Marsily, G. (1997). Calculating equivalent permeability : a review. *Advances in Water Resources*, 20(5-6) :253–278. *(Cited page 46)*

Rongier, G. (2016). *Connectivité de corps sédimentaires chenalisés : stratégies d'analyse et de simulation en modélisation de subsurface*. PhD thesis, Université de Lorraine. *(Cited pages 62, 63, 70, 73, 74, 75, 76, and 85)*

Rongier, G. and Collon, P. (2014). Conduits Karstiques en 3D : une méthode de simulation stochastique. *Karstologia*, 63(1) :58–60. *(Cited pages 80, 81, and 82)*

Rongier, G., Collon, P., and Renard, P. (2015a). A new application of L-systems to model channel system architecture and connectivity Using L-system for channel generation. In *35thGocad Meeting*, pages 1–15, Nancy, France. *(Cited page 74)*

Rongier, G., Collon, P., and Renard, P. (Subm.). Stochastic simulation of channelized sedimentary bodies using a constrained L-system. *Computers and Geosciences*. *(Cited pages 73 and 74)*

Rongier, G., Collon, P., Renard, P., and Ruiu, J. (2015b). Channel simulation using L-system, potential fields and NURBS. In *35thGocad Meeting*, pages 1–5, Nancy, France. *(Cited page 73)*

Rongier, G., Collon, P., Renard, P., Straubhaar, J., and Sausse, J. (2015c). Quality analysis of geostatistical simulations through their connected structures. In *EAGE - Petroleum Geostatistics 2015*, Biarritz, France. *(Cited page 63)*

Rongier, G., Collon, P., Renard, P., Straubhaar, J., and Sausse, J. (2016b). Comparing connected structures in ensemble of random fields. *Advances in Water Resources*, 96 :145–169. *(Cited pages 63, 64, 65, and 86)*

Rongier, G., Collon-Drouaillet, P., and Filipponi, M. (2014a). Simulation of 3D karst conduits with an object-distance based method integrating geological knowledge. *Geomorphology*, 217 :152–164. *(Cited page 80)*

Rongier, G., Collon-Drouaillet, P., and Renard, P. (2014b). Channel axis simulation based on Lindenmayer systems. In *34th Gocad Meeting*, pages 1–27, Nancy, France. *(Cited page 73)*

Rongier, G., Collon-Drouaillet, P., Renard, P., Straubhaar, J., and Sausse, J. (2013). Reproduction assessment of connected geobodies in multiple-point simulation. In *33rd Gocad Meeting*, pages 1–32, Nancy, France. *(Cited page 63)*

Rossman, L. A. (2000). *EPANET 2 Users Manual, US Environmental Protection Agency*, volume 45268. USGS, Cincinnati, OH. *(Cited page 37)*

Royer, J. (2014). Hydraulic Fracturing in Transverse Isotropic Media - A Theoretical Framework. In EAGE, editor, *ECMOR XIV*. *(Cited page 43)*

Ruiu, J., Caumon, G., and Viseur, S. (2015). Semiautomatic interpretation of 3D sedimentological structures on geologic images : An object-based approach. *Interpretation*, 3(3) :SX63—-SX74. *(Cited page 74)*

Scheidegger, A. E. (1966). Statistical Description of River Networks. *Water Resources Research*, 2(4) :785–790. *(Cited page 59)*

Scheidegger, A. E. (1967). On the Topology of River Nets. *Water Resources Research*, 3(1) :103–106. *(Cited page 59)*

Schiller, A. and Renard, P. (2016). An optical laser device for mapping 3D geometry of underwater karst structures : First tests in the Ox Bel'Ha system, Yucatan, Mexico. *Boletin Geologico y Minero*, 127(1) :99–110. *(Cited pages 82, 83, and 88)*

Sethian, J. A. (1999). Fast Marching Methods. *SIAM Review*, 41(2) :199–235. *(Cited page 80)*

Sherwood, J. and Younger, P. (1994). Modelling ground water rebound after coalfield closure : an example from County Durham. In *5th international mine water association congress*, pages 769–777, Nottingham, UK. University of Nottingham. *(Cited page 37)*

Siavashi, M., Blunt, M. J., Raisee, M., and Pourafshary, P. (2014). Three-dimensional streamline-based simulation of non-isothermal two-phase flow in heterogeneous porous media. *Computers & Fluids*, 103 :116–131. *(Cited page 41)*

Smart, J. S. (1969). Topological Properties of Channel Networks. *Geological Society of America Bulletin*, 80 :1757–73. *(Cited page 59)*

Sprague, K. B. and de Kemp, E. A. (2005). Interpretive tools for 3-D structural geological modelling part II : Surface design from sparse spatial data. *GeoInformatica*, 9(1) :5–32. *(Cited page 54)*

Steefel, C. I., Appelo, C. A. J., Arora, B., Jacques, D., Kalbacher, T., Kolditz, O., Lagneau, V., Lichtner, P. C., Mayer, K. U., Meeussen, J. C. L., Molins, S., Moulton, D., Shao, H., Simunek, J., Spycher, N., Yabusaki, S. B., and Yeh, G. T. (2015). Reactive transport codes for subsurface environmental simulation. *Computational Geosciences*, 19(3) :445–478. *(Cited page 32)*

Steefel, C. I., DePaolo, D. J., and Lichtner, P. C. (2005). Reactive transport modeling : An essential tool and a new research approach for the Earth sciences. *Earth and Planetary Science Letters*, 240(3) :539–558. *(Cited page 32)*

Strahler, A. N. (1952). Hypsometric (area-altitude) analysis of erosional topography. *Bulletin Geological Society of America*, 63 :1117–1142. *(Cited page 70)*

Strebelle, S. S. (2002). Conditional Simulation of Complex Geological Structures Using Multiple-Point Statistics. *Mathematical Geology*, 34(1) :1–21. *(Cited page 73)*

Streit, L., Federl, P., and Sousa, M. (2005). Modelling Plant Variation Through Growth. *Computer Graphics Forum*, 24(3) :497–506. *(Cited page 71)*

Tan, X., Tahmasebi, P., and Caers, J. (2014). Comparing Training-Image Based Algorithms Using an Analysis of Distance. *Mathematical Geosciences*, 46(2) :149–169. *(Cited page 62)*

Trocmé, V., Albouy, E., Callot, J.-P., Letouzey, J., Rolland, N., Goodarzi, H., and Jahani, S. (2011). 3D structural modelling of the southern Zagros fold-and-thrust belt diapiric province. *Geological Magazine*, 148(5-6) :879–900. *(Cited page 58)*

Vaute, L., le Pape, P., Collon-Drouaillet, P., and Fabriol, R. (2010). Modelling the long-term evolution of groundwater's quality in a flooded iron-ore mine using a reactive transport pipe network model. In Wolkersdorfer, C. and Freund, A., editors, *International Mine Water Association Symposium – Mine Water and Innovative Thinking*, pages 317–320, Sydney, Nova Scotia. CBU Press. *(Cited pages 39, 40, and 41)*

Vigouroux, R., Collon-Drouaillet, P., and Henrion, V. (2010). New parameters for the characterization of karst geometry. In *30th Gocad Meeting*, pages 1–10, Nancy, France. *(Cited pages 60 and 70)*

Villermaux, J. (1993). *Génie de la réaction chimique, conception et fonctionnement des réacteurs*. TEC & DOC Lavoisier, 2e éd. edition. *(Cited page 36)*

Viseur, S. (2001). *Simulation stochastique basée-objet de chenaux*. PhD thesis, Institut National Polytechnique de Lorraine, Vandoeuvre-l{è}s-Nancy, France. *(Cited page 73)*

Vitel, S. (2007). *Méthodes de discrétisation et de changement d'échelle pour les réservoirs fracturés 3D*. PhD thesis, Institut National Polytechnique de Lorraine. *(Cited page 70)*

Vitel, S. and Mallet, J.-L. (2005). A generic network for flow grids. In *25th Gocad Meeting*, pages 1–12. *(Cited page 70)*

Voillemont, J. (2003). *Caractérisation par micro-sismicité induite des propriétés des massifs poreux fracturés. Modélisations par la méthode des lignes de courant d'un*

site géothermique HDR (Soultz-sous-Forêts, France). PhD thesis, Institut National Polytechnique de Lorraine, Nancy, France. *(Cited page 41)*

Voillemont, J. and Royer, J. (2002). Streamline-based 3D reservoir simulator of solute transport using high simulation TVD schemes. In *ECMOR VIII*, volume E62 of *3-6*, pages 1–8, Freiberg, Germany. *(Cited page 41)*

Vuilleumier, C. and Collon-Drouaillet, P. (2012). Statistical Analysis of Karst Geometry. In *32nd Gocad Meeting*, pages 1–14, Nancy, France. *(Cited pages 60 and 70)*

Wen, X.-H. and Gómez-Hernández, J. (1996). Upscaling hydraulic conductivities in heterogeneous media : An overview. *Journal of Hydrology*, 183(1-2) :ix–xxxii. *(Cited page 46)*

Wietzerbin, L. (1994). *Modéisation et paramétrisation d'objets naturels de formes complexes en trois dimensions. Application à la simulation stochastique de la distribution d'hétérogénéités au sein des réservoirs pétroliers*. PhD thesis, Institut National Polytechnique de Lorraine, Vandoeuvre-l{è}s-Nancy, France. *(Cited page 73)*

Williams, P. W. and Williams (1972). Morphometric Analysis of Polygonal Karst in New Guinea. *Geological Society of America Bulletin*. *(Cited page 59)*

Woldenberg, M. J. (1966). Horton's Laws Justified in Terms of Allometric Growth and Steady State in Open Systems. *Bulletin of Geological Society of America*, 77 :431–434. *(Cited page 59)*

Troisième partie

Sélection de Publications

Vous trouverez ici une sélection de 6 publications que j'estime représentatives de la variété de mes travaux de recherche.

1. Collon P., Pichat A., Kergaravat C., Botella A., Caumon G., Ringenbach J.C., Callot J.P. (2016), 3D modelling from outcrop data in a salt tectonic context : Example from the Inceyol mini-basin, Sivas Basin, Turkey. *Interpretation*, 4(3) :pp. SM17–SM31.

2. Rongier G., Collon P., Renard P., Straubhaar J., Sausse J. (2016), Comparing connected structures in ensemble of random fields. *Advances in Water Resources*, 96 :pp. 145–169.

3. Collon P., Steckiewicz-laurent W., Pellerin J., Gautier L., Caumon G., Reichart G., Vaute L. (2015), 3D geomodelling combining implicit surfaces and Voronoi-based remeshing : A case study in the Lorraine Coal Basin (France). *Computers & Geosciences*, 77 :pp. 29–43.

4. Rongier G., Collon-Drouaillet P., Filipponi M. (2014), Simulation of 3D karst conduits with an object-distance based method integrating geological knowledge. *Geomorphology*, 217 :pp. 152–164.

5. Collon-Drouaillet P., Henrion V., Pellerin J. (2012), An algorithm for 3D simulation of branchwork karst networks using Horton parameters and A* Application to a synthetic case. *Geological Society, London, Special Publications*, 370(1) :pp. 295–306.

6. Hamm V., Collon-Drouaillet P., Fabriol R. (2008), Two modelling approaches to water-quality simulation in a flooded iron-ore mine (Saizerais, Lorraine, France) : A semi-distributed chemical reactor model and a physically based distributed reactive transport pipe network model. *Journal of Contaminant Hydrology*, 96(1-4) :pp. 97–112.

3D modeling from outcrop data in a salt tectonic context: Example from the Inceyol minibasin, Sivas Basin, Turkey

Pauline Collon[1], Alexandre Pichat[2], Charlie Kergaravat[2], Arnaud Botella[3], Guillaume Caumon[1], Jean-Claude Ringenbach[4], and Jean-Paul Callot[5]

Abstract

We have developed a 3D modeling strategy of the encased minibasin of Inceyol in Sivas (Turkey). The challenge lies in the combination of sparse outcrop data and the complex interpretive geometry of geologic structures that come from salt tectonics. We have succeeded in modeling the convoluted salt surface using an explicit indirect surface patch construction method followed by a manual mesh improvement. Then, we modeled the minibasin sediments with an implicit approach. The result highlighted the remarkable geometry of the convoluted salt horizon and its associated minibasin by extending in 3D the geologist's interpretive 2D sections. This case study proved that building complex geometries is feasible with the existing tools and a good expertise in the various geomodeling techniques. Our work also underlined the need for new methods to ease the modeling of such tectonic features from sparse data. We have developed a 3D view of the model thanks to WebGL technology, as well as downloadable data to constitute a reference case study.

Introduction

Salt plays a significant role in tectonic, thermal, and fluid migration processes owing to its peculiar physical properties, and especially so in hydrocarbon trap formation (Fossen, 2010). Economic interests associated with halokinesis have motivated a large number of studies to increase knowledge of the geometry of diapiric features at depth (Hudec and Jackson, 2007; Rowan et al., 2014) and the associated tectonic mechanisms (Vendeville et al., 1995; Rowan and Vendeville, 2006; Giles and Rowan, 2012). These studies demonstrate a large variety of halokinetic structures and highlight ambiguities in interpreting conventional seismic images (Fossen, 2010; Jackson et al., 2014). To help their understanding, outcrop analogs are precious and sought after. They are the only way to get a direct 2D observation of many subseismic evaporite-related geometries. Sometimes, particular outcropping conditions even allow access to some 3D geometries. This knowledge strongly helps the interpretation of structures poorly imaged by reflection seismic data (Giles and Lawton, 2002; Jackson and Harrison, 2006; Ringenbach et al., 2013; Callot et al., 2014).

In addition to field work, quantitative 3D modeling can help understanding of the 3D organization of halokinetic features. Their complex geometry is indeed not easily assessed by 2D cross sections only. Moreover, quantitative 3D models further clear the way to numerical simulations as, e.g., structural restoration or constrained potential field inversion (Backé et al., 2010; Gernigon et al., 2011; Lindsay et al., 2012). Building 3D models essentially calls for interpolation and/or extrapolation techniques. This is generally achieved by creating smooth surfaces between data (Caumon et al., 2009). There are, however, many different and complex features in salt tectonics, mostly because salt deformation and migration do not particularly generate minimal surfaces (Giles and Lawton, 2002; Jackson and Harrison, 2006; Fossen, 2010). This probably partly explains why no formal modeling framework has yet been defined for this specific environment, making extrapolation of salt geometry particularly challenging and interpretive in sparse data settings. Trocmé et al. (2011) propose a 3D structural model of the southern Zagros diapiric province (Jahani et al., 2009). Using a large amount of data — ranging from geologic surface data,

[1]Université de Lorraine, CNRS, CREGU ENSG, Vandœuvre-lès-Nancy Cedex, France. E-mail: pauline.collon@univ-lorraine.fr; guillaume.caumon@ensg.univ-lorraine.fr.

[2]Total S.A., CSTJF, Pau, France and Université de Pau et des pays de l'Adour, LFC-R, Pau, France. E-mail: alexandre.pichat@univ-pau.fr; charlie.kergaravat@univ-pau.fr.

[3]Université de Lorraine, CNRS, CREGU ENSG, Vandœuvre-lès-Nancy Cedex, France and INRIA Lorraine-LORIA, Project ALICE, Villers-lès-Nancy, France. E-mail: arnaud.botella@univ-lorraine.fr.

[4]Total S.A., CSTJF, Pau, France. E-mail: jean-claude.ringenbach@total.com.

[5]Université de Pau et des pays de l'Adour, LFC-R, Pau, France. E-mail: jean-paul.callot@univ-pau.fr.

Manuscript received by the Editor 31 October 2015; revised manuscript received 29 February 2016; published online 15 June 2016; corrected version published online 29 June 2016. This paper appears in *Interpretation*, Vol. 4, No. 3 (August 2016); p. SM17–SM31, 14 FIGS.

http://dx.doi.org/10.1190/INT-2015-0178.1.

such as outcrop surveys and dip measurements, to subsurface information coming from seismic interpretations and well wireline data — they use an explicit surface-based structural modeling approach to provide a 3D regional model of the area. The large scale of their study limited the halokinetic features that could be represented in the model. This work also highlighted the limitations of explicit approaches in relation to modeling coherent stratigraphic formations when data are sparse. The implicit stratigraphic model building protocol proposed by Caumon et al. (2013) eases this task while providing some tools to directly exploit 3D geomorphologic features in stratigraphic interpolation. The application of the implicit stratigraphic modeling method to La Popa Basin in Mexico (Caumon et al., 2013), however, also generated a regional model that locally simplified the actual geometry of the diapiric structures and associated stratigraphy.

In this paper, we focus on the Inceyol minibasin located in the Sivas Basin, Turkey. The high-quality but sparse information and the complex geometries observed at outcrop present a real challenge for 3D geologic model building. Our purpose is mainly to demonstrate the feasibility of such a 3D modeling task. After modeling the salt surface using an explicit indirect surface patch construction method, we used an implicit method for the minibasin sedimentary deposits. This required an intermediate step of volumetric mesh generation (Figure 1). Because only outcrop data are available, extrapolation at depth is bound to be quite concept driven. Our result is a coherent 3D model reflecting the interpretive scenario of salt infill. It constitutes a necessary basis for further quantitative studies (e.g., implying potential field data or for uncertainty management). Finally, we discuss challenges and avenues to more objectively address 3D modeling in salt-tectonic context.

The Inceyol minibasin: Geologic setting

The Sivas Basin formed from the Paleocene to the Pliocene in a foreland fold-and-thrust belt basin setting

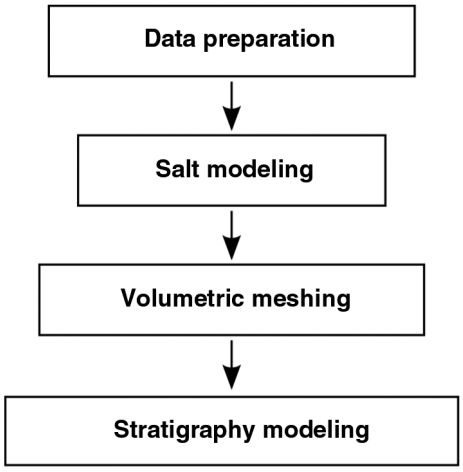

Figure 1. Geomodeling workflow adopted in this case study.

is located in the Central Anatolian Plateau, Turkey (Figure 2a) (Kurtman, 1973; Cater et al., 1991; Guezou et al., 1996; Poisson and Guezou, 1996; Gündogan et al., 2005). At the end of the Eocene, a huge accumulation of marine evaporitic deposits occurred in the Sivas Basin. Their deformation accommodated the development of several kilometric-scale continental to marine minibasins of Oligo-Miocene age. Striking evidences of such halokinetic structures are well-observed in the central part of the Sivas Basin, which exhibits a typical wall and basin structure (WABS) characterized by minibasins surrounded by polygonal network of evaporite walls and welds (Ringenbach et al., 2013; Callot et al., 2014; Ribes et al., 2015, 2016; Kergaravat, 2016). Minibasins exhibit several salt tectonic structures, such as halokinetic sequences, resulting from the interplay between sediment accumulation and salt flow (Ribes et al., 2015, 2016; Kergaravat, 2016).

The Inceyol minibasin is located in the central WABS domain of the Sivas Basin (Figure 2b and 2c). It belongs to a set of several small-scale encapsulated secondary minibasins that developed within a north–south regional compressional setting over deflating diapiric structures (Kergaravat, 2016; Ribes et al., 2016). The Inceyol minibasin is approximately 700 m wide by 800 m long. It is filled by more than 300 m of saline lacustrine to sebkhaic deposits of Oligocene age. The minibasin is structured as an encased system of synclinal folds displaying an elliptical shape in overall outline (Figure 3). It is surrounded on its north, east, and west borders by diapiric evaporites along which strata are strongly rotated into subvertical or locally overturned orientations (Pichat et al., 2015; Kergaravat, 2016). On its south and southeastern parts, landslides made of gypsum screes cover the minibasin sediments (Figure 4a). The diapiric evaporites are characterized by a chaotic amalgamation of massive gypsum to anhydrite blocks and mega blocks, more or less sheared to brecciated and mixed with red to green clays (Figure 4a–4c). Locally, diapiric structures also display brecciated to well-bedded crystalline gypsum (selenitic facies) (Pichat et al., 2015). In diapirs, measurements of bedding (S_0) and schistosity (S_1) are most often parallel to the neighboring salt/sediment contacts. We could only observe two salt-sediment contacts correctly, mainly due to the combination of landslides, meteoritic alteration, brecciation, and vegetation cover. On these places, the diapir-sediment contact displays a centimeter to meter thick shear zone in which clasts and slivers of gypsum/anhydrite are embedded in a shale gouge affected by several fractures filled with satin-spar gypsum (Figure 4b).

In detail, the Inceyol minibasin forms a single syncline in the north that splits to the south into two individualized tight synclines (Figure 3a and 3b). The two synclines are separated by an exposed gypsum wall, interpreted at depth as a weld or a thin wall. At the outcrop, both sides of the salt wall are marked by steep to overturned flanking strata (Figure 3c). The strong dip variations across the synclines highlight the progressive

rotation of the minibasin flanks, which we interpreted as a synsedimentary minibasin subsidence during the salt flow (Kergaravat, 2016). Dip measurements in the sediments are difficult to determine at the immediate proximity of the salt-sediment contact due to the previously described alteration. Thus, we extrapolated the contact angles between salt and sediments from the closest measurements. A discordant contact seems to be dominant along the central diapir that splits the minibasin. At the outer boundaries of the minibasin, dip measurements indicate a more conformable salt-sediment contact.

In more detail, small normal faults cut the strata in the two synclines with an estimated throw less than 2–3 m (Figure 3a). We also observed equivalent local reverse faults in the core of the eastern syncline. Small-scale folding occurs in some sebkhaic deposits and are believed to accommodate flexure. Finally, along the eastern border of the basin, the observation of one strata overturned more than 180° could possibly highlight a halokinetic sequence (Figure 4a). Nevertheless, the outcrop quality prevented clear definition of the geometry of the structure and no other observation allowed us to extrapolate it elsewhere in the minibasin.

Methodology

Field geologists first deemed the Inceyol geologic structures to be too complex to model in 3D. Our objectives were to find one way to succeed and identify future numerical developments that would ease the modeling of halokinetic features. To extend in 3D the 2D interpretations of geologists, we decided to use the simplest topological interpretation for the minibasin compatible with the modeling scale and the field observations. It corresponds to the cross section in Figure 3c. Hence, the minibasin sediments are interpreted as conformable to the salt boundary on the external part and at depth, but with a discordant contact along the central gypsum wall. We also decided to ignore the small-scale features, such as the small faults and folds observed in the sediments, as well as the overturned strata observed along the eastern border of the minibasin in which no clear geometry was stated. Their dimensions are indeed below the current resolution of the model, which is 10 m for the sediments.

We built the model with the SKUA-GOCAD geomodeling software (Paradigm, 2016), StructuralLab (Frank et al., 2007; Caumon et al., 2013), and GoPy (Antoine and Caumon, 2008) research plugins, and the VorteXLIB library (Botella et al., 2014). The global workflow, calling for various techniques, consists of four main steps (Figure 1). After data collection and integration into the geomodeling software, we built the triangulated surface corresponding to the salt top with an explicit indirect surface construction method. Then, we generated a 3D volumetric mesh conformable to this salt surface. Finally, we reconstructed the sedimentary filling of the minibasin with an implicit surface modeling method.

Data and information

Available data to model the Inceyol minibasin are a digital elevation model (DEM), satellite images, and strata orientation measurements. The covered area extends more than 980 m north–south and 1080 m east–west (Figure 5). These data are complemented with interpretive cross sections (Figure 3c). To ensure spatial coherency, all data were georeferenced in the Universal Transverse Mercator (UTM — Zone 37) projection in the World Geodetic System 1984 (WGS84). To allow further use of this case study, dip measurements, DEM, satellite images, and interpreted curves of the stratigraphic levels and salt boundary are all available for download on the RING team website at this

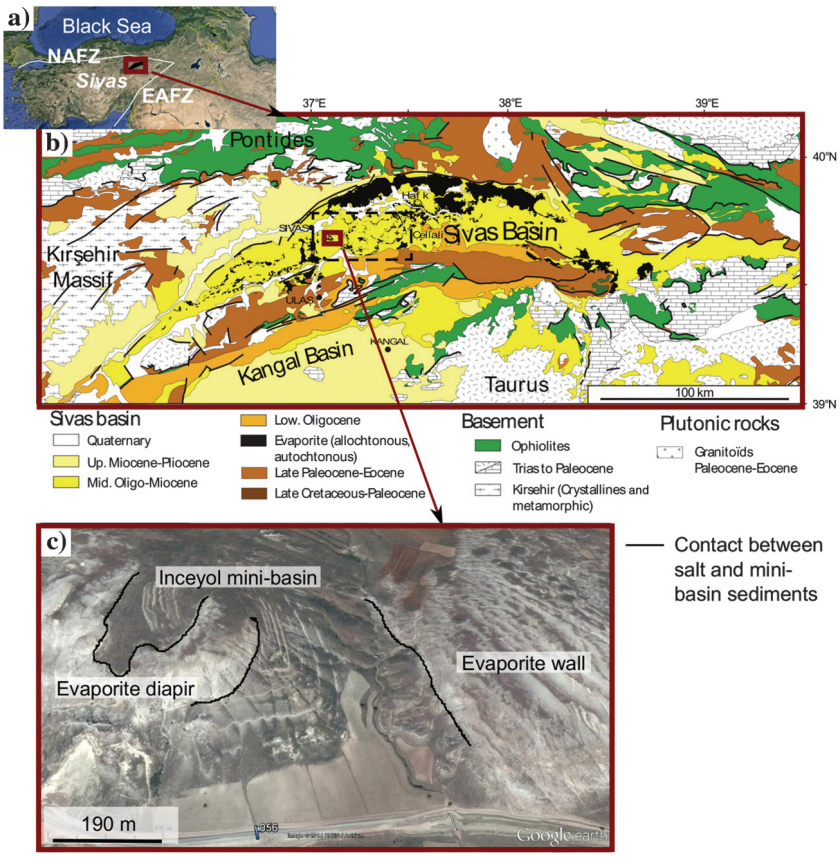

Figure 2. Location of the Sivas Basin and the Inceyol minibasin. (a) Tectonic map of Turkey, with the main continental blocks, major suture zones and Oligo-Miocene Sivas Basin deposits (adapted from Ribes et al., 2015). (b) Location of the Inceyol minibasin in the geologic setting of the Sivas Basin (geologic map adapted from Ringenbach et al., 2013). (c) Satellite image (Google Earth) of the Inceyol minibasin in which the salt/sediment contact can be identified.

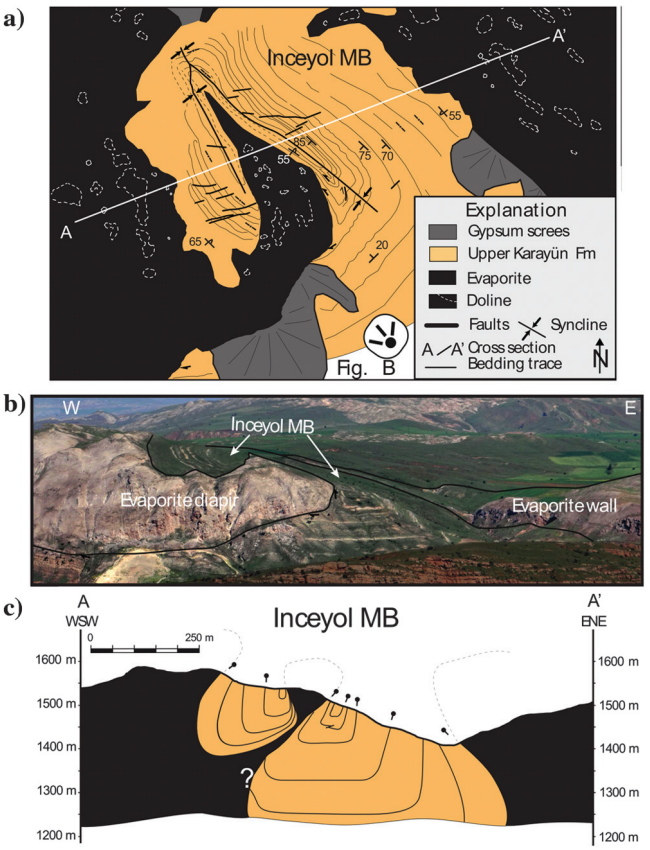

Figure 3. The Inceyol encased minibasin (MB): geologic conceptual model (Kergaravat, 2016). (a) Map view showing the location of the AA′ cross section and photography of panel (b). (b) Photography of the minibasin taken from the south and showing the splitting of the minibasin by an exposed gypsum wall. (c) AA′ cross section: one interpretation of the minibasin at depth (Kergaravat, 2016).

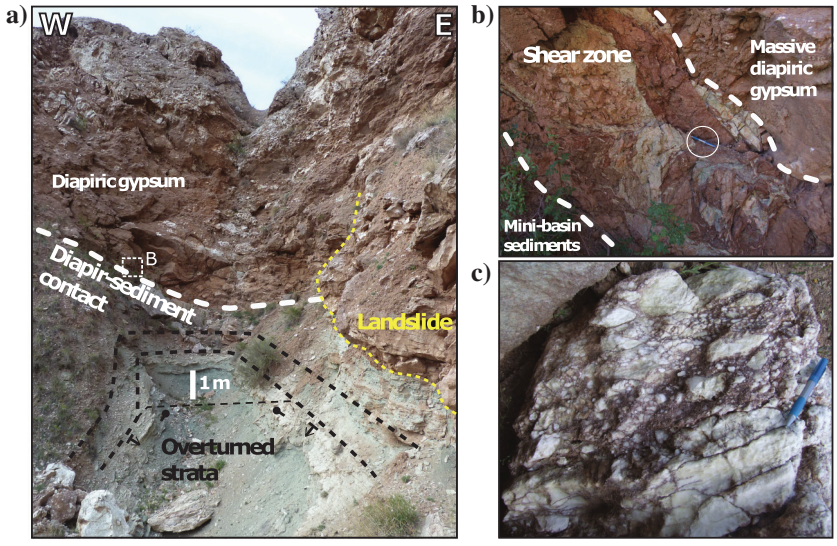

Figure 4. (a) Overturned lacustrine deposits against the eastern bordering diapiric wall. (b) Focus on the diapir-sediment contact marked by a shale gouge in which are embedded reworked diapiric gypsum clasts. (c) Diapiric breccia of massive gypsum/anhydrite.

url: http://ring.georessources.univ-lorraine.fr/ring_dl/public/models/Sivas_onLine_Data.zip.

Digital elevation model

The DEM used in this work has a 5 m horizontal resolution and approximately 50 cm vertical precision. In the zone of interest, elevation ranges between 1348 and 1595 m. We imported the DEM into the SKUA-GOCAD geomodeling software as a point set, and we reconstructed the topographic surface by connecting all these points by a Delaunay triangulation.

Interpreted satellite images

Satellite images were extracted from an ArcGIS Web Map Service (2014), maintained by the Open Geospatial Consortium. They were imported, georeferenced, and vertically projected on the topographic surface. We interpreted these images to provide a set of curves corresponding to: (1) the salt/sediment contact and (2) the stratigraphic traces (Figure 5b).

Orientation measurements

In total, 76 stratigraphic orientation measurements were taken in the field. These data points were positioned using a GPS system with a precision close to 1 m. We integrated them directly as a pointset containing the strike (right convention) and dip properties. The normal vectors to the stratigraphic surfaces were then computed from azimuth and dip and constitute a 3D vector property associated with each point (Figure 5a).

Conceptual model

From outcrop data only, geomodel building is clearly an underconstrained problem, and the extrapolation at depth is bound to be quite concept-driven. Thus, we completed the field data set with interpretive cross sections of the minibasin, illustrating the conceptual geometries at depth. The cross section presented in Figure 3c was imported in the geomodeling software and georeferenced. Interpretation lines were digitized from this section and then used as a guide for the 3D model construction (Figure 6). Three other cross sections were georeferenced and reinterpreted directly in 3D. Overall, we created three east–west and two north–south numerical cross sections. Their geologic interpretations are based on the observation of similar structures imaged by seismic data (Ringenbach et al., 2013) and on our local knowledge of halokinetic structures in the Sivas Basin (Ringenbach et al., 2013; Callot et al., 2014; Pichat et al., 2015; Ribes et al., 2015, 2016). In particu-

lar, we supposed that the minibasin is approximately 300 m deep on the eastern part, and 150 m deep on the western part. To ensure consistency with dip measurements and similarity with the other minibasins observed in the Sivas area, we assumed the eastern and western parts to have a particular coin purse shape.

Modeling choices

Various techniques exist for modeling geologic interfaces, such as horizons and faults. They can be classified in two main strategies (Frank et al., 2007; Caumon et al., 2009; Collon et al., 2015): (1) the classical modeling approaches, also called explicit approaches, which consist of building surfaces — generally triangulated surfaces — that fit available data; (2) and the more recent implicit approaches that consider geologic interfaces as isovalues of a 3D scalar field $f(x, y, z)$. In this work, to compute the scalar field, we used an optimization method that consists of minimizing a weighted sum of various constraints including the data misfit (Frank et al., 2007; Caumon et al., 2013).

Implicit approaches automatically prevent overlapping or leaking layers. But at the same time, the 3D scalar field continuity can only handle conformable stratigraphic blocks: Each discontinuity implies a new 3D scalar field definition that is interpolated independently of the previous one. Thus, the discordant salt-sediment contacts observed along the central diapir require separate consideration of the salt surface from the minibasin sedimentary deposits.

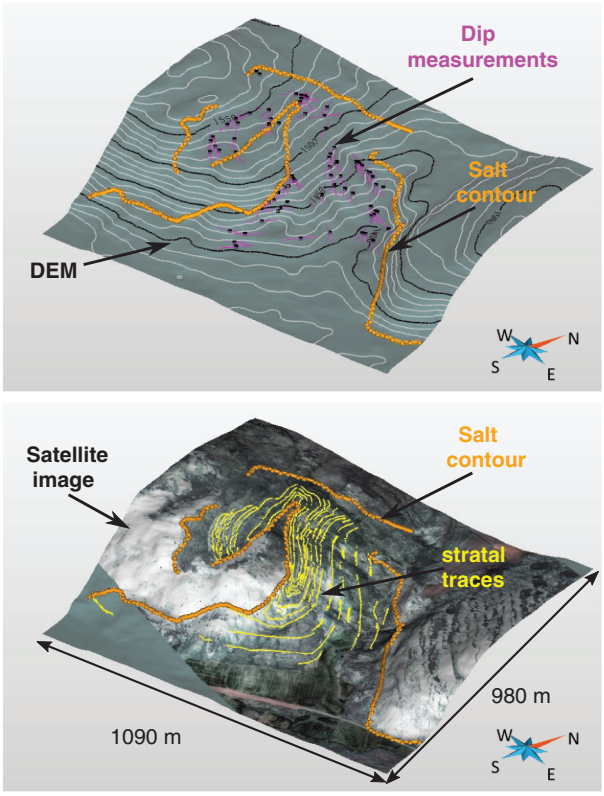

Figure 5. Outcrop data: we realized the modeling using a 5 m resolution DEM (black lines each 50 m), 76 dip measurements of strata, salt contours, and stratigraphic lines interpreted from a satellite image.

Modeling the salt surface

With only five numerical cross sections and a particularly convoluted shape, the construction of a salt surface that fits the geologic interpretation is quite challenging. We tested two approaches for this purpose.

Implicit approach

Each digitized curve was used as a constraining data to interpolate a 3D scalar field $f(x, y, z)$ on the whole volume of interest in an implicit approach. Here, we used a discrete interpolation scheme, meaning that the scalar field is defined by a piece-wise linear interpolation of the values stored at the vertices of a tetrahedral mesh. Once this 3D scalar field is computed, any stratigraphic surface can be explicitly constructed by extracting the corresponding isovalue surface. We defined the salt surface to be reconstructed as the implicit surface corresponding to $f(x, y, z) = 0$.

First, we built a surface with digitized curves as the only constraint using the SKUA-GOCAD structure and stratigraphy workflow. The resulting surface honors the line data, but has a complex topology with diapir-shaped minibasin geometry that is inconsistent with our interpretation (Figure 7).

Second, polarity information was added using the implicit method implemented in the StructuralLab SKUA-GOCAD research plugin, which includes the possibility to impose inequality constraints as defined by Frank et al. (2007). Two vertical surfaces were manually built in the center of both minibasin synclines (Figure 8a). We attached a "greater than" constraint to each of these surfaces. Two inequality control points, chosen arbitrarily on each side of the surface to build, were also used: one with the constraint $f(x, y, z) \geq 5$

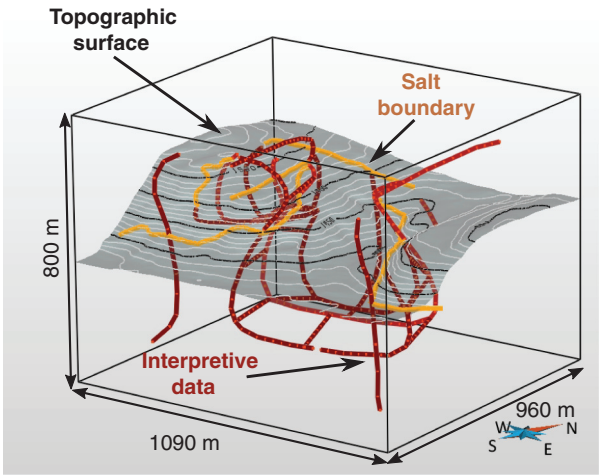

Figure 6. Data points used to model the salt surface: The red lines are interpretive data coming from the geologic conceptual model.

and the other one with the constraint $f(x,y,z) \leq -5$. The scalar field was computed on a tetrahedral mesh made of 545,642 tetrahedra corresponding to a 30 m average tetrahedron edge length. Note that we performed a similar computation with a finer mesh (2,162,146 tetrahedra for an average tetrahedron edge length of 18 m) without noticeable differences in the results but a significant increase of memory cost and computation time (passing from approximately 1 min to 3.5 h for the scalar field computation). With such additional constraints, the resulting salt surface is clearly improved with a global shape closer to the geologic interpretation (Figure 8b). In detail, however, the result still shows some unsatisfactory parts (Figure 8c–8e).

First, when the salt boundary is not clearly visible at outcrop — and thus imposed by a digitized curve — the salt surface is smoothed and looses its purse shape (Figure 8c). This is completely consistent with the interpolation principle that minimizes the variations of the scalar field gradient (Frank et al., 2007): If no data "forces" the surface to twist, the surface tends to be planar, whereas interpretation would suggest locally cylindrical structures. This is also observed at the edge of the domain of interest: In the southern part, the surface tends to plunge at depth instead of keeping a flat bottom; no flattening is obtained either on the aerial (eroded) parts. Moreover, a protuberance is produced at outcrop in the southeast because the outcropping salt boundary changes its orientation (Figure 8b). To

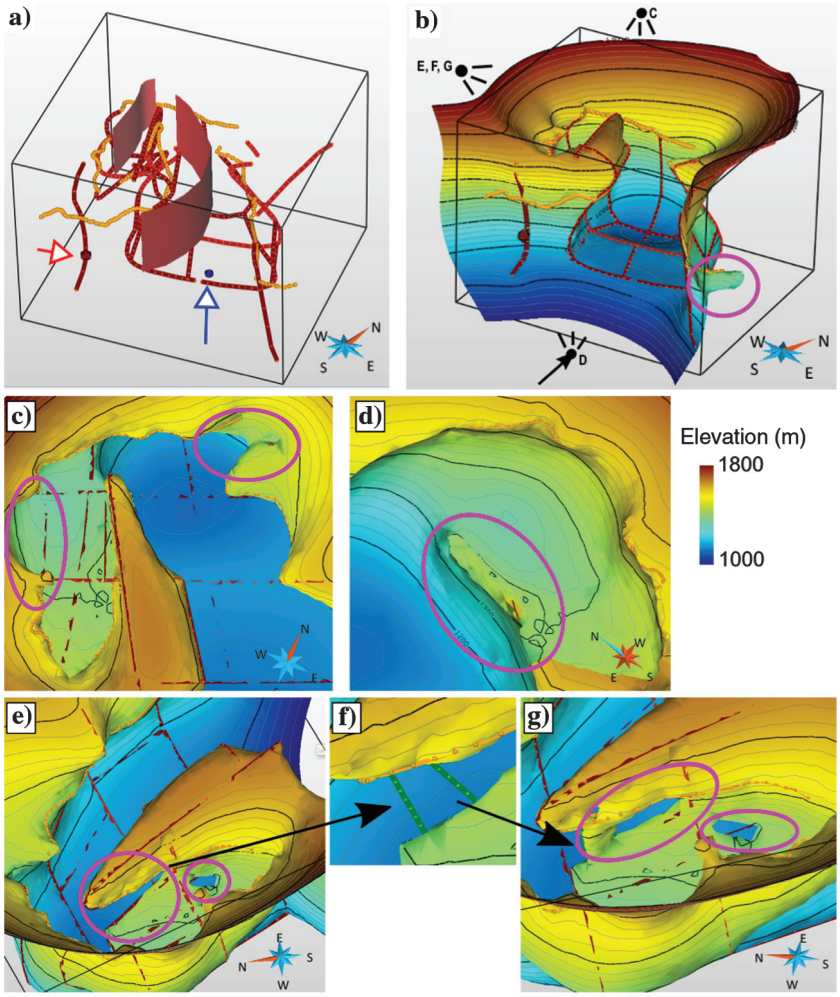

Figure 8. Implicit modeling of the salt surface with inequality constraints. (a) Additional information used to impose the surface polarity: two surfaces are defined inside the minibasin as well as one point (in red). They are attached to a greater than constraint (Frank et al., 2007). One point is used at depth (in blue) to define the other side of the surface using a less than constraint. (b) Result obtained using a volumetric tessellation of 30 m resolution. (c) Top view and magnification on the model (b). (d) Bottom view on the central diapir showing the local fusion of the two sides and the artifacts due to mesh resolution. (e) Side view of the central diapir highlighting the unwanted "hole" in the salt. (f) Additional curves used to force the interpolation to close this hole and corresponding result (g).

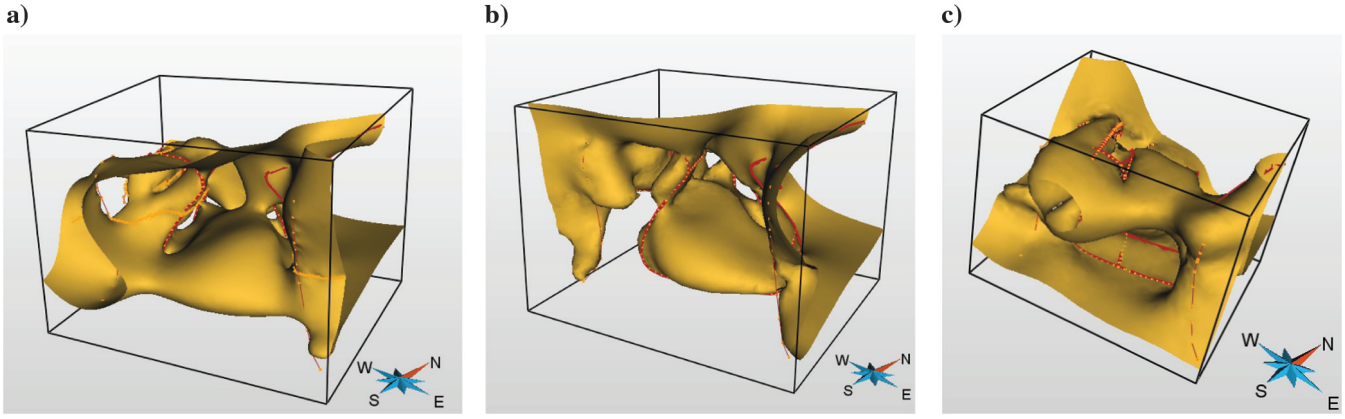

Figure 7. Implicit modeling of the salt surface with digitized curve constraints alone. Panels (a-c) show models built with volumetric mesh resolutions of (a) 10, (b) 20, and (c) 30 m.

avoid this, additional interpretive curves should be added on the topography, at depth, and above the topography, iteratively, until the computed result would be satisfactory.

Second, the central diapir is not well-modeled and a hole appears in the salt wall (Figure 8e). Locally, the two sides of this central diapir also locally vanish, which is visible when looking from bottom (Figure 8d). Indeed, the outcrop data indicate a progressive closure of the salt wall and, at this location, the distance between the two sides is lower than 30 m. Two reasons explain this result: The volumetric mesh resolution that is equivalent to this distance and, again, the polarity of the surface that is locally underconstrained. To solve this last issue, we made a last try by adding two curves representing the salt neck (Figure 8f). Unfortunately, this only managed to partially close the hole (Figure 8g). However, the thinness of this zone could ultimately be managed with an adaptive mesh comprising smaller tetrahedra or incorporating an explicit salt weld in this zone. Thereupon, iterative addition of constraining data would again be necessary to obtain the desired representation.

Explicit approach

To more directly obtain a salt model whose topology matches our interpretation, we finally chose to use an explicit modeling method. Its principle is to deform an initial surface to minimize the distance between the surface and the data points, by the mean of various interpolation methods (Haecker, 1992; Mallet, 1992; Caumon et al., 2009; Kaven et al., 2009; Collon et al., 2015). Thus, an interactive surface editing allows more flexibility to meet interpretive concepts: It permits a direct control on the surface topology and a local application of the constraints.

The indirect surface construction calls for projecting points onto the interpolated surface along specific directions, called shooting directions (Figure 9c). The high sinuosity of the salt horizon and the pinched geometry of the central salt wall make this task challenging when a single initial surface is used, especially as its geometry is not yet definitive. This is why we decided to use a divide-and-conquer strategy that consists of creating surface patches, fitting them to the data, and merging them into the final surface (Figure 9). In detail, we partitioned the input curves into simple domains, i.e., subsets for which projecting onto the best-fit plane is single valued (Figure 9a–9c). Selecting slightly overlapping domains was important to ensure continuity between surface patches. Surface patches were fitted to data using discrete smooth interpolation implemented in Gocad, which minimizes a weighted sum of the surface roughness and data misfit in a least-squares sense (Mallet, 1992, 2002) (Figure 9d). Manual control and updating of the shooting directions was necessary during the interpolation steps. Then, we manually cut the overlapping parts (Figures 9e and 10a). New surface parts

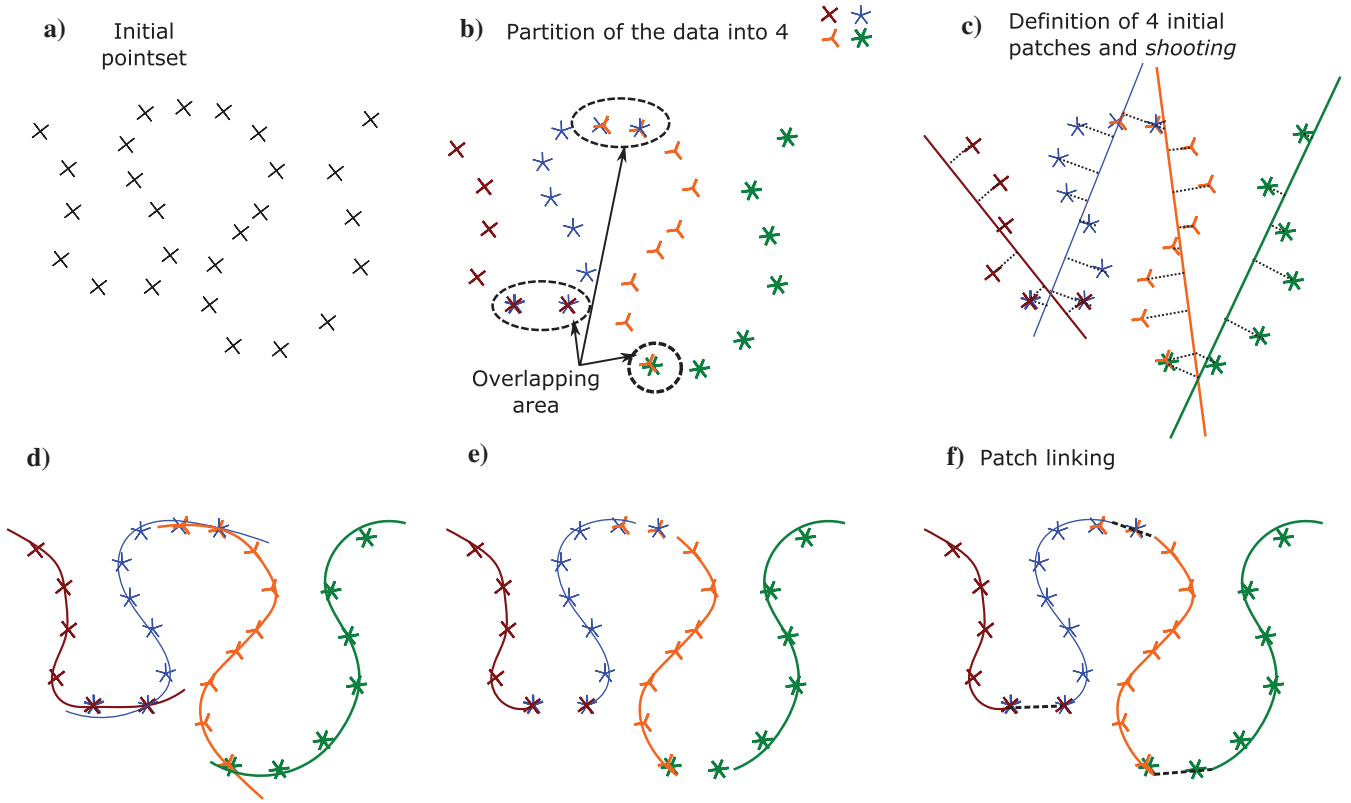

Figure 9. Principles of the divide and conquer strategy used to model the salt surface. To ease visualization, the steps are presented on a synthetic 2D case.

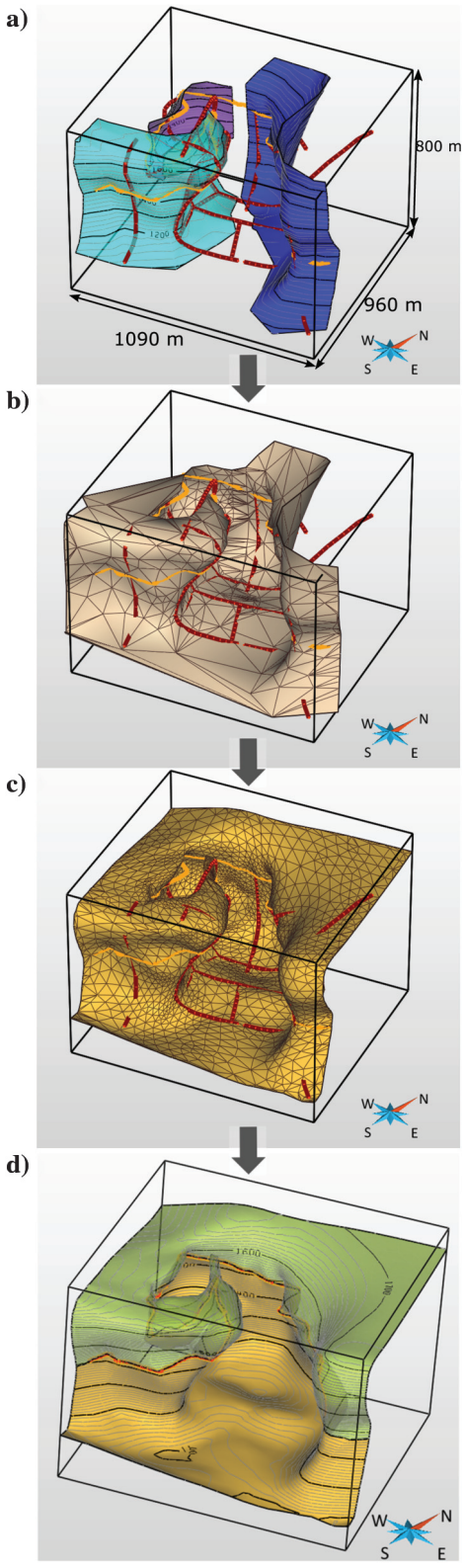

Figure 10. Modeling the salt surface: (a) surface patches are cut and (b) small surfaces are built by direct triangulation between adjacent borders to link the patches. Then all connected parts are merged to produce a single surface. (c) The mesh is manually cleaned, and local refinement is performed to obtain a final smooth surface that fits the data. (d) The final salt surface: The green part is located above the topography, whereas the yellow part is below.

were built by direct triangulation between opposite borders of the various surface patches to connect them coherently (Figure 9f). The resulting connected components were merged to generate a single surface (Figure 10b). Finally, some additional interpolation steps were performed to improve the data fit, and we manually refined and cleaned the surface mesh until obtaining the final salt surface (Figure 10c and 10d). Such an approach requires mastery of the modeling techniques, but the resulting salt surface is directly the expression of interpretive concepts.

Modeling the minibasin stratigraphy

The synclinal structure of the minibasin, with steepened to vertical or overturned strata, allows the major part of the stratigraphic layers to outcrop. The traces of the strata on the topography are, however, discontinuous due to vegetation and surface processes (erosion and scree). The orientation measurements are also a crucial piece of information that has to be integrated into the modeling process. In such a case, implicit modeling methods have several advantages to coherently build stratigraphic series at once as compared with explicit methods (Caumon et al., 2013; Collon et al., 2015). Those methods consider geologic interfaces as isovalues of a 3D scalar field $f(x, y, z)$ and the outcropping stratigraphic lines correspond to level-set curves. These curves and the orientation data are used as constraining data to interpolate a 3D scalar field on the whole volume of interest. Once this 3D scalar field has been computed, any stratigraphic surface can be explicitly constructed by extracting the corresponding isovalue surface. Consequently, despite the discontinuity of the stratigraphic lines on the topography, overlapping or leaking layers will be prevented inside the minibasin. Here, we used a discrete interpolation scheme, meaning that the scalar field is defined by a piecewise linear interpolation of the values stored at the vertices of a volumetric mesh. Thus, the scalar field computation required to first build a volumetric mesh.

Volumetric mesh generation

The exposed gypsum wall that separates the eastern and western parts of the minibasin is particularly pinched, with an observed width lower than 15 m in the thinnest part and a very abrupt closure (Figure 11). This wall splits one single syncline in the north into two individualized synclines in the south. Stratigraphic orientations are very different on both sides of the wall, demonstrating that it acts geometrically as a discontinuity. As a result, sedimentary layers must be interpolated independently on each side of this central diapir. In implicit modeling, integrating such a discontinuity can be handled by creating a tetrahedral mesh that is conformable to the discontinuity (Frank et al., 2007). Conformable means that tetrahedron facets that are located on one discontinuity surface are the same triangles as the one meshing the discontinuity surface. The

thin gypsum wall is, however, a complex area difficult to manage by meshing generators without making the number of mesh elements impractically large. Indeed, to compute an accurate enough interpolation of the scalar field, the tetrahedron edge length of this area should be less than 5 m, implying high memory and computational costs (this also motivated the choice of the explicit modeling for the salt surface). To simplify this area, we decided to create an equivalent model by replacing the pinched part by a discontinuity surface that can be assimilated to a weld. The salt surface was consistently truncated and closed to ensure a sealed contact of both surfaces as required by meshing generators (Figure 11).

The volumetric mesh was then generated using the two-step method proposed by Botella et al. (2014) and implemented in the research library VorteXLib: (1) generation of the final vertices of the mesh from the boundary surfaces and (2) generation of a tetrahedral mesh constrained by the salt surface and the computed vertices using TetGen (Si, 2015). The final mesh is conformable to the salt surface, and it is made of approximately 4.5 million tetrahedra with an average edge length of 9 m (Figure 12). For minimizing the memory cost while keeping a small tetrahedron edge length, the size of the initial zone of interest was reduced, particularly by removing the parts above the topography (Figure 12).

Scalar field computation

In the implicit modeling method we used, all constraints can be weighted according to their relative reliability. In other words, when two constraints act on the same point, the higher their weight W is, the more they influence the interpolated scalar field value. As for the salt surface modeling, our concern was to use all available outcrop data (stratigraphic lines and orientation measurements) and to limit as much as possible the addition of more interpretations. Thus, higher weights were attached to field data than to interpretive constraints. Five constraints with different weights W were sufficient and necessary to build a model of the minibasin filling that fits our geologic concepts (Figure 13):

1) The first three constraints impose directly the scalar field values:
   - Each set of lines corresponding to the same interpreted strata defines a value of the scalar field ($W = 100$).
   - These lines are completed by a few interpretive lines manually digitized to impose the shape above the topography ($W = 50$). Values are attached to them consistently with the previous set of lines.
   - A surface located at 5 m from the external salt surface boundary accounts for the conformity of the sediment deposits right above the evaporitic substratum of the minibasin ($W = 1$).
2) The two last ones act indirectly by imposing the scalar field gradient:
   - Orientation measurements are used with a high weight $W = 100$.
   - They are completed by a constant gradient constraint $W = 20$, necessary to smooth the scalar field away from the data points.

The scalar field values assigned to the stratigraphic line constraints have to be consistent with the constant

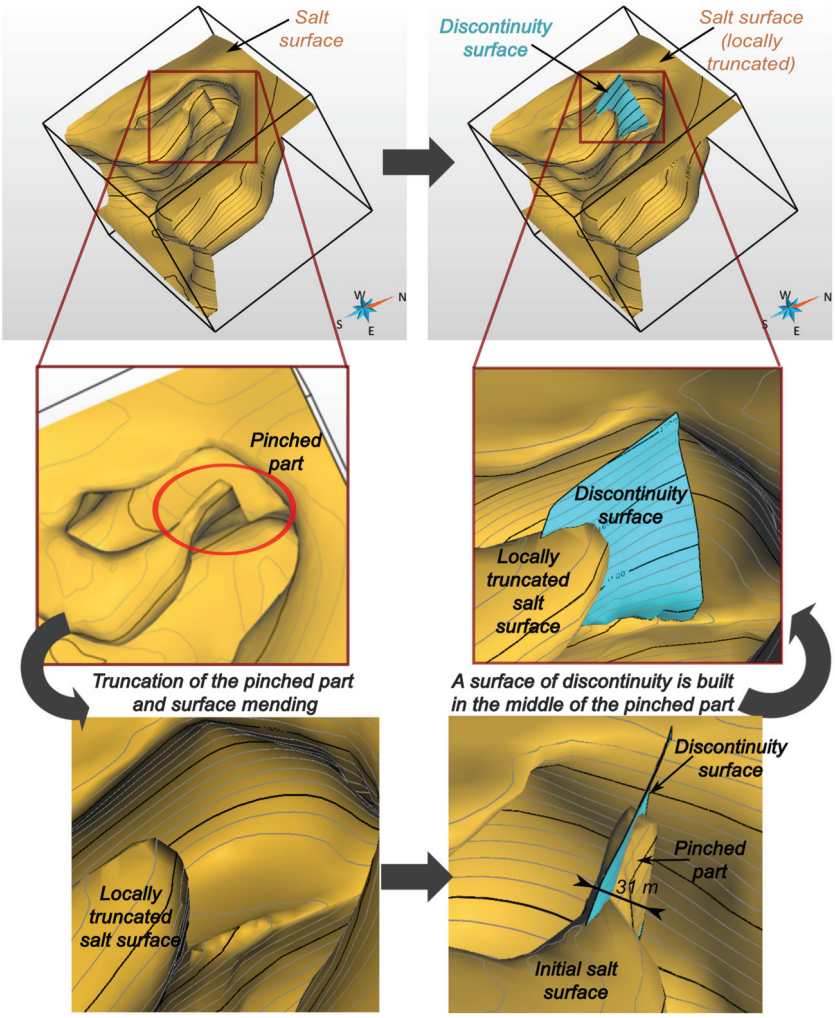

Figure 11. Equivalent model used for the volumetric mesh generation: we truncated the pinched part of the salt surface and replaced it by an equivalent surface of discontinuity. Surfaces are closed and mutually cut to ensure the sealed model required by mesh generators.

norm imposed by the constant gradient constraint, i.e., they must evolve proportionally to their interdistances. For that purpose, we used values proportional to the average apparent thickness between surfaces, ranging from 1 to 47 (Figure 13a and 13b). A value of 52 was also attached to the surface located at 5 m from the external salt surface boundary. On the external border, this surface was vertically extended upward to avoid a collapsing effect above the topographic surface, which the extrapolation of the upward tightening of the minibasin would otherwise have induced (i.e., edge effect). It was also cut along the central salt wall to authorize discordant contacts between sediment layers and this halokinetic feature as observed on the field. The chosen weights give priority to field data while preserving global coherency far from them. Note that there is no relation between weights that express our confidence in the data and the scalar field values that express the relative distance of the data from the zero isosurface. The resulting scalar field is shown in Figure 13e. For visualization purposes, each surface corresponding to an isovalue imposed by an interpreted stratigraphic level has been extracted to produce the final model presented in Figure 14. Thanks to WebGL technology, the model can also be viewed in 3D at this url: http://ring.georessources.univ-lorraine.fr/model_3d_html/Sivas.html.

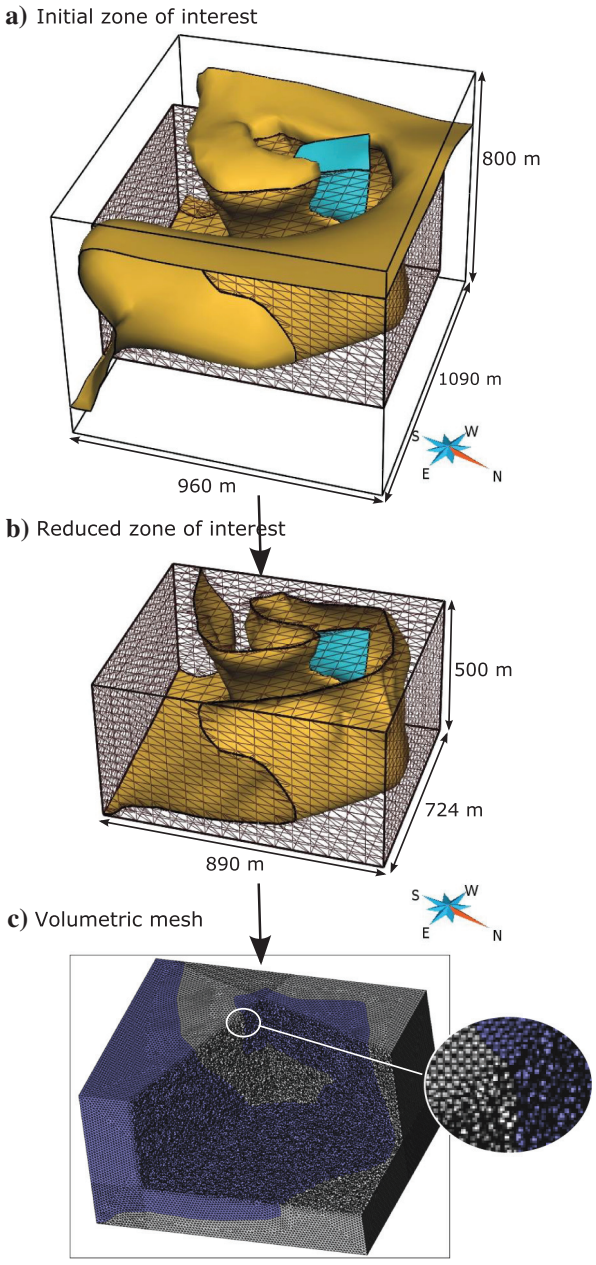

Figure 12. Volumetric mesh generation: (a) we restrained the initial zone of interest to (b) limit the memory cost. We generated a volumetric mesh conformable to salt surface with the VorteXLib research library (Botella et al., 2014). (c) Here, the mesh is partially sliced to propose an excavated view of the meshed minibasin (in blue) and the diapiric body (in gray).

Discussion

The resulting geomodel of the Inceyol minibasin fits all outcrop data while integrating previous geologic interpretations. It reflects the ground observations at the chosen scale, but could not be validated as this would call for subsurface data, which are currently unavailable. Thus, the model complements quantitatively an existing interpretation of the data: It allows a 3D visualization of the complex and nonintuitive geometry of such a salt-related structure. In itself, it is already an interesting achievement because such geometries are not easily reproduced with standard 3D geomodeling workflows and call for adapted strategies.

The various technical choices made to realize this model can still be discussed. The first one is the choice of the order of the modeling steps. In the field, the global "coin-purse" shape of the minibasin is mostly deduced from the dip measurements of the outcropping strata, profile views in outcrop, analogy with neighboring minibasins, and our conceptual analysis. In this concept-driven approach, the minibasin infill has constrained the interpretive salt surface morphology. Based on that interpretation, the modeling workflow used the salt-sediment relation inversely: We decided to start modeling the salt surface to provide a geospatial constraint for the deepest layers of sediments. We chose that because modeling one surface is technically easier than modeling set of conformable surfaces, especially in areas of high curvature that are numerous in this case study. Furthermore, implicit methods require the separation of the various sedimentary blocks to consistently interpolate the scalar field in independent areas. It is thus more suited to directly generate a mesh conformable to the minibasin boundaries (here, the salt surface) with implicit methods. With explicit methods, indeed, we would create an approximate volumetric mesh with arbitrary vertical surfaces of discontinuity that might turn out to be misplaced at the end of the process.

A second point relates to the size of the represented structures. The central part of the study area is charac-

terized by very tight features, particularly at the core of the syncline. With a syncline width smaller than 10 m, the average tetrahedron edge length of 9 m is not small enough to adequately describe the central horizon (corresponding to the value one of the scalar field) in the most strongly deformed areas of tight folds. Indeed, it supposes that the same value is observed twice on a single tetrahedron edge, which is not possible as values are carried by vertices and linearly interpolated along the edges. This limitation could be overcome with an adaptive mesh generation. It would require us to use an additional surface, for example, the isosurface corresponding to the value 10, to impose a refinement inside the central part (Botella et al., 2014) followed by reinterpolation.

Third, to constrain the sediment layers to drape the salt horizon at the external part of the minibasin, a controlling surface parallel to the salt surface has been created. This surface has been cut approximately 100 m above the minibasin bottom to allow a discordant contact along the central salt wall edges, similarly to what was observed in the field. This depth choice is arbitrary, but it allows us to fit the field observations and to reproduce the geometries of the conceptual cross sections. Somewhat equivalent solutions could have been obtained with a slightly upper or lower cut. In addition, the sediment/salt contact along the central salt wall is the result of the smooth interpolation between the syncline data constraints on the younger strata and the conformable trend on the oldest layers. Thus, a tight fold of the strata is obtained against the central salt wall edges and the strata are conformable one to another. Salt tectonics is, however, often characterized by more specific features such as halokinetic sequences and their associated hook and wedge halokinetic sequence end members (Giles and Rowan, 2012). Moreover, in the absence of clear data, the use of a constant gradient term is questionable because it will tend to minimize the stratigraphic layer thickness variations. Being able to reproduce the tabular and/or tapered composite halokinetic sequences (Giles and Rowan, 2012; Hearon et al., 2014) and their associated end members would be an interesting perspective of this work that would require further numerical developments. Indeed, in an implicit workflow, unconformity surfaces can be defined, but they are interpolated as independent conformable sequences (Calcagno et al., 2006; Durand-Riard et al., 2013), which can be limiting in sparse data settings.

The fourth point concerns the strategy chosen to build the salt surface. Even if the retained method was a patch-by-patch explicit approach, we think it could also be feasible with an implicit method. An adaptive tetrahedral mesh refined in the central area would be necessary to get the desired thin shape of the central gypsum wall; and it would require to add iteratively interpretive inputs until the scalar field computation would end in a satisfactory result. Our modeling choice was mainly guided by our own expertise and the possibility to directly and efficiently control the topology of the surface with the explicit approach. Thus, for deterministic modeling purposes, it is difficult at this point to make a general recommendation about one method versus another because it depends on the level of user expertise, data density, and surface complexity. When dealing with uncertainty, implicit modeling should clearly be preferred because it makes model perturbation much easier (Wellmann et al., 2010; Lindsay et al., 2012; Cherpeau and Caumon, 2015). In that case, it is always possible to build a base implicit representation from available data and some manually generated explicit surface. Moreover, the salt surface construction method based on patches was quite fast for an experienced modeler but more dedicated tools could be imag-

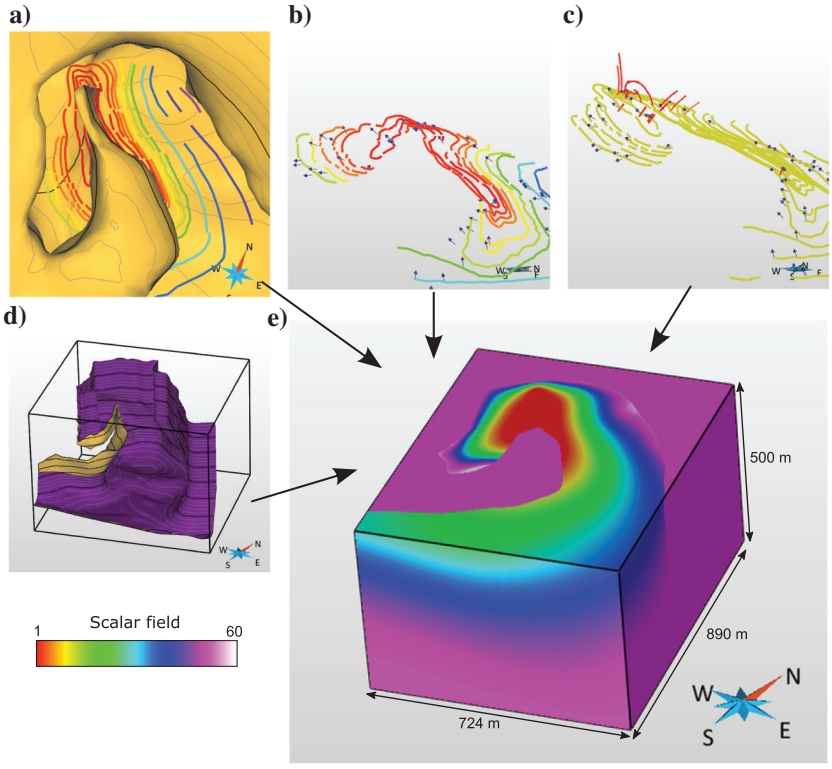

Figure 13. Various constraints are used to compute the 3D scalar field (e): (a) a scalar field value is affected to the stratigraphic lines observed on the topography; (b) dip measurements impose a local scalar field gradient direction; (c) additional interpretive lines imposes values above the topography; (d)a surface located at 5 m from the salt boundary imposes the scalar field value on the external flanks of the minibasin to ensure the deposit conformity to the salt layer on this area.

ined to ease salt feature reproduction. Nonuniform rational B-splines (NURBS) have proven their ability to model complex tectonic structures (Sprague and de Kemp, 2005) and/or sedimentological structures, such as channels, clinoform, and lobes (Ruiu et al., 2014, 2015). A similar approach could be developed for salt features.

Overall, this work produced only one possible 3D model of the complex architecture of the Inceyol minibasin. High uncertainties are associated to its deep geometry and the validation of such a representation can still be debated. Exploring these uncertainties by incorporating small perturbations on the salt surface could be done in a similar way as proposed by Tertois and Mallet (2007) for fault networks. This method could also be used for local model update. But in the current state of the art, more important changes on the salt geometry would require manually rebuilding the complete model because automated model updating methods still have a limited capacity to address large-scale changes in input parameters. Perturbing the stratigraphy inside the minibasin for a given salt geometry would probably be a more accessible goal in this framework based on implicit approach. Layer geometry could indeed be perturbed by adding realizations of a random field $r(x, y, z)$ to the 3D scalar field $f(x, y, z)$ (Caumon, 2010; Mallet, 2014; Cherpeau and Caumon, 2015). In all cases, additional data would be necessary to later reduce the uncertainties.

Conclusions

The Inceyol minibasin constitutes a real challenge for geomodeling: It has a specific geometry of an encased synclinal split southward into two tight synclines by the rise of a central salt wall. Classical geomodeling tools or integrated strategies are not adapted to reproduce the convoluted salt surface shape in a context of very sparse data. In such concept-driven approach, we succeeded by using a careful patch-by-patch explicit surface modeling, completed by a manual mesh improvement step. The combined use of an implicit modeling approach, with specific weighted interpolation constraints, allowed us to generate a 3D model of the minibasin sedimentary deposits consistent with the outcrop data and the interpretive cross sections. With the inherent specificities of a case study, this work proves that building such complex models is feasible with the existing tools and a good expertise in the various geomodeling techniques.

The resulting geomodel could constitute a good basis for supporting the quantitative interpretation of potential field data. Potential field data have indeed proven to help gaining insights into the geometric definition of equivalent geologic structures; but they need to be associated with 3D geomodels to be fully exploitable. This work also raises a lot of interesting perspectives for dedicated numerical tool development, ranging from specific salt-related shape construction to halokinetic sequences reproduction, while better managing the associated uncertainties. In that aim, input data are proposed for download to constitute a reference case study.

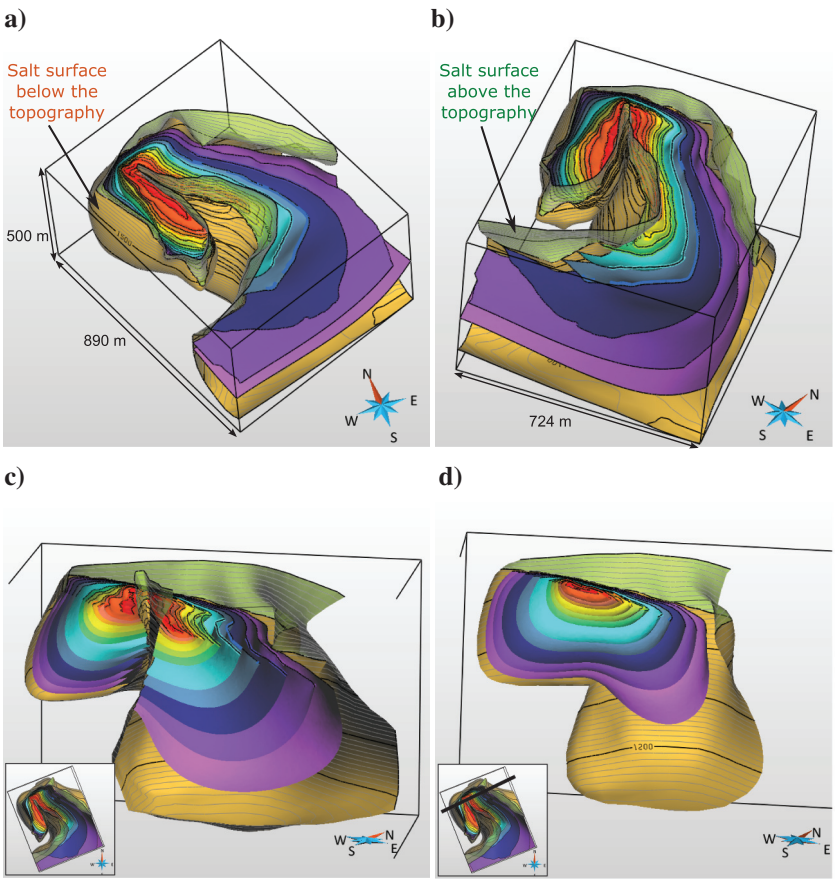

Figure 14. Resulting 3D model of the Inceyol minibasin. The stratigraphic surfaces correspond to the extraction of the following isovalues of the scalar field: 1, 3, 4.5, 6, 10, 13.5, 18, 30, 36.5, 43, 47, and 50. (a and b) Two different views; (c and d) two different slices in the 3D model. The model can also be viewed in 3D at this url: http://ring.georessources.univ-lorraine.fr/model_3d_html/Sivas.html.

Acknowledgments

Many persons contributed more or less directly to this case study. We warmly thank all of them: the M.S. students of the Nancy School of Geology (University of Lorraine), who measured the stratigraphic orientations during a field trip: They have made this an enjoyable adventure: O. Favreau; G. Fuss; G. Godefroy; M. Lerat; A. Mazuyer; M. Parquer; J. Charreau, associate professor in Nancy, who initiated the field trip by putting us in touch with our teams in

Nancy and Pau and accompanied us in the field; K. Kavak and H. Temiz, both professors at Cumhuriyet University (Sivas, Turkey), who so warmly welcomed us in Sivas; G. Laurent, research fellow in Nancy, who gave us good ideas and suggestions for implicit modeling of the salt surface; Total S.A. and ASGA, who funded the field trip; A. Graham Leslie and E. de Kemp, both reviewers, who gave constructive remarks. This work was performed in the frame of the RING project at the Université de Lorraine. We would like to thank the industrial and academic sponsors of the RING-Gocad Research Consortium managed by ASGA for their support. We also thank Paradigm for providing the SKUA-GOCAD software and API.

References

Antoine, C., and G. Caumon, 2008, Rapid algorithm prototyping in Gocad using Python plugin: Proceedings of the 28th Gocad Meeting, 4.

ArcGIS Web Map Service, 2014, http://services.arcgisonline.com/arcgis/rest/services, accessed 9 June 2016.

Backé, G., G. Baines, D. Giles, W. Preiss, and A. Alesci, 2010, Basin geometry and salt diapirs in the Flinders Ranges, South Australia: Insights gained from geologically-constrained modeling of potential field data: Marine and Petroleum Geology, **27**, 650–665, doi: 10.1016/j.marpetgeo.2009.09.001.

Botella, A., B. Lévy, and G. Caumon, 2014, A new workflow for constrained tetrahedral mesh generation: Application to structural models and hex-dominant meshing: Proceedings of the 34th Gocad Meeting, ASGA.

Calcagno, P., G. Courrioux, A. Guillen, D. Fitzgerald, and P. McInerney, 2006, How 3D implicit geometric modeling helps to understand geology: The 3DGeoModeller Methodology: Proceedings of the IAMG 2006.

Callot, J.-P., C. Ribes, C. Kergaravat, C. Bonnel, H. Temiz, A. Poisson, B. Vrielynck, J.-F. Salel, and J.-C. Ringenbach, 2014, Salt tectonics in the Sivas Basin (Turkey): Crossing salt walls and minibasins: Bulletin de la Société géologique de France, **185**, 33–42, doi: 10.2113/gssgfbull.185.1.33.

Cater, J. M. L., S. S. Hanna, A. C. Ries, and P. Turner, 1991, Tertiary evolution of the Sivas Basin, central Turkey: Tectonophysics, **195**, 29–46, doi: 10.1016/0040-1951(91)90142-F.

Caumon, G., 2010, Towards stochastic time-varying geological modeling: Mathematical Geosciences, **42**, 555–569, doi: 10.1007/s11004-010-9280-y.

Caumon, G., P. Collon-Drouaillet, C. Le Carlier de Veslud, S. Viseur, and J. Sausse, 2009, Surface-based 3D modeling of geological structures: Mathematical Geosciences, **41**, 927–945, doi: 10.1007/s11004-009-9244-2.

Caumon, G., G. Gray, C. Antoine, and M.-O. Titeux, 2013, Three-dimensional implicit stratigraphic model building from remote sensing data on tetrahedral meshes: Theory and application to a regional model of La Popa Basin, NE Mexico: IEEE Transactions on Geoscience and Remote Sensing, **51**, 1613–1621, doi: 10.1109/TGRS.2012.2207727.

Cherpeau, N., and G. Caumon, 2015, Stochastic structural modeling in sparse data situations: Petroleum Geoscience, **21**, 233–247, doi: 10.1144/petgeo2013-030.

Collon, P., W. Steckiewicz-Laurent, J. Pellerin, L. Gautier, G. Caumon, G. Reichart, and L. Vaute, 2015, 3D geomodeling combining implicit surfaces and Voronoi-based remeshing: A case study in the Lorraine Coal Basin (France): Computers and Geosciences, **77**, 29–43, doi: 10.1016/j.cageo.2015.01.009.

Durand-Riard, P., C. Guzofski, G. Caumon, and M.-O. Titeux, 2013, Handling natural complexity in three-dimensional geomechanical restoration, with application to the recent evolution of the outer fold and thrust belt, deep-water Niger Delta: AAPG Bulletin, **97**, 87–102, doi: 10.1306/06121211136.

Fossen, H., 2010, Structural geology: Cambridge University Press.

Frank, T., A.-L. Tertois, and J.-L. Mallet, 2007, 3D-reconstruction of complex geological interfaces from irregularly distributed and noisy point data: Computers and Geosciences, **33**, 932–943, doi: 10.1016/j.cageo.2006.11.014.

Gernigon, L., M. Brönner, C. Fichler, L. Løvas, L. Marello, and O. Olesen, 2011, Magnetic expression of salt diapir-related structures in the Nordkapp Basin, western Barents Sea: Geology, **39**, 135–138, doi: 10.1130/G31431.1.

Giles, K. A., and T. F. Lawton, 2002, Halokinetic sequence stratigraphy adjacent to the El Papalote diapir, northeastern Mexico: AAPG Bulletin, **86**, 823–840.

Giles, K. A., and M. G. Rowan, 2012, Concepts in halokinetic-sequence deformation and stratigraphy: Geological Society, London, Special Publications, **363**, 7–31.

Guezou, J.-C., H. Temiz, A. Poisson, and H. Gürsoy, 1996, Tectonics of the Sivas basin: The Neogene record of the Anatolian accretion along the inner Tauric suture: International Geology Review, **38**, 901–925, doi: 10.1080/00206819709465371.

Gündogan, I., M. Önal, and T. Depçi, 2005, Sedimentology, petrography and diagenesis of Eocene–Oligocene evaporites: The Tuzhisar Formation, SW Sivas Basin, Turkey: Journal of Asian Earth Sciences, **25**, 791–803, doi: 10.1016/j.jseaes.2004.08.002.

Haecker, M. A., 1992, Convergent gridding: A new approach to surface reconstruction: Geobyte, **7**, 48–53.

Hearon, T. E., M. G. Rowan, K. A. Giles, and W. H. Hart, 2014, Halokinetic deformation adjacent to the deep-water Auger diapir, Garden Banks 470, northern Gulf of Mexico: Testing the applicability of an outcrop-based model using subsurface data: Interpretation, **2**, no. 4, SM57–SM76, doi: 10.1190/INT-2014-0053.1.

Hudec, M. R., and M. P. A. Jackson, 2007, Terra infirma: Understanding salt tectonics: Earth-Science Reviews, **82**, 1–28, doi: 10.1016/j.earscirev.2007.01.001.

Jackson, C. A.-L., C. R. Rodriguez, A. Rotevatn, and R. E. Bell, 2014, Geological and geophysical expression of a primary salt weld: An example from the Santos Basin, Brazil: Interpretation, **2**, no. 4, SM77–SM89, doi: 10.1190/INT-2014-0066.1.

Jackson, M. P. A., and J. C. Harrison, 2006, An allochthonous salt canopy on Axel Heiberg Island, Sverdrup Basin, Arctic Canada: Geology, **34**, 1045–1048, doi: 10.1130/G22798A.1.

Jahani, S., J.-P. Callot, J. Letouzey, and D. de Lamotte, 2009, The eastern termination of the Zagros Fold-and-Thrust Belt, Iran: Structures, evolution, and relationships between salt plugs, folding, and faulting: Tectonics, **28**, 1–22, doi: 10.1029/2008TC002418.

Kaven, J., R. Mazzeo, and D. Pollard, 2009, Constraining surface interpolations using elastic plate bending solutions with applications to geologic folding: Mathematical Geosciences, **41**, 1–14, doi: 10.1007/s11004-008-9201-5.

Kergaravat, C., 2016, Dynamique de formation et de déformation de mini-bassins en contexte compressif: Approche terrain, implications structurales multi-échelles et réservoirs (exemple du bassin de Sivas, Turquie): Ph.D. thesis, Université de Pau et des Pays de l'Adour.

Kurtman, F., 1973, Geologic and tectonic structure of the Sivas-Hafik-Zara and Imranli Region: Bulletin Mineral Research and Exploration (Ankara, Turkey), **80**, 1–32.

Lindsay, M. D., L. Aillères, M. W. Jessell, E. A. de Kemp, and P. G. Betts, 2012, Locating and quantifying geological uncertainty in three-dimensional models: Analysis of the Gippsland Basin, southeastern Australia: Tectonophysics, **546–547**, 10–27, doi: 10.1016/j.tecto.2012.04.007.

Mallet, J.-L., 1992, Discrete smooth interpolation: Computer-Aided Design, **24**, 178–191, doi: 10.1016/0010-4485(92)90054-E.

Mallet, J.-L., 2002, Geomodeling: Oxford University Press, Applied Geostatistics.

Mallet, J.-L., 2014, Elements of mathematical sedimentary geology: The GeoChron model: EAGE.

Paradigm, 2016, Skua-Gocad Software, http://www.pdgm.com/products/skua-gocad/, accessed 9 June 2016.

Pichat, A., G. Hoareau, J.-M. Rouchy, C. Ribes, C. Kergaravat, J.-P. Callot, and J.-C. Ringenbach, 2015, Deposition and evolution of the Sivas basin evaporites (Turkey): Geophysical Research Abstract, EGU General Assembly, 9091.

Poisson, A., and J. C. Guezou, 1996, Tectonic setting and evolution of the Sivas Basin, Central Anatolia, Turkey: International Geology Review, **38**, 838–853, doi: 10.1080/00206819709465366.

Ribes, C., C. Kergaravat, C. Bonnel, P. Crumeyrolle, J.-P. Callot, A. Poisson, H. Temiz, and J.-C. Ringenbach, 2015, Fluvial sedimentation in a salt-controlled mini-basin: Stratal patterns and facies assemblages, Sivas Basin, Turkey: Sedimentology, **62**, 1513–1545, doi: 10.1111/sed.12195.

Ribes, C., C. Kergaravat, P. Crumeyrolle, M. Lopez, C. Bonnel, A. Poisson, K. S. Kavak, J.-P. Callot, and J.-C. Ringenbach, 2016, Factors controlling stratal pattern and facies distribution of fluvio-lacustrine sedimentation in the Sivas mini-basins, Oligocene (Turkey): Basin Research, 1–26, doi: 10.1111/bre.12171.

Ringenbach, J.-C., J.-F. Salel, C. Kergaravat, C. Ribes, C. Bonnel, and J.-P. Callot, 2013, Salt tectonics in the Sivas Basin, Turkey: Outstanding seismic analogues from outcrops: First Break, **31**, 93–101.

Rowan, M. G., T. E. Hearon, F. J. Peel, S. Stewart, O. Ferrer, J. C. Fiduk, S. Holdaway, W. U. Mohriak, V. Mount, D. G. Quirk, and T. Seeley, 2014, Introduction to special section: Salt tectonics and interpretation: Interpretation, **2**, no. 4, SMi, doi: 10.1190/INT2014-0925-SPSEINTRO.1.

Rowan, M. G., and B. C. Vendeville, 2006, Foldbelts with early salt withdrawal and diapirism: Physical model and examples from the northern Gulf of Mexico and the Flinders Ranges, Australia: Marine and Petroleum Geology, **23**, 871–891, doi: 10.1016/j.marpetgeo.2006.08.003.

Ruiu, J., G. Caumon, and S. Viseur, 2015, Semiautomatic interpretation of 3D sedimentological structures on geologic images: An object-based approach: Interpretation, **3**, no. 3, SX63–SX74, doi: 10.1190/INT-2015-0004.1.

Ruiu, J., G. Caumon, S. Viseur, and C. Antoine, 2014, Modeling channel forms using a boundary representation based on non-uniform rational B-splines, *in* E. Pardo-Igúzquiza, C. Guardiola-Albert, J. Heredia, L. Moreno-Merino, J. J. Durán, and J. A. Vargas-Guzmán, eds., Mathematics of planet earth: Springer Berlin Heidelberg, 581–584.

Si, H., 2015, TetGen, a delaunay-based quality tetrahedral mesh generator: ACM Transactions on Mathematical Software, **41**, 1–36, doi: 10.1145/2732672.

Sprague, K. B., and E. A. de Kemp, 2005, Interpretive tools for 3-D structural geological modeling. Part II: Surface design from sparse spatial data: GeoInformatica, **9**, 5–32, doi: 10.1007/s10707-004-5620-8.

Tertois, A. L., and J. L. Mallet, 2007, Editing faults within tetrahedral volume models in real time: Geological Society, London, Special Publications, **292**, 89–101, doi: 10.1144/SP292.5.

Trocmé, V., E. Albouy, J.-P. Callot, J. Letouzey, N. Rolland, H. Goodarzi, and S. Jahani, 2011, 3D structural modeling of the southern Zagros fold-and-thrust belt diapiric province: Geological Magazine, **148**, 879–900, doi: 10.1017/S0016756811000446.

Vendeville, B., H. Ge, and M. P. A. Jackson, 1995, Scale models of salt tectonics during basement-involved extension: Petroleum Geoscience, **1**, 179–183, doi: 10.1144/petgeo.1.2.179.

Wellmann, J. F., F. G. Horowitz, E. Schill, and K. Regenauer-Lieb, 2010, Towards incorporating uncertainty of

structural data in 3D geological inversion: Tectonophysics, **490**, 141–151, doi: 10.1016/j.tecto.2010.04.022.

Pauline Collon received a Ph.D. (2003) in hydrology and civil engineering from INPL, Nancy, France. She was a teaching assistant in hydrology at ENGEES Engineering School in Strasbourg (2004–2005) and became an associate professor in the Université de Reims-Champagne-Ardennes (2005–2007). In 2007, she moved to the Nancy School of Geology, Université de Lorraine, as an associate professor of geomodeling and hydrogeology. She is part of the research team in integrative numerical geology led by Guillaume Caumon.

Alexandre Pichat is a Ph.D. candidate at the University of Pau, France. His thesis focuses on the evaporitic deposits related to the halocinetic context of the Sivas Basin (Turkey) and on their impact on the diagenesis of silicoclastic reservoirs located in minibasins.

Charlie Kergaravat received an M.S. in geology from the University of Montpellier and a Ph.D. in geology from the University of Pau. Currently, he is working toward a postdoctoral degree in structural geology with Total SA and the University of Pau. His scientific research interests include the influence of salt tectonics on deformations at various scales using field studies, physical models, and seismic data.

Arnaud Botella received an engineering degree in earth sciences from the Nancy School of Geology, an M.S., and a Ph.D. in numerical geology from the Université de Lorraine. He is working toward a postdoctoral degree in geomechanics and modeling with Total SA and Association Scientifique pour la Géologie et ses Applications. His main scientific interest is in developing new meshing capabilities to better model rock heterogeneities at various scales.

Guillaume Caumon received a Ph.D. (2003) in geosciences from INPL, Nancy. He was a postdoctoral scholar in petroleum engineering at Stanford University (2003–2004) and visiting professor in geophysics at Colorado School of Mines (2015). He is the professor of geomodeling at the Nancy School of Geology at the Université de Lorraine, in which he directs the research team in integrative numerical geology and the Gocad Research Consortium.

Jean-Claude Ringenbach received a Ph.D. in geodynamics from Nice University. Since 1992, he occupied specialist and operational positions in ELF and TOTAL in France, Norway, and Libya. Currently, he is a senior advisor in structural geology located in the Total technical center in Pau.

Jean-Paul Callot received a Ph.D. (2002) in geodynamics from Ecole Normale Supérieure. He worked for nine years at IFP-EN, specializing in fold and thrust belts, salt tectonics, analog modeling, and fluid rock interactions. Since 2011, he has been the professor in charge of the structural geology chair at the University of Pau and Pays de l'Adour.

Advances in Water Resources 96 (2016) 145–169

Contents lists available at ScienceDirect

Advances in Water Resources

journal homepage: www.elsevier.com/locate/advwatres

Comparing connected structures in ensemble of random fields

Guillaume Rongier[a,b,*], Pauline Collon[a], Philippe Renard[b], Julien Straubhaar[b], Judith Sausse[a]

[a] GeoRessources (UMR 7359, Université de Lorraine / CNRS / CREGU), Vandoeuvre-lès-Nancy, F-54518, France
[b] Centre d'Hydrogéologie et de Géothermie, Université de Neuchâtel, 11 rue Emile-Argand, 2000 Neuchâtel, Switzerland

ARTICLE INFO

Article history:
Received 17 November 2015
Revised 27 May 2016
Accepted 16 July 2016
Available online 18 July 2016

Keywords:
Stochastic simulations
Comparison
Static connectivity
Indicators
Dissimilarity

ABSTRACT

Very different connectivity patterns may arise from using different simulation methods or sets of parameters, and therefore different flow properties. This paper proposes a systematic method to compare ensemble of categorical simulations from a static connectivity point of view. The differences of static connectivity cannot always be distinguished using two point statistics. In addition, multiple-point histograms only provide a statistical comparison of patterns regardless of the connectivity. Thus, we propose to characterize the static connectivity from a set of 12 indicators based on the connected components of the realizations. Some indicators describe the spatial repartition of the connected components, others their global shape or their topology through the component skeletons. We also gather all the indicators into dissimilarity values to easily compare hundreds of realizations. Heat maps and multidimensional scaling then facilitate the dissimilarity analysis. The application to a synthetic case highlights the impact of the grid size on the connectivity and the indicators. Such impact disappears when comparing samples of the realizations with the same sizes. The method is then able to rank realizations from a referring model based on their static connectivity. This application also gives rise to more practical advices. The multidimensional scaling appears as a powerful visualization tool, but it also induces dissimilarity misrepresentations: it should always be interpreted cautiously with a look at the point position confidence. The heat map displays the real dissimilarities and is more appropriate for a detailed analysis. The comparison with a multiple-point histogram method shows the benefit of the connected components: the large-scale connectivity seems better characterized by our indicators, especially the skeleton indicators.

1. Introduction

Connectivity is a key aspect of a geological study for its influence on fluid circulations. From a reservoir engineering perspective, it relates to geological structures with high and low permeabilities. But it also relates to the spatial distribution of these structures and the resulting inter-connections, which define the static connectivity. An incorrect connection can bias the results of the flow simulations (Gómez-Hernández and Wen, 1998; Journel and Alabert, 1990). Reproducing the geological bodies together with their relations is so of prime importance (e.g., Deutsch and Hewett, 1996; King and Mark, 1999).

Stochastic simulations aim at generating possible representations of the geological bodies with respect to the available data. Several methods exist, with a usual separation in two main categories:

- Pixel-based methods simulate one cell at a time, based on a prior model describing the structures of interest. In sequential indicator simulation (SIS) (Deutsch and Journel, 1992), the prior is a variogram built upon the two-point statistics of the data. Hard data conditioning with such method is easy. But the simulated structures do not look like geological bodies. This is especially true for bodies with curvilinear geometries such as channels, whose continuity is badly preserved. The plurigaussian simulation (PGS) (Galli et al., 1994) limits this difficulty by accounting for the facies relationships. Multiple-point simulations (MPS) go a step further by borrowing multiple-point statistics not from the data but from an external representation of the expected geology, the training image (TI) (Guardiano and Srivastava, 1993).
- Object-based methods rely on the definition of geometric forms and their associated parameters. Each form represents a particular geological body (e.g., Viseur, 2001; Deutsch and Tran, 2002). The objects are then randomly placed in the domain of interest with parameters drawn in statistical laws. More recent approaches introduce some genetic aspects to improve the

* Corresponding author.
E-mail address: guillaume.rongier@univ-lorraine.fr (G. Rongier).

http://dx.doi.org/10.1016/j.advwatres.2016.07.008
0309-1708/

object organization (e.g., Lopez, 2003; Pyrcz et al., 2009). They provide more geologically consistent results. For instance channel continuity and relationships are better preserved than with pixel-based methods. But this is at the cost of the ease of parametrization. And object-based approaches have difficulty to condition the objects to data.

All these methods have advantages and drawbacks. This will influence the choice of a method and its parameter values when dealing with a case study.

But few work aims at systematically analyzing the quality of a set of realizations regarding their static connectivity. The quality control often consists in comparing the histogram and variogram of several realizations with those of the data, or of the training image if any (e.g., Strebelle, 2002; Mariethoz et al., 2010; Tahmasebi et al., 2012). If more than the first two-order statistics are necessary to simulate geological bodies (e.g., Guardiano and Srivastava, 1993; Journel, 2004), the same conclusion must apply when comparing realizations. Some authors propose to also use the higher-order statistics for quality analysis. Boisvert et al. (2010) and Tan et al. (2014) propose to analyze the multiple-point histogram. De Iaco and Maggio (2011) and De Iaco (2013) also explore the multiple-point statistics with high-order cumulants.

The purpose of most simulation methods is to reproduce statistics from a prior. Analyzing statistics highlights the method success in this reproduction, not if the realizations are geologically consistent. To do that, the statistical analysis is often completed by a visual evaluation of the global structures. The geological structures are compared to what is expected from the known geology, with a focus on the further use of the realizations. This use is often related to fluid circulations, and requires an assessment of the static connectivity, which is not directly imposed by the simulation methods contrary to the statistics. But a visual analysis remains subjective and limited to a few realizations, often in two-dimensions (e.g., Yin et al., 2009; Tahmasebi et al., 2012).

Yet, some studies focus on analyzing the connectivity of the realization bodies. For instance Meerschman et al. (2012) use the connectivity function with the histogram and variogram to analyze the simulation parameter impact for the Direct Sampling MPS method (Mariethoz et al., 2010). Deutsch (1998) uses directly the connected components determined from lithofacies, porosity and permeability models. He computes indicators such as the number of connected components or their sizes to rank the realizations. De Iaco and Maggio (2011) and De Iaco (2013) also use some measures related to the connected components, such as their number or their mean surface and volume. Comunian et al. (2012) rely on some of the previous indicators to analyze the quality of three-dimensional structures simulated from two-dimensional training-images. They also consider the equivalent hydraulic conductivity tensor as an indicator. However, this requires to have an idea of the hydraulic conductivities for the simulated facies.

Connected components enable to characterize the geometry and topology of the geological bodies, which is the purpose of the visual comparison of realizations. They also enable to study the static connectivity of the geological bodies, while being easy to compute. Contrary to a visual analysis of the realization, indicators from connected components are unbiased and can compare many realizations. Contrary to statistical or hydraulic property indicators, they focus on the sedimentary bodies by characterizing their connectivity and are more easy to apprehend. However, current methods based on the connected components are limited to few simple indicators, often analyzed independently.

This leads to the question of the result visualization to analyze more effectively the indicators. Scheidt and Caers (2009) and Tan et al. (2014) both rely on the computation of dissimilarity values between the realizations. Those dissimilarities are computed based on the quality indicators measured on each realization. They are then visualized based on a MultiDimensional Scaling (MDS) (e.g., Torgerson, 1952; Shepard, 1962a; 1962b). MDS represents the realizations as points, with the distance between the points as close as possible to the dissimilarities. The global analysis of the realization dissimilarities is so easier.

The present work aims at analyzing and discussing a set of indicators to quantify the quality of stochastic simulations from the viewpoint of static connectivity. This method performs on categorical three-dimensional images representing the facies constituting the geological bodies of interest. It can be applied on realizations from one or several stochastic simulation methods and/or parameter values. Conceptual images representing ideally the structures to simulate can also be considered. The chosen set of indicators relies on quantitative measurements on connected components and their skeletons (Section 2). The indicators are used in dissimilarity computations to analyze the quality more directly (Section 3). Several realizations obtained with different simulation methods (Section 4.1) are then used to test the method and compare it to the multiple-point histograms (Section 4), and discuss the results (Section 5).

2. Indicators to measure simulation quality

The quality analysis fits in a stochastic process implying the simulation of many realizations in a grid. It further investigates the differences of static connectivity between these realizations.

2.1. About grids and grid cells

Many methods to simulate geological structures rely on a discretized representation of the domain of interest: a grid. The grid is a volumetric mesh composed of simple elements, hereinafter called cells.

Many types of grid exist, with different cell types (e.g., tetrahedron or hexahedron). Most of the stochastic simulation methods rely on hexahedral grids, either regular or irregular. Irregular hexahedral grids help to be as conform as possible to the geological structures such as horizons and faults. The sedimentary bodies are then simulated within the parametric space of the grid (e.g., Shtuka et al., 1996). The parametric space mimics a deposition space to get rid of the deformation and faulting occurring after deposition and materialized in the grid geometry.

Consequently, the indicators are computed on hexahedral grids, both regular and irregular. Similarly to the simulation, the indicator computation is done in the parametric space of the grid. Thus, the indicators based on volumes or surfaces are rather computed using number of cells and number of faces. This avoids biases related to different grid geometries, which give different indicator values even if the objects are the same when transferred in the same grid.

Within a grid, the cells are connected one to another by their faces, their edges and/or their corners (Renard and Allard, 2013). In the case of the hexahedral grids used for this work, one cell has three possible neighborhoods (Fig. 1):

1. One neighborhood composed of six face-connected cells.
2. One neighborhood composed of eighteen face- and edge-connected cells.
3. One neighborhood composed of twenty-six face-, edge- and corner-connected cells.

This definition of the connectivity between a cell and its neighborhood can be extended to form connected components.

2.2. Basic element: the connected component

The connected components result from the widening of the neighborhoods. They rely on the following definition of the con-

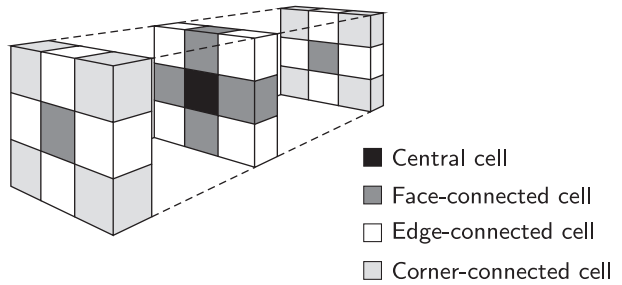

Fig. 1. Possible neighborhoods for a given central cell in a regular grid (modified from Deutsch (1998)).

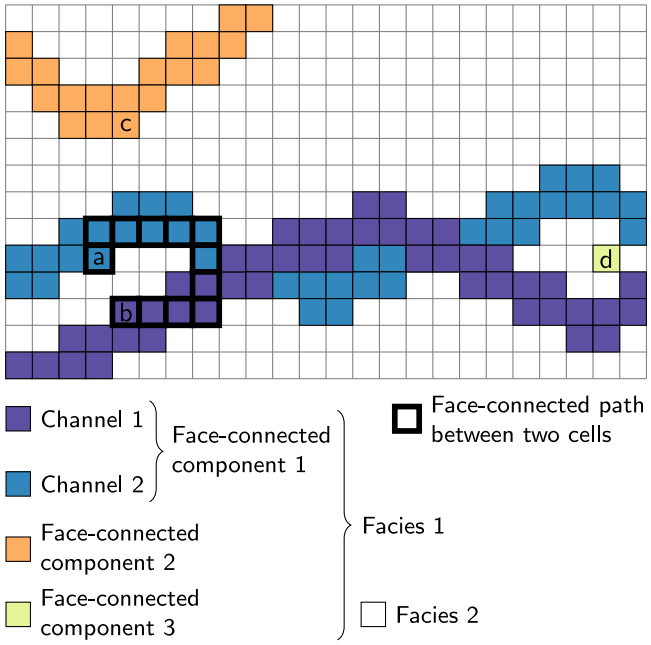

Fig. 2. Connected components of a given facies in a two-dimensional structured grid. The cells *a* and *b* are connected and belong to the same connected body. There is no possible connected path between those cells and *c*, which belongs to another connected body. The cell *d* constitutes a third connected body in the case of a face-connected neighborhood. In the case of an edge- or corner-connected neighborhood, *d* belongs to the connected body 1.

nectivity between two cells: two cells belonging to the same facies are connected if a path of neighboring cells remaining within the same facies exists (Fig. 2). Applying this definition to all the cells of a facies gives the connected components of this facies.

This leads to a distinction between the geological objects, such as a channel or a crevasse splay, and the connected components. Indeed, the geological objects often tend to cross each others, giving one connected body where there is in fact several geological objects (Fig. 2). The range of possible shapes is larger for the connected components than for the individual object. This aspect complicates the comparison between images. But determining the connected components is far easier than trying to retrieve the geological objects. This is also close to the functioning of pixel-based methods, which do not try to reproduce geological objects but groups of cells, and therefore connected components.

2.3. Basic element: the skeleton

A curve-skeleton – simply called here skeleton – is a thin one-dimensional representation of a three-dimensional shape. It is composed of nodes linked together by one or more segments

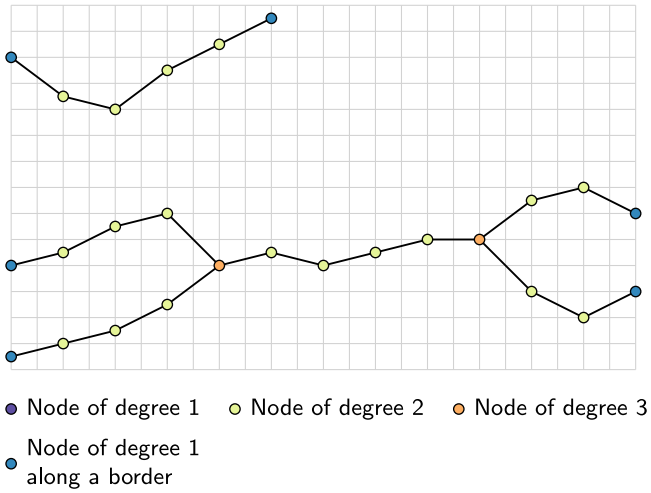

Fig. 3. Example of skeletons for the connected components of the Fig. 2. Here the nodes connected to only one segment – the nodes of degree 1 – are all along a grid border. Two nodes of degree three highlight the local disconnections between the channels at the bottom. The connected component at the top has no node of degree higher than two, which shows the complete connectivity of all its cells, even locally.

(Fig. 3). The degree of a node is the number of segments connected to that node. Skeletons are often used to study some geometrical and topological features of a shape. Here the skeletons are those of the connected components. They enable to further characterize the global shape of the connected components, while giving more details about their topology than indicators directly computed on the components.

Several methods exist to compute skeletons (e.g., Serra, 1983; Jain, 1989; Brandt and Algazi, 1992). The method considered for this work is based on slicing the grid along a given axis. The grid is subdivided into parallel slices of a given thickness. On each slice the connected components are computed and one node is assigned to each component. The nodes are then linked by computing the connected components over two adjacent slices. If two components from two slices form one connected component when the slices are combined, their nodes are linked. If they form several components, their nodes are not linked.

2.4. Indicators

The indicators studied in this paper focus on analyzing the connectivity of the geological bodies within a three-dimensional image. This static connectivity analysis is possible thanks to the connected components. All the indicators are quite simple and each one gives only partial information about the connectivity and its structure. But their combination provides a more detailed characterization.

Appendix A defines in detail all the indicators. Table 1 summarizes the indicator definition, by focusing on their relationship with the connected components.

We distinguish three categories of indicators:

- **Global indicators:** The global indicators characterize a facies and not necessarily an individual connected component. Among them, the facies proportion is a classical indicator to compare realizations. Some others, such as the facies connection probability (Renard and Allard, 2013), the connected component density or the traversing component proportion give an idea of the global connectivity.
- **Shape indicators:** Global measures such as facies proportions are not sufficient to characterize precisely the impact of the

Table 1
The set of indicators with their definitions. The indicator definitions is given by a numerator and a denominator because the majority of the indicators comes from a ratio. Some ratios are computed on a single connected component, and their values are combined to obtain one indicator value per facies. We use the term "component" instead of "connected component" for the sake of simplicity.

Category	Indicator	Symbol	Numerator	Denominator	Value for a facies
Global indicators	Facies proportion	p	Number of component cells	Number of cells of the grid	Sum of all the component values
	Facies adjacency proportions	p^a	Number of component cells adjacent to a cell of a given other facies	Number of cells of the facies adjacent to a cell of any other facies	Sum of all the component values
	Facies connection probability	Γ	Squared number of component cells	Squared number of cells of the facies	Sum of all the component values
	Connected component density	ϵ	Number of components	Number of cells of the grid	–
	Unit component proportion	p^u	Number of components of one cell	Number of components	–
	Traversing component proportion	p^c	Number of components linking two opposite borders of the grid	Number of components	–
Shape indicators	Number of component cells	n	Number of component cells	–	Average of the non-unit-component values
	Box ratio	β	Number of cells of a component	Number of cells of the axis-aligned bounding box of the component	Average of the non-unit-component values
	Faces/cells ratio	ζ	Number of faces composing a component surface	Number of cells of a component	Average of the non-unit-component values
	Sphericity	ϕ	Surface area of a sphere	Surface area of the connected component	Average of the non-unit-component values
Skeleton indicators	Inverse branch tortuosity	t	Distance between the extremities of a branch	Branch curvilinear length	Average of all the branch values
	Node degree proportions	p^n	Number of node connected to n segments	Total number of node for all the skeletons	Sum of all the skeleton values

related facies on the flow (e.g., Western et al., 2001; Mariethoz, 2009). In particular, Oriani and Renard (2014) showed the influence of the connected component geometry – i.e., their shape – on the equivalent hydraulic conductivity, and therefore on the flow behavior. The shape indicators characterize the connected component shape through simple surface and volumetric measures. They all give one value per component. The arithmetic mean of those values provides a value of the indicator for a given facies. This makes the indicator comparison easier.

Skeleton indicators: The skeletons help to better characterize the topology and global geometry of their connected components: their one-dimensional representation is easier to analyze. Here two indicators are introduced. The inverse branch tortuosity characterizes the geometry of the skeleton. Its values for all the branches of all the skeletons related to a facies are averaged to obtain a single value for the facies. It completes the shape indicators in the characterization of the connected component shape. The node degree proportion depicts the topology of the skeletons. It helps to analyze the connectivity more precisely.

3. Quality analysis considerations

The final purpose of this work is to easily and objectively compare several realizations. The indicators are thus computed on large sets of realizations, which may come from different methods and/or parameters. Then dissimilarity values based on the indicators help to compare the realizations.

3.1. Influence of different grid dimensions

Some cases imply to compare realizations on different grids, and the grids may have different dimensions. For instance in MPS, the training image is often larger than the simulation grid to maximize pattern repeatability.

The grid dimensions influence the size of the traversing connected components, such as channels. This impacts in particular the connected component density and the number of component cells. When the grid size varies along the channel direction, the number of cells for the channels also varies. And even though the number of channels does not necessarily change, the grid volume does, impacting the density. These indicators highlight expected differences in such cases. Their direct use is then detrimental to the quality analysis.

We propose two workarounds to compensate for different grid sizes:

- Either sampling the images from the different grids so that all the samples have the same dimensions. The sample size are the largest dimensions common to all the grids. Each sample is randomly extracted and each image may be sampled several times to still catch the characteristics of the whole image.
- Or correcting the indicators of the difference between the grid dimensions. The smallest grid dimensions among all the grids form a hypothetical reference grid. The indicators are corrected to their expected value in such reference grid. Appendix B details this correction.

The sampling exempts from correcting the indicators, but it adds a step and requires the analysis of more images, which could slow down the process. If they are valid, the corrections should give similar results than the sampling in a more efficient process.

3.2. Indicator rescaling

The rescaling ensures that the differences between the ranges of indicator values will not affect the comparison. The histogram-based indicators – facies proportion, facies adjacency proportion

and node-degree proportion – are not rescaled, to preserve their histogram behavior for the dissimilarity computation (Section 3.3). Two methods can be used for rescaling: normalization and standardization.

The normalization method consists in rescaling linearly the indicators values between 0 and 1. The indicator I_i is the ith indicator of the set previously defined. When computed for the facies f of the realization r, we will denote the computed indicator I^r_{if}. The normalization is then obtained by rescaling it between its minimum and maximum values:

$$\text{norm}(I^r_{if}) = \frac{I^r_{if} - m_{if}}{M_{if} - m_{if}} \tag{1}$$

with M_{if} the maximum value for the same indicator and facies among all the images and m_{if} the minimal value for the same indicator and facies among all the images.

The standardization method consists in using reduced-centered indicator values. For an indicator i the standardized value for a facies f of a realization r is obtained using the following formula:

$$\text{stand}(I^r_{if}) = \frac{I^r_{if} - \mu_{if}}{\sigma_{if}} \tag{2}$$

with μ_{if} the mean for the same indicator and facies among all the images and σ_{if} the standard deviation for the same indicator and facies among all the images. Standardization is an interesting option to focus on the indicator variance. The normalization on the other hand decreases the influence of outliers and gives precise limits to the indicator values.

3.3. Dissimilarity calculation

The principle of comparing two images is to determine how dissimilar these images are. The indicators can be seen as coordinates of the compared images. These indicators are heterogeneous: they are either based on histograms or on continuous values. The computation of a dissimilarity value between two images requires a heterogeneous metric.

Following the example of Wilson and Martinez (1997), two different metrics are combined into a heterogeneous Euclidean/Jensen–Shannon metric. It uses the Jensen–Shannon distance, square root of the Jensen–Shannon divergence (Lin, 1991; Rao, 1987), for the histogram-based indicators – facies proportion, facies adjacency proportion and node-degree proportion – and the Euclidean distance for all the other indicators. The distance between two images r and s for a given indicator i of a given facies f is given by:

$$d(I^r_{if}, I^s_{if}) = \begin{cases} d_{JS}(I^r_{if}, I^s_{if}) \text{ if } I^r_{if} \text{ and } I^s_{if} \text{ are histograms} \\ d_E(I^r_{if}, I^s_{if}) \text{ if } I^r_{if} \text{ and } I^s_{if} \text{ are continuous values} \end{cases} \tag{3}$$

with I the indicator values. d_{JS} represents the Jensen–Shannon distance:

$$d_{JS}(H^r_i, H^s_i) = \sqrt{\frac{1}{2}\sum_{j=1}^{n}\left[H^r_{ij}\log\left(\frac{H^r_{ij}}{\frac{1}{2}(H^r_{ij}+H^s_{ij})}\right) + H^s_{ij}\log\left(\frac{H^s_{ij}}{\frac{1}{2}(H^r_{ij}+H^s_{ij})}\right)\right]} \tag{4}$$

with H^r_i and H^s_i the histograms of the indicator i for respectively the images r and s, n the number of classes for each histogram, H^r_{ij} and H^s_{ij} the proportions for the class j in the corresponding histograms. d_E represents the Euclidean distance used with rescaled indicators:

$$d_E(I^r_{if}, I^s_{if}) = \sqrt{(\text{resc}(I^r_{if}) - \text{resc}(I^s_{if}))^2} \tag{5}$$

with I^r_{if} and I^s_{if} the values of the indicator i for the facies f of respectively the images r and s and *resc* either *norm* (formula 1) or *stand* (formula 2). The final dissimilarity δ between two images r and s given their respective sets of indicators I^r and I^s is:

$$\delta(I^r, I^s, \omega, \nu) = \sqrt{\omega_1 d_{JS}(I^r_1, I^s_1, \nu)^2 + \sum_{i=2}^{12}\sum_{f=1}^{n}\omega_i \nu_f d(I^r_{if}, I^s_{if})^2} \tag{6}$$

with I^r_1 and I^s_1 the facies proportion histogram for the two images, I^r_{if} and I^s_{if} all the other indicator values depending on the indicator and the facies and n the number of facies. ω represents the set of weights ω_i that control the impact of each indicator. ν represents the set of weights ν_f that control the impact of each facies. Note that the facies proportion histograms are the only indicators with one result for all the facies. Thus the facies proportions are treated differently from all the other indicators. The Jensen–Shannon distance used in that case is slightly modified:

$$d_{JS}(H^r_i, H^s_i, \nu) = \sqrt{\frac{1}{2}\sum_{f=1}^{n}\nu_f\left[H^r_{if}\log\left(\frac{H^r_{if}}{\frac{1}{2}(H^r_{if}+H^s_{if})}\right) + H^s_{if}\log\left(\frac{H^s_{if}}{\frac{1}{2}(H^r_{if}+H^s_{if})}\right)\right]} \tag{7}$$

The dissimilarity values computed by formula 6 between all the images constitute a non-negative symmetric matrix. This matrix has a zero diagonal corresponding to the dissimilarity between an image and itself. The dissimilarity matrix can be directly visualized with a heat map or treated by multidimensional scaling to get a more practical visualization.

3.4. Heat map

The heat map is a simple graphical representation of a matrix where the matrix values correspond to colors. In our case, the heat map is a two-dimensional representation. This colored representation highlights patterns in the dissimilarity matrix, either between realizations or between simulation methods. The main advantage of the heat map is to show the real dissimilarity values, contrary to the multidimensional scaling described in the next subsection.

The heat map also enables to classify the images and/or to apply clustering methods on it. A simple yet informative classification is the ranking according to the dissimilarities of the images toward one particular image. When using more advanced clustering methods, the matrix rows and columns are permuted to gather close values into the same cluster.

3.5. Multidimensional scaling

Multidimensional scaling (MDS) [e.g., Torgerson, 1952; 1958, see Cox and Cox, 1994 for a review] is a set of data visualization methods to explore dissimilarities between objects – represented by a dissimilarity matrix – through a dimensionality reduction: it aims at producing a configuration of the objects as optimal as possible in a lower dimensional representation.

3.5.1. Principle and method used

Finding the configuration of the images in a k dimensional representation consists in locating a set of points representing the objects in a k-dimensional Euclidean space – with k being at most equal to the number of images minus one. The point positioning is done so that the Euclidean distance d between two points matches

as closely as possible the dissimilarities between the images:

$$d_{r,s} = \sqrt{\sum_{i=1}^{k} (x_{ri} - x_{si})^2} \tag{8}$$

with r and s two images, k the dimension number of the Euclidean space, x_{ri} and x_{si} the coordinates of respectively r and s in the ith dimension. The number of dimension k for the MDS representation is an input parameter. When equal to the number of images minus one, the distances are normally equal to the dissimilarities. When k is lower, the MDS misrepresents more or less the dissimilarities.

Several multidimensional scaling methods have been proposed (e.g., Cox and Cox, 1994), depending on the type of dissimilarities and on the way to match the dissimilarities with the distances. The classical scaling (Gower, 1966; Torgerson, 1952; 1958) is the usual method for multidimensional scaling (e.g., Scheidt and Caers, 2009; Tan et al., 2014). It assumes that the dissimilarities already are Euclidean distances. If this assumption can be relaxed to a metric assumption, i.e., the dissimilarities are distances, Euclidean or not, the classical scaling may further misrepresents dissimilarities based on a heterogeneous metric.

Here we use a different method: the Scaling by MAjorizing a COmplicated Function (SMACOF) (De Leeuw, 1977; De Leeuw and Heiser, 1977; 1980). Its goal is to get distances as close as possible from the dissimilarities using a majorization, i.e., the optimization of a given objective function called stress, through an iterative process. The stress derives from the squared difference between the dissimilarities and the distances. It is positively defined and equals to 0 only when the distances are equal to the dissimilarities. The optimization process corresponds to a minimization of the stress. The final stress value helps to assess the choice of the number of dimensions: the lower the stress is, the better is that choice.

3.5.2. Validation of the number of dimensions

Following the chosen number of dimensions for the representation, the point configuration matches more or less the dissimilarity values. Verifying that the dimension number is enough for a good match between the dissimilarities and the distances is so of prime importance. Two approaches allow testing the chosen dimension number:

- **The scree plot:** It represents the stress of the SMACOF against the dimension number. The stress follows a globally convex decreasing function that tends toward 0 when the dimension number increases. A stress close or equal to zero means that the higher dimensions are unnecessary to represent the dissimilarities. The best number of dimensions is between the point with the highest flexion of the curve and the beginning of the sill at zero. The dimension value right after the point with the highest flexion is generally enough for a decent representation.
- **The Shepard diagram:** It represents the distances against the dissimilarities. The better the correlation, the better the choice of dimension number.

Two-dimensions are more practical for an analysis purpose. A three-dimensional representation remains a possibility if the improvement is significant enough from a two-dimensional representation.

3.5.3. Estimation of the point position confidence

The point position confidence is another way to assess the MDS ability to represent the dissimilarities. For each point r, an error e highlights the mismatch between the dissimilarities δ and the distances d with all the other points s:

$$e_r = \sum_s |(a\delta_{r,s} + b) - d_{r,s}| \tag{9}$$

with a and b the linear regression coefficients found on the Shepard diagram. This measure gives a more local representation of the miss-representation than the scree plot or the Shepard diagram.

For visualization purpose, that error is then normalized, giving the confidence c for a given image r:

$$c_r = 1 - \frac{e_r - e_{min}}{e_{max} - e_{min}} \tag{10}$$

with e_{max} and e_{min} respectively the greatest and the lowest error values amongst the errors of all the images. This confidence can then be attributed to its corresponding point in the MDS representation through the point transparency: the less transparent the point is, the best the dissimilarities related to this point with all the other points are represented.

4. Example of method application

The method, as described in the previous sections, consists in three steps:

1. Indicator computation.
2. Dissimilarity computation in a matrix.
3. Dissimilarity visualization and analysis, especially with multidimensional scaling.

The first two steps were implemented in a C++ plugin for the SKUA-GOCAD geomodeling software (Paradigm, 2015). The last step was realized using the software environment for statistical computing R (R Core Team, 2012) with the addition of the R packages SMACOF (De Leeuw and Mair, 2009) and ggplot2 (Wickham, 2009).

4.1. Dataset

The dataset falls within the simulation of a channelized system. It contains several realizations representing the same sedimentary environment simulated with different methods. The analysis aims at highlighting the indicator ability to capture the differences of static connectivity between the realizations, and especially between the realizations from different methods. As it concerns a sole case, it would be inappropriate to draw general conclusions on the simulation methods themselves.

The channelized system is composed of sandy channels with levees into a mudstone environment. A conceptual model, called the training image (TI) (Fig. 4, image at the top), provides an ideal representation of this system. The case study falls within the scope of a MPS study: several simulation methods are used to reproduce the sedimentary bodies observed in the training image. MPS performs better when the training image is larger than the realizations, to ensure enough pattern repeatability. It involves two grids: the first one for the training image (Fig. 4, image at the top) and the second one for the realizations (Fig. 4, images at the bottom).

The training grid contains two sets of images:

- **TI:** One object-based realization simulated using the object-based method of the software Petrel (Schlumberger, 2015) (see Appendix C, Table C.6, for the simulation parameters).
- **Analog:** 100 object-based realizations simulated with the same method and parameters used to simulate the TI (Appendix C, Table C.6).

The simulation grid contains four sets of images:

- **DeeSse:** 100 MPS realizations simulated with the DeeSse implementation (Straubhaar, 2011) of the direct sampling method (Mariethoz et al., 2010). Contrary to more traditional MPS methods, the direct sampling bypasses the conditional probability computation and resamples randomly the training

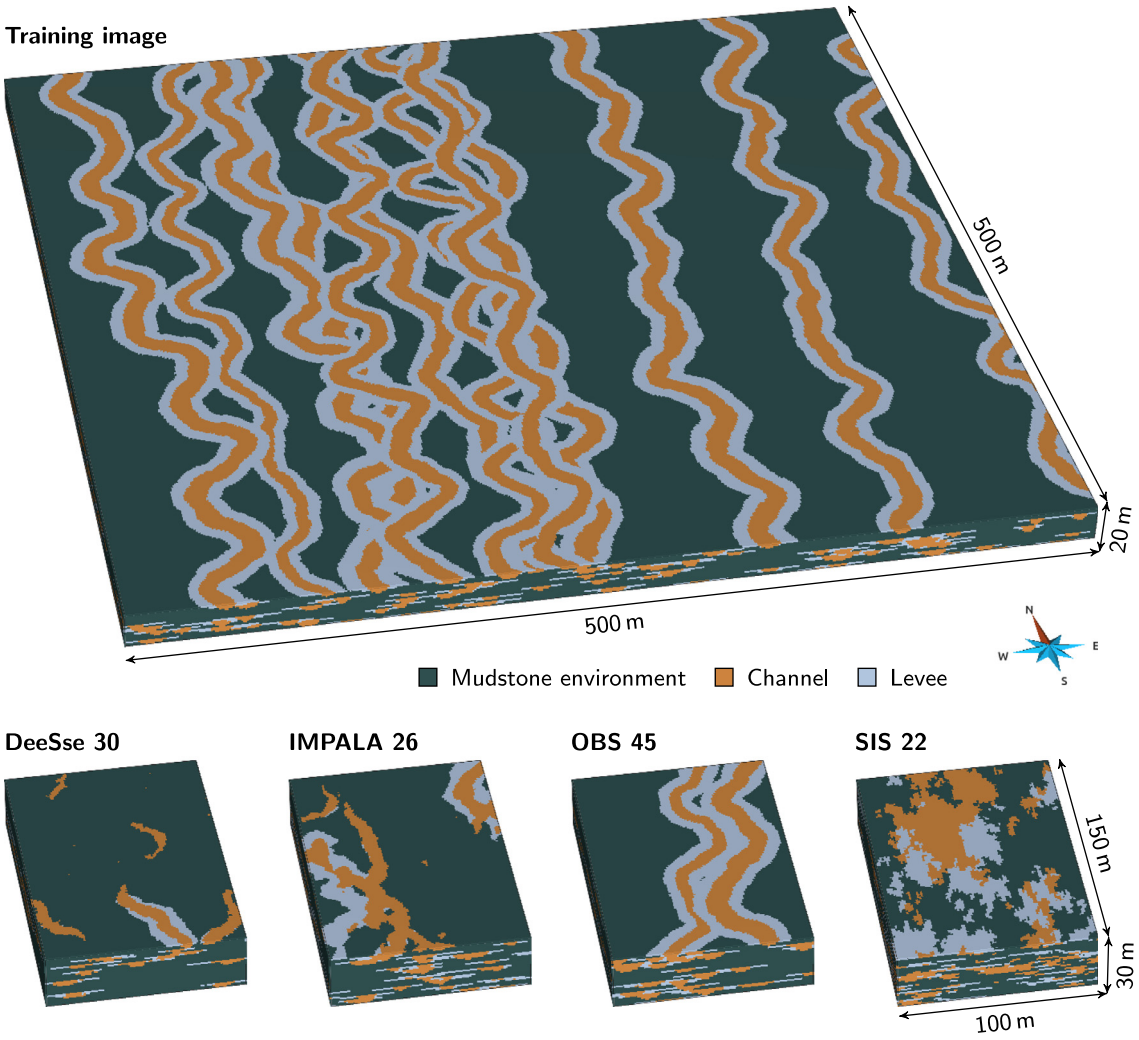

Fig. 4. Training image and examples of realizations for each category.

image. It relies on the compatibility measured with a distance between the conditioning data and the patterns scanned in the training image. The resampling step selects the first pattern with a distance lower than a given threshold. The training image is the TI and the set of parameters is given in Table C.4) in the appendix.

IMPALA: 100 MPS realizations simulated with the method IMPALA (Straubhaar et al., 2011, 2013). Contrary to the DeeSse, IMPALA still computes the conditional probabilities during the simulation. To improve the efficiency of this computation, the method stores the training image patterns in a list. The training image is scanned once at the beginning and the list is used instead during the simulation. The training image is the TI and the set of parameters is given in Table C.5) in the appendix.

OBS: 100 object-based realizations simulated with the same method and parameters used to simulate the TI (Appendix C, Table C.6).

SIS: 100 sequential indicator simulation realizations simulated using variograms based on the facies in the TI (Appendix C, Table C.7).

4.2. Analysis setting

The purpose here is to compare the realizations with the TI. It should lead to retain the method and associated parameters that reproduce at best the static connectivity of the TI for the studied case. The indicators used in this case study (Table 2) rely on the face-connected components, because the face-connectivity between cells is the most frequently used (Renard and Allard, 2013). All the indicators are equally considered ($\omega_i = 1$ for all i in formula 6). This avoids any subjective bias that could arise from favoring a

Table 2
Set of indicators used for the case study. The indicator definitions are summarized in Table 1 and more detailed descriptions are in Appendix A.

Category	Indicator	Symbol	Weight
Global indicators	Facies proportion	p	1
	Facies adjacency proportion	p^a	1
	Facies connection probability	Γ	1
	Connected component density	ϵ	1
	Unit connected component proportion	p^u	1
	Traversing connected component proportion	p^c	1
Shape indicators	Number of connected component cells	n	1
	Box ratio	β	1
	Faces/cells ratio	ζ	1
	Sphericity	ϕ	1
Skeleton indicators	Node degree proportions	p^n	1
	Inverse branch tortuosity	t	1

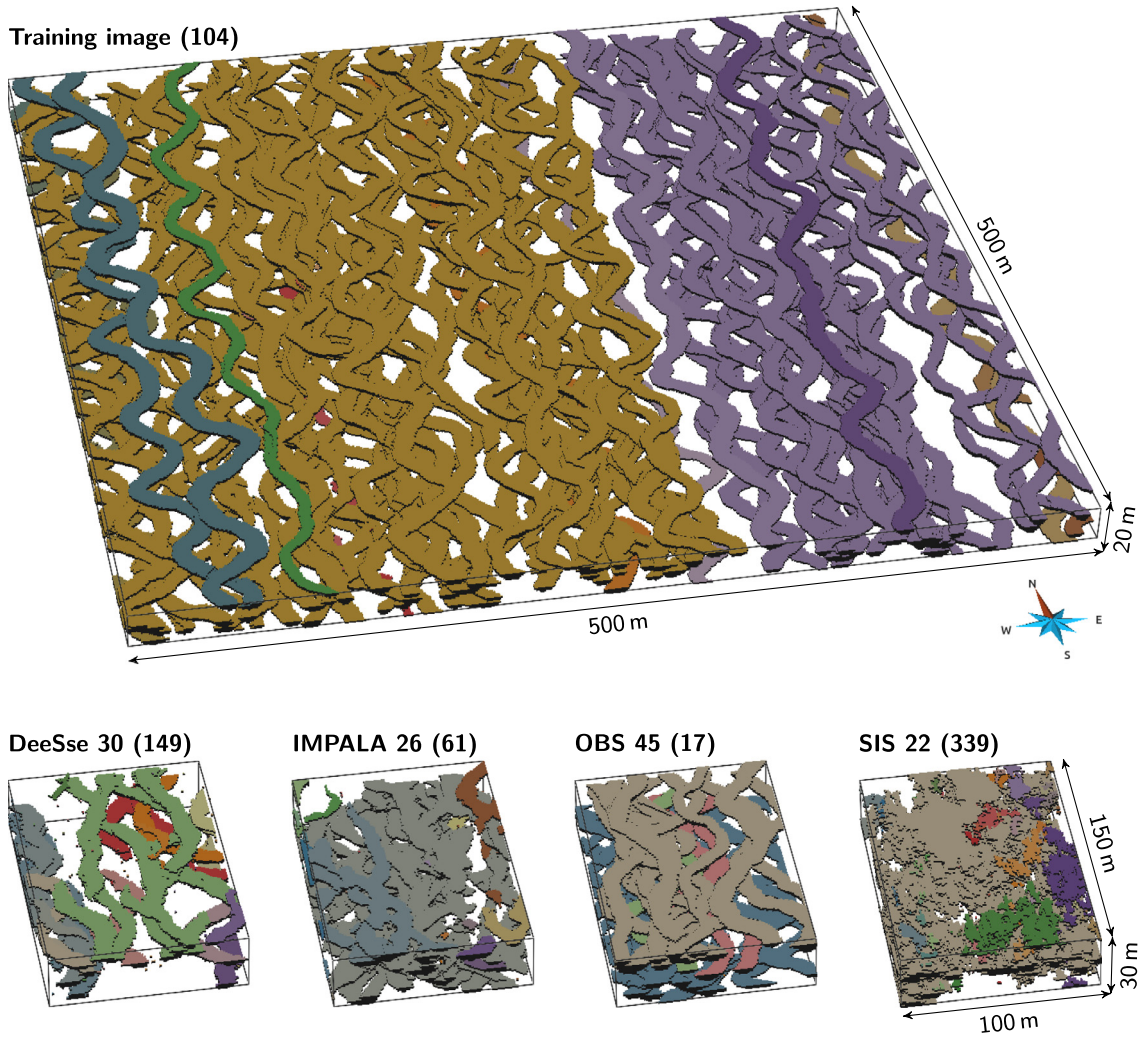

Fig. 5. View of all the channel connected components within the TI and examples of realizations for each categories. The number in parentheses are the number of connected components of each image.

given indicator. The mudstone environment is the resultant of the channels and levees placement. It has so no precise shape by itself and may blur the analysis. It gets a weight of 0 while channels and levees both get each a weight of 1 ($\nu_{mudstone} = 0$, $\nu_{channel} = 1$ and $\nu_{levee} = 1$). Channels and levees are considered equally important to reproduce, but this aspect is related to the case study and could be further discussed. The indicators are normalized to cancel the differences of different indicator ranges. Slices of 17 cells along the grid axis with the same orientation than the channels are used for the skeletonization.

Several samples are also randomly extracted from the grids to evaluate the suitability of correcting the indicators when dealing with different grid sizes. The training grid having 500 × 500 × 20 cells and the simulation grid 100 × 150 × 30 cells, the common largest dimensions for the samples are 100 × 150 × 20. The training grid is almost 10 times larger than the simulation grid. Therefore, 20 samples are extracted from the TI and each analog, whereas 2 samples are extracted from each DeeSse, IMPALA, OBS and SIS realization.

4.3. Visual inspection of the realizations

Looking at the connected components (Fig. 5) highlights some expectations for the dissimilarity analysis. Two aspects must be analyzed: the reproduction of the sedimentary body shapes and the reproduction of their connectivity, especially concerning the channels. In the studied case, the reproduction of the shape is pretty easy to analyze visually. The SIS realizations do not display any objects similar to channel/levee systems and are so far dissimilar from the TI. The OBS realizations look similar to the TI, which is what is expected considering that they come from the same method and parameters. DeeSse realizations have objects similar to channels, even if some continuity issues appear. They also seem to have an insufficient number of channels. IMPALA realizations have quite linear objects but which poorly reproduce channel and levee shapes.

Estimating the static connectivity in three-dimensional images is more difficult. The TI channels seem highly connected. The objects in the SIS realizations do not locally intersect like channels do and are far too connected. DeeSse realizations contain less objects and seem under-connected compared to the TI. The distinction between OBS and IMPALA realizations is difficult concerning the connectivity. Looking at the skeletons of the connected components (Fig. 6) corroborates those observations. DeeSse realizations are clearly under-connected compared with the other categories. SIS ones are over-connected. IMPALA realizations seem a bit more connected than OBS ones. The static connectivity within the training image is clearly heterogeneous.

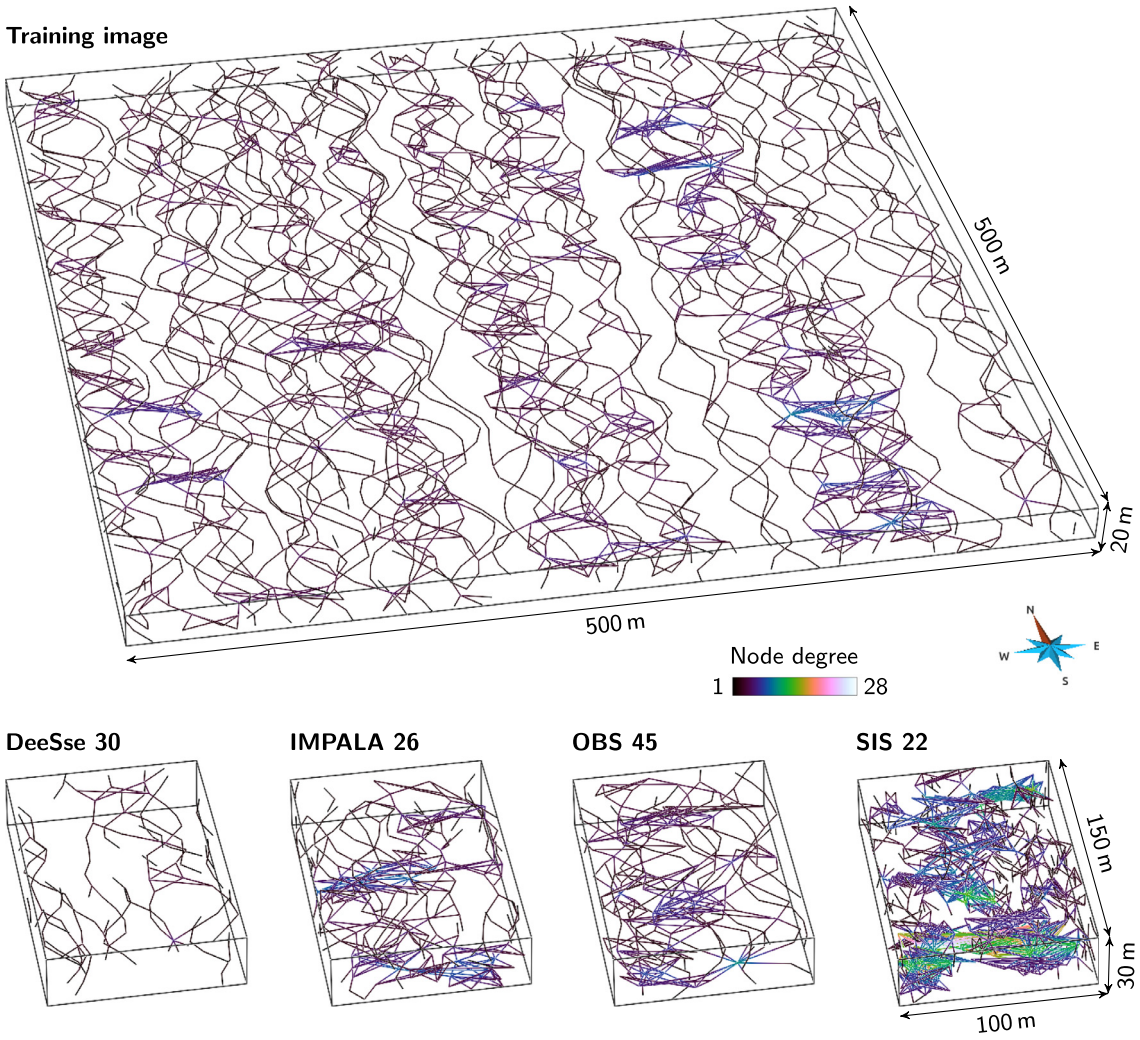

Fig. 6. View of all the skeletons of the connected components for the TI and for a realization of each category.

4.4. Effect of different grid dimensions on the analysis

The TI, analogs and OBS realizations come from the same method with the same parameter values. The grid size is the only difference between all these images: the grid of the TI and analogs – the training grid – is larger than that of the OBS realizations – the simulation grid.

This difference of grid dimensions directly impacts the connected component density and the number of connected component cells, which are corrected to take into account such difference (Appendix B). But the realizations coming from the same method still differ when looking at the dissimilarities (Fig. 7, MDS representation from the original images). The OBS realizations within the simulation grid stand out from the TI and the analogs within the training grid. Such difference is absent from the samples, where all the images have the same size (Fig. 7, MDS representation from the image samples). The grid size seems to clearly impact the dissimilarity values.

However, both MDS representations (Fig. 7) have high stress values with two dimensions and can not be fully trusted. The heat maps (Fig. 8) clarify that situation.

The heat map from the original images (Fig. 8, bottom left) appear non-homogeneous. A red square symbolizes the significant dissimilarities between the TI and analogs on one side and the OBS realizations on the other side. The heat map from the samples if far more homogeneous, without red square. They confirm the impact of the grid size observable on the MDS representations.

Thus, correcting the connected component density and the number of connected component cells is not adequate, and other indicators are impacted by the grid dimensions. The TI, the analogs and the OBS realizations have all similar channel and levee proportions (Fig. 9). The channels and levees occupy the same volume inside the two grids. But the facies connection probabilities for both channels and levees differ between the realizations in the two grids (Fig. 9). The probability that two cells of the same facies belong to the same connected component is higher in the training grid than in the simulation grid. This is consistent with the difference of grid dimensions. When the grid dimension along the channel direction increases, the probability that two channels cross each other to form a single connected component increases too, especially here with sinuous channels. In such case, the grid size impacts the characteristics of the connected components and the associated indicator values.

Comparing samples appear to be essential with grids of different dimensions. And using samples reveals other aspects of the images. For instances, the different samples coming from the TI are highly dissimilar. This illustrates the non-stationarity of the TI concerning the connectivity: some areas contain only one connected component as the channels are all connected, whereas other areas contain more connected bodies.

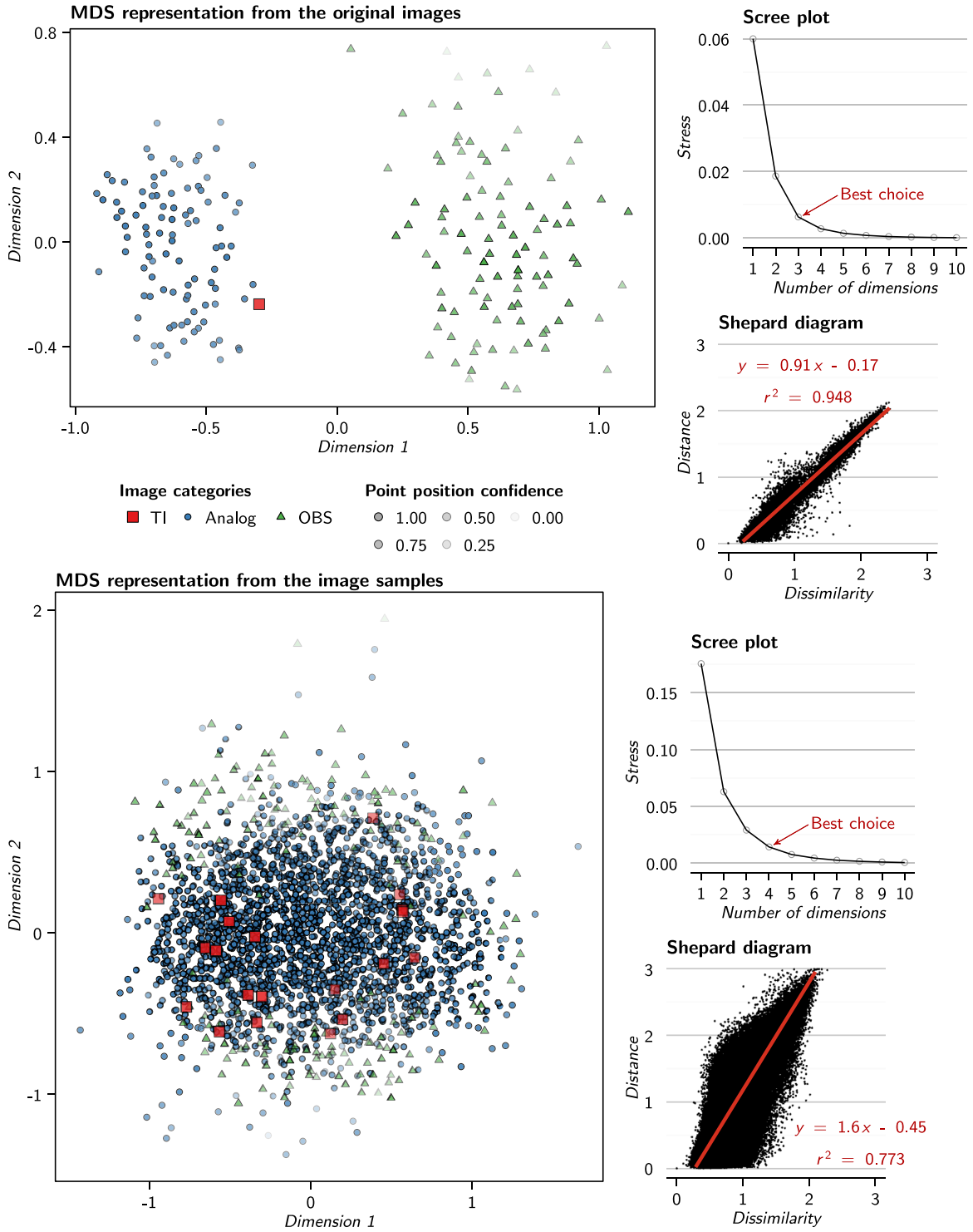

Fig. 7. MDS representations of the dissimilarity matrices for the original images (with corrections of the indicators to cancel the effect of the grid dimensions) and samples (of same size). The scree plot for the original images only displays the stress values up to 10 dimensions on 200 possible. The scree plot for the samples only displays the stress values up to 10 dimensions on 2220 possible.

4.5. Comparing the connectivity of the training image and of the realizations

The purpose is now to compare the training image to all the realizations. These realizations come from different methods, but all borrow their input from the training image and have to reproduce the sedimentary bodies of the training image. All the following analysis relies on the image samples and not on the original images to avoid any bias due to the difference of size between the training image and the realizations.

4.5.1. Analysis of the dissimilarities

The dissimilarities give a first insight on the relationships between the different realizations (Fig. 10). The training image

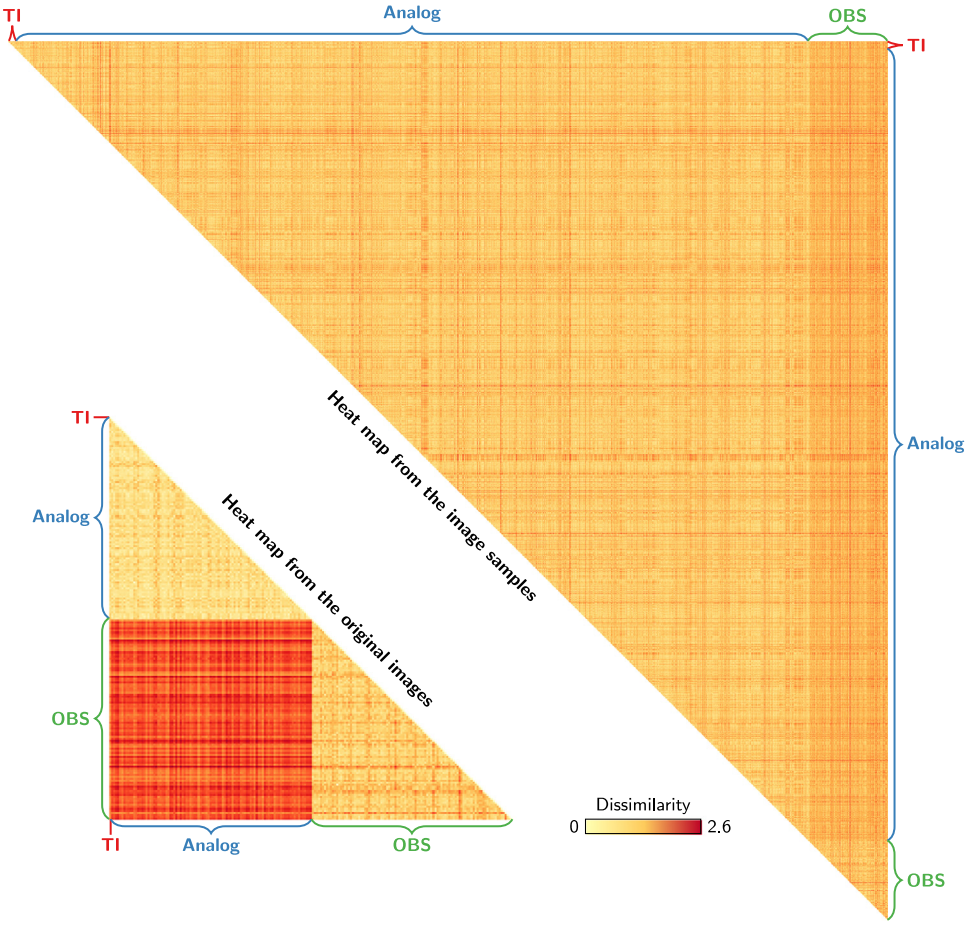

Fig. 8. Heat map representations of the dissimilarity matrices for the original images (with corrections of the indicators to cancel the effect of the grid dimensions) and samples (of same size). Only one triangle of the symmetric matrices is represented.

samples fall within the OBS samples, highlighting the similarity of these images. The samples from the multiple-point methods, DeeSse and IMPALA, are close to the OBS samples, but they do not mix up much. All these images are so not completely similar. Furthermore, the DeeSse and IMPALA samples remain away from the TI samples. The SIS samples are clearly distinct from all the other samples, and are the most distant from the TI samples.

If the confidence of the two-dimensional MDS representation is not high, the heat map confirms those observations (Fig. 11). The first row shows the dissimilarities between the training image samples and the realization samples. The whitest samples, the OBS ones, are the closest to the TI. The reddest samples, the SIS ones, are the furthest from the TI samples. The DeeSse and IMPALA samples fall in between, and seem equally close to the TI samples. Globally, the differences between all the methods are significant, as highlighted on the MDS.

As observed in the previous section, the training image samples are dissimilar one from the other. It shows the heterogeneity of static connectivity within the training image. Concerning the realizations, the OBS realizations are also dissimilar one from the other, whereas the SIS realizations are all really close. Both DeeSse and IMPALA realizations are more spaced than the SIS ones, but not as much as the OBS realizations. All this tends toward a variable diversity concerning the static connectivity for the different methods in that case study. Going back to the indicators helps to further analyze such behavior.

4.5.2. Analysis of the indicators

The indicator values for the channels (Figs. 12 and 14) and levees (Figs. 13 and 15) differ depending on the category. The differences are more or less clear depending on the indicator, whose behavior differs between the two sedimentary body types.

The OBS samples being similar to the training image samples appear also on the indicator values. These values are close – and for many indicators the closest – to the TI values for the channels. That trend is less obvious with the levees, with less close values. But the levee density is the only indicator to be really away from the TI values. All this confirms the close relationship between the training image and the OBS realizations concerning the static connectivity. It also confirms the visual observations. This is consistent with the use of the same method and parameters to simulate the training image and the OBS realizations.

Similarly, the significant dissimilarity between the SIS samples and the TI samples also appears on the indicator values. This is obvious on the traversing component proportion or the component density. The high component density means a higher number of connected components compared to the other samples. On the other side, the average number of component cells is quite low, meaning that most of these numerous components are small. The low traversing component proportion signifies that most of these components are not continuous enough to represent channels nor levees. Concerning channels, the significant difference between the SIS and TI samples for the shape indicators – number of component cells, box ratio, faces/cells ratio and sphericity – implies that the SIS components do not look like channels. This different shape

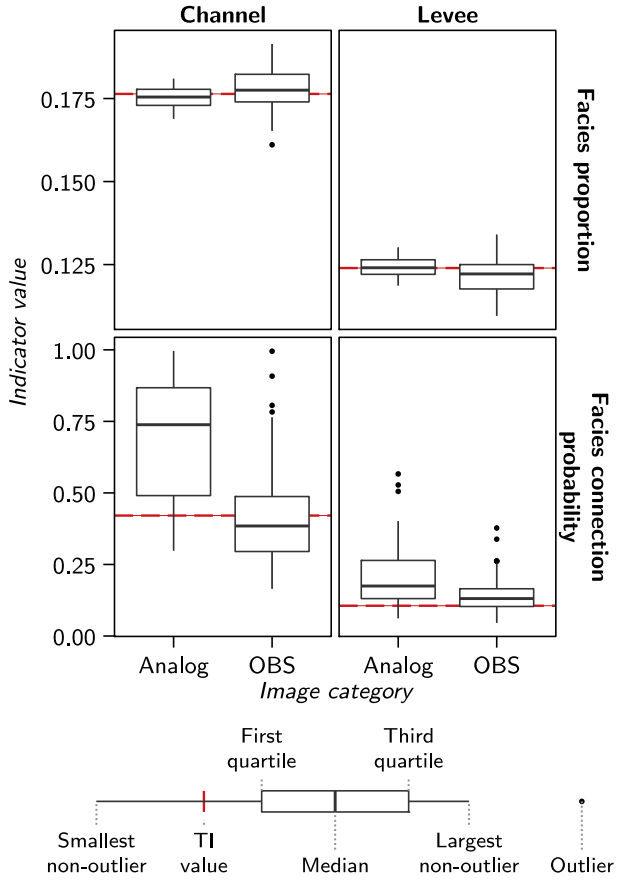

Fig. 9. Box-plots comparing the facies proportions and facies connection probability for the TI, some TI analogs and the OBS realizations.

also appears on the node degrees, with far higher node degree values than for the other categories, implying a less linear shape. Despite numerous and small components, the channel connection probability remains high. This means that these samples must contain one large component. This component must be traversing, as the traversing component proportion is not equal to zero. All those observations are consistent with the visual inspection of the realization, and confirm a significant difference of static connectivity between the training image and the SIS realizations. Many indicators also display a narrow range of values. This confirms the low variability between the SIS samples concerning the connectivity, as seen with the dissimilarities.

DeeSse and IMPALA samples have similarities with the SIS samples, especially more, and smaller, connected components than in the training image, as visible on the component density and the number of component cells. Similarly, the shape indicators show a significant difference between the TI samples and both the DeeSse and IMPALA samples. The higher sphericity implies in particular less linear shapes for the channels. Despite being equally dissimilar to the TI samples, the other indicators show significant differences between the DeeSse and IMPALA samples and the TI samples. The DeeSse samples have far lower channel and levee proportions. This impacts the facies adjacency, with channels and levees being more adjacent to the mudstone. But the most relevant difference between the DeeSse and IMPALA samples comes from the channel connection probability: the connection probability of the DeeSse samples is lower than that of the TI samples, whereas the connection probability of the IMPALA samples is higher than that of the TI samples. The IMPALA samples have a behavior similar to that of the SIS, with a few large component among smaller ones. But these component connectivity is not completely similar to that of the SIS. This is especially visible on the node degree proportions, with the IMPALA samples having an intermediary behavior between the TI and the SIS samples. On the other side, the DeeSse sample connectivity seems lower. The higher degree two proportion of the DeeSse samples implies few intersections between channels. The higher degree one proportion also implies more discontinuous components. Again, all of this is consistent with the visual observations: DeeSse channels are clearly identifiable but discontinuous, whereas IMPALA channels are less visible, with many intersections.

In this case, the indicators confirm what comes from the dissimilarities: the OBS realizations are the most similar to the training image from a static connectivity perspective. This is consistent with the visual observations, and with the use of the same method to simulate the TI and the OBS realizations. The next section endeavors to compare those results from what can be obtained with multiple-point histograms.

4.6. Comparison with multiple-point histograms

Multiple-point histograms or pattern histograms have made their way as indicators of a realization quality with MPS methods (e.g., Boisvert et al., 2010; Tan et al., 2014). We propose here to compare the results obtained with those histograms to the previous results. The histograms are based on a $3 \times 3 \times 3$ pattern and are computed on three levels of multi-grids (Tran, 1994), giving three histograms per image. The dissimilarity δ between two images r and s is adapted from the work of Tan et al. (2014):

$$\delta(H^r, H^s) = \sum_{l=1}^{3} \frac{1}{2^l} D_{JS}(H_l^r, H_l^s) \tag{11}$$

with H^r and H^s the sets of three histograms for each image, l the multi-grid level and D_{JS} the Jensen–Shannon divergence, which is the squared Jensen–Shannon distance. A multi-grid level l of 1 corresponds to the finest level and here 3 is the coarsest level. The coarser levels characterize the large-scale behavior of the sedimentary bodies. But they induce a loss of information. This justifies the decreasing weights when the multi-grid level increases. Similarly to the work using multiple-point histograms, the comparison is directly made on the original images, not on samples.

The observations about the category relationships made with the previous indicators (Fig. 10) remain valid on the MDS representation from the multiple-point histogram (Fig. 16). The training image falls within the OBS realizations. The DeeSse and IMPALA realizations are close from the OBS ones, but with a clear separation. They all remain separated from the TI. Again, the SIS realizations are far away from all the other images, including the TI. The main difference with the previous indicators comes from the variability within a category. This is especially noticeable with the SIS realizations, which seem to have a significant pattern variability.

The two-dimensional MDS representation is here again a poor representation of the dissimilarities, with a high stress. Only the dissimilarities with the training image are kept to directly study them and compare the ranking between different indicators (Fig. 17). Looking at all the connected component indicators – i.e., all the indicators described in Table 1 – points out the conclusions coming from Fig. 10: the OBS realizations are the closest to the TI, the SIS ones the furthest, and the DeeSse and IMPALA realizations stand in between. Similar rankings come from the shape indicators – i.e., number of component cells, box ratio, faces/cells ratio and sphericity – and the skeleton indicators – i.e., node degree proportions and inverse branch tortuosity.

The multiple-point histograms have also a similar ranking, with a clearer separation between the SIS realizations and the other re-

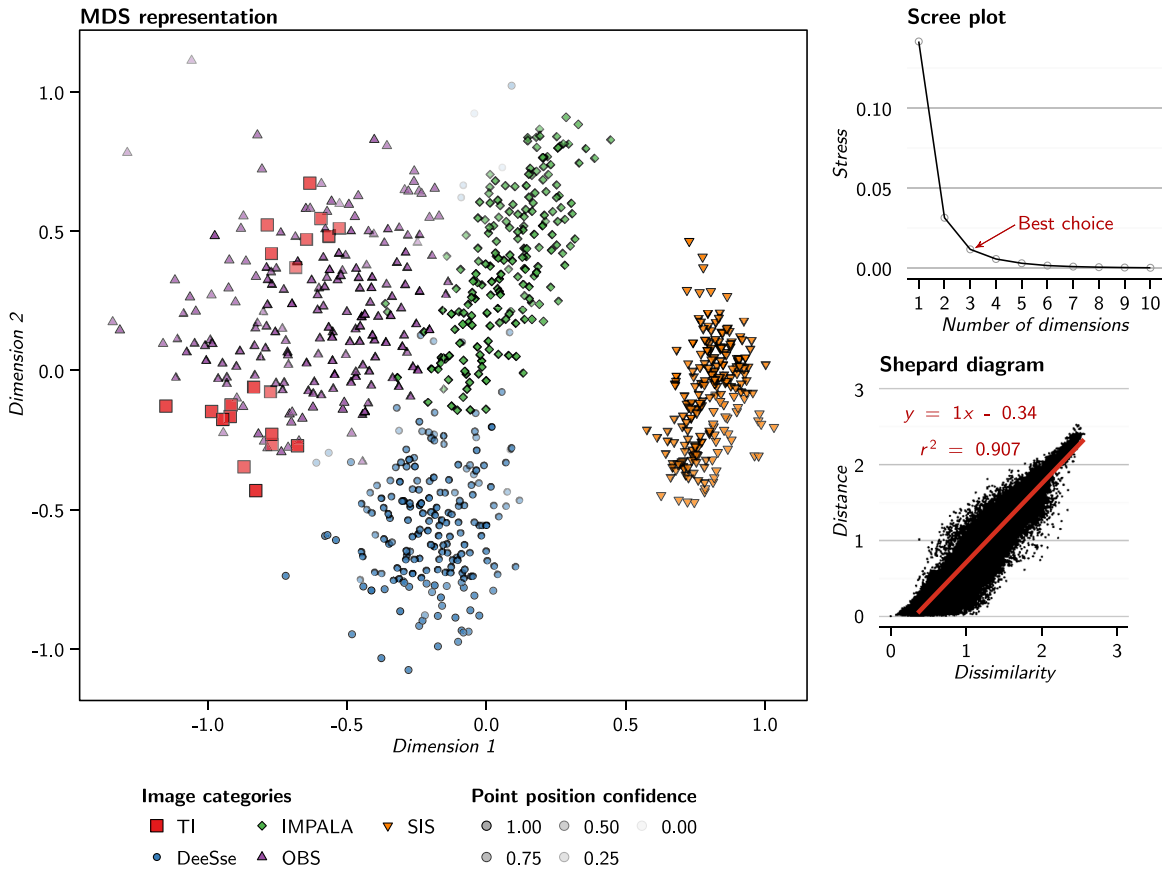

Fig. 10. MDS representation of the dissimilarities between the samples of the case study generated using SMACOF and validation graphs. The scree plot only displays the stress values up to 10 dimensions on 820 possible.

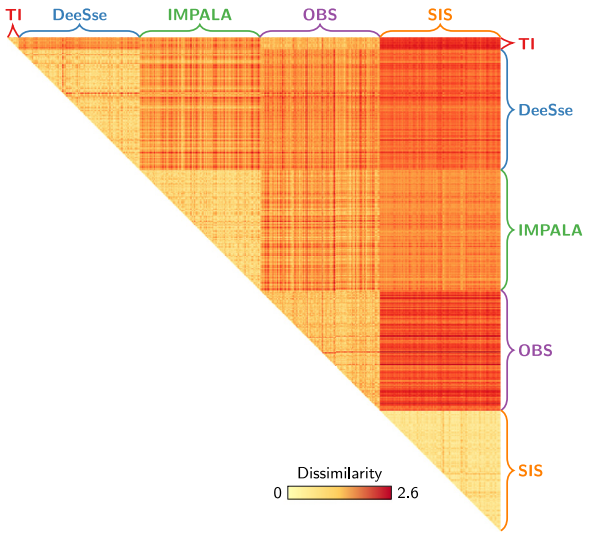

Fig. 11. Heat map representation of the dissimilarity matrix computed based on the samples of the case study.

alizations (Fig. 17, All the multi-grid levels). However, the dissimilarities between the training image and the DeeSse realizations vary significantly between the multi-grid levels. The largest multi-grid level even places the DeeSse realizations closer to the TI than the OBS realizations. This level characterizes the large-scale behavior of the sedimentary bodies. Such ranking is then particularly surprising due ot the presence of discontinuous bodies within the DeeSse realizations, but neither within the OBS ones nor within the TI. These continuity differences are confirmed by the skeletons, especially the higher proportion of node of degree one inside the grid for the DeeSse than for the OBS realizations.

5. Discussion

The previous section highlights the ability of the method to distinguish realizations by focusing on the static connectivity through the connected components. This section discusses some aspects of the analysis process.

5.1. About the indicators

All the indicators proposed here rely more or less directly on the connected components. Some of them are classical, such as the facies proportion, but as highlighted on Fig. 9 the facies proportion is not enough to characterize the static connectivity. New indicators are introduced here compared to previous studies on connected components (De Iaco and Maggio, 2011; Deutsch, 1998). Some indicators lead to better characterize the component organization, such as the traversing component proportion or the component density. Other indicators aim to better characterize the component shape, such as the sphericity. Using skeletons is also a new feature to compare realizations. The node degree proportion appears to give many details about the connectivity. The branch tortuosity has been less useful for the studied case, with a poorer discrimination of the realizations. This is due to the parameterization of the skeletonization, which favor the topology at the cost of the geometry of the skeletons.

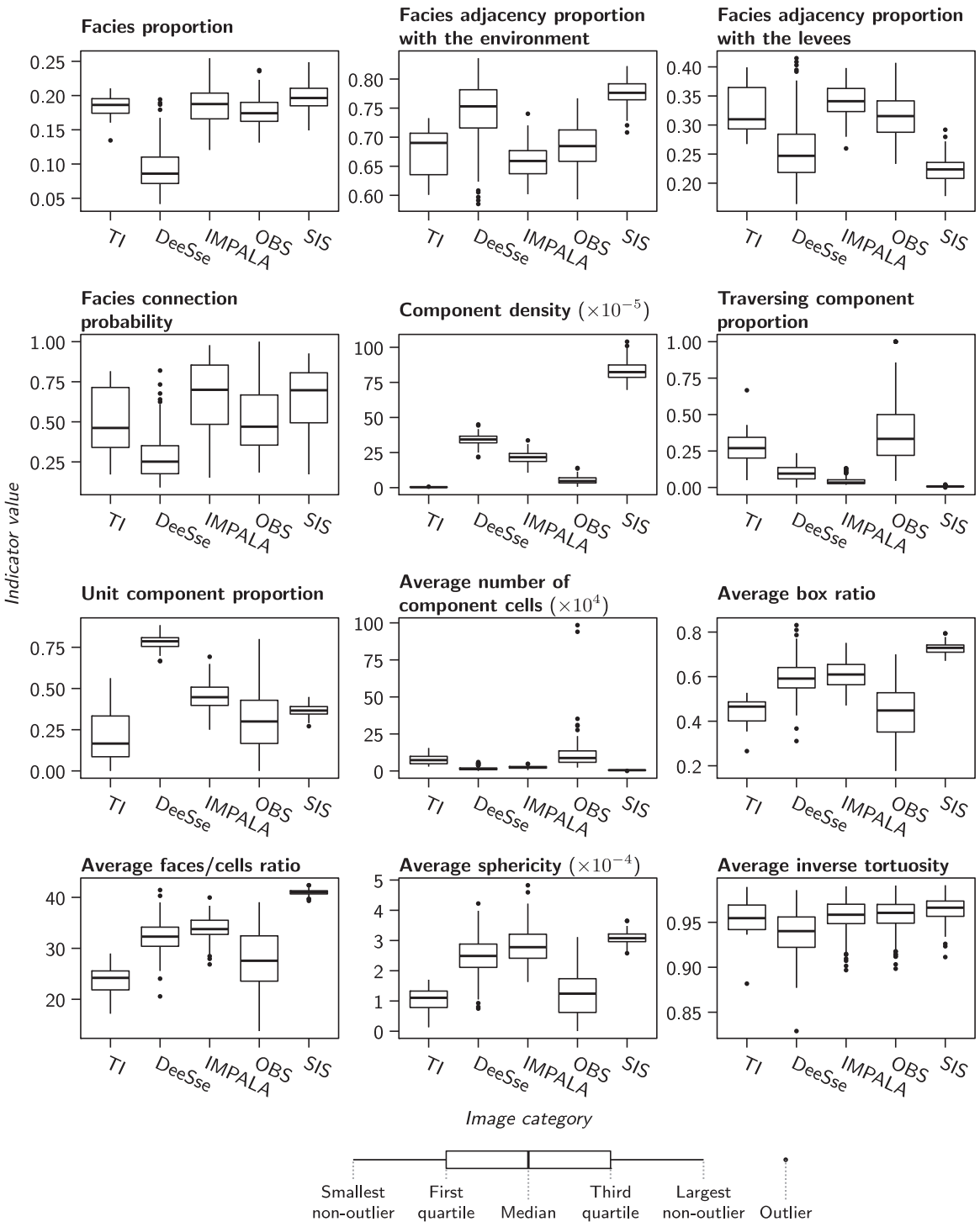

Fig. 12. Box-plots comparing the range of indicators computed on the channels for the different categories, except the node degree proportions.

The use of multiple-point histograms as indicators in a method similar to Tan et al. (2014) shows a ranking close to that with the connected component indicators. However, they do not characterize the realizations in the same way. The multiple-point histograms of the finest multi-grid or multi-resolution level characterize in details the shape of the sedimentary bodies. The shape indicators are global measures over a whole connected component. As connected components can have variable shapes due to the sedimentary bodies intersections, being able to characterize more finely the component shape is an interesting asset. From this point of view, the multiple-point histograms could bring further information on the connected component shape.

However, the multiple-point histograms do not measure the static connectivity: they compare the patterns between the images, but not really the relationships between the patterns. The study of the coarsest multi-grid or multi-resolution levels attempts to look at the large scale behavior of the sedimentary bodies. But many details are lost in the process, what justifies the lower weights for these levels in the dissimilarity from multiple-point histograms (Tan et al., 2014). And it still not characterizes the static connectiv-

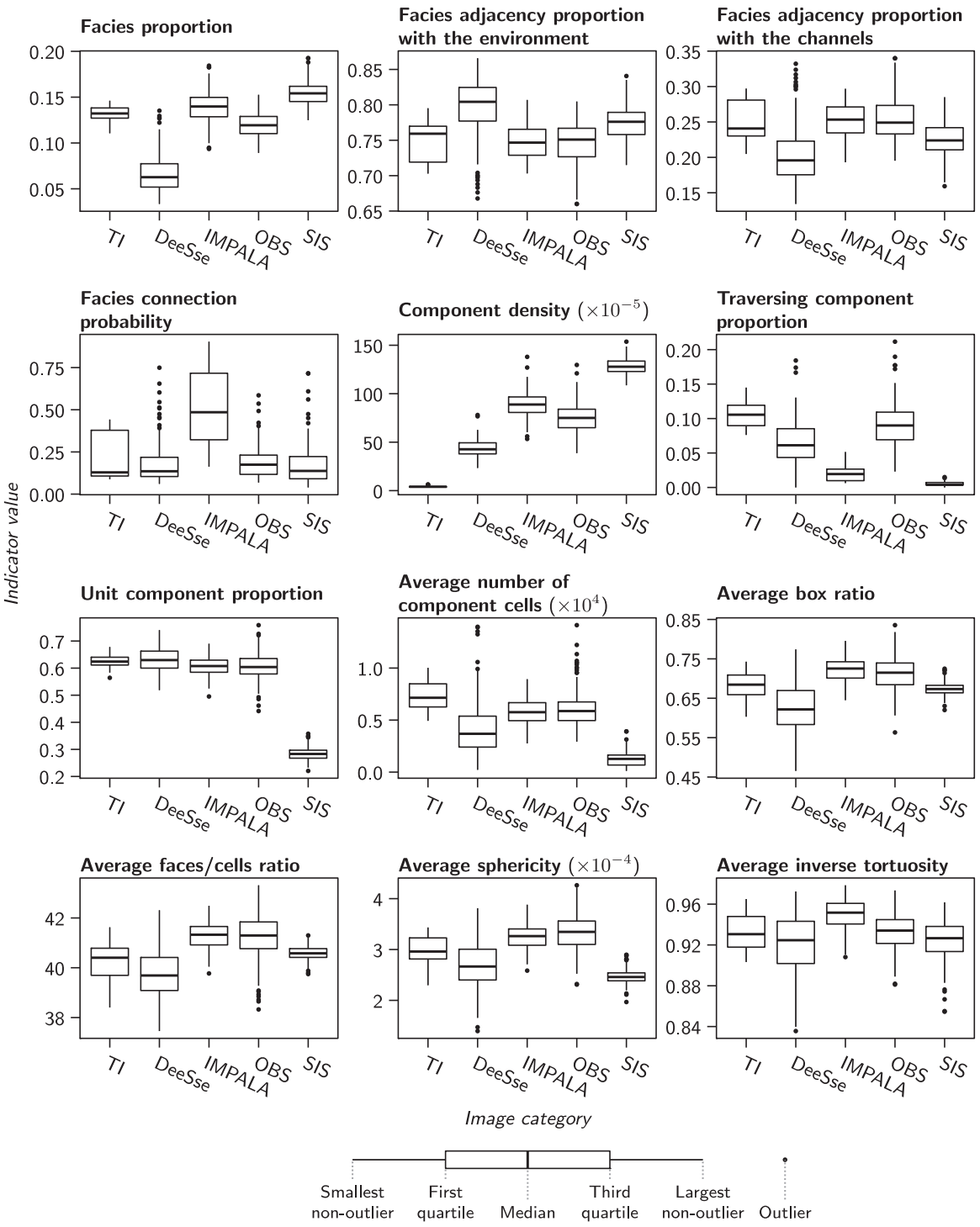

Fig. 13. Box-plots comparing the range of indicators computed on the levees for the different categories, except the node degree proportions.

ity. From this point of view, the skeletons describe more precisely the large-scale behavior of the components and their connectivity.

5.2. About indicator comparison

As stated in the previous section, a single indicator is not enough to fully characterize the static connectivity. Comparing several indicators lead to more relevant information about the realizations and how much they differ from the viewpoint of connectivity. Comparing realizations on grid of different dimensions leads to issues non-addressed by previous studies (De Iaco and Maggio, 2011; Deutsch, 1998). A correction on the two most affected indicators is not sufficient to compensate for different grid dimensions. Sampling the images appears to be more efficient, and also helps to analyze the connectivity heterogeneity within the images. The question of the sampling representativeness remains to be explored.

Using a metric is very useful, because it gathers all the indicator values into one dissimilarity value and facilitates the comparison of the realizations and the analysis. Tan et al. (2014) already used such process with multiple-point histograms. We have applied a similar principle to connected components, gathering many indi-

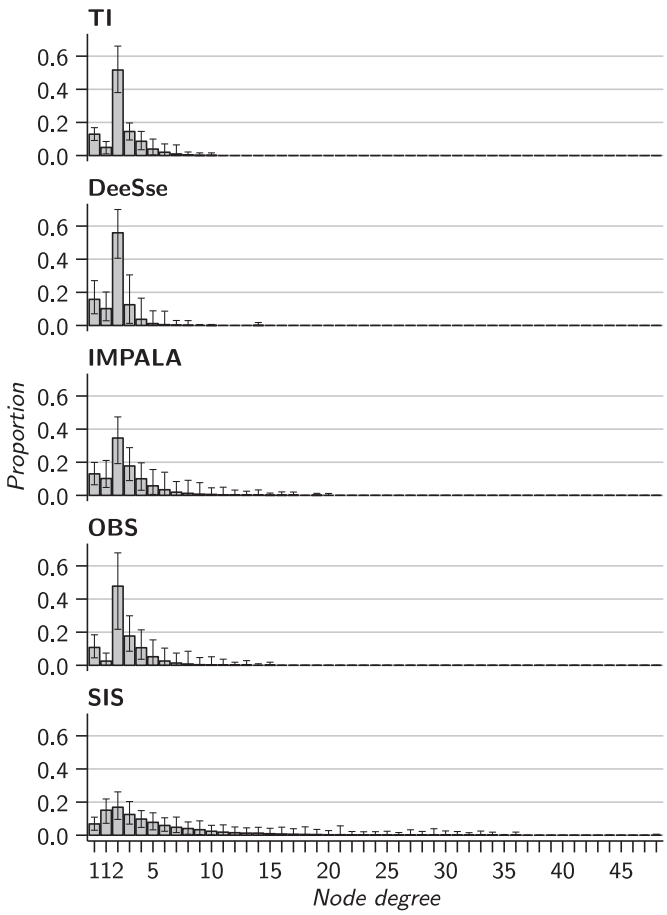

Fig. 14. Mean node degree proportions of the channel skeletons for each category. The error bars display the minimum and maximum proportions. The first node degree 1 corresponds to the nodes of degree one along a grid border. The second node degree 1 corresponds to the nodes of degree one inside the grid.

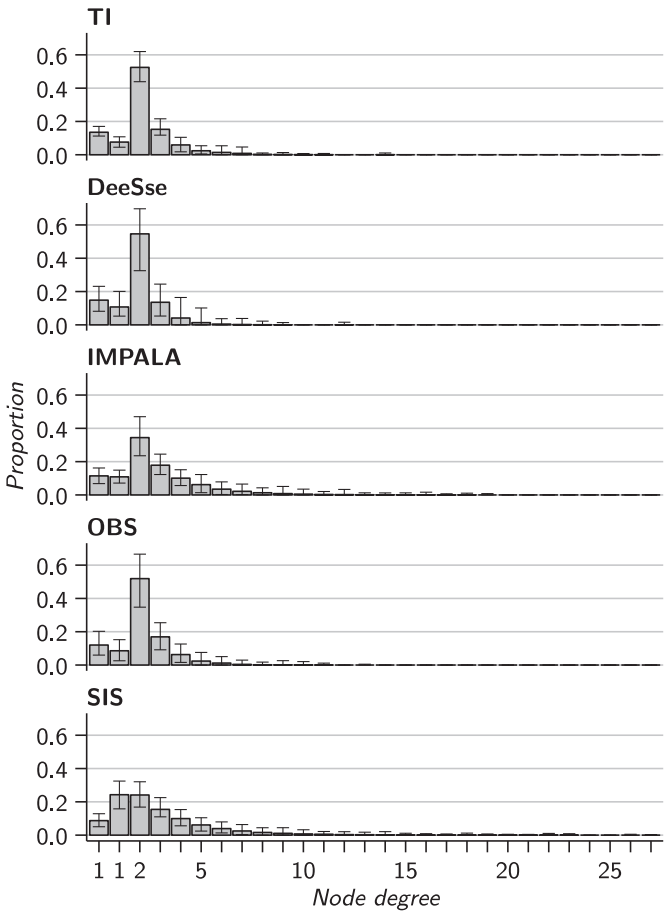

Fig. 15. Mean node degree proportions of the levee skeletons for each category. The error bars display the minimum and maximum proportions. The first node degree 1 corresponds to the nodes of degree one along a grid border. The second node degree 1 corresponds to the nodes of degree one inside the grid.

cators into values easier to analyze. The introduction of a heterogeneous metric gives the opportunity to gather indicators of different types and further improves the method ability to characterize the realization static connectivity. At the end, the dissimilarities distinguish the realizations from different methods and parameter values, but also characterize the static connectivity variability between the realizations of a given method and parameter values.

Adding weights to the indicators in the metric computation means more flexibility for the user. Indeed, not all the indicators are significant to all the applications. For instance with a flow simulation purpose, the unit component proportion is not necessarily significant due to a fewer impact of the unit-volume component on the flow than channels. But such weights remain optional. In the case study, we did not discriminate the indicators with weights, because we wanted to study the information provided by all the indicators on the realizations. Studying the indicator values after the dissimilarities remains essential to better understand the static connectivity of the realizations.

5.3. About the skeletonization method

Skeletons enable to better characterize both the geometry and the topology of connected components. However, the skeletonization method influences both the geometry and the topology of the resulting skeletons. Among all the skeletonization methods, Cornea et al. (2007) distinguish the thinning-based method as the method with the best control on the skeleton connectivity. This section aims at comparing the result of a thinning-based method with the method introduced in Section 2.3 based on slicing the grid and computing the connected components, denoted as the slicing-based method. The slicing-based method used hereafter is the algorithm defined by Lee et al. (1994) and implemented in the geomodeling software Gocad by Barthélemy and Collon-Drouaillet (2013).

The thinning-based method appears to perform better in two dimensions than the slicing-based method. But in three dimensions it tends to generate many small-scale loops (Fig. 18) which perturb both the topology and the geometry of the skeletons. The primary goal of the skeletons is to better characterize the large-scale topology – and possibly the geometry – of the connected components. The skeletons from the thinning-based method seem too perturbed to help in that characterization. The slicing-based method on the other side does not necessarily capture those small-scale elements due to the slice size. A large slice size may not capture the small components or all the component irregularities, but this is compensated in some way by the other indicators, in particular the shape indicators. Moreover, the thinning-based method tends to generate skeletons with many nodes, which are heavy to manipulate. The slicing-based method does not have the same issue when using quite high slice thicknesses. This aspect can be essential when dealing with several hundreds of images.

All this leads to favor the slicing-based method in this work. Some aspects still need to be explored, such as the impact of the slice size. But many more skeletonization methods exist, even if skeletonizing three-dimensional shapes is an open debate. Further

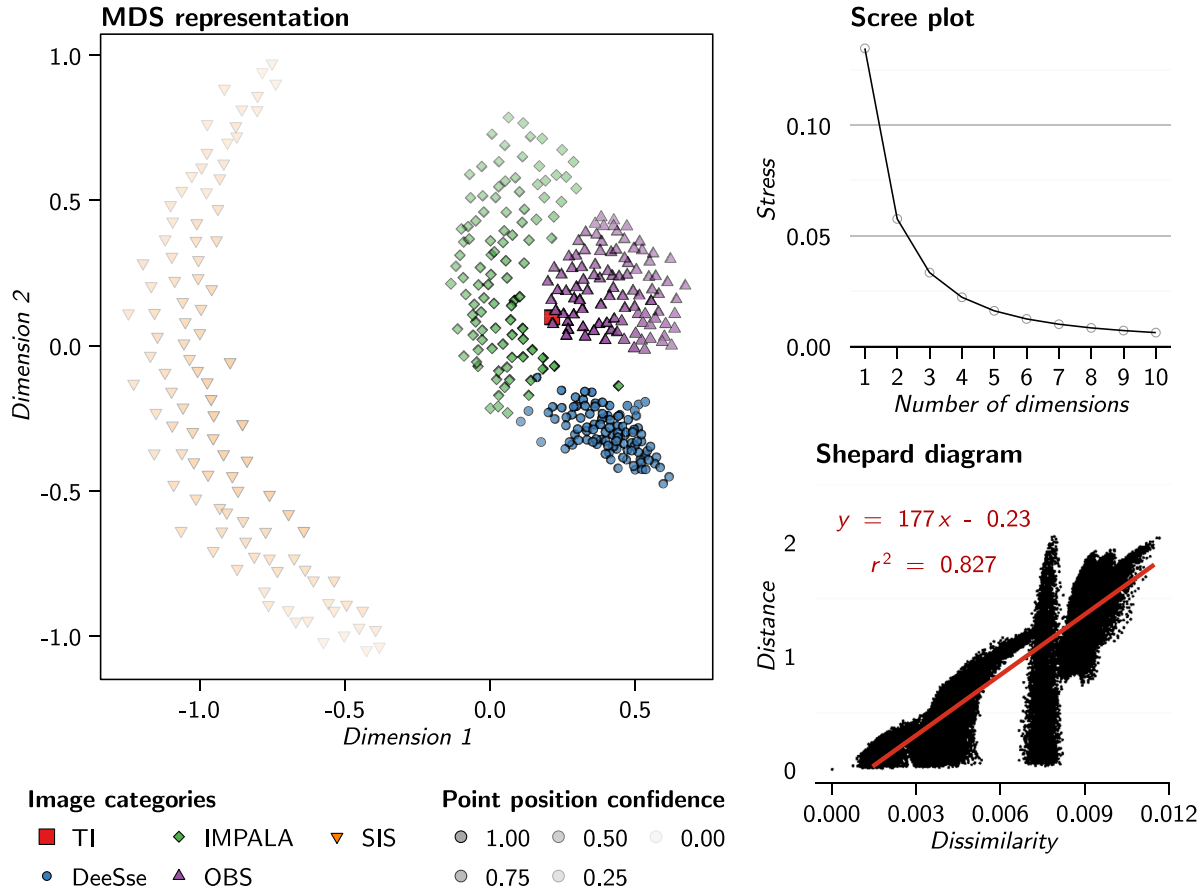

Fig. 16. MDS representation of the dissimilarities between the images of the case study generated using SMACOF and validation graphs. The dissimilarities are based on the multiple-point (MP) histograms of the images. The scree plot only displays the stress values up to 10 dimensions on 400 possible.

work could be done to study other methods and the topology and geometry of resulting skeletons.

5.4. About MDS methods and accuracy

We rely on the Scaling by MAjorizing a COmplicated Function as multidimensional scaling method to represent the dissimilarities. The SMACOF significantly facilitates the dissimilarity analysis. However, the dimensionality reduction makes the MDS representations imprecise, and the distances between the points tend to differ from the dissimilarities.

Thus, the MDS is not a simple visualization tool and can impact the analysis. This can be illustrated by comparing the MDS representation from the classical scaling (Fig. 19) and that from the SMACOF (Fig. 20) to analyze the dissimilarities between the original realizations and the original training image (and not the samples). Normally, the TI should stand from the realizations (see Fig. 7). But the classical scaling puts the TI close from the OBS and IMPALA realizations. Only the point position confidence shows that the TI position is wrong on the representation. The SMACOF representation separates more clearly the TI from the other images.

Moreover, if the global relationships between the realization categories are similar between the two representations, the relative position of the images can be significantly different. This is clear with the TI, but also with other images (Table 3). This appears more largely on the Shepard diagram, with a better coefficient of determination r^2 for the SMACOF than for the classical scaling. The classical scaling tends here to decrease the dissimilarities. As a result, the realization ranking can differ between the dissimilarities and the MDS distance (Table 3). Thus, analyzing the sole MDS representation can lead to erroneous interpretations.

Table 3
Comparison of dissimilarities and distances between the TI and DeeSse realization 12 and 76 for to MDS methods.

Compared images	Dissimilarity	Classical scaling distance	SMACOF distance
TI - DeeSse 12	1.579	0.596	1.414
TI - DeeSse 76	1.358	0.854	1.265
DeeSse 12 - DeeSse 76	0.905	0.259	0.203

The choice of the MDS method is significant, so as the choice of the number of dimensions. We have privileged two-dimensional MDS representations for the sake of visibility, but three-dimensional representations would be worth testing. In any case, the MDS representation should always be cautiously studied and its misrepresentation of the dissimilarities should be kept in mind. From this point of view, the heat map facilitates the analysis of the real dissimilarity values. Analyzing a single row or column of the dissimilarity matrix – so comparing an image with all the others – is as easy to analyze as a MDS representation, but only on a subset of the images.

As the MDS facilitates the dissimilarity analysis, the dissimilarity simply makes the indicator analysis easier. After looking the MDS representation, it is essential to go back to the dissimilarity values to validate the observations. Similarly, studying the indicator values validates the observations and helps to further understand the difference of connectivity between the images.

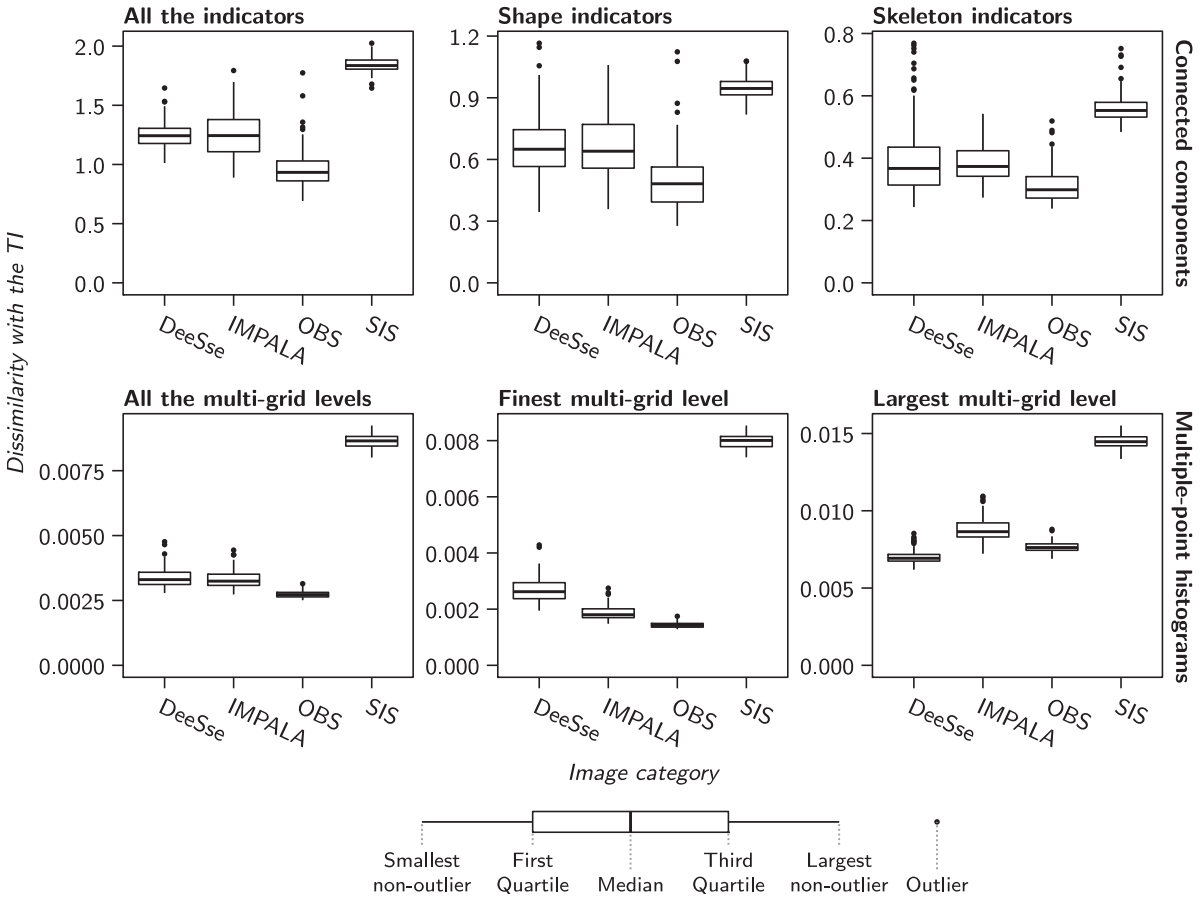

Fig. 17. Box-plots comparing the realizations of each method with the TI. The dissimilarities depend on different indicators in each box-plot. Only the multiple-point histograms compare the original image directly, with one dissimilarity value with the TI per image. The other categories are based on image samples, and have several dissimilarity values with the TI per image. These values are averaged to obtain a single dissimilarity value with the TI.

5.5. Impact of the connected components on the flow

Facies heterogeneity shapes the fluid flow in subsurface. Thus, the petrophysical property simulation, directly correlated to the facies modeling, constitutes a preliminary step to further simulate flows. Being able to assess the static connectivity at the beginning of the workflow could constitute a real advantage in term of resources and time. It is also a way to ensure a better geological consistency, which in itself allows a better integration of field observations and measurements (seismic information, well data, etc.).

It would be interesting to apply the method on more detailed facies models than those of the case study. For instance, both channel and levee deposits are often heterogeneous, regardless of the sedimentary environment, with porous deposits more or less nested between flow barriers (e.g., Hubbard et al., 2011; Hansen et al., 2015). Such flow barriers take the shape of mudstone drapes along the channel margins, of margin failure deposits, of channel abandonment deposits, etc. They can have a significant impact of the fluid flow (e.g., Labourdette et al., 2006; Pranter et al., 2007; Alpak et al., 2013; Issautier et al., 2013) and on the aquifer compartmentalization, with sometimes important consequences when they are ignored (see for instance Gainski et al., 2010, in a oil exploitation context). Our method could clearly help to distinguish between several images from their differences in static connectivity such images including realizations from different methods and/or parameter values or referring models. From this perspective, the case study shows the method ability to identify the simulation methods that produce subsurface models consistent with the static connectivity of a referring model.

Such approach is particularly adapted for fluvial and turbiditic channelized environments where channels tend to form high connectivity corridors, leading to channelized flow path. However, the static connectivity of a sedimentary body is not always representative of the flow behavior. For example, flow channeling can also emerge from non-channelized but highly heterogeneous bodies (e.g., Park et al., 2008; Fiori and Jankovic, 2012). It highlights the dependence of the hydrodynamic connectivity on many parameters: the permeability contrasts between the different media, the internal heterogeneity of each media, etc. Flow simulations then require to assign the petrophysical properties to each facies – usually with geostatistical methods (e.g., Deutsch and Journel, 1992). Our metrics obviously do not anticipate the results of such procedures and, thus, just measure the consistency of the facies simulations in term of static connectivity.

Depending on the studied environment, the reproduction of the static connectivity could be secondary and one could directly work on hydraulic connectivity through the corresponding properties. If reproducing the static connectivity does not guarantee to reproduce the exact hydraulic connectivity, it remains a step toward a better integration of geological information and knowledge in the physical description of the media. Our method provides a simple and objective basis for the comparison of large sets of realizations from this static connectivity point of view.

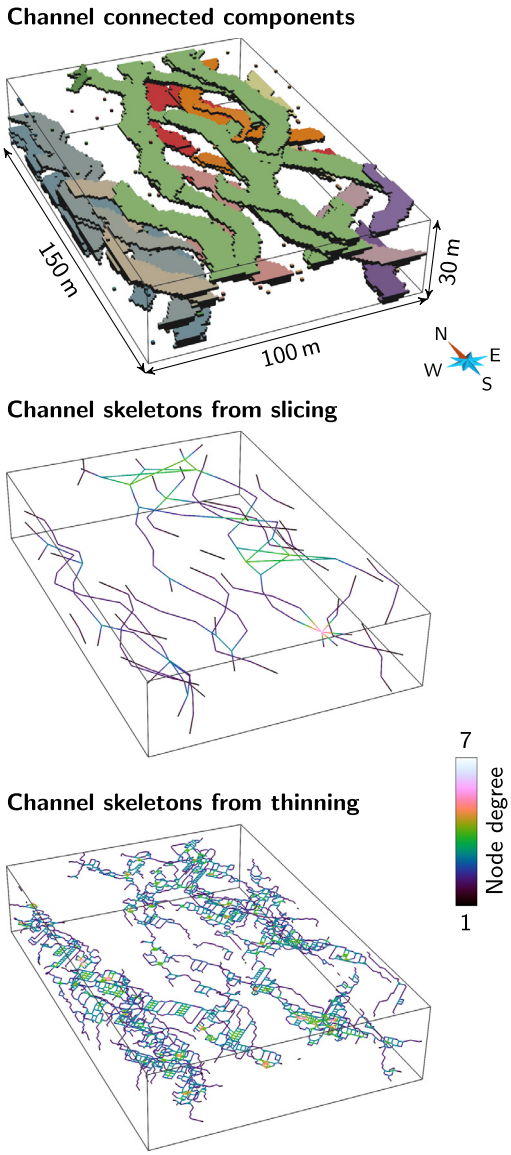

Fig. 18. Skeletons from the channels of the realization DeeSse 30 generated with two methods: the slicing method used in the case study and the thinning method.

6. Conclusions and perspectives

This work develops an analysis process to compare several categorical images in terms of static connectivity. The process relies on the computation of dissimilarities from a given set of indicators. The indicators rely on connected components. They cover various aspect of the realizations, from their facies proportions to the size of their components. Their analysis in the presented case highlights their ability to distinguish between realizations simulated with different methods.

The multidimensional scaling summarizes all this information through low-dimensional representations of the dissimilarities. It is a powerful and practical visualization tool to get a first idea of the relationships between the images. But it should be kept in mind that MDS representations provide only a partial view of the dissimilarities. Moreover, the representation and its quality are method-dependent. The MDS representation should so always be interpreted cautiously. Analyzing the dissimilarity matrix shall always be favored rather than analyzing the MDS representations. The heat map helps to have an easier check on the MDS interpretation. Then an analysis should be done on particular rows or column of the matrix depending on the studied cases. This gives access to simple but powerful visualization tools that work on the real dissimilarities.

A detailed analysis shows the consistency of the indicator behaviors. Indicators of the connected component shape are interesting for their simplicity. But their sensitivity to the grid size is a real issue. A correction is proposed here, but it does not remove completely the error, and analyzing image samples is a better choice. Multiple-point histograms also seem a valid option to analyze more locally the component shape. Skeleton-based indicators appear to be promising. The node degree proportions provide a simple way to compare connectivity structures. Further work should be done on the skeletons to better characterize both the connected component topology and geometry.

Thus, the present work shows that analyzing the behavior of various indicators needs to be continued. More case studies should be considered. Channels are known to have a heterogeneous filling, with shale acting as a flow barrier. It could be interesting to model and work on the component formed by the reservoir facies rather than by the sedimentary objects they belong to. Starting with real data would also be beneficial. If the proposed indicators focus on the static connectivity, an interesting perspective would be to explore their link with the dynamic connectivity.

Acknowledgments

This work was performed in the frame of the RING project at Université de Lorraine. We would like to thank the industrial and academic sponsors of the Gocad Research Consortium managed by ASGA for their support and Paradigm for providing the SKUA-GOCAD software and API. We also thank Sebastien Strebelle for its helpful remarks which influenced this research. We would like to thank the reviewers, including Aldo Fiori, for constructive comments which helped improve this paper.

Appendix A. Detailed definitions of the indicators

The following appendix describes more precisely all the indicators, starting with the indicators computed on the connected components and ending with those computed on the skeletons.

A1. Global indicators

The global indicators do not characterize a particular connected component but an ensemble of connected components. They provide one value per facies.

A1.1. Facies proportion

The facies proportion is of major importance in reservoir modeling considering its influence on porosity and permeability simulation. The proportion p of a facies f is defined as:

$$p_f = \frac{n_f}{n_t} \tag{A.1}$$

with n_f the number of cells of facies f and n_t the total number of cells.

A1.2. Facies adjacency proportion

The adjacency proportion between the facies quantifies the spatial relationships between those facies. The proportion p^a of a facies f adjacent to a facies j is defined as:

$$p^a_{f,j} = \frac{n_{f,j}}{n_{f,t}} \tag{A.2}$$

with $n_{f,j}$ the number of cells of facies f adjacent to the facies j and $n_{f,t}$ the total number of cells of f adjacent to a facies different from f.

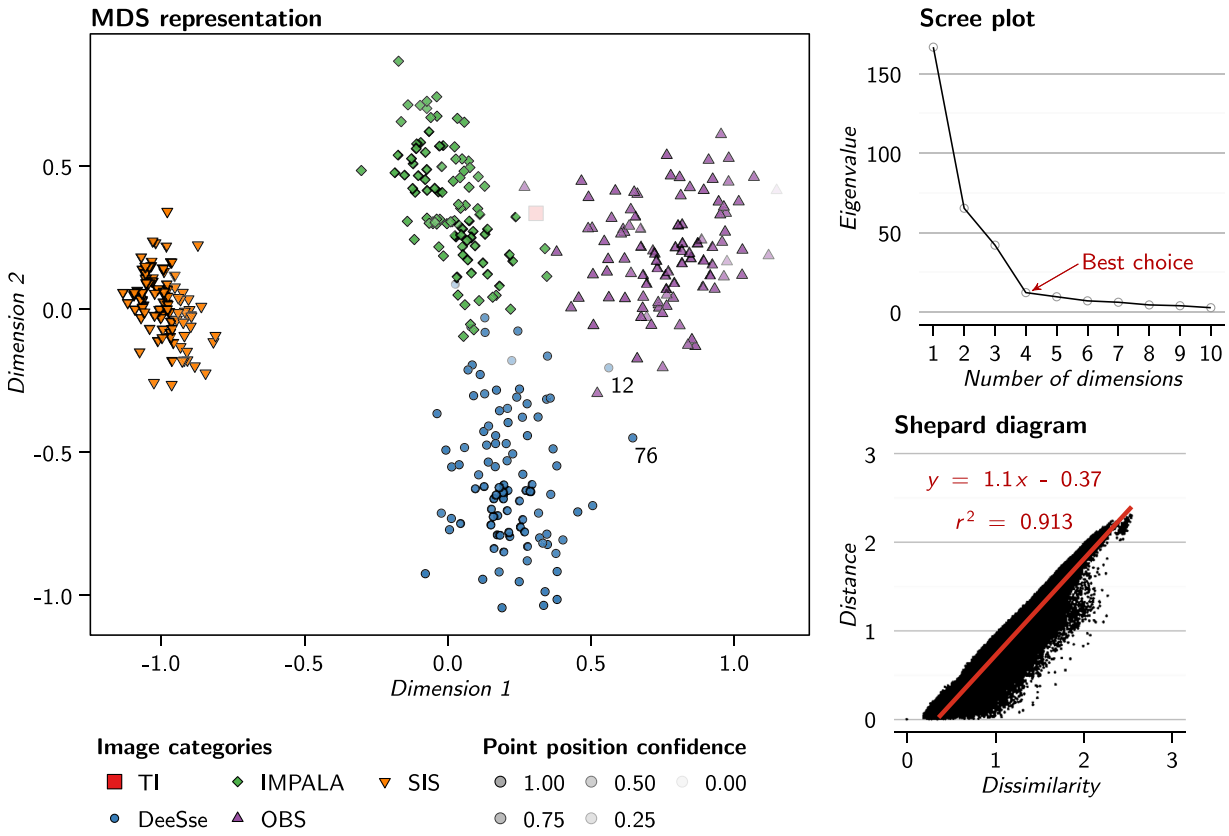

Fig. 19. MDS representation of the dissimilarities between the images of the case study generated using classical scaling and validation graphs. The scree plot only displays the eigenvalues up to 10 dimensions on 400 possible.

A1.3. Facies connection probability

The connection probability Γ quantifies the global connectivity of a given facies f. It is calculated as the proportion of pairs of connected cells among all the pairs of cells of the considered facies (Renard and Allard, 2013):

$$\Gamma_f = \frac{1}{n_f^2} \sum_{i=1}^{N_f} (n_f^i)^2 \tag{A.3}$$

with n_f the total number of cells of facies f, N_f the number of connected components of the facies f and n_f^i the number of cells of the connected component i associated to facies f.

A1.4. Connected component density

The density ϵ of connected components for a facies f expresses the number of components per image cells:

$$\epsilon_f = \frac{N_f}{n_t} \tag{A.4}$$

with N_f the number of connected components of the facies f and n_t the total number of cells.

A1.5. Unit connected component proportion

The unit connected component proportion quantifies the number of connected components constituted by only one cell. The creation of such bodies may correspond to some erroneous and unwanted small scale noise. In that case, it is better to avoid them for the shape indicator computation (see Section A.2). The proportion p^u of unit volume connected components of a facies f is:

$$p_f^u = \frac{N_f^u}{N_f} \tag{A.5}$$

with N_f^u the number of unit volume connected components of the facies f and N_f the number of connected components for the same facies.

A1.6. Traversing connected component proportion

Connected components can have various behaviors against the grid: they can be in the middle of the grid without contact with a border (Fig. 2, connected component 3), along one border, along two adjacent borders (Fig. 2, connected component 2) or traversing the grid completely from one border to the opposite border (Fig. 2, connected component 1). These last components having a main impact on the flow, their reproduction is of prime importance. The proportion p^c of traversing connected components of facies f is defined as the proportion of connected components that connect one border to the opposite one:

$$p_f^c = \frac{N_f^c}{N_f - N_f^u} \tag{A.6}$$

with N_f^c the number of traversing components for the facies f, N_f the total number of components for the facies f and N_f^u the number of unit components for the facies f.

A2. Shape indicators

Shape indicators all give one value per component. The arithmetic mean of those values provides a value of the indicator for a given facies. This makes the indicator comparison easier. The unit-volume connected components (see Section A.1.5) give little information on the shape of the most important connected bodies considering flow circulation: the channels. But they can have a

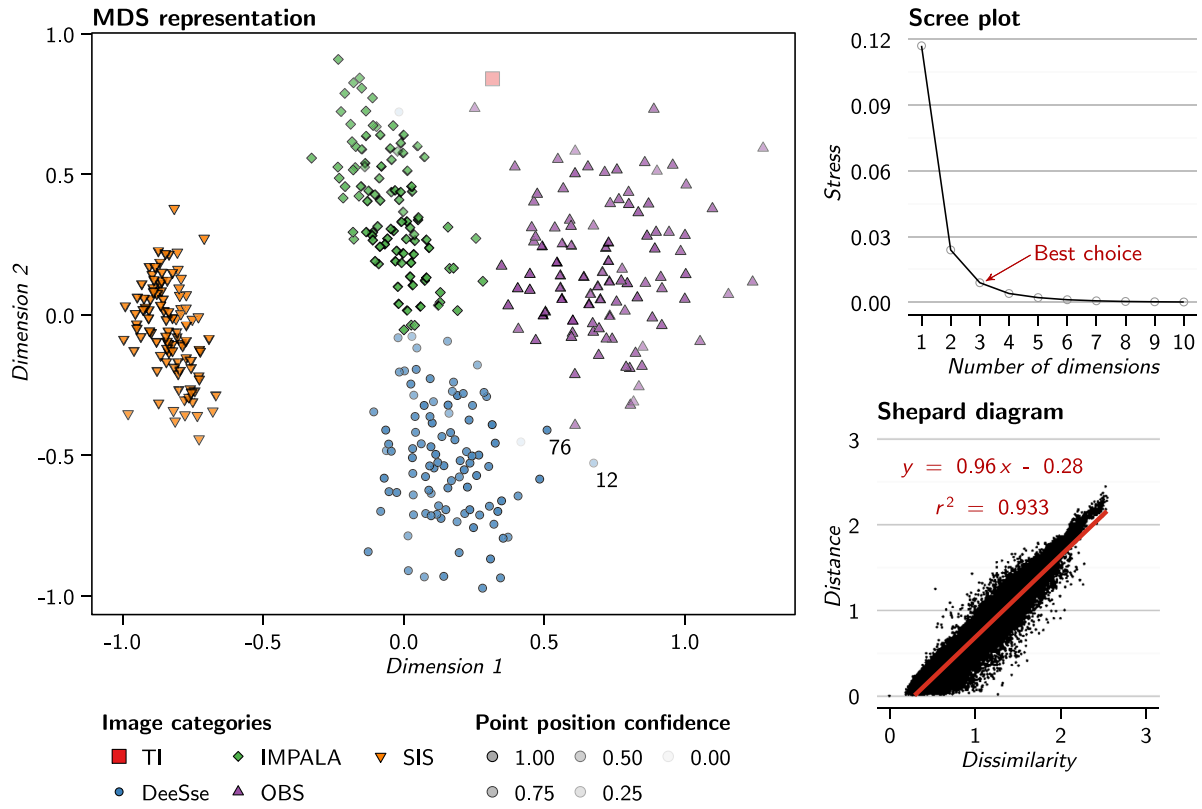

Fig. 20. MDS representation of the dissimilarities between the images of the case study generated using SMACOF and validation graphs. The scree plot only displays the stress values up to 10 dimensions on 400 possible.

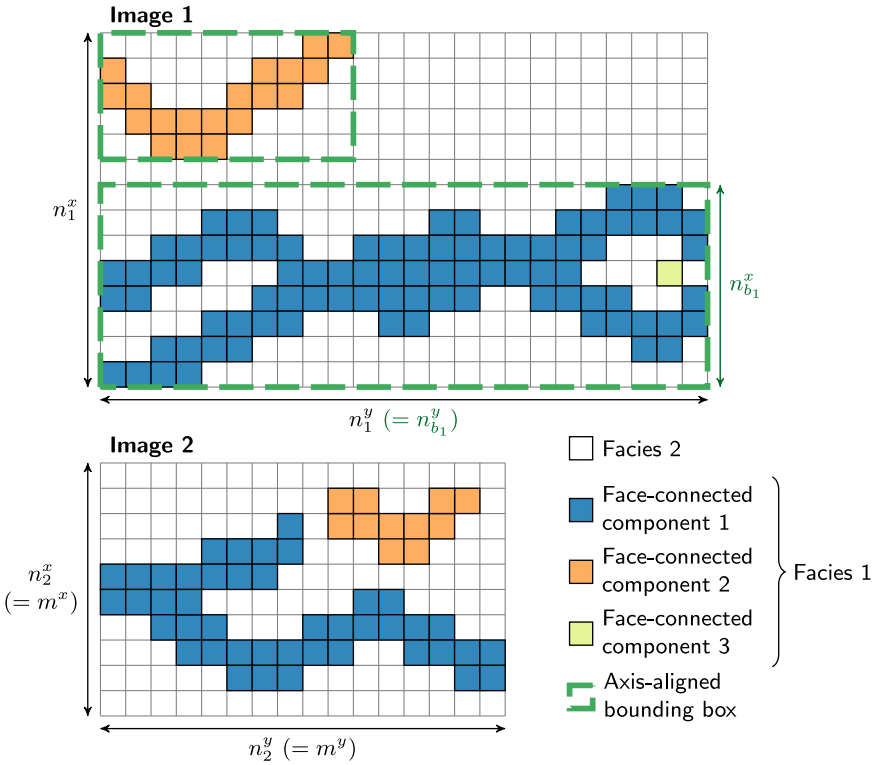

Fig. A.21. Connected components of Fig. 2 represented with their bounding boxes (image 1). Image 2 is another image in a different grid. The two grids have different dimensions along the x axis, which can influence both the number of connected components and the number of grid cells. But they also have different dimensions along the y axis, along which the channels are oriented. Changes along the y axis influence the number of grid cells, but not the number of channels. In that case, the comparison of the density of the two images is biased. The same principle stands for the number of cells of each components. Differences between the number of cells for the component 1 of each image mainly come from the difference in grid dimension along y, not from real differences of connectivity. n_1^x and n_1^y represent the number of cells along the axis x and y for image 1, n_2^x and n_2^y the number of cells along the axis x and y for image 2 and $n_{b_1}^x$ and $n_{b_1}^y$ the number of cells along the axis x and y for the axis-aligned bounding box b of the connected component 1. m^x and m^y are the lower sizes between the two grids for the axis x and y (see Appendix B for more details).

significant influence on the averaged shape indicators (Section A.2). They are so ignored in the average computation.

A2.1. Number of connected component cells

The number of cells n_f^g within a connected component g of a facies f represents the size of a connected component.

A2.2. Box ratio

The box ratio is based on the axis-aligned bounding boxes of the components (Fig. A.21). It is related to the tortuosity of a component and to its orientation relative to the grid axis. The box ratio β of the connected component g of the facies f is expressed between 0 and 1 using the following formula:

$$\beta_f^g = \frac{n_f^g}{n_f^b} \tag{A.7}$$

with n_f^g the number of cells of the connected component g of the facies f and n_f^b the number of cells occupied by its axis-aligned bounding box.

A2.3. Faces/cells ratio

The faces/cells ratio is equivalent to the surface/volume ratio, which compares the surface area of a component with its volume. Deutsch (1998) uses it as a measure of the tortuosity of the components, but it is also affected by their roughness. The faces/cells ratio ζ of the connected component g of the facies f is expressed as:

$$\zeta_f^g = \frac{m_f^g}{n_f^g} \tag{A.8}$$

with m_f^g the number of faces along the surface of the connected component g of the facies f and n_f^g its number of cells.

A2.4. Sphericity

The sphericity ϕ compares the shape of a connected component g for a facies f with a sphere (Wadell, 1935). It ranges between 0 and 1, where 1 corresponds to a sphere, and is expressed as:

$$\phi_f^g = 36\pi \frac{(n_f^g)^2}{(m_f^g)^3} \tag{A.9}$$

with n_f^g the number of cells of the connected component g of the facies f and m_f^g its number of faces along its surface.

A2.5. Skeleton indicators

Skeletons are one-dimensional representations of the connected components, on which measures of geometry and topology are done.

A2.6. Node degree proportion

The node degree proportion is based on the number of segments connected to a given node (Fig. A.22). It is related to the topology of the skeleton and gives access to a deeper study of the connectivity of the structures of interest. The proportion p^n of nodes of degree n over all the skeletons for a given facies f is expressed as:

$$p_f^n = \frac{o_f^n}{o_f} \tag{A.10}$$

with o_f^n the number of nodes of degree n for all the skeletons of the connected components of the facies f and o_f the total number of nodes of the skeletons of the connected components for the facies f. Here we separate into two different classes the nodes of degree one along a border of an image and those in the middle of the image. The first ones relate to component terminations due to the limited size of the image. The other ones may relate to a bad body reproduction, for instance with channels that should be continuous and without dead-ends. The proportions for the different degrees give a histogram of node degrees.

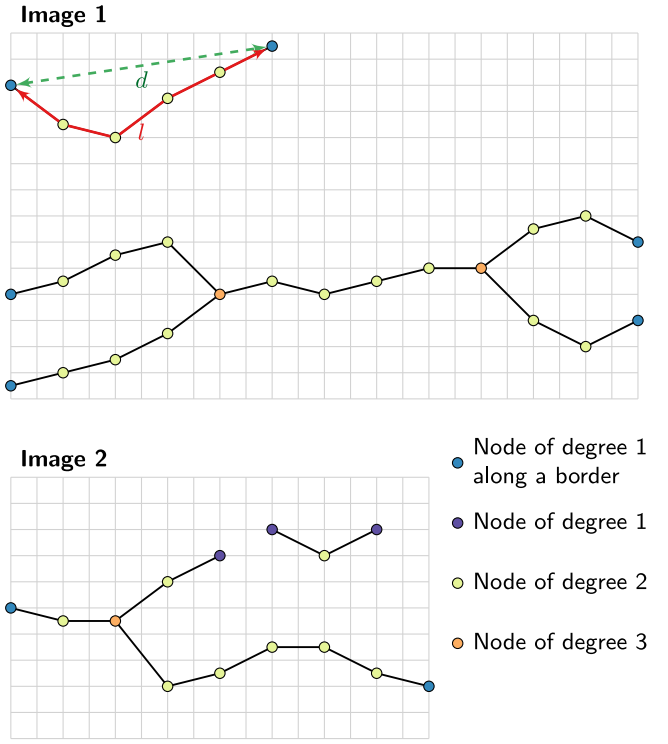

Fig. A.22. Example of skeletons for the connected components of the Fig. A.21. If image 2 has no connection with a degree higher than 3, such as image 1, it displays some dead-ends highlighted by nodes with a degree one in the middle of the grid. This difference emphasize mis-reproductions of the channel connectivity. In image 1, l represents the curvilinear length of the branch and d the distance between its extremities. Those measures are used to compute the tortuosity, which can also differ between the images.

A2.7. Inverse branch tortuosity

A branch is a part of a skeleton defined as an ensemble of segments that link nodes of degree 2 and delimited by two nodes of degree different from 2 (Fig. A.22). The inverse tortuosity t quantifies how twisted a branch b is, with values ranged between 0 and 1. This measure is related to the geometry of the skeleton. It is expressed for a branch b belonging to a skeleton s of a component of a given facies as:

$$t_s^b = \frac{d_s^b}{l_s^b} \tag{A.11}$$

with l_s^b the curvilinear length of the branch b of the skeleton s and d_s^b the Euclidean distance between the two extremity nodes of the same branch. The values for all the branches of all the skeletons related to an image are averaged to obtain one indicator value for that image.

Appendix B. Indicator correction for different grid dimensions

The following appendix describes the corrections applied to the connected component density and the number of component cells when the analysis implies different grid dimensions.

B1. Correction for the connected component density

When some connected components of a facies are traversing (see Section A.1.6), reducing the grid dimension along the component traversing extension can change the component size but not necessarily their number. For instance changing the grid size along the channel orientation does not change the number of channels. But it changes the grid volume and so does the density. Comparing two images of different sizes can affect the density whereas there is nothing wrong about the quality.

To overcome this aspect, the connected component density (formula A.4) is replaced by:

$$\epsilon_f = \frac{N_f}{\vartheta_t} \tag{B.1}$$

with N_f the number of connected components of the facies f and ϑ_t is a corrected number of grid cells corresponding to a mix between the dimensions of each compared images:

$$\vartheta_t = \vartheta^x \times \vartheta^y \times \vartheta^z \tag{B.2}$$

with ϑ^x, ϑ^y and ϑ^z respectively the corrected number of cells along the axis x, y or z. Those corrected numbers of cells are chosen depending on the smallest axis size among all the compared images and the size of the connected components. For an ensemble S of images to be compared, we note m^i the minimal size along the axis i over the images in S:

$$m^i = \min_{s \in S}(n_s^i) \quad i \in \{x, y, z\} \tag{B.3}$$

with n_s^i the number of cells along the axis i for the image s. Determining the corrected numbers of axis cells for a given image r of S depends on the size of its connected components:

$$\vartheta^i = \begin{cases} m^i \text{ if } \exists\, g \in r,\ n_g^i \geq m^i \\ n_r^i \text{ otherwise} \end{cases} \quad i \in \{x, y, z\} \tag{B.4}$$

with g a connected component of r, n_r^i the number of cells along the axis i for the image r and n_g^i the number of cells along the axis i for the component g.

For instance in (Fig. A.21), the component 1 of image 1 is larger than image 2 along the y axis. On the other hand, no component of that facies is larger than image 2 along the other axes. The corrected volumes for the image 1 $\vartheta_{t,1}$ and for the image 2 $\vartheta_{t,2}$ are so:

$$\begin{aligned} \vartheta_{t,1} &= n_1^x \times n_2^y \times n_1^z \\ \vartheta_{t,2} &= n_2^x \times n_2^y \times n_2^z \end{aligned} \tag{B.5}$$

with n_1^x, n_1^y and n_1^z the number of cells along the axis x, y and z for image 1 and n_2^x, n_2^y and n_2^z the number of cells along the axis x, y and z for image 2. Image 1 is so considered as truncated to limit the effect of the traversing bodies on the density.

B2. Correction of the number of connected component cells

The objects are expected to have roughly the same range of sizes in all the images. But this expectation is no longer relevant in the case of traversing structures (see Section A.1.6), whose dimensions must vary following the size of the supporting grid. As for the connected geobody density, the possible difference of image sizes imposes to rescale the number of cells of a connected component.

The rescaling is based on the estimation of the component bounding box size if this component was transfered within the grid of the smallest size. That bounding box size can be defined following a number of cells ϑ_b:

$$\vartheta_b = \vartheta^x \times \vartheta^y \times \vartheta^z \tag{B.6}$$

with ϑ^x, ϑ^y and ϑ^z respectively the corrected numbers of cells of the bounding box along the axis x, y or z. Those corrected numbers of cells are following the same principles as to find the corrected number of cells for the density. Determining the corrected numbers of axis cells requires the same parameter m^i (formula B.3):

$$\vartheta^i = \begin{cases} m^i \text{ if } n_b^i \geq m^i \\ n_b^i \text{ otherwise} \end{cases} \quad i \in \{x, y, z\} \tag{B.7}$$

with n_b^i the number of cells along the axis i for the bounding box of the component. Finally the corrected number of cells ϑ_f^g for the component g of the facies f is proportional to the ratio between the number of cells of its corrected bounding box ϑ_b and the number of cells of its actual bounding box n_b:

$$\vartheta_f^g = n_f^g \times \frac{\vartheta_b}{n_b} \tag{B.8}$$

For instance the component 1 on image 1 of Fig. A.21 has a corrected number of cells ϑ_1 of:

$$\vartheta_1 = n_1 \times \frac{n_{b_1}^x \times n_2^y \times n_{b_1}^z}{n_{b_1}^x \times n_{b_1}^y \times n_{b_1}^z} = n_1 \times \frac{n_2^y}{n_{b_1}^y} \tag{B.9}$$

with n_1 the number of cells of component 1, $n_{b_1}^x$, $n_{b_1}^y$ and $n_{b_1}^z$ the numbers of cells of its axis-aligned bounding box along the axis x, y or z and n_2^x, n_2^y and n_2^z the numbers of cells of image 2 along the axis x, y or z. This reflects the impossibility to make that component fit into image 2. Its size needs so to be rescaled to be compared with objects of image 2.

Appendix C. Simulation parameters for the realizations

Table C.4
Parameters used to simulate the channelized environment with DeeSse.

Parameters	Values
Maximum number of neighbors	64
Acceptance threshold	0.05
Maximal scan fraction of the TI	0.33

Table C.5
Parameters used to simulate the channelized environment with IMPALA.

Parameters	Values
Number of multi-grids	4
Number of multi-grid levels in each direction	4 × 4 × 1
Search template type	Elliptic
Size of the search template (radii in m)	7 × 7 × 4
Maximal number of neighbors in the template	64

Table C.6
Parameters used to simulate the channelized environment with the object-based method of Petrel. The distributions used are all triangular.

Simulation parameters	Min	Mode	Max
Channels			
Proportion (in %)	21.21	21.21	21.21
Orientation (in °)	0	0	0
Amplitude (in m)	10	15	40
Wavelength (in m)	60	70	100
Width (in m)	7	10	13
Thickness (in m)	1.5	2	4
Levees			
Proportion (in %)	8.79	8.79	8.79
Width (in m)	4	7	11
Thickness (relative to channel thickness)	0.25	0.35	0.6

Table C.7
Variogram parameters used to simulate the channelized environment with SIS.

Variogram parameters	Channels	Levees	Mudstone environment
Azimuth (in °)	0	0	0
Dip (in °)	0	0	0
Sill	0.145	0.109	0.210
Nugget	0	0	0
Range 1 (in m)	23	26	70
Range 2 (in m)	12	14	34
Range 3 (in m)	3	1	2.5
Type	Spherical	Exponential	Exponential

References

Alpak, F.O., Barton, M.D., Naruk, S.J., 2013. The impact of fine-scale turbidite channel architecture on deep-water reservoir performance. AAPG Bull. 97 (2), 251–284. http://dx.doi.org/10.1306/04021211067.

Barthélemy, C., Collon-Drouaillet, P., 2013. Simulation of Anastomotic Karst networks. In: Proc. 32nd Gocad Meeting. Nancy, p. 13.

Boisvert, J.B., Pyrcz, M.J., Deutsch, C.V., 2010. Multiple point metrics to assess categorical variable models. Nat. Resour. Res. 19 (3), 165–175. http://dx.doi.org/10.1007/s11053-010-9120-2.

Brandt, J.W., Algazi, V.R., 1992. Continuous skeleton computation by Voronoi diagram. CVGIP 55 (3), 329–338. http://dx.doi.org/10.1016/1049-9660(92)90030-7.

Comunian, A., Renard, P., Straubhaar, J., 2012. 3D multiple-point statistics simulation using 2D training images. Comput. Geoscie. 40 (0), 49–65. http://dx.doi.org/10.1016/j.cageo.2011.07.009.

Cornea, N.D., Silver, D., Min, P., 2007. Curve-skeleton properties, applications, and algorithms. Visual. Comput. Graph. IEEE Trans. 13 (3), 530–548. http://dx.doi.org/10.1109/TVCG.2007.1002.

Cox, T.F., Cox, M.A., 1994. Multidimensional Scaling. Chapman and Hall, London.

De Iaco, S., 2013. On the use of different metrics for assessing complex pattern reproductions. J. Appl. Stat. 40 (4), 808–822. http://dx.doi.org/10.1080/02664763.2012.754853.

De Iaco, S., Maggio, S., 2011. Validation Techniques for geological patterns simulations based on Variogram and multiple-point statistics. Mathe. Geoscie. 43 (4), 483–500. http://dx.doi.org/10.1007/s11004-011-9326-9.

De Leeuw, J., 1977. Applications of convex analysis to multidimensional scaling. In: Barra, J.R., Brodeau, F., Romier, G., Van Cutsem, B. (Eds.), Recent Developments in Statistics. North holland publishing company, Amsterdam, pp. 133–146.

De Leeuw, J., Heiser, W.J., 1977. Convergence of correction matrix algorithms for multidimensional scaling. In: Geometric Representations of Relational Data, pp. 735–752.

De Leeuw, J., Heiser, W.J., 1980. Multidimensional scaling with restrictions on the configuration. Multivar. Anal. 5, 501–522.

De Leeuw, J., Mair, P., 2009. Multidimensional scaling using majorization: SMACOF in R. J. Stat. Softw. 31 (3), 1–30.

Deutsch, C., Tran, T., 2002. FLUVSIM: a program for object-based stochastic modeling of fluvial depositional systems. Comput. Geosci. 28 (4), 525–535. http://dx.doi.org/10.1016/S0098-3004(01)00075-9.

Deutsch, C.V., 1998. Fortran programs for calculating connectivity of three-dimensional numerical models and for ranking multiple realizations. Comput. Geosci. 24 (1), 69–76. http://dx.doi.org/10.1016/S0098-3004(97)00085-X.

Deutsch, C.V., Hewett, T.A., 1996. Challenges in reservoir forecasting. Math. Geol. 28 (7), 829–842. http://dx.doi.org/10.1007/BF02066003.

Deutsch, C.V., Journel, A.G., 1992. GSLIB: Geostatistical Software Library and User's Guide. Oxford University Press, New York.

Fiori, A., Jankovic, I., 2012. On preferential flow, channeling and connectivity in heterogeneous porous formations. Math. Geosciences 44 (2), 133–145. http://dx.doi.org/10.1007/s11004-011-9365-2.

Gainski, M., MacGregor, A.G., Freeman, P.J., Nieuwland, H.F., 2010. Turbidite reservoir compartmentalization and well targeting with 4D seismic and production data: Schiehallion Field, UK. Geological Society, London, Special Publications 347 (1), 89–102. http://dx.doi.org/10.1144/SP347.7.

Galli, A., Beucher, H., Loc'h, G.L., Doligez, B., Group, H., 1994. The Pros and Cons of the Truncated Gaussian Method. In: Armstrong, M., Dowd, P.A. (Eds.), Geostatistical Simulations. In: Quantitative Geology and Geostatistics. Springer Netherlands, pp. 217–233. http://dx.doi.org/10.1007/978-94-015-8267-4_18.

Gómez-Hernández, J., Wen, X.-H., 1998. To be or not to be multi-Gaussian? A reflection on stochastic hydrogeology. Adv. Water Resour. 21 (1), 47–61. http://dx.doi.org/10.1016/S0309-1708(96)00031-0.

Gower, J.C., 1966. Some distance properties of latent root and vector methods used in multivariate analysis. Biometrika 53 (3-4), 325–338. http://dx.doi.org/10.1093/biomet/53.3-4.325.

Guardiano, F.B., Srivastava, R.M., 1993. Multivariate Geostatistics: Beyond Bivariate Moments. In: Soares, A. (Ed.), Geostatistics Tróia '92. In: Quantitative Geology and Geostatistics. Springer Netherlands, pp. 133–144.

Hansen, L.A.S., Callow, R.H.T., Kane, I.A., Gamberi, F., Rovere, M., Cronin, B.T., Kneller, B.C., 2015. Genesis and character of thin-bedded turbidites associated with submarine channels. Marine Petrol. Geol. 67, 852–879. http://dx.doi.org/10.1016/j.marpetgeo.2015.06.007.

Hubbard, S.M., Smith, D.G., Nielsen, H., Leckie, D.A., Fustic, M., Spencer, R.J., Bloom, L., 2011. Seismic geomorphology and sedimentology of a tidally influenced river deposit, Lower Cretaceous Athabasca oil sands, Alberta, Canada. AAPG Bull. 95 (7), 1123–1145.

Issautier, B., Fillacier, S., Le Gallo, Y., Audigane, P., Chiaberge, C., Viseur, S., 2013. Modelling of CO_2 injection in fluvial sedimentary heterogeneous reservoirs to assess the impact of geological heterogeneities on CO_2 storage capacity and performance. Energy Proc. 37, 5181–5190. http://dx.doi.org/10.1016/j.egypro.2013.06.434.

Jain, A.K., 1989. Fundamentals of Digital Image Processing, vol. 3. Prentice-Hall Englewood Cliffs.

Journel, A., Alabert, F., 1990. New method for reservoir mapping. J. Petrol. Technol. 42 (2), 212–218. http://dx.doi.org/10.2118/18324-PA.

Journel, A.G., 2004. Beyond covariance: the advent of multiple-point geostatistics. In: Geostatistics Banff 2004, pp. 225–233.

King, M., Mark, M., 1999. Flow Simulation of Geologic Models. SPE Reserv. Eval. Eng. 2 (4), 351–367. http://dx.doi.org/10.2118/57469-PA.

Labourdette, R., Poncet, J., Seguin, J., Temple, F., Hegre, J., Irving, A., 2006. Three-dimensional modelling of stacked turbidite channels in West Africa: impact on dynamic reservoir simulations. Petrol. Geosci. 12 (4), 335–345. http://dx.doi.org/10.1144/1354-079306-705.

Lee, T.C., Kashyap, R.L., Chu, C.N., 1994. Building Skeleton Models via 3-D Medial Surface Axis Thinning Algorithms. CVGIP 56 (6), 462–478. http://dx.doi.org/10.1006/cgip.1994.1042.

Lin, J., 1991. Divergence measures based on the Shannon entropy. Inf. Theory IEEE Trans. 37 (1), 145–151. http://dx.doi.org/10.1109/18.61115.

Lopez, S., 2003. Modélisation de Réservoirs Chenalisés Méandriformes : Une Approche Génétique et Stochastique. Ph.D. thesis. Ecole Nationale Supérieure des Mines de Paris.

Mariethoz, G., 2009. Geological Stochastic Imaging for Aquifer Characterization. Université de Neuchâtel Ph.D. thesis.

Mariethoz, G., Renard, P., Straubhaar, J., 2010. The direct sampling method to perform multiple-point geostatistical simulations. Water Resour. Res. 46 (11), W11536. http://dx.doi.org/10.1029/2008WR007621.

Meerschman, E., Pirot, G., Mariethoz, G., Straubhaar, J., Meirvenne, M.V., Renard, P., 2012. A practical guide to performing multiple-point statistical simulations with the direct sampling algorithm. Comput. Geosc. 52, 307–324. http://dx.doi.org/10.1016/j.cageo.2012.09.019.

Oriani, F., Renard, P., 2014. Binary upscaling on complex heterogeneities: the role of geometry and connectivity. Adv. Water Resour. 64, 47–61. http://dx.doi.org/10.1016/j.advwatres.2013.12.003.

Paradigm, 2015. SKUA® Software Suite by Paradigm®. http://www.pdgm.com/products/skua-gocad/

Park, C.-H., Beyer, C., Bauer, S., Kolditz, O., 2008. A study of preferential flow in heterogeneous media using random walk particle tracking. Geosci. J. 12 (3), 285–297. http://dx.doi.org/10.1007/s12303-008-0029-2.

Pranter, M.J., Ellison, A.I., Cole, R.D., Patterson, P.E., 2007. Analysis and modeling of intermediate-scale reservoir heterogeneity based on a fluvial point-bar outcrop analog, Williams Fork Formation, Piceance Basin, Colorado. AAPG Bull. 91 (7), 1025–1051. http://dx.doi.org/10.1306/02010706102.

Pyrcz, M., Boisvert, J., Deutsch, C., 2009. ALLUVSIM: a program for event-based stochastic modeling of fluvial depositional systems. Comput. Geosci. 35 (8), 1671–1685. http://dx.doi.org/10.1016/j.cageo.2008.09.012.

R Core Team, 2012. R: A Language and Environment for Statistical Computing. R Foundation for Statistical Computing, Vienna, Austria.

Rao, C.R., 1987. Differential metrics in probability spaces. In: Differential Geometry in Statistical Inference, 10, pp. 217–240. http://dx.doi.org/10.1214/lnms/1215467062.

Renard, P., Allard, D., 2013. Connectivity metrics for subsurface flow and transport. Adv. Water Resour. 51, 168–196. http://dx.doi.org/10.1016/j.advwatres.2011.12.001.

Scheidt, C., Caers, J., 2009. Representing spatial uncertainty using distances and kernels. Math. Geosci. 41 (4), 397–419. http://dx.doi.org/10.1007/s11004-008-9186-0.

Schlumberger, 2015. Petrel E&p Software Platform. http://www.software.slb.com/products/platform/Pages/petrel.aspx

Serra, J., 1983. Image Analysis and Mathematical Morphology. Academic Press, Inc., Orlando, FL, USA.

Shepard, R.N., 1962. The analysis of proximities: Multidimensional scaling with an unknown distance function. I.. Psychometrika 27 (2), 125–140. http://dx.doi.org/10.1007/BF02289630.

Shepard, R.N., 1962. The analysis of proximities: multidimensional scaling with an unknown distance function. II. Psychometrika 27 (3), 219–246. http://dx.doi.org/10.1007/BF02289621.

Shtuka, A., Samson, P., Mallet, J.L., 1996. Petrophysical simulation within an object-based reservoir model. In: European 3-D reservoir modelling conference, pp. 47–56.

Straubhaar, J., 2011. MPDS Technical Reference Guide. Technical Report. Centre d'hydrogéologie et géothermie, University of Neuchâtel, Neuchâtel.

Straubhaar, J., Renard, P., Mariethoz, G., Froidevaux, R., Besson, O., 2011. An improved parallel multiple-point algorithm using a list approach. Math. Geosci. 43 (3), 305–328. http://dx.doi.org/10.1007/s11004-011-9328-7.

Straubhaar, J., Walgenwitz, A., Renard, P., 2013. Parallel multiple-point statistics algorithm based on list and tree structures. Math. Geosci. 45, 131–147. http://dx.doi.org/10.1007/s11004-012-9437-y.

Strebelle, S., 2002. Conditional simulation of complex geological structures using multiple-point statistics. Mathe. Geol. 34 (1), 1–21. http://dx.doi.org/10.1023/A:1014009426274.

Tahmasebi, P., Hezarkhani, A., Sahimi, M., 2012. Multiple-point geostatistical modeling based on the cross-correlation functions. Comput. Geosci. 16 (3), 779–797. http://dx.doi.org/10.1007/s10596-012-9287-1.

Tan, X., Tahmasebi, P., Caers, J., 2014. Comparing Training-Image based algorithms using an analysis of distance. Mathe. Geosci. 46 (2), 149–169. http://dx.doi.org/10.1007/s11004-013-9482-1.

Torgerson, W.S., 1952. Multidimensional scaling: I. Theory and method. Psychometrika 17 (4), 401–419. http://dx.doi.org/10.1007/BF02288916.

Torgerson, W.S., 1958. Theory and Methods of Scaling. John Wiley & Sons, New York.

Tran, T.T., 1994. Improving variogram reproduction on dense simulation grids. Comput. Geosci. 20 (7), 1161–1168. http://dx.doi.org/10.1016/0098-3004(94)90069-8.

Viseur, S., 2001. Simulation Stochastique Basée-Objet de Chenaux. Institut National Polytechnique de Lorraine, Vandoeuvre-lès-Nancy, France Ph.D. thesis.

Wadell, H., 1935. Volume, shape, and roundness of quartz particles. J. Geol. 250–280.

Western, A.W., Blöschl, G., Grayson, R.B., 2001. Toward capturing hydrologically significant connectivity in spatial patterns. Water Resour. Res. 37 (1), 83–97. http://dx.doi.org/10.1029/2000WR900241.

Wickham, H., 2009. GGPLOT2: Elegant Graphics for Data Analysis. Springer.

Wilson, D.R., Martinez, T.R., 1997. Improved heterogeneous distance functions. J. Artif. Intell. Res. 6, 1–34. http://dx.doi.org/10.1613/jair.346.

Yin, Y., Wu, S., Zhang, C., Li, S., Yin, T., 2009. A reservoir skeleton-based multiple point geostatistics method. Sci. China Ser. D 52 (1), 171–178. http://dx.doi.org/10.1007/s11430-009-5004-x.

Computers & Geosciences 77 (2015) 29–43

Contents lists available at ScienceDirect

Computers & Geosciences

journal homepage: www.elsevier.com/locate/cageo

3D geomodelling combining implicit surfaces and Voronoi-based remeshing: A case study in the Lorraine Coal Basin (France)

Pauline Collon [a,*], Wendy Steckiewicz-Laurent [a,b], Jeanne Pellerin [a], Gautier Laurent [a,1], Guillaume Caumon [a], Guillaume Reichart [a,b], Laurent Vaute [b]

[a] GeoRessources UMR7359, Université de Lorraine, CNRS, CREGU, ENSG, 2 rue du doyen Marcel Roubault, TSA 70605, 54518 Vandœuvre-lès-Nancy Cedex, France

[b] BRGM, 1 avenue du Parc de Brabois, 54500 Vandoeuvre-lès-Nancy, France

ARTICLE INFO

Article history:
Received 12 August 2014
Received in revised form
15 October 2014
Accepted 15 January 2015
Available online 16 January 2015

Keywords:
Geomodelling
3D surface-based model
Implicit modelling
Surface remeshing
Post-mining
Geothermics

ABSTRACT

In this paper we demonstrate how recent geomodelling techniques can be combined and used to build a 3D geological model on a real case study: the former coal mine of Merlebach (France), that is targeted to be exploited for low-temperature geothermal energy production. From geological maps, cross-sections, borehole and mine exploitation data, we build a 3D model in which are identified the rocks and infrastructures having significantly different permeabilities. First, a structural model of the main geological interfaces in our area of interest (2 horizons and 13 faults) is built with classical geomodelling techniques. Then, we propose to model by surfaces the 71 irregularly stacked, very close and very thin, sub-vertical coal beds. To ease their construction, we use an implicit method which represents 3D surfaces as isovalues of a scalar field defined in a 3D tetrahedral grid of the area. The corresponding triangulated surfaces are remeshed with a recently proposed method based on Voronoi diagrams so that the exploited parts of the coal beds, now filled by sand, can be computed. The 3D surface-based geological model, in which infrastructures can be inserted as piecewise lines, can be volumetrically meshed. It is available for download as supplemental material, as well as a volumetric grid.

1. Introduction

Lorraine has been one of the most important regions of coal extraction in France until the closure of the last coal mine, La Houve, in 2004. Unlike the neighbouring Lorraine Iron Basin where the impact of mine flooding on water quality is studied for water supply concerns (e.g. Collon et al., 2005, 2006; Hamm et al., 2008), the great depth (up to 1.5 km) and the favourable local geothermal gradient (around 3.5 °C/100 m) in the Lorraine Coal Basin make it a potential resource of low-temperature geothermal energy. Preliminary investigations were carried out by Hamm and Bazargan Sabet (2010), who identified the area of the Merlebach mine, centred around the *Vouters 2* mineshaft (Fig. 1), as the most suitable place for a future full-scale demonstration facility. As suggested by Renz et al. (2009), Hamm and Bazargan Sabet (2010) realised a simplified model of the Merlebach mine to investigate the geothermal potential of the site. Their encouraging results have demonstrated that the heat production capacity would not only depend on the well locations and production rates, but also highly on the rock permeabilities and on the geometry of the underground structures. Thus, modelling the hydraulic and thermal behaviour of the targeted geothermal site is crucial for a reliable evaluation of different exploitation scenarios.

For this purpose, we built a volumetric 3D model of the Merlebach mine. 3D geomodelling of formerly mined areas is a challenging task as data are often scattered, in various formats and the objects to represent are numerous and variable in shape and size (e.g. Li et al., 2013; Kaufmann and Martin, 2008). Our model should distinguish the different types of rock encountered in the former mine so that the permeability field, that drives groundwater flow, can be correctly modelled. So, it must take account for the main mine infrastructures (galleries, mineshafts and ramps), for the surrounding formations and for the faults. The modelling of the coal beds is particularly challenging as they are sub-vertical, very thin (around 5 m thick), and irregularly stacked on a thickness of 1.8 km. Classical geomodelling methods (Caumon et al., 2009) would imply to explicitly build each of these surfaces individually while ensuring that they do not intersect. To overcome this particularly difficult task, we used recent geomodelling techniques: an implicit modelling approach (Frank et al., 2007; Caumon et al., 2013) and a geological surface remeshing (Pellerin

* Corresponding author.
[1] Now at: School of Earth, Atmosphere and Environment, Monash University, PO Box 28E, Victoria, Australia.

http://dx.doi.org/10.1016/j.cageo.2015.01.009
0098-3004/

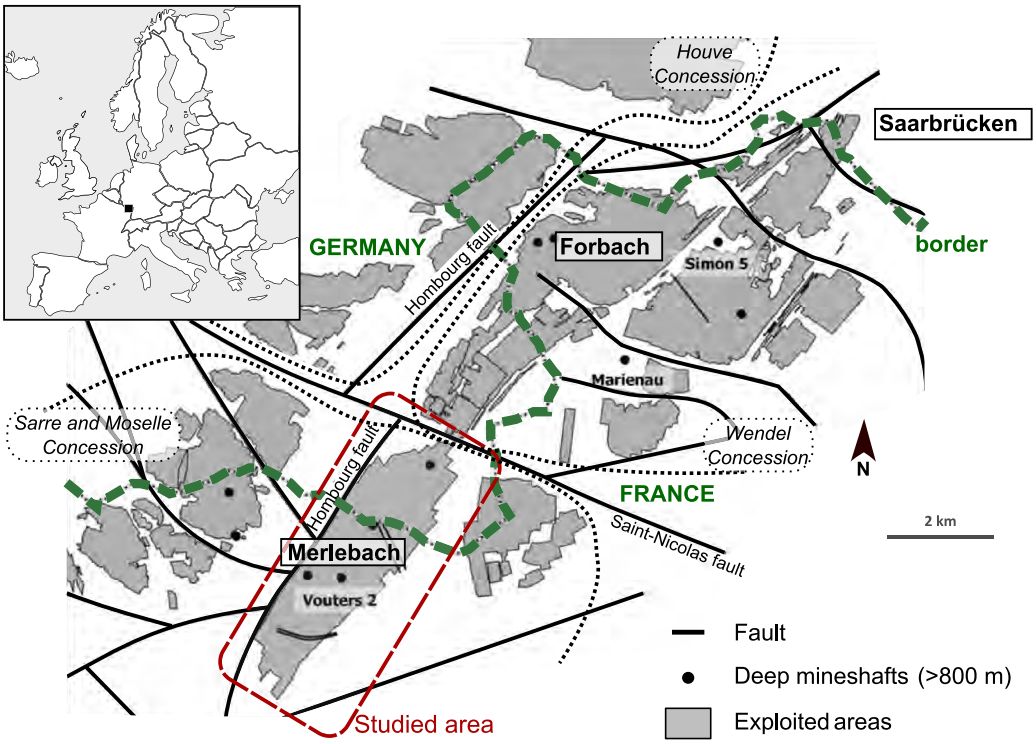

Fig. 1. Location of the Lorraine Coal Basin and map of the exploited areas. The studied zone of the Merlebach mine is surrounded by several faults, among which the Saint-Nicolas fault in the north and the Hombourg fault in the west. This map was realised with data provided by Charbonnage de France.

et al., 2014).

The available data were first processed and imported into the software (Section 3.1). The adopted strategy to model the different objects is presented in Section 3.2. First, we built a model of the interfaces between the different rock lithologies in our zone of interest (faults, horizons, topography) (Section 3.3). Second, the surfaces corresponding to the 71 coal beds referenced in the mine and the digitised infrastructures were added to this structural model (Section 3.4). Third, the resulting surface-based model was finally rasterised to obtain a 3D regular Cartesian grid in which exploited coal, unexploited coal, infrastructures, and surrounding formations are identified. This grid has less than 135 million cells, the maximum number allowed by the groundwater modelling software (MARTHE[2]) chosen to simulate flows in the continuity of the work of Hamm and Bazargan Sabet (2010). We discuss the workflow in Section 4.

2. Settings

2.1. Geological settings

The Lorraine Coal Basin (LCB), 140 km by 70–80 km, is located in the Moselle department, in the east of France, on the edge of the Paris basin (Fig. 1). It starts 30 km north of Metz and extends toward the north across the Franco-German border. The exploitation, that concerned the shallowest north-eastern part of the basin, has been subdivided into three sectors: (i) the Wendel concession, (ii) the Houve concession, and (iii) the Sarre and Moselle concession. The Merlebach mine is part of the Sarre and Moselle concession. The studied area has an extension of about 7.5 km by 2.2 km (Fig. 1).

The LCB is an intra-mountain coal depression formed during the Hercynian Orogeny between Carboniferous and Permian (Donsimoni, 1981) and interpreted as a strike-slip basin (Korsch and Schäfer, 1995; Izart et al., 2005). This context has favoured organic matter-rich clastic deposits. The anaerobic decomposition of organic matter in water has produced the coal bearing deposits of the Westphalian and Stephanian age (Carboniferous – equivalent of the Pennsylvanian age in ICS-stage) (e.g. Izart et al., 2005). They consist of intercalated beds in a complex sequence of claystones, sandstones, and conglomerates that show lateral variations both in terms of nature and thickness. Coal beds generally have a thickness between a few centimetres and 5 m, reaching exceptionally 15 m. The late Hercynian compression (Saalian phase) has affected all deposits inducing the formation of a North-East/South-West, asymmetrical, and overturned anticline and of numerous faults (Donsimoni, 1981; Fleck et al., 2001; Barchi et al., 2008; Cartannaz, 2008). The most important faults bind mining zones, as the NE/SW Hombourg fault and the W-NW/E-SE Saint-Nicolas fault (Fig. 1). In this basin, folds can be interpreted as fault-propagation folds characterised by the progressive tightening of the fold hinge and a steepening of the front limb (Averbuch, pers. com.). Upper Permio-Triassic conglomerates unconformably cover these units (Fig. 2) (Donsimoni, 1981; Barchi et al., 2008; Cartannaz, 2008).

2.2. Mining exploitation

The studied area corresponds to a small part of the eastern limb of the regional Merlebach anticline. Coal beds are globally striking 38 °N and are sub-vertical, their dips varying between 60°SE and 90°. Coal was exploited at depths ranging from 150 m to 1250 m with a *cut-and-fill* technique where extraction starts at the lowest level and goes up while hydraulically filling the exploited volumes with sand (Fig. 3). The consequence is that these exploited volumes have a high hydraulic conductivity that should strongly influence the underground water flows and must be distinguished

[2] http://www.brgm.eu/content/scientific-software

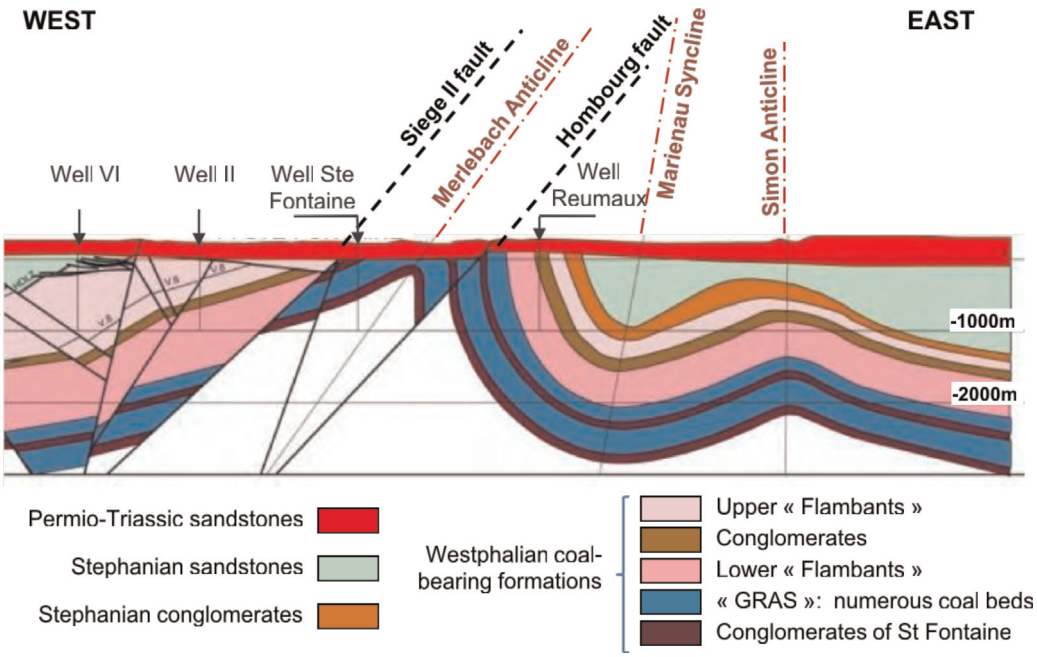

Fig. 2. West–East general cross-section of the Lorraine Coal Basin. The coal exploitations of Merlebach are east of the Hombourg fault, just above the Reumaux well (modified from Cartannaz, 2008).

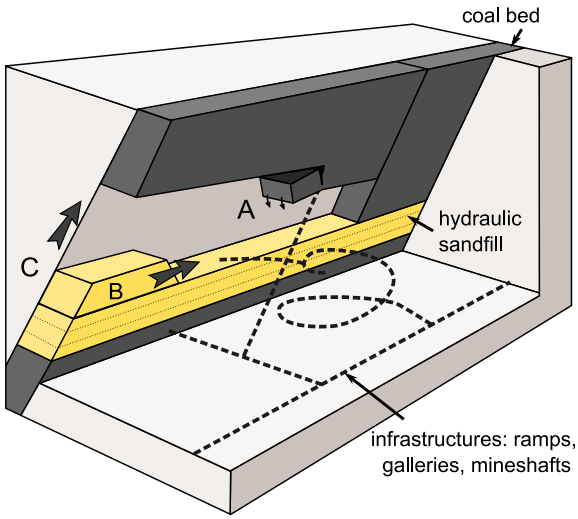

Fig. 3. Cut-and-fill mining technique (modified from Hamrin, 1997). Extraction starts at the lowest level and goes up while hydraulically filling the exploited volumes with sand. A: coal blocks are extracted at the roof; B: voids are filled with sand; C: exploitation goes up.

in our model from the unexploited parts of the coal beds that have a lower permeability.

The infrastructures developed for this exploitation consist of a network of interconnected sub-horizontal galleries linked by vertical pipes (Hamm and Bazargan Sabet, 2010). Fifty-eight mineshafts were bored, of which three are still accessible: Vouters 2, Marienau, and Simon 5 (Fig. 1). These infrastructures were left as they were and are now underground voids that drain fluid flows and must be integrated in our model of the area.

2.3. Geological and infrastructure data

Charbonnage de France has managed the mines until 2004 and part of its employees are now working for the BRGM in UTAM-Est (Post-Mining Territorial Unit) at Freyming-Merlebach. They provided us with a large amount of data collected through the mine lifetime (Table 1), most of it being provided as DraWinG (DWG) documents generated by AutoCAD.[3] Their preparation and processing represent a significant part of this work.

Digital elevation model: Provided by IGN, the French National Institute of Geographical Information, the Digital Elevation Model (DEM) has a 50 m horizontal resolution and around a one meter vertical precision. In the zone of interest, elevation ranges between 148 and 343 m FOD (French Original Datum).

Table 1
Information provided by the various data sources.

Data	Type	Mining			Geology			
		Mineshaft location	Infra structures	Exploitation	Topo.	Permio-Trias. base	Faults	Coal beds
DEM					×			
1 regional map	png				×		×	
3 structural maps	jpg						×	
16 mineshaft records	pdf	×	×			×		
22 mining level maps	dwg	×	×				×	×
33 cross-sections	dwg	×	×	×			×	×
63 vertical coal bed maps	dwg	×	×	×			×	
Isobaths	dwg					×		
3D view Vouters mineshaft	dwg		×					

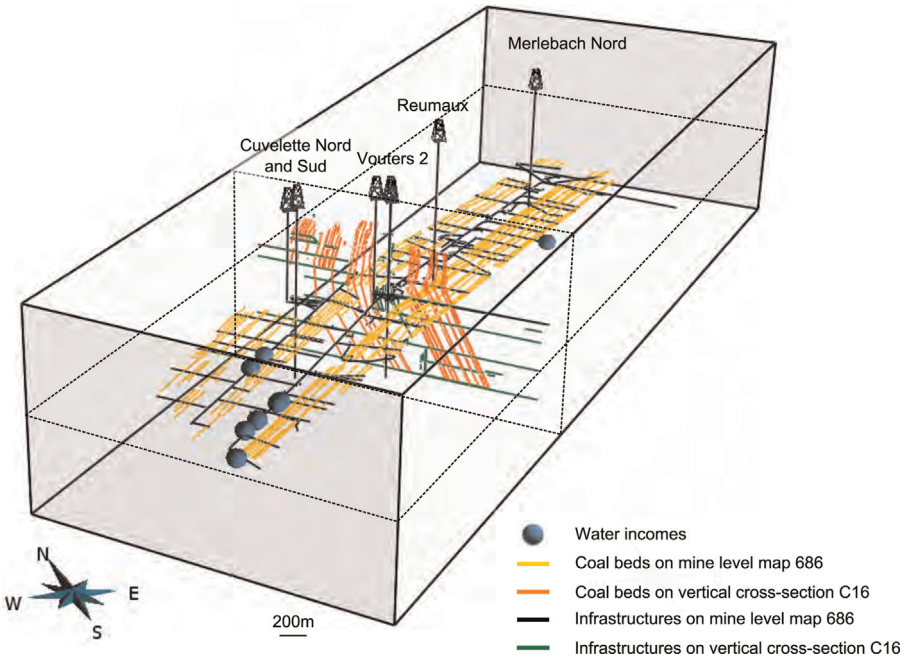

Fig. 4. 3D view of the information provided by the reference mining level map #686 (686 m depth) and the C16 cross-section (data from Charbonnage de France).

Regional geological map: The regional geological map gives very little information on the studied zone below the Permio-Triassic unit. It provides essentially data on the fault network.

Three structural maps: Three interpretative maps, that represent the structures at the surface, at 400 m and 1500 m depth, have been used for 3D fault network construction.

One map of the isobaths of the Permio-Triassic sandstone base horizon: Provided by Charbonnage de France, this map was the result of a geological study lead by Donsimoni (1981). It gives interpretative contour lines of the Permio-Triassic base horizon which is the top horizon of the coal-bearing formation. It gathers various data collected during the exploitation, but only covers the southwestern part of our zone of interest.

Sixteen mineshaft records: They refer to the well locations, the geological logs, the intersected gallery depths, the initial external water level (with its year of measure), technical well information, and the current state of the structure (closed, opened, etc.). Globally, well logs are very succinct and only three geological layers are identified: lower Triassic sandstones, Permian sandstones and the Carboniferous coal-bearing formation.

Twenty two mining level maps and thirty three NW-SE cross-sections: The horizontal mining level maps give the exact location of the galleries, the mineshafts and the faults. They are indexed by their depth value. The vertical cross-sections are perpendicular to the coal beds. They give information on the traces of coal beds, intersected infrastructures and faults in a vertical section and are thus complementary to the mining level maps (Fig. 4). They are located on horizontal mining level map #686 (686 m depth).

Sixty three exploited vertical coal bed maps: They result from the projection of the exploited zones of the non-planar coal beds on vertical planar surfaces (Fig. 5). They map zones that have been exploited and filled by sand. They need to be clearly identified in our model for they may act as drains. Because of gaps in these maps, the contours of the exploited zones were hand picked.

3D view of the infrastructures around the Vouters mineshaft: This image gives information on the infrastructures connecting the different mining levels (Fig. 6).

[3] http://www.autodesk.com/products/autodesk-autocad/overview

3. Geological model building

The global workflow consists of three main steps (Fig. 7). After data preparation, a surface-based model is built. It calls for various techniques to manage the modelling of the topographic surface, the faults, the Permio-Triassic base horizon, the coal beds (exploited or not), and the infrastructures. The third and final step is the rasterisation of the surface-based model into a 3D grid adequate for the flow simulator chosen for future investigations.

3.1. Data preparation

After converting the DWG files in DXF format, all data were imported into the Gocad geomodelling software. To ensure their spatial consistency, they first had to be georeferenced. The chosen coordinate system is the Lambert 1 (NTF) in the French coordinate system datum. To consistently georeference X–Y mining level maps whose depth is known, the mineshafts coordinates were used as points of reference. Mining level map #686 localises the thirty three cross-sections. It permits to accurately georeference each cross-section by combining them with the information about the infrastructures and coal beds on the other level maps (Fig. 4). From the 3D view, oblique ramps and infrastructures are digitised by hand into piecewise linear curves. Combined with the galleries extracted from the mining level maps, they constitute a complete network of infrastructures (Fig. 8). The exploited vertical coal bed maps are georeferenced on the vertical planes passing through the corresponding traces on mining level map #686. It was necessary to hand pick contours of exploited parts because of gaps in the input data.

Resulting from a long exploitation history, 107 different coal bed names are used on cross-sections and mining level maps. These names are either simple numbers (e.g. “27”, “10A”) or first names (e.g. “Irma”, “Henriette”). However, a careful quality check of data consistency in 3D shows that some of these names obviously refer to the same coal bed (or to two beds closer than 2 m that could be confused). As a result, we identified only 71 different coal beds that will have to be represented in the final model. Correspondence with input data is given in Appendix A.

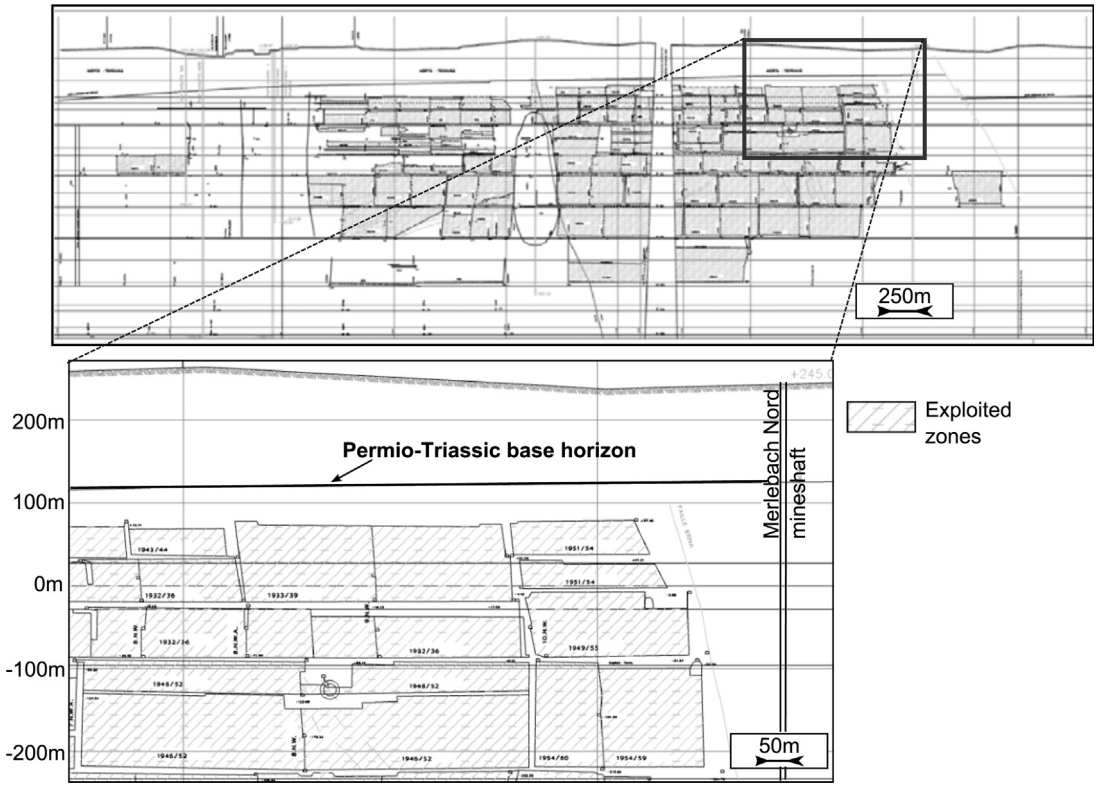

Fig. 5. One of the 63 exploited vertical coal bed maps from which sand filled exploited areas are determined.

3.2. Modelling choices

The different volumes to distinguish in the model are the sandstones surrounding the coal beds, the Permio-Triassic cover, the non-exploited parts of the coal beds, the exploited parts of the coal beds, and the mining infrastructures. Infrastructures are modelled by the lines obtained from digitising available data and are not further modified. Coal beds are very thin and could be modelled as surfaces. Sandstones and Permio-Triassic layers are thick layers present throughout the area of interest, hence should be represented as volumes.

To model volumetric layers, it is particularly convenient to represent them by their boundary surfaces, i.e. the horizons and faults delimiting them, which are generally triangulated. This kind of representation is called a surface-based structural model. Caumon et al. (2009) give a review of ways to manage its building. Around the Merlebach mine, several faults cut the layers, the Permio-Triassic formation is delimited by the topography and by the unconformity underlying the Permio-Triassic units. After building the structural model of the area from these surfaces (Section 3.3), we built the coal beds surfaces, then the identified exploited parts (Section 3.4).

3.3. Structural model

To better constrain the construction of the structural model and ensure its consistency with data around the exact zone of interest, that is the Merlebach mine, we build it for a larger area comprising 13 faults. This model of the main subsurface discontinuities is built with classical geomodelling approaches, also called explicit approaches, that consist in building surfaces that fit available data. Surfaces are built one by one in an order that has to be carefully thought, and their consistency must be carefully checked, both points requiring time and expertise in complex cases (Caumon et al., 2009).

Two main approaches can be used to build explicitly surfaces, the direct triangulation of data points and the indirect surface construction. The first is particularly adapted to regularly distributed points like a DEM, and is used here to build the topographic surface (Fig. 7). The indirect approach is more robust to deal with irregular, scarce, noisy data, such as those available for the thirteen faults or the Permio-Triassic base horizon. It consists in deforming a surface so as to minimise the distance between the surface and the data points. Several interpolation methods can be used (e.g., Haecker, 1992; Kaven et al., 2009). In this work, we use the *Discrete Smooth Interpolation* (DSI) implemented in Gocad (Mallet, 2002). This method minimises a weighted sum of the surface roughness and data misfit in the least squares sense (Mallet, 1992, 2002). Some of the data are exactly respected by inserting the data points into the mesh (e.g. well markers), while less reliable data are only honoured to a degree chosen by the user (e.g. isobath curves, interpretative cross-sections) (Fig. 7).

The faults were built one after another from their traces on the geological map, on the three structural maps and on the cross-sections. Following the methodology presented in the teacher's aide of Caumon et al. (2009), the fault network consistency was ensured by a complete check of all fault branch lines, older faults being cut by younger ones. Then, well markers provided on mineshaft indexes, isobath curves (southwestern part) and cross-sections were used as data point constraint to build the Permio-Triassic bottom surface. This surface was cut by the faults before interpolation in order to disconnect fault blocks. The obtained surface structural model is shown in Fig. 9.

3.4. Coal bed surfaces

The construction of the 71 coal bed surfaces was particularly challenging because they are sub-vertical, are generally distant from 5 to 10 m, have an extension of 10.2 km by 1.3 km, and are irregularly stacked on a width of 1.8 km. We used recently

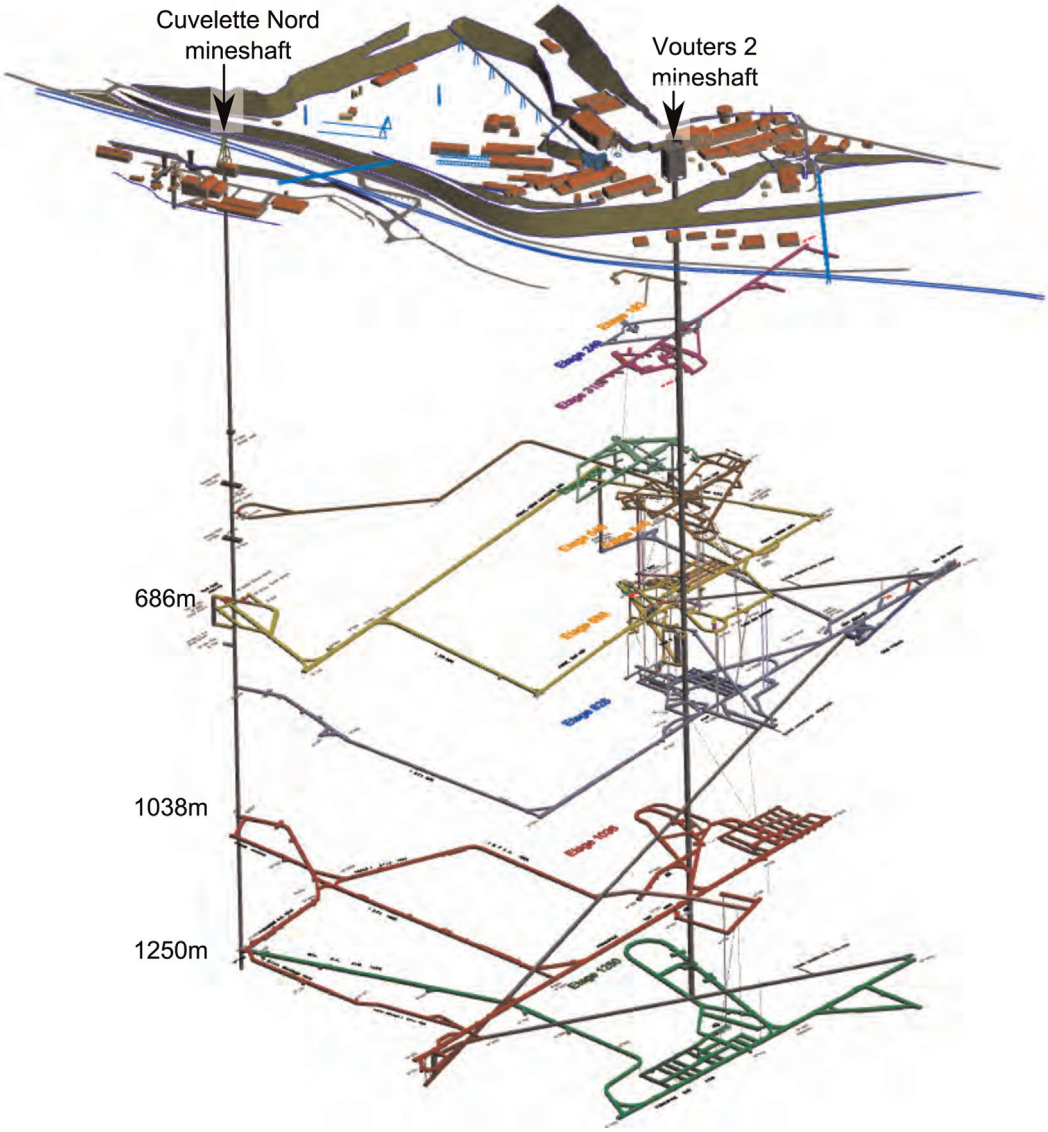

Fig. 6. 3D view of the infrastructures around Vouters mineshaft (data from Charbonnage de France, modified from Hamm and Bazargan Sabet, 2010).

developed techniques to achieve this goal.

3.4.1. Implicit coal bed construction

Implicit approaches consider geological interfaces as isovalues of a 3D scalar field $f(x, y, z)$. This scalar field is interpolated from the data with either continuous interpolation schemes, such as radial basis function or dual kriging (Carr et al., 2001; Chilès et al., 2004), or discrete interpolation schemes (Moyen et al., 2004; Frank et al., 2007; Caumon et al., 2013). With the discrete approach, the scalar field is defined by a piece-wise linear interpolation of the values stored at the vertices of a volumetric mesh. In the implementation used here (Caumon et al., 2007, 2013), the values at the vertices are obtained by an optimisation method that consists in minimising a weighted sum of various constraints including the data misfit. This method has the advantage to ease interactive editing. Moreover, dual kriging and radial basis function methods seem limited by the amount of information points. In both approaches, once the scalar field is calculated, any surface can be explicitly constructed by extracting the corresponding isovalue surface (Fig. 7). The two crucial advantages of implicit modelling as compared to explicit approaches are that implicit methods provide some built-in model consistency rules preventing the occurrence of overlapping or leaking layers and that they do not rely on data-to-surface projections, making them particularly suitable to generate stack of surfaces, like the coal beds discussed in this paper.

We use the implicit method implemented in the Gocad research plugin StructuralLab (Caumon et al., 2007, 2013) which requires a tetrahedral mesh of the volume of interest conformable to the triangulated fault surfaces. Conformable means that tetrahedron facets that are located on one fault are the same triangles than the ones meshing the fault surfaces. In the zone of interest, restricted to Merlebach, only seven faults have to be considered. We generated a tetrahedral isotropic mesh with the Delaunay-based tessellation package provided in the Gocad-Skua software. The mesh is made of 673,916 tetrahedra corresponding to a 72 m average tetrahedra edge length. This length was chosen to be consistent with the fault surface mesh size (around 85 m). Eight fault blocks are defined in our zone of interest (Fig. 10a). The Permio-Triassic base horizon, eroding the coal bearing formation and thus constituting a top boundary, is not accounted for in the mesh because it is sufficient to cut the coal beds by that surface afterwards. This facilitates the mesh generation step and further updates of the Permio-Triassic base horizon since otherwise the whole model would have to be rebuilt.

To compute the scalar field, two constraints are used: (i) a value

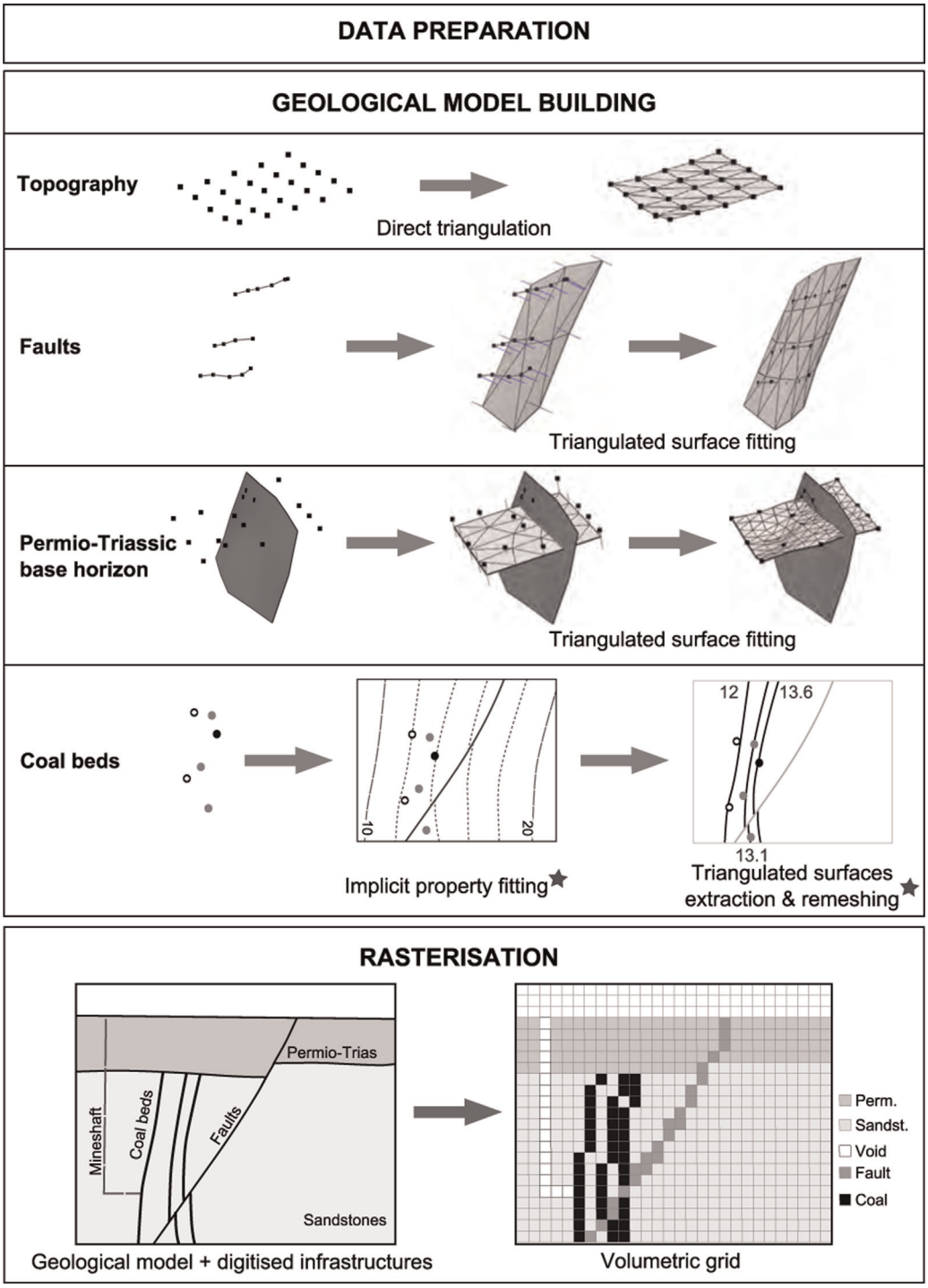

Fig. 7. Geomodelling workflow adopted for the present study. Stars indicate recent techniques.

of the scalar field that is attached to each set of lines corresponding to the same coal bed and (ii) constraints on the gradient of the scalar field so that it is orthogonal to the coal bed lines and has a constant norm, to be consistent with the more or less parallel coal beds. This last constraint is particularly useful to interpolate the scalar field where there are few data (in the northern and southern parts). Values assigned to the coal beds have to be consistent with this constant norm, i.e. they must evolve proportionally to the inter-bed distances. For that purpose, appropriate values have been computed for each coal bed, started with the value of 2 for the first one. The value of the scalar field associated to each of the other coal beds was computed by adding its average distance to the reference coal bed. In that way, the last modelled coal bed was assigned a value of 1335 (Fig. 10b and Appendix A). The 3D scalar field is then interpolated in each fault block with DSI (Mallet, 2002) giving more weight to the line point constraint (1) than to the gradient constraint (0.5), thus giving priority to data while preserving global consistency far from them. In this process, the modelling process does not make any hypothesis on cylindricity of the regional fold and thicknesses vary when data indicate so. The resulting scalar field is shown in Fig. 10c.

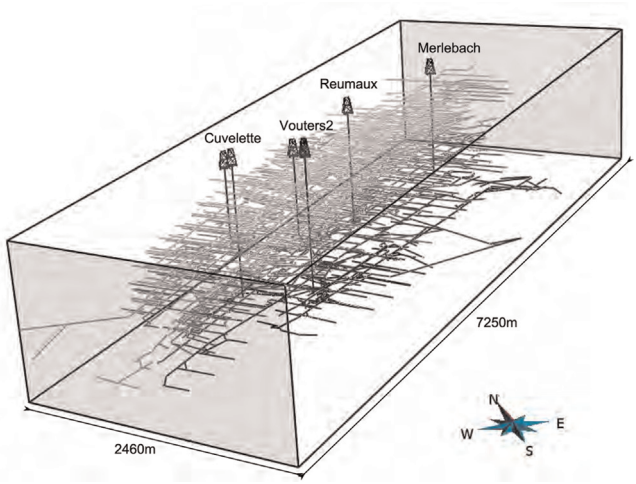

Fig. 8. 3D view of the complete infrastructure network determined from the processing of the 22 mining level maps, 33 cross-sections, 16 mineshaft records, and the 3D view around Vouters 2. Infrastructures are represented by 3586 piecewise linear curves.

3.4.2. Coal bed surface remeshing

The isosurfaces of the computed volumetric property represent the coal beds (Fig. 10c). However, it is difficult to visualise or compute geometrical properties for such surfaces, and in our case, to determine the exploited and unexploited zones of the coal beds. So, we need to convert these implicitly represented surfaces into explicit surfaces (e.g. triangulated surfaces) which we can use for further geometrical computations. The desired triangular mesh should correctly approximate the implicit surfaces with a minimal number of elements, in particular there should be no intersection between two coal bed surfaces. This is a particularly challenging task given the very narrow space between the surfaces. To ensure the robustness of further geometrical computations, this mesh should also have a good quality, i.e. to have triangles close to equilateral. Triangle quality can be measured as $Q = 6A/(\sqrt{3}\, h_{max}\, p)$ where A is the triangle area, h_{max} the length of its longest edge, and p its half-perimeter (Frey and Borouchaki, 1999). The maximal value of Q is 1 and is obtained for equilateral triangles.

Triangulated surfaces are first generated from the implicit model with a marching-tetrahedra algorithm (Gueziec and Hummel, 1995). These surfaces do not intersect but the quality of their mesh is very poor (Fig. 11), with an average of 0.549 (see Table 2 for additional statistics). Moreover, they have around 2 million triangles, slowing down any computation done on these surfaces. To remesh the surfaces, i.e. adapt the resolution of the triangles and improve their quality, we used a recent surface remeshing method that is adapted to geological models (Pellerin et al., 2014).

The key ideas of this method are to use a centroidal restricted Voronoi diagram optimisation (Du et al., 1999) to place the vertices of the output mesh, and to consider the different parts of the model to locally build the triangles of the output mesh. The main advantages of this remeshing method are that (1) it is fully automatic, (2) all surfaces are remeshed simultaneously, (3) the number of triangles in the output mesh is globally (as opposed to locally) controlled, (4) the quality of the triangles in the output mesh is very good, even if the input mesh quality is very poor.

This method is implemented in a plugin of the research modelling software *Graphite*,[4] which is interfaced in the geomodeller Gocad through the plugin Tweedle (Pellerin et al., 2010). The automatic remeshing of the 71 vein surfaces was performed on a consumer PC in less than 5 min. The total number of triangles was divided by ten. An additional manual quality control was necessary to ensure the complete validity of the remeshed surfaces, and remove approximately ten remaining intersections between surfaces, as discussed by Pellerin et al. (2014). The average output quality is 0.84686 (Fig. 11 and Table 2).

Finally, to identify the exploited parts of the coal beds, the boundaries of the exploited areas were horizontally projected from the exploitation vertical coal bed maps onto the corresponding coal bed surfaces. Each coal bed surface was then cut with these curves and new surfaces corresponding to the exploited coal bed parts were extracted (Fig. 12).

Cutting the coal beds with the Permio-Triassic horizons and combining them with the faults surfaces, we obtained a complete

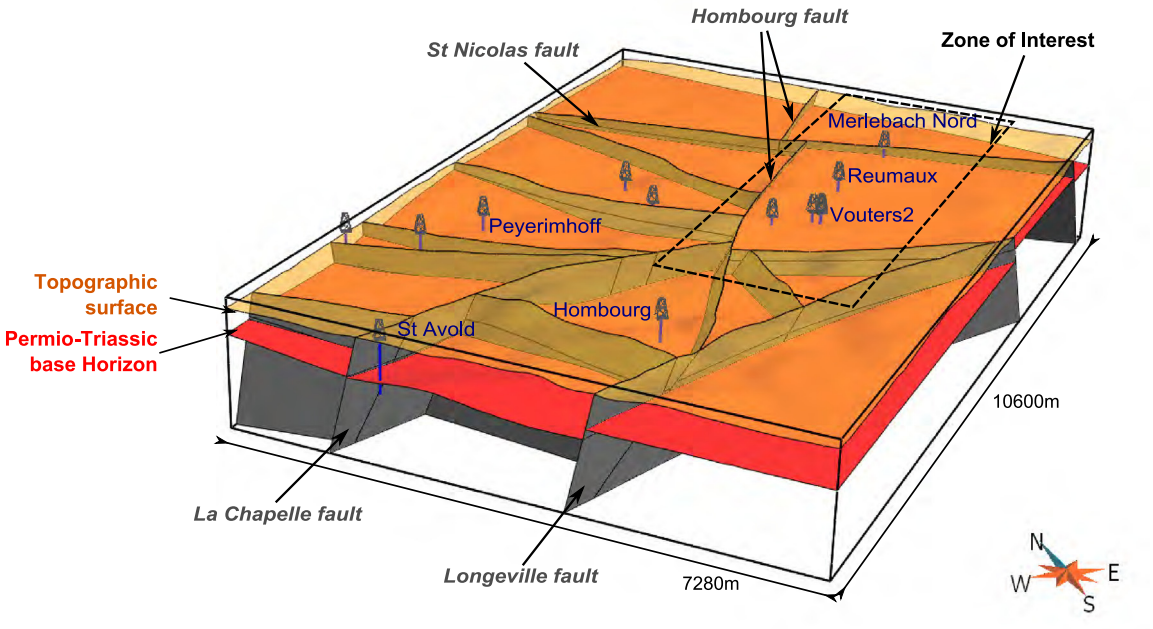

Fig. 9. Surface-based structural model of the extended zone of interest.

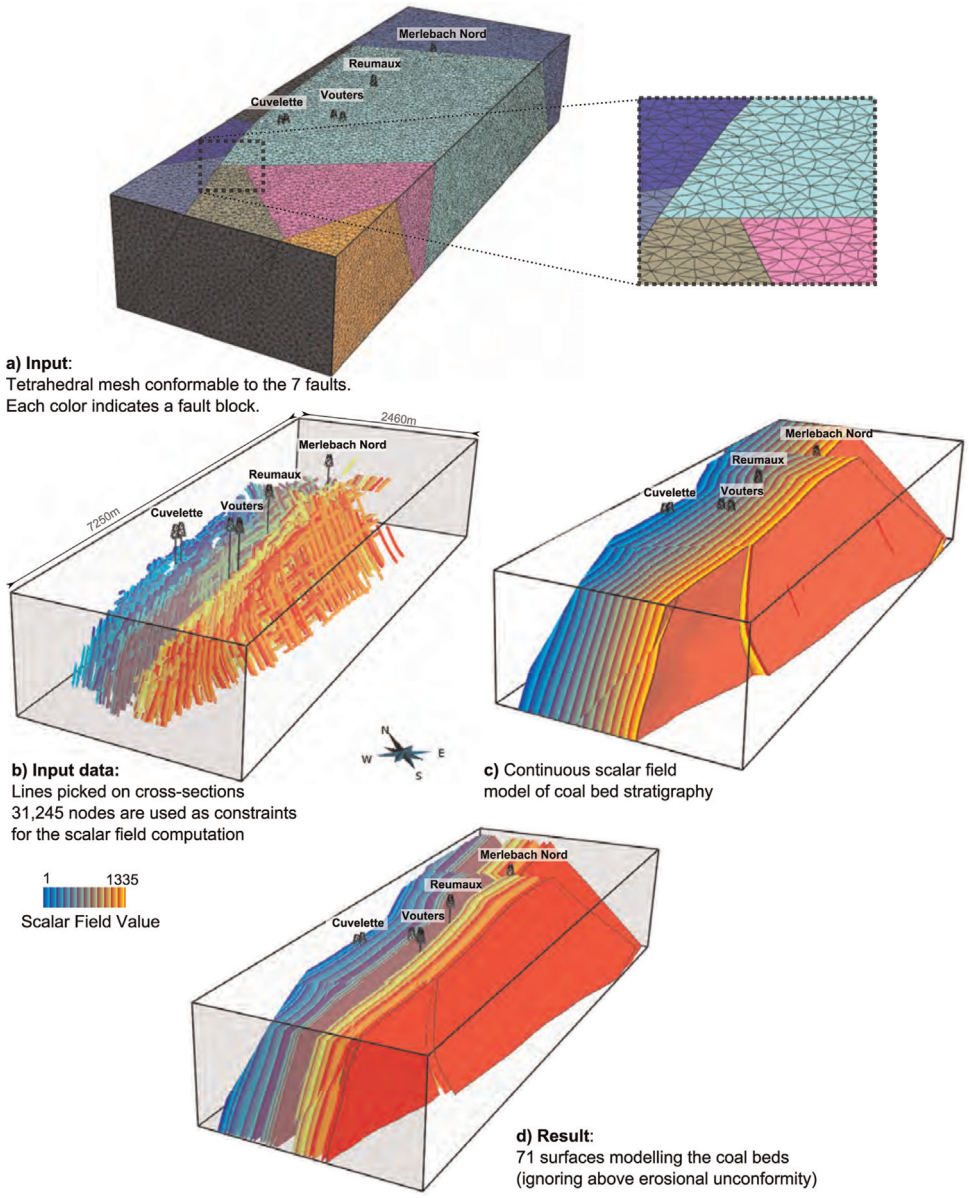

Fig. 10. Implicit modelling of the coal beds.

3D surface geological model of the Merlebach mine (Fig. 13). This 3D model is available for download as additional material to this paper in Gocad text file format, which can also be loaded by the open-source *Graphite* software.[5]

3.5. Volumetric model generation

One of the prospects of this model is to perform flow simulations to characterise the fluid behaviour in the context of a potential geothermal exploitation of the abandoned mine. In the continuity of the pre-study performed by Hamm and Bazargan Sabet (2010), two different strategies are currently being tested using the groundwater modelling software (MARTHE[6]): the classical continuum approach, in which all the voids are considered as porous material; and the coupled approach, in which the remaining open mining structures are modelled as discrete conduits and can exchange flow with the surrounding porous material. To this purpose, a 3D regular volumetric grid has to be generated from the 3D surface-based model, with a property defining the ground type on each cell. One of the main interest of representing a model by surfaces is that it can be used to generate various volumetric meshes with various mesh sizes.

The maximum number of cells that the groundwater modelling software can handle has to be considered when building this grid. Here, the MARTHE software imposes to build a grid with less than 135 million cells. We define a structured regular grid of $1275 \times 410 \times 240$ cells. It produces a final grid that contains 125.46 millions cells of approximately 6 m side. This cell size allows representing the various small structures that are present in the particular context of mine workings while keeping a reasonable number of cells considering that the zone of interest is 2.46 km large for 7.25 km long. Indeed, coal beds are generally distant from 5 to 10 m and their average thickness, as well as the diameter of the underground galleries, is around 5 m, which is of the same size order than cells.

A discrete property defines the ground type with the following

[4] http://alice.loria.fr/software/graphite
[5] alice.loria.fr/software/graphite/
[6] http://www.brgm.eu/content/scientific-software

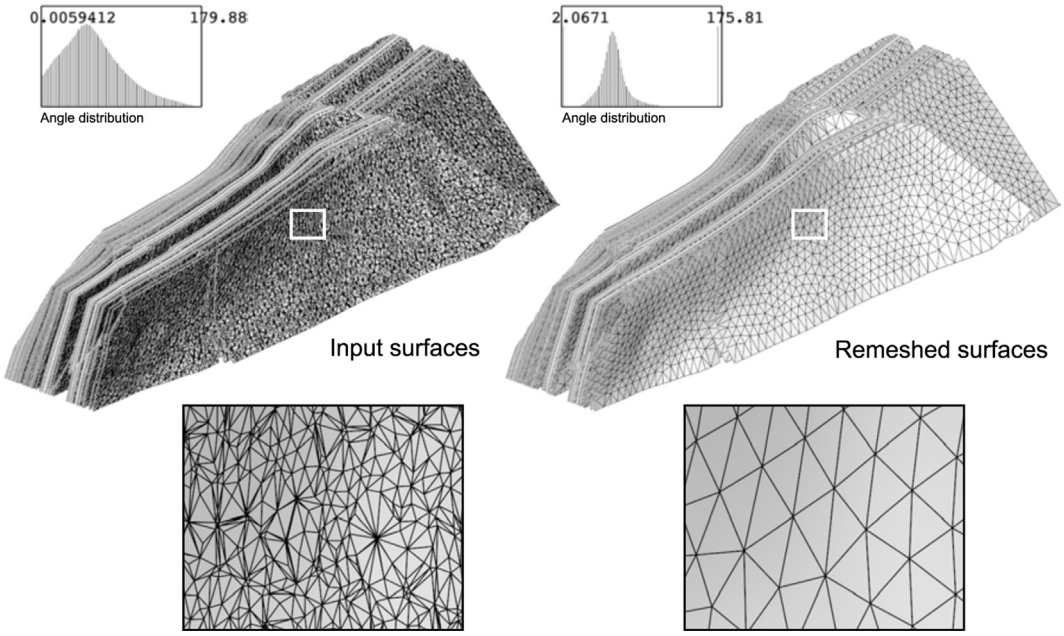

Fig. 11. Remeshing of the 71 coal bed triangulated surfaces with triangles as equilateral as possible. The input surfaces have more than 2 million triangles of very poor quality, the output surfaces have around 180,000 triangles of much better quality.

Table 2
Evaluation of the triangulated coal bed surface remeshing.

		Initial	Remeshed
# Vertices		1,084,218	100,171
# Triangles		2,097,489	179,835
Angles (deg.)	Min	0.0059	2.07
	Max	179.8	175.8
	<30 or >150 (%)	21.98	1.295
Quality	Min	0.00018	0.032
	Average	0.55	0.85

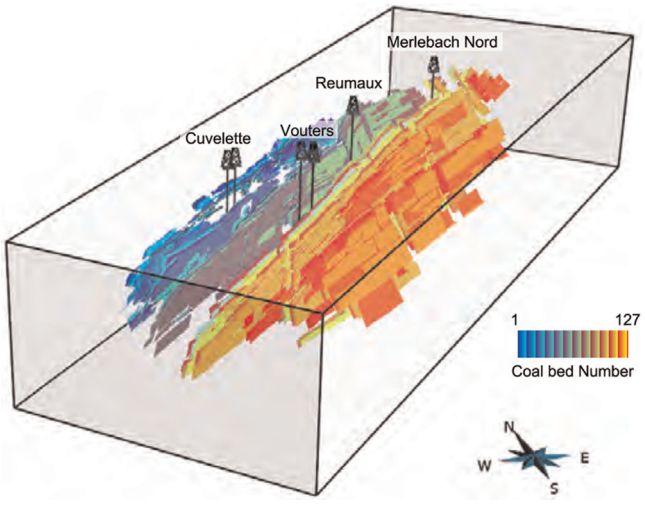

Fig. 12. Exploited parts of the 71 coal beds.

values: 1 for the Permio-Triassic formations, 2 for the sandstones, 3 for the unexploited coal beds, 4 for the exploited coal beds now filled with sand, 5 for the infrastructures (i.e. voids) and 6 for the faults (Fig. 14). Regions have been defined for each discrete property allowing to compute the corresponding volumes (Table 3). The resulting grid is available for download as additional material to this paper in Gocad text file format.

4. Discussion

The resulting volumetric grid fits the specification of the flow simulator: a Cartesian grid with less than 135 millions cells containing the required information to later impose appropriate permeability values for flow simulations. Of course these specifications have drawbacks. Cell dimension could have been reduced to 5 m (the average infrastructure diameter) but there would have been about 216.8 millions of cells ($1530 \times 492 \times 288$). This number of cells can be handled by other flow simulators like GMS-Modflow[7] which authorises up to 300 millions of cells (1 millions per layer and 300 layers[8]). Like MARTHE, it uses Cartesian grids that may involve aliasing problems when the modelled objects are not aligned with the grid, e.g. stair steps geometries or inappropriately corner-connected cells. One solution would be to take this into account when assigning permeability properties as done in classical upscaling process (e.g. Karim and Krabbenhoft, 2010). Another solution would be to use a different flow simulation software that is based on the more flexible unstructured meshes. The crucial advantage of the workflow presented in this paper is that we did not directly build the final grid but produced an intermediate 3D-surface-based model that does not depend on this grid. Various volumetric meshes can be generated from this surface model (similar to the boundary represented or B-Rep model used in CAD) like stratigraphic or tartan grids (Cartesian grids with an adaptive mesh resolution).

Naturally, the precision/accuracy of the model is strongly linked to the quality of the data. In the used data set, uncertainties due to positioning and resolution are considered as not really significant. However, 2D maps propose fault traces which are not always consistent when placed in three dimensions (i.e., fault lines corresponding to the same surface may induce unrealistic curvature, or may simply be missing on some 2D sections). The least-squares interpolation and the rasterisation of objects in the grid tend to mitigate these inconsistencies when the discrepancy is of the

[7] http://www.aquaveo.com/software/gms-groundwater-modelling-system-introduction
[8] http://www.scientificsoftware-solutions.com/pages.php?pageid=96#Limitation_of_PM

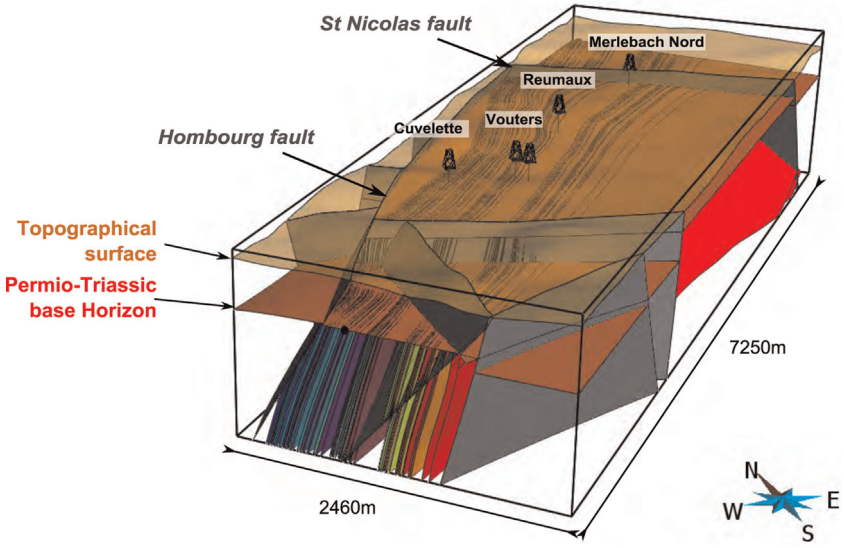

Fig. 13. 3D surface-based structural model of the Merlebach mine.

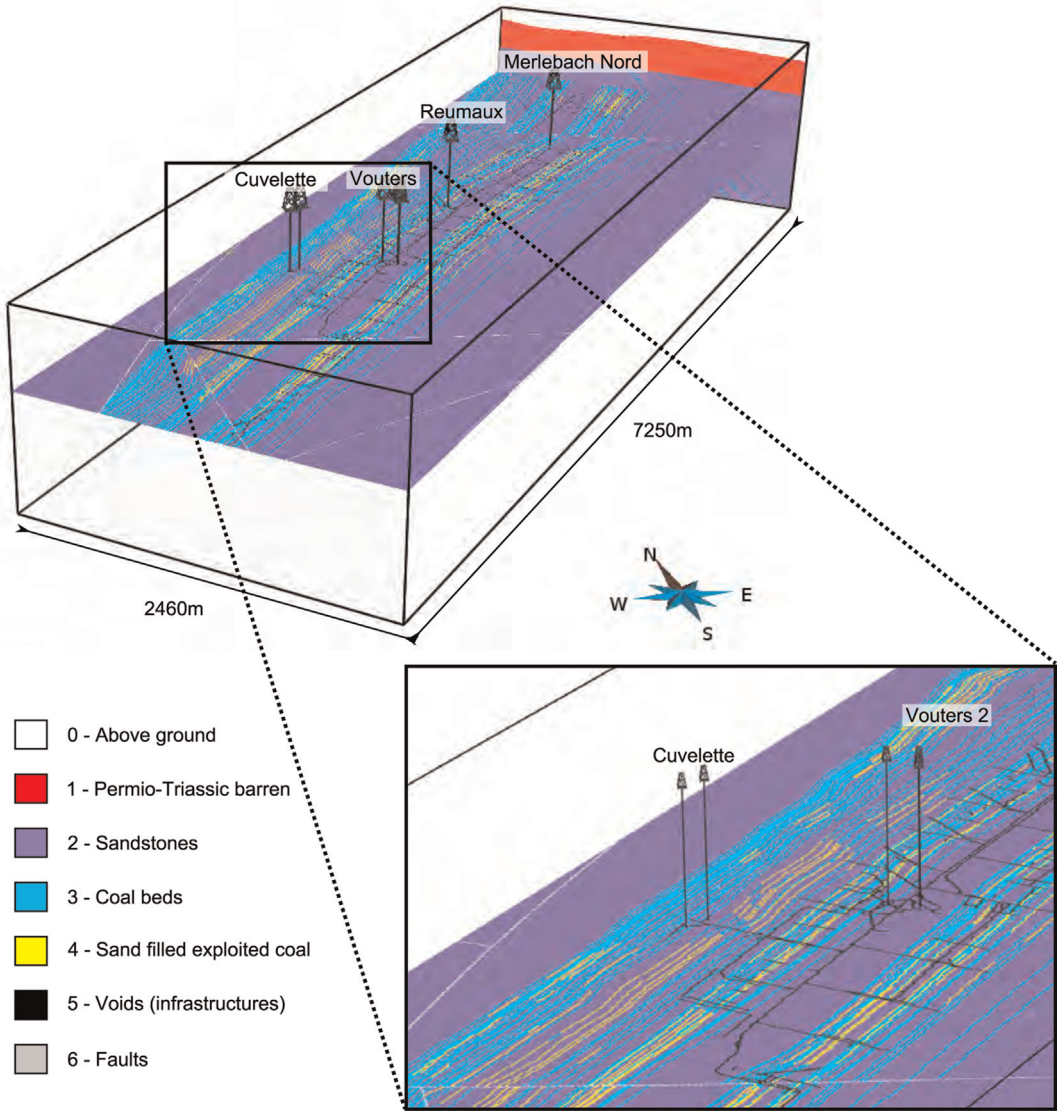

Fig. 14. Slices in the 3D regular Cartesian volumetric grid of the Vouters 2 mining area. The grid contains about 125 million cubic cells of 6 m side.

Table 3
Volumes computed on a Cartesian volumetric grid of 125 million cells of 6 m side.

Rock type	Volume (in 10^7 m^3)
Permio-Triassic	416.56
Sandstones	1625.81
Coal beds (unexploited)	286.71
Sand filled exploited coal	36.48
Voids (infrastructures)	2.06
Faults	8.02

same order of magnitude as the grid resolution. Locally, larger differences exist between input fault traces but they are always outside of the target area for geothermal exploitation, hence should not have much impact on the simulation results. Nevertheless, more rigorous uncertainty assessment still remains a possible way to improve this work.

In this paper, we showed how a geomodelling software can be used to integrate various data into a unique and consistent geological three dimensional model. The proposed combination of methods is the key point to achieve such a task since a conventional explicit approach would not have allowed us to create the 71 sub-vertical coal beds so easily while honouring data and geological consistency. In such context where surfaces have a kilometric extent but have a metric inter-distance, frequent crossovers occur unless the mesh is refined and the complete process requires an important manual quality control. This study demonstrates the potential of the implicit modelling package we have used Caumon et al. (2007, 2013) in a real case study with a relatively dense data set. The efficient surface remeshing method proposed by Pellerin et al. (2014) was a very complementary tool to improve the quality and adapt the number of triangles of the triangulated surfaces obtained with the implicit approach. During this work, hundreds of surfaces and thousands of curves have been created and manipulated. Efficiency in the repetitive tasks was possible thanks to a recently developed Gocad plugin, Gopy (Antoine and Caumon, 2008), that permits to script Gocad commands in Python. It was used for simple operations such as global renaming of surfaces or curves, but also for more complex tasks: (i) to create and initialise new properties given an existing one, e.g. for the scalar field value given the coal bed ID; (ii) to extract the 71 surfaces given the corresponding list of isovalues; (iii) to project and extract the exploited parts from the 63 exploited coal bed surfaces; (iv) to control the quality of initial data by creating groups of curves depending on their names or property values.

5. Conclusion

To conclude, this paper presents an efficient workflow to build a volumetric geomodel in a post-mining context using recent geomodelling tools. The modelling of the coal beds represents the principal challenge of this paper due to their proximity and intimately related geometry. This paper demonstrates that this hurdle is overturned when using appropriate tools: (1) discrete implicit modelling for the interpolation of geological data (Caumon et al., 2007, 2013), coupled with (2) a variational remeshing tool for geological surfaces (Pellerin et al., 2014), and (3) serial processing with scripts (Antoine and Caumon, 2008). This paper also illustrates how implicit and explicit approaches are complementary. We take full advantage of the strength of both methods: using implicit surfaces while building the vein surfaces and going back to the explicit scheme when accurate geometry processing is required. As a result of this study, two 3D models are proposed for download as supplemental material: the 3D surface-based model and a volumetric grid.

Perspectives of these work reside on the flow simulation aspects that will focus on the geothermal potential of the site. These simulations, planned for the next years, would also benefit from the in situ monitoring of temperature and conductivity that is currently performed in the accessible mineshaft of Vouters 2.

Acknowledgements

We thank the BRGM (French Geological Survey) and Charbonnage de France for providing us initial data and authorising us to publish them. We also thank the industrial and academic members of the Gocad Consortium managed by the ASGA (Association Scientifique pour la Géologie et ses Applications), INRIA – Alice team for providing some of the algorithms used in the surface remeshing and Paradigm for providing the Gocad Software and API. Both reviewers, Olivier Kaufmann and Andrea Zanchi, are thanked for their constructive remarks that helped improve this paper. Wendy Steckiewicz-Laurent built a first version of the model during her final year project at the Nancy School of Geology (ENSG) based on a preliminary regional model built by Marie Sallilas-Sorrosal and Adeline Moignard during short internships. This work was performed in the frame of the “Investissements d'avenir” Labex RESSOURCES21 (ANR-10-LABX-21).

Appendix A. List of modelled coal beds

List of modelled coal beds: their initial names on mining maps, their number, their ID after quality control and the corresponding scalar value used for the implicit modelling.

Coal bed names on mining maps	Automatic number	ID	Scalar field values
27	1	1	2
26	2	2	17
25A	3	3	30
25	4	4	37
24BO	5	6	43
24BE	6		
24W	7	7	49
24O	8		

24E	9		
24	10	10	53
23	11	11	66
22	12	12	76
21A	13	13	82
21	14	14	85
20BO	15	17	99
20BE	16		
20W	17		
20E	18	18	102
20A	19		
20	20	20	105
19A	21	22	125
19	22		
18	23	23	137
17A	24	24	141
17	25	25	158
16C	26	26	168
16B	27	27	175
16A	28	28	193
16	29	29	208
15A	30	31	245
15	31		
14A	32	33	265
14	33		
13A	34	35	285
13	35		
12	36	36	295
11A	37	37	323
11	38	38	333
10BE	39	42	370
10W	40		
10E	41		
10	42		
9_3	43	43	392
9	44	44	430
8_1	45	45	490
8A	46		
8	47		
7_3	48	47	500
7_1	49		
7	50	50	510
6_1	51	52	520
6	52		
5_7	53	56	535
5_2	54		
5_1	55		
5	56		
4_2	57	59	552
4_1	58		
4	59		
3_4	60	62	558
3_1	61		
3	62		
2A	63	63	561
2O	64		
2W	65	65	572
2ME	66	66	575
2E	67	67	580
2	68		
1_4	69	71	605
1_2	70		
1	71		
0	72	72	610
0A	73		
0B	74		

Y	75	75	615
X	76	76	648
ANNA1	77	92	855
ANNA2	78	93	861
ANNA3	79	94	880
BERTA1	80	95	895
BERTA2	81	96	905
BERTA3	82	98	910
BERTA4	83		
CECILE	84	99	918
CECILE2	85	100	920
DORA	86	101	925
ERNA1	87	102	950
ERNA2	88	103	955
ERNA3	89	104	958
ERNA4	90		
FRIEDA1	91	106	1010
FRIEDA1E	92	107	1019
FRIEDA2	93	108	1025
FRIEDA3	94	109	1030
FRIEDA4	95	110	1036
FRIEDA5	96	111	1048
FRIEDAE	97		
FRIEDAW	98		
GABRIELLE	99	114	1077
GEORGETTE	100	115	1083
HENRIETTE	101	116	1130
IRMA	102	117	1146
J	103	120	1160
J_2	104		
JACQUELINE	105		
K_L	106	126	1265
LOUISE	107	127	1335

Appendix B. Supplementary data

Supplementary data associated with this paper can be found in the online version at http://dx.doi.org/10.1016/j.cageo.2015.01.009.

References

Antoine, C., Caumon, G., 2008. Rapid algorithm prototyping in Gocad using Python plugin. In: Proceedings of 28th Gocad Meeting, Nancy, p. 4.

Barchi, P., Cartannaz, C., Fourniguet, G., 2008. Projet Minewater – Géologie du bassin houiller lorrain et potentialité géothermique BRGM/RP-56096-FR. Technical Report, BRGM.

Carr, J.C., Beatson, R.K., Cherrie, J.B., Mitchell, T.J., Fright, W.R., McCallum, B.C., Evans, T.R., 2001. Reconstruction and representation of 3D objects with radial basis functions. In: SIGGRAPH '01: Proceedings of the 28th Annual Conference on Computer Graphics and Interactive Techniques. ACM, New York, NY, USA, pp. 67–76.

Cartannaz, C., 2008. "MINEWATER" PROJECT. Geology of the mine reservoir of the Lorraine Coal Basin Vouters 2 and Simon 5 shafts (Scale Analysis). BRGM/RP-56257-GB. Technical Report, BRGM.

Caumon, G., Antoine, C., Tertois, A.-L., 2007. Building 3D geological surfaces from field data using implicit surfaces. In: Proceedings of 27th Gocad Meeting, Nancy, p. 6.

Caumon, G., Collon-Drouaillet, P., Le Carlier de Veslud, C., Viseur, S., Sausse, J., 2009. Surface-based 3D modeling of geological structures. Math. Geosci. 41 (September (8)), 927–945.

Caumon, G., Gray, G., Antoine, C., Titeux, M.-O., 2013. Three-dimensional implicit stratigraphic model building from remote sensing data on tetrahedral meshes: theory and application to a regional model of La Popa Basin, NE Mexico. IEEE Trans. Geosci. Remote Sens. 51 (March (3)), 1613–1621.

Chilès, J.-P., Aug, C., Guillen, A., Lees, T., 2004. Modelling the geometry of geological units and its uncertainty in 3D from structural data: the potential-field method. In: Proceedings of Orebody Modelling and Strategic Mine Planning, pp. 313–320.

Collon, P., Fabriol, R., Buès, M., 2005. Evolution of water quality in the abandoned iron mines of Lorraine: towards a semi-distributed modelling approach. C. R. Geosci. 337 (16), 1492–1499.

Collon, P., Fabriol, R., Buès, M., 2006. Modelling the evolution of water quality in abandoned mines of the Lorraine Iron Basin. J. Hydrol. 328 (3–4), 620–634.

Donsimoni, M., 1981. Le Bassin houiller Lorrain. Synthèse géologique. Technical Report, Mém. BRGM, 117.

Du, Q., Faber, V., Gunzburger, M., 1999. Centroidal Voronoi tessellations: applications and algorithms. SIAM Rev. 41 (4), 637–676.

Fleck, S., Michels, R., Izart, A., Elie, M., Landais, P., 2001. Palaeoenvironmental assessment of Westphalian fluvio-lacustrine deposits of Lorraine (France) using a combination of organic geochemistry and sedimentology. Int. J. Coal Geol. 48 (December (1–2)), 65–88.

Frank, T., Tertois, A.-L., Mallet, J.-L., 2007. 3D-reconstruction of complex geological interfaces from irregularly distributed and noisy point data. Comput. Geosci. 33 (7), 932–943.

Frey, P.J., Borouchaki, H., 1999. Surface mesh quality evaluation. Int. J. Numer. Methods Eng. 45 (1), 101–118.

Gueziec, A., Hummel, R., 1995. Exploiting triangulated surface extraction using tetrahedral decomposition. IEEE Trans. Vis. Comput. Graph. 1 (4), 328–342.

Haecker, M.A., 1992. Convergent gridding: a new approach to surface reconstruction. Geobyte 7 (3), 48–53.

Hamm, V., Bazargan Sabet, B., 2010. Modelling of fluid flow and heat transfer to assess the geothermal potential of a flooded coal mine in Lorraine, France. Geothermics 39 (June (2)), 177–186.

Hamm, V., Collon-Drouaillet, P., Fabriol, R., 2008. Two modelling approaches to water-quality simulation in a flooded iron-ore mine (Saizerais, Lorraine,

France): a semi-distributed chemical reactor model and a physically based distributed reactive transport pipe network model. J. Contam. Hydrol. 96 (1–4), 97–112.
Hamrin, H., 1997. Guide to Underground Mining Methods and Applications. AB Atlas Copco.
Izart, A., Palain, C., Malartre, F., Fleck, S., Michels, R., 2005. Paleoenvironments, paleoclimates and sequences of Westphalian deposits of Lorraine coal basin (Upper Carboniferous, NE France). Bull. Soc. Géol. France 176 (May (3)), 301–315.
Karim, M.R., Krabbenhoft, K., 2010. New renormalization schemes for conductivity upscaling in heterogeneous media. Transp. Porous Media 85 (April (3)), 677–690.
Kaufmann, O., Martin, T., 2008. 3D geological modelling from boreholes, cross-sections and geological maps, application over former natural gas storages in coal mines. Comput. Geosci. 34 (March (3)), 278–290.
Kaven, J., Mazzeo, R., Pollard, D., 2009. Constraining surface interpolations using elastic plate bending solutions with applications to geologic folding. Math. Geosci. 41 (1), 1–14.
Korsch, R., Schäfer, A., 1995. The Permo-Carboniferous Saar-Nahe Basin, south-west Germany and north-east France: basin formation and deformation in a strike-slip regime. Geol. Rundsch. 84 (June), 2.
Li, X., Li, P., Zhu, H., 2013. Coal seam surface modeling and updating with multi-source data integration using Bayesian Geostatistics. Eng. Geol. 164 (September), 208–221.
Mallet, J.-L., 1992. Discrete Smooth Interpolation. Comput.-Aided Des. 24 (4), 263–270.
Mallet, J.-L., 2002. Geomodeling. Applied Geostatistics. Oxford University Press, New York, NY.
Moyen, R., Mallet, J.-L., Frank, T., Leflon, B., Royer, J.-J., 2004. 3D-Parameterization of the 3D geological space – The GeoChron model. In: Proceedings of European Conference on the Mathematics of Oil Recovery (ECMOR IX), p. 8.
Pellerin, J., Lévy, B., Caumon, G., 2010. Advanced geometry processing in Gocad using graphite. In: Proceedings of 30th Gocad Meeting, Nancy, p. 8.
Pellerin, J., Lévy, B., Caumon, G., Botella, A., 2014. Automatic surface remeshing of 3D structural models at specified resolution: a method based on Voronoi diagrams. Comput. Geosci. 62 (January), 103–116.
Renz, A., Rühaak, W., Schätzl, P., Diersch, H.-J.G.J., 2009. Numerical modeling of geothermal use of mine water: challenges and examples. Mine Water Environ. 28 (January (1)), 2–14.

Geomorphology 217 (2014) 152–164

Contents lists available at ScienceDirect

Geomorphology

journal homepage: www.elsevier.com/locate/geomorph

Simulation of 3D karst conduits with an object-distance based method integrating geological knowledge

Guillaume Rongier [a,*], Pauline Collon-Drouaillet [a], Marco Filipponi [b]

[a] GeoRessources UMR7359, Université de Lorraine, CNRS, CREGU, ENSG, 2 Rue du Doyen Marcel Roubault, TSA 70605, 54518 Vandœuvre-Lès-Nancy Cedex, France
[b] Bauen im Karst, Alte Spinnerei, CH-8877 Murg, Switzerland

ARTICLE INFO

Article history:
Received 4 July 2013
Received in revised form 2 April 2014
Accepted 22 April 2014
Available online 2 May 2014

Keywords:
Karst conduit
Shape
Stochastic simulation
Skeleton
Inception feature

ABSTRACT

Karst conduit shapes have a high influence on fluid flows. As these underground hidden systems are partially inaccessible, their stochastic simulation is an essential tool to assess the uncertainties related to these highly exploited water resources. The object-distance simulation method (ODSIM) is a hybrid dual-scale approach that has been recently proposed to model geological underground structures due to late processes such as dolomitized rocks, mineralized veins or karsts. Using a perturbed Euclidean distance field around a curve representing roughly the conduit centre and called a skeleton, the resulting shapes are globally cylindrical-like 3D envelopes. But at a drain scale, karstic conduits are elongated along weakness planes such as lithostratigraphic horizons, bedding planes, fractures or faults. In addition to those planes the influence of the water table is added. This work presents different improvements of ODSIM methodology for simulating more realistic shapes in the particular case of karst. Firstly, we propose using a custom distance field computed with a fast marching method. Considering the "velocity" field to be proportional to the permeability allows the resulting features to be elongated along the weakness planes. Secondly, to handle specific shapes due to the proximity of the water table, such as trenches or notches, we impose areas of higher velocity between the skeleton and the water table. Finally, we generate a custom random threshold with several variograms and/or distributions depending on the different features integrated in the "velocity" field. Applied on different models, it is shown that the resulting karst conduits have more realistic shapes than those obtained with the previous workflow, while the variability of structures which can be modelled with ODSIM is preserved.

1. Introduction

Karstic systems are underground hydrographic networks made of conduits and caves that have grown by dissolution of the surrounding rocks. They cover approximately 20% of the planet's dry ice-free land (e.g., Ford & Williams, 2007; De Waele et al., 2009) and are therefore important fluid reservoirs, providing water for probably 20 to 25% of the world's population (Ford & Williams, 2007). Development of caves is also responsible for substantial human and financial disasters by causing sinkholes in urbanized zones. These karst features can be dramatic as the surface land usually stays intact until there is insufficient support: the soil suddenly collapses, swallowing everything above (e.g., (Brinkmann et al., 2008; Frumkin et al., 2009; Parise et al., 2009)). Recent works have shown that karsts may also be a major source of paleoclimate records (e.g., Mongelli, 2002; Horvatinčić et al., 2003; Onac & Constantin, 2008; Kuo et al., 2011). Nowadays human activities are a major threat for karstic environments (e.g., De Waele et al., 2011), and furthermore climate changes may have a considerable impact on them in the future (e.g., Viles, 2003; Hartmann et al., 2012).

Despite the importance of karstic networks, their location and exact geometry remain poorly known, mainly due to the partial inaccessibility of these underground systems. These networks actually play a major role in the flow regime of most carbonate aquifers and reservoirs (e.g., Lü et al., 2008; Chaojun et al., 2010): their conduits act as preferential flow paths and concentrate the fluids. As conduit shapes result from a complex dissolution process (e.g., Ford & Williams, 2007), a straightforward modelling approach of fluid flows would represent karstic conduits as equivalent to cylindrical tubes. This approach does not take into account the shape variations like abrupt narrowings or enlargements which also greatly impact fluid flows (e.g., Field & Pinsky, 2000; Hauns et al., 2001; Goldscheider, 2008; Morales et al., 2010). Thus, knowing and modelling the shapes of these three-dimensional geological objects could be an important improvement for both water and oil and gas reservoir exploitation. The goal of this paper is to propose a tool to realize such three-dimensional modelling of karstic systems.

Two different contexts of application are examined. First, as large parts of cave systems are still unexplored, three-dimensional stochastic simulations offer a way to better assess the associated uncertainty. However, the current methods focus on the global architecture of the conduit networks (e.g., Borghi et al., 2012; Collon-Drouaillet et al.,

* Université de Lorraine - ENSG, 2 Rue du Doyen Marcel Roubault, TSA 70605, 54518 Vandœuvre-Lès-Nancy Cedex, France.
E-mail addresses: guillaume.rongier@gocad.org (G. Rongier), pauline.collon@univ-lorraine.fr (P. Collon-Drouaillet), marco.filipponi@bauen-im-karst.info (M. Filipponi).

http://dx.doi.org/10.1016/j.geomorph.2014.04.024
0169-555X/

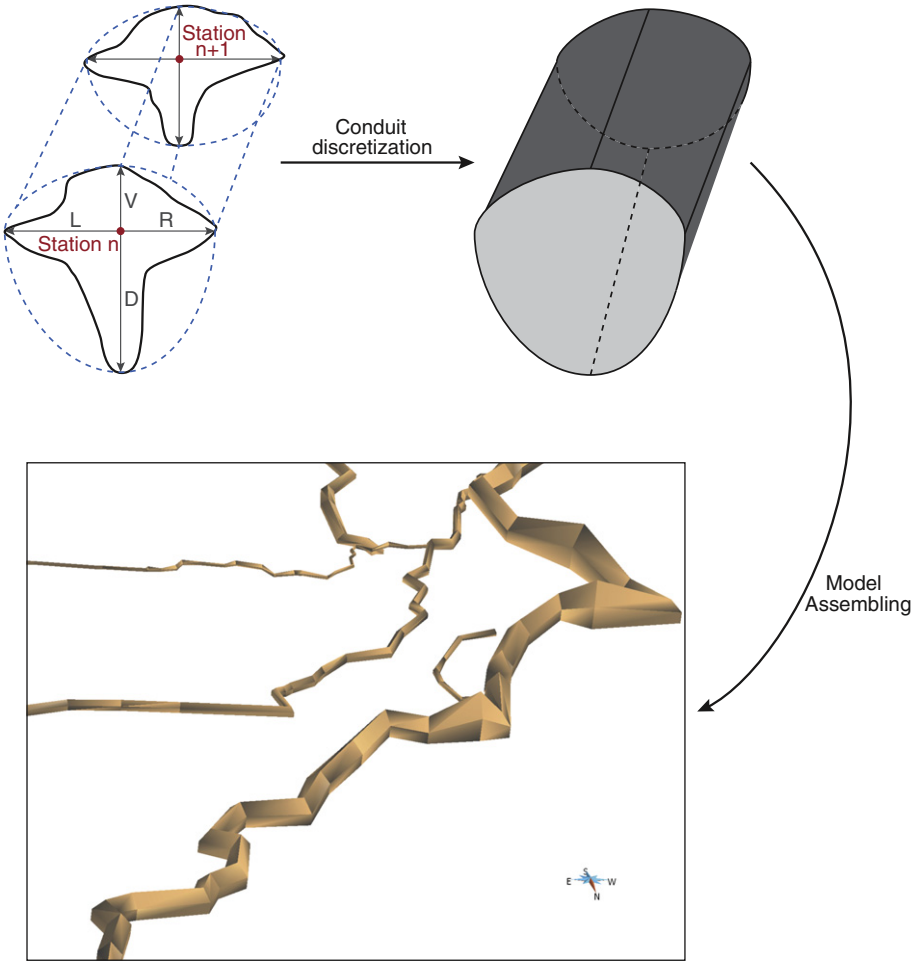

Fig. 1. Classical conduit discretization process and 3D "reconstruction" used in common speleological programs (here with GHTopo).

2012; Pardo-Igúzquiza et al., 2012). They stochastically generate several possible skeletons representing roughly the conduit centre and highlighting the uncertainties related to the conduit location. The proposed methodology is complementary to those works by providing volumetric information around those skeletons consistent with local geological settings, highlighting the uncertainties related to the conduit size and shape. Second, it provides a solution to reconstruct the three-dimensional geometry of explored and monitored cave systems. Indeed, new technologies like LiDAR have permitted precise mapping of cave conduits (e.g., Jaillet et al., 2011). But this type of acquisition is time consuming, needs specific equipment and requires a post-treatment of huge amounts of data. It is thus far more adapted to explore and model karst at the drain scale. For larger scales, there are two categories of data: i) two-dimensional maps (plan and/or profile views) which result of a projection of a three-dimensional network on a two-dimensional plane — this is the oldest and most common type of data; ii) three-dimensional information provided by "modern" cave survey. In the latter case, the underground topographic information is given by a sequence of topographic stations, located in order to fit exploration requirements: access easiness, clear sight along the cave passages, etc. At each station only distances to walls are recovered left, right, up and down (LRUD). The numerical treatment of these data leads to a discretization that represents the conduits with elliptical or rectangular section shapes (Fig. 1). Dealing with both categories of data, the 3D reconstruction remains a problem that is currently solved in common speleological programs with a linear interpolation between the various two-dimensional sections leading to more or less realistic shapes (e.g., Survex,[1] VisualTopo[2] or GHTopo[3]).

In both contexts, few works have been conducted on modelling more realistic 3D karstic conduit shapes (e.g., Labourdette et al., 2007; Henrion et al., 2010; Boggus & Crawfis, 2009). The object-distance simulation method (ODSIM) proposed by (Henrion et al., 2010) generates an envelope along a curve skeleton whose shape is irregular at fine scale but globally cylindrical at the first order. To integrate a geological constraint on the shape, e.g., for the development of hydrothermal dolomites around fractures, they use plane skeletons instead of curves. But the resulting envelope retains a round aspect at the plane extremities. Contrary to geometries generated with this simple approach, karstic shapes are more elongated along given inception features (e.g., Jameson, 1985; Filipponi, 2009) that favour karst conduit development. Thus, depending on the local geological context, the cross-section geometry of karstic conduits varies from circle to lens or "keyhole" (Section 2). These particular shapes are not reproduced by ODSIM (Section 3). In this paper, we propose a new methodology to integrate various geological features influencing conduit shapes by using a custom distance field generated with a fast marching method instead of a Euclidean distance field (Section 4). This involves the creation of a

[1] http://survex.com/.
[2] http://vtopo.free.fr/.
[3] http://siliconcavings.chez-alice.fr/.

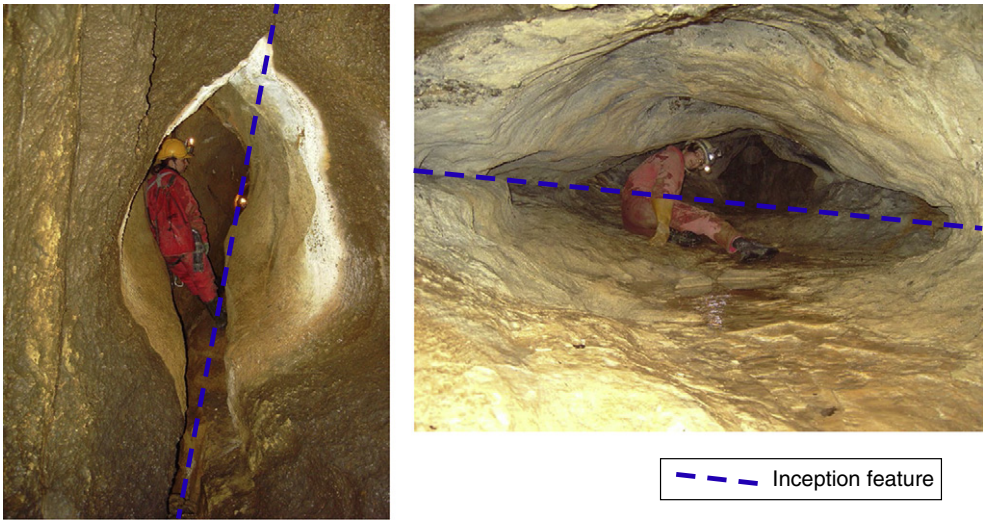

Fig. 2. Examples of karstic conduits showing shapes strongly elongated along inception features (left: Cave O80, Switzerland; right: Grottes aux fées, Switzerland).

"velocity" field that controls the front propagation of the fast marching method (Section 4). This new methodology allows us to simulate specific shapes that are realistic and consistent with geological settings and speleological knowledge of the system (Section 5).

2. Geomorphological analysis of the karstic conduits

Because karsts result from fluid circulation and dissolution capacity, the vulnerability to dissolution of the surrounding rocks plays a major role in their genesis. More particularly, karstic networks tend to develop along weakness features — either lithostratigraphic inception features, such as beds or bedding planes, or tectonic inception features, such as fractures or faults (e.g., Jameson, 1985; Lowe, 1992; Faulkner, 2006; Filipponi, 2009). These features are characterized by a strong contrast with the surrounding formations in terms of physical, lithological and/or chemical properties, such as the permeability. This contrast has a major influence on karst genesis (Filipponi, 2009; Filipponi et al., 2010): the inception features favour primary fluid circulations because of it and, thus, primary rock dissolution.

The dissolution process and the path development are not uniform in space due to the three-dimensional nature of the genesis processes and the geometrical anisotropy of the inception features. These features favour a differential dissolution, leading to an elongation of the conduits along them — often with pronounced angles — and explaining their non-cylindrical appearance in cross-section (Fig. 2). The resulting shapes are consequently more or less elliptical depending, for instance, on the dissolution capacity of the fluids or on the contrast in permeability or in carbonate content between the inception feature and the surrounding formations (Filipponi, 2009).

According to various authors, the groundwater table has a major influence on conduit development (e.g., Jameson, 1985; Ford & Williams, 2007; Farrant & Smart, 2011; Jaillet et al., 2011). In the phreatic zone, corresponding to the saturated zone below the water table, the inception features are the most influential factor upon the resulting shapes (Filipponi et al., 2009). The dissolution acts on whole conduits and in all directions. The shapes are then more or less jagged, depending on the fluids, on the surrounding rocks and on the presence of other inception features (Figs. 2, 4.1) (e.g., Jameson, 1985; Lauritzen & Lundberg, 2000; Filipponi, 2009). The vadose zone corresponds to the zone above the current water table. But the observed conduits are usually the result of a long process that has involved a past phreatic development. Keyhole passages are among the most common cross-sectional conduit geometries that are encountered (Field, 2002). They are characterized by an entrenchment, a canyon passage commonly narrower than the original passage, also called the trench. Indeed, a drop of the water table puts the original conduits in phreatic conditions. The fluids circulating in the conduits with high velocities are led by gravity, incising the floor, generating these typical cross-sectional keyhole shapes (Figs. 3, 4.2) (e.g., Jameson, 1985; Lauritzen & Lundberg, 2000; Filipponi, 2009; Jaillet et al., 2011). Horizontal dissolution notches are less common. They develop at the water table interface when conduits are partially flooded and water level variations are small enough to favour a lateral incision (e.g., Lauritzen & Lundberg, 2000; Ford & Williams, 2007; Farrant & Smart, 2011). Geometrically speaking, notches have a rounder aspect than shapes linked to inception features (Fig. 4.3).

In the following, we explain how these different observed geometries can be integrated in the ODSIM method to improve the realism of simulated karst conduits.

3. Principle of the object-distance simulation method

Henrion et al. (2010) proposed an object-distance simulation method (ODSIM) that models a three-dimensional envelope around a

Fig. 3. Example of a keyhole passage (Sieben Hengste Cave System, Switzerland).

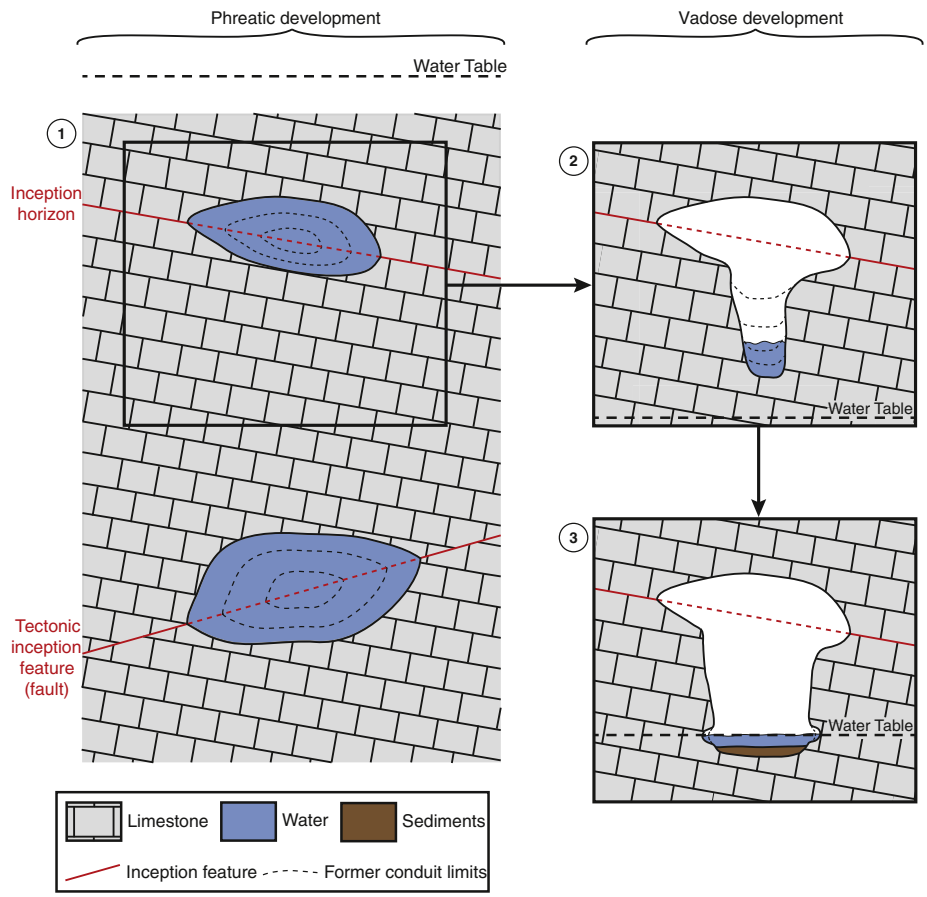

Fig. 4. Evolution of a karstic conduit depending on its position relative to the water table: 1. Genesis and growth of two conduits in the phreatic zone following different weakness planes (a lithostratigraphic horizon for the upper one, a fault for the other). 2. Following a fall of the water table, the upper conduit goes through the vadose zone which progressively generates a keyhole passage by cutting a trench. 3. Following a rise of the water table, notches grow at the trench bottom.

skeleton. For the explored parts of a karst, that skeleton can be provided by field data, such as two-dimensional maps or LRUD (Left, Right, Up and Down) data. Otherwise, stochastic simulations can be used to obtain several skeletons and take into account the uncertainties related to the conduit location (e.g., Pardo-Igúzquiza et al., 2011; Borghi et al., 2012; Collon-Drouaillet et al., 2012). The ODSIM method consists of computing a Euclidean distance field around the skeleton and perturbing it using a random threshold (Fig. 5). This threshold can be generated using a sequential Gaussian simulation (SGS) or other stochastic simulation methods (e.g., Deutsch & Journel, 1997; Goovaerts, 1997). As a stochastic simulation method, the SGS can provide an infinity of thresholds. This allows us to build several envelopes for a given skeleton, thus catching the uncertainties around the conduit shape. The perturbation is done using the following indicator function:

$$I_B(p) = \begin{cases} 1 \text{ if } D(p) \leq \varphi(p) \\ 0 \text{ else} \end{cases} \quad (1)$$

$D(p)$ is the 3D distance field computed at each point $p = [p_x p_y p_z]^T$ of a grid G and $\varphi(p)$ is the random threshold. The computed indicator property $I_B(p)$ is equal to 1 in the geological body, 0 outside. The 3D envelope corresponds to the surface at the interface between the interior and the exterior of the region corresponding to 1, or equivalently to points at a given distance of the network: $D(p) \leq \varphi(p)$. In this method, the simulated conduits can be complied with hard data conditioning (like well data or LRUD distances to walls) thanks to an iterative Gibbs sampling algorithm (Geman & Geman, 1984) with inequality constraints (Freulon & de Fouquet, 1993).

With this approach, the only way to avoid a globally cylindrical shape is to use plane skeletons instead of curves. However, the resulting envelope keeps a round aspect at the plane extremities because of the Euclidean distance. Furthermore this approach lacks flexibility when dealing with various and complex shapes, such as those seen in Section 2.

4. Integration of geomorphological information in ODSIM

The proposed methodology keeps the basic principle of ODSIM: the "distance" to an object model controls the first-order features while a random field provides the fine-scale features (Henrion et al., 2010). Our proposal is to play on these two scales. First, by using a custom distance field generated by a fast marching method and constrained to geomorphological information. This allows us to take into account simultaneously various elements involved in the conduit genesis and so influencing the conduit shapes. Second, we propose to build a random threshold by combining different variograms and/or distributions depending on the elements constraining the custom distance field (Fig. 6).

4.1. Using of a custom distance field instead of an Euclidean distance field

The fast marching method (Sethian, 1996; Sethian, 1999a; Sethian, 1999b) concerns the propagation of a front knowing its speed. The principle is to solve the Eikonal equation:

$$|\nabla T| F = 1. \quad (2)$$

T is the time field and F the velocity field. $1/F$ gives a slowness field.

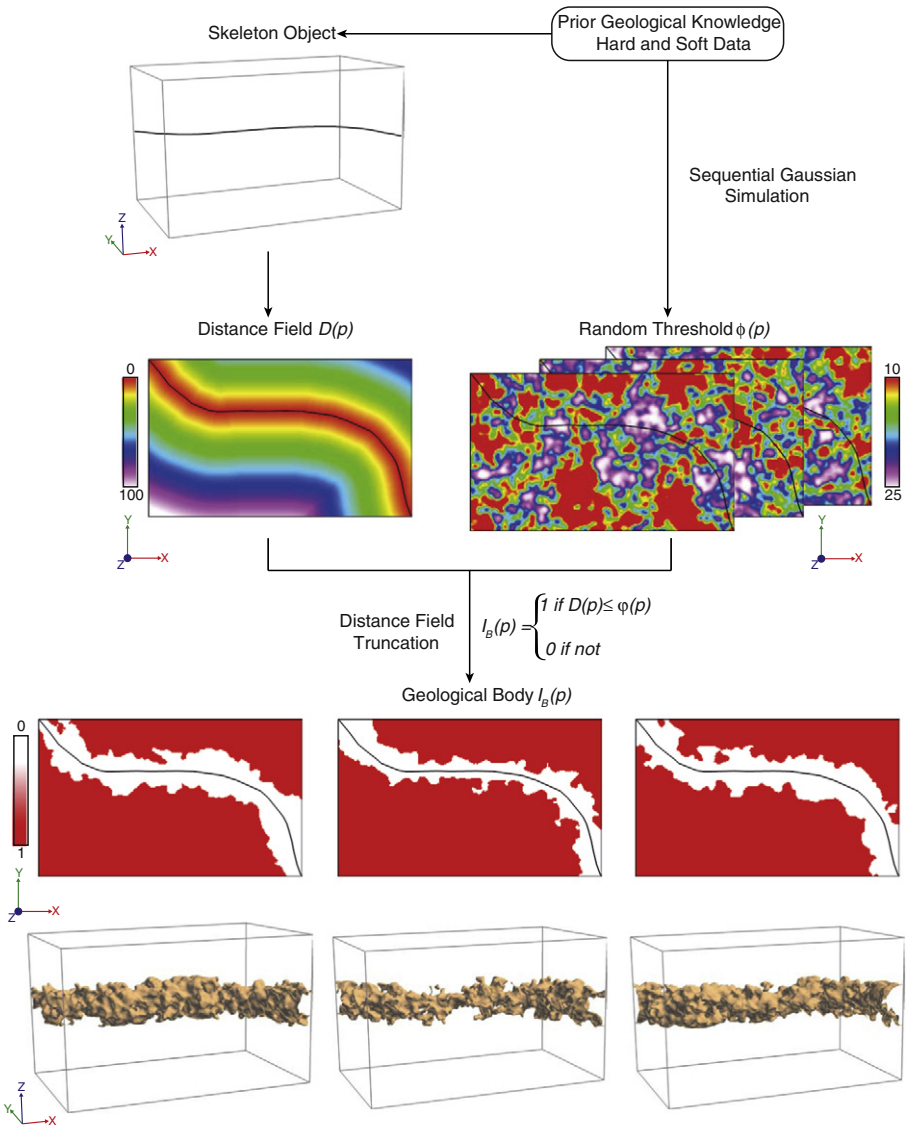

Fig. 5. ODSIM workflow (modified from Henrion et al. (2010)) applied to a karstic conduit generation. The distance field $D(p)$ is truncated with the random threshold $\varphi(p)$ giving an indicator property $I_B(p)$ of the karstic conduits and caves.

This method creates a scalar field corresponding to the arrival time $T(x, y, z)$ at which the propagation front reaches the position (x, y, z), depending on a predetermined velocity field (or equivalently a slowness field) (Fig. 7). This velocity field characterizes the speed of the front for each position (x, y, z).

In a modelling approach, a convenient aspect is that the choice of the velocity field constrains the evolution of the front and the resulting arrival time field. Putting higher values for inception features in the velocity field constrains the time field in such a way that it contains geomorphological information, providing the custom distance field (Fig. 7). Using a fast marching method gives thereby a greater flexibility to ODSIM. Nevertheless, the property used to compute the velocity field has to be thoughtfully chosen. As underlined by Borghi et al. (2012), contrasts between the values are more important than values themselves when using the fast marching method. The velocity field has to be linked with a property of the medium that respects this contrast rule.

As the notion of contrast controls both the fast marching and the karst genesis, the velocity field is built by using the permeability (or the hydraulic conductivity). This provides emphasis on the weakness planes, and moreover simplifies the choice of the property values. However, it is not sufficient to model specific structures like those encountered in the vadose zone and specific strategies need to be developed.

4.2. Building the velocity field for the vadose zone

Structures developed in vadose conditions are the result of several speleogenetic phases, corresponding to several water table positions. The goal of our method is not to reproduce each of these phases one after the other as a genetic model would do it. Instead, we propose numerical strategies to reproduce directly final conduit geometries consistent with the speleologist's observations and knowledge.

For reproducing the keyhole geometry, and more specifically the trenches appearing on the conduit floors, we propose to use an "attraction level" with high velocity values similar to those of the inception features. This attraction level may correspond to the present water table. A vertical plane between the skeleton and the attraction level is then considered as a high velocity zone by extending the attraction level values (Fig. 8). This modification constrains the front propagation which goes toward that level.

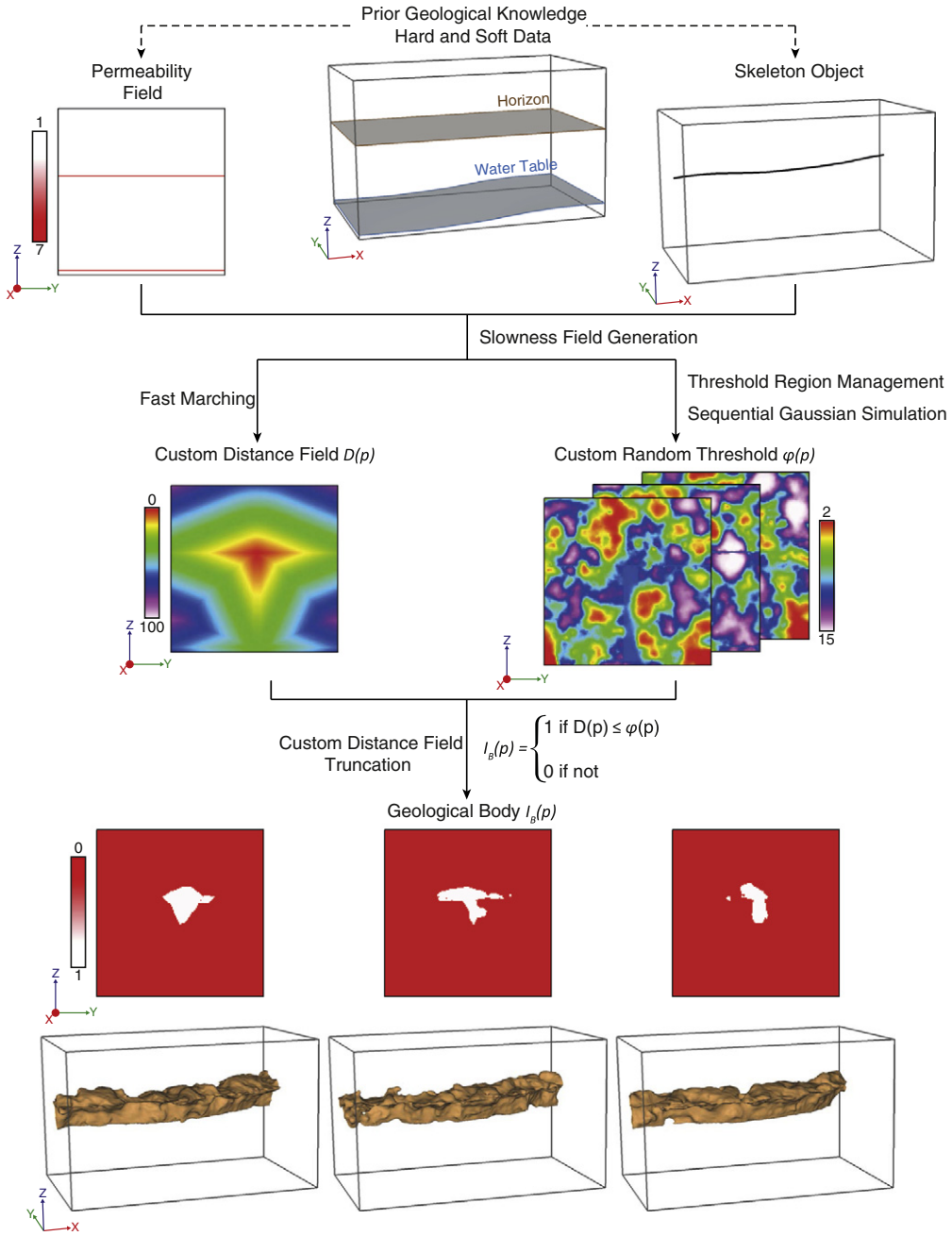

Fig. 6. New workflow for ODSIM. The original method is obtained by using a constant velocity or slowness field and the same parameters for the whole threshold. *Slowness field generation* and *fast marching* steps are further detailed in Sections 4.1 and 4.2; *threshold region management* step is detailed in Section 4.3.

To limit the effects of the attraction level on the highest conduits, a parameter representing the maximum allowed distance $d_{\max}$ between the skeleton and the attraction level is added to generate these trenches. Moreover, the distance between the skeleton and the attraction level d is used to obtain shorter depths for trenches as the conduits move away from the water table. To do that, the permeability values of the attraction level in the vertical plane building the trenches are multiplied by a factor integrating $d/d_{\max}$, giving the vertical trench plane velocity values v:

$$v(x_s, y_s, z) = m \times \left(1 - \frac{d(x_s, y_s)}{d_{\max}}\right) \times p_w(x_s, y_s, z_w) \quad (3)$$

(x_s, y_s, z_s) is a point of the skeleton, (x_w, y_w, z_w) is a point of the attraction level, z is bounded by z_s and z_w, m is a multiplication factor defined by the user, $d_{\max}$ sizes the zone of influence of the attraction level, v is the velocity value of the vertical plane at a given point (x_s, y_s, z), d is the distance between the skeleton and the attraction level at the same horizontal coordinates (x_s, y_s) and p_w is the permeability value at the attraction level at the same horizontal coordinates (x_s, y_s).

Using d causes trench depth to evolve smoothly with the distance between the skeleton and the attraction level and avoids sharp entrenchment endings on the boundaries of the influence zone (Fig. 9).

If the difference between the velocity values of the attraction level and those of the surrounding formation is not significant, the

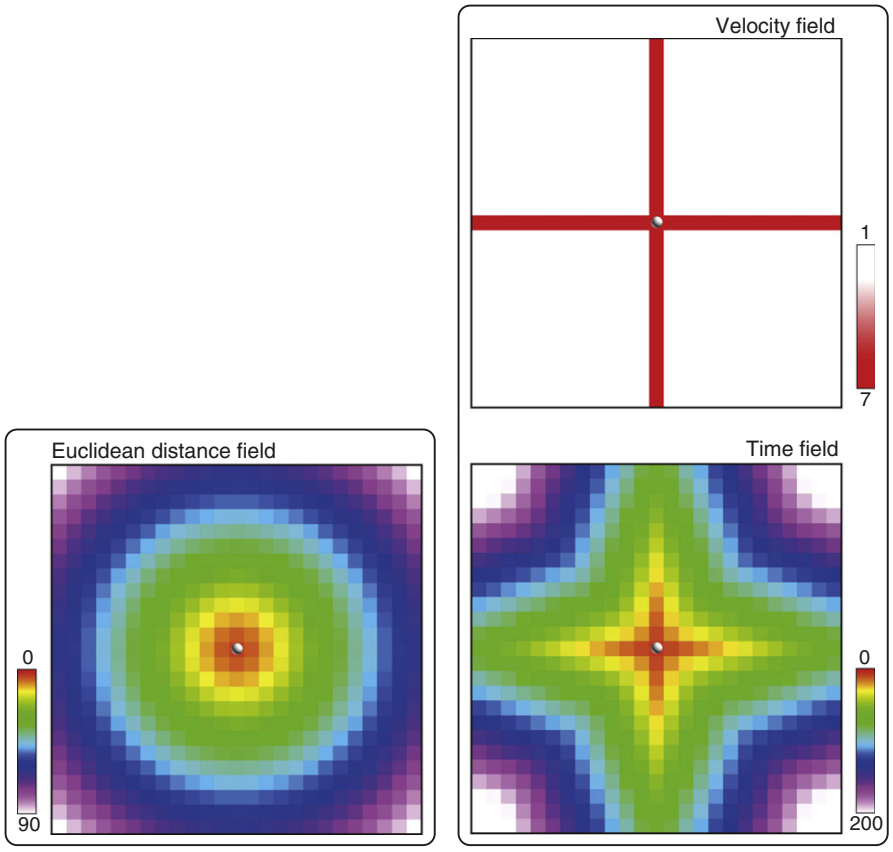

Fig. 7. Comparison between an Euclidean distance field and a field generated by fast marching. Both fields are generated from the central node of the grid, but the time field is constrained by the differences of speed given by the velocity field.

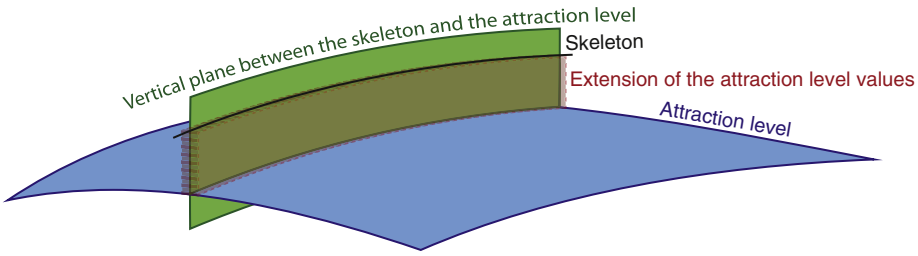

Fig. 8. Foundations for trench modelling: a vertical plane between the skeleton and the attraction level is considered. The values of the attraction level crossed by the plane are extended vertically up to the skeleton.

factor $(1 - d/d_{max})$ can invert their contrast, leading to lower velocity values for the vertical plane and so a poor front propagation. The multiplication factor m solves this issue and gives the user a control on the trench depth.

With only one column of cells representing the vertical trench plane in the grid, the resulting trenches are V-shaped and do not show vertical sides or a flat bottom. Thus, several parameters are added to give more control to the propagation of the front and be sure it gives a satisfying shape to the envelope. The main point is to extend the vertical plane sideways, using a width w and a "beginning distance" d_b to ensure straighter sides of the trenches (Fig. 10.1).

Notches are often smooth shapes created while the water table is superimposed on the conduits. These features can be easily modelled by thickening the (paleo)water table(s) in the velocity field using a factor n (Fig. 10.2). The thickening controls the smoothness and the height of the notch shape. The notch depth can be controlled by applying a multiplication factor on the velocity values around the (paleo)water table(s).

4.3. Management of the different scales of perturbations on the envelope

As said before, the velocity field controls the coarse-scale shape of the conduits, but the focus of the ODSIM approach is to combine this

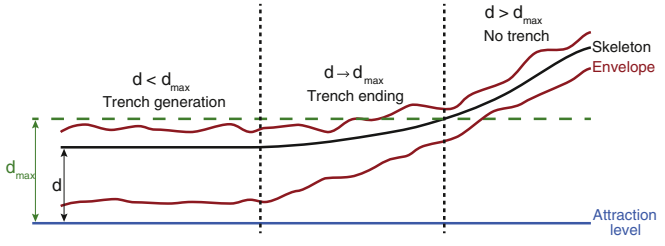

Fig. 9. Consequences on the envelope of the variations of the distance d between the skeleton and the attraction level, illustrating the impact of the formula (3). The permeability values p_w are taken from the attraction level and the distance d_{max} is defined by the user and represents the maximum allowed distance to generate a trench.

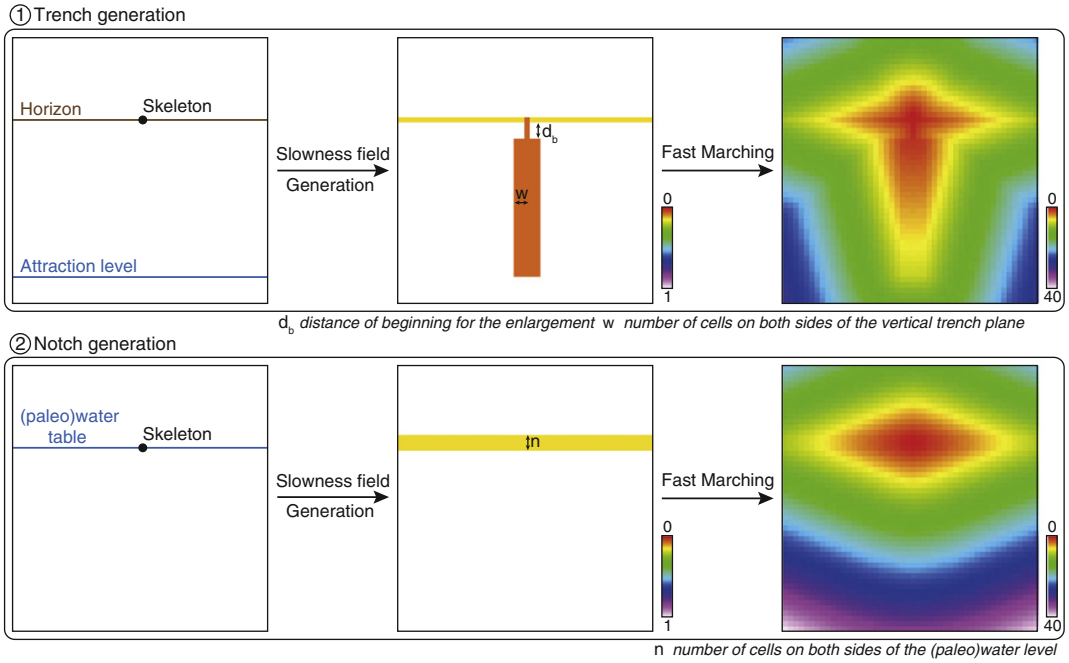

Fig. 10. Modifications of the slowness field allowing the generation of trenches and notches. The global shape of these elements is clearly visible in the field created by fast marching.

field with a random threshold that perturbs this "perfect" geometry by introducing fine-scale variability and also allows hard data conditioning. In their paper, Henrion et al. (2010) have proposed to introduce a locally variable mean into the sequential Gaussian simulation in order to accommodate a spatial trend. But this kind of modification would equally affect roof, walls and floors of the conduits by a progressive growing or narrowing.

Considering cave conduit geometries, it appears that these fine-scale variabilities are not identically affecting the roof, the walls or the floor. Due to many different factors, like breaking-down, mechanical and chemical erosion, it is common to have more variabilities along a roof than, particularly, on the bottom of a trench. Thus, conduit irregularities are not symmetrical and, moreover, their variations do not range between the same extrema (Fig. 11). Such differences between conduit ceiling, floor and/or sides can be noticed in several conduits, such as in the Abracurrie Main Chamber, Nullarbor, Australia (James et al., 2012) or in the Clearwater Cave, Gunung Mulu, Sarawak (Farrant & Smart, 2011).

Fig. 11. Example of a passage with different scales of perturbation: the top and the floor of the conduit are roughly flat whereas its sides are more wavy (Mammoth Cave, US).

To model a smooth trench floor, for instance, we propose to separate the grid in two areas: the first one contains the vertical trench planes — with eventually an extension around the planes to avoid trench side protuberances to develop below the trench floor when using very high perturbations, and the second one the rest of the grid. Then two distinct variograms and/or distributions are defined in each area. The sequential Gaussian simulation generating the random threshold has to preserve a continuous resulting field between those areas (Fig. 12).

Increasing the range of the variogram used on the trench planes smoothes their bottom while preserving small scale perturbation on the trench sides. Reducing the amplitude of the values used for the probability density function (PDF) on the trench planes avoids obtaining a large range of variation for the conduits at the bottom (Fig. 13). The same method can be applied to reduce the roughness along weakness planes. Eventually, the use of several variogram models and/or distributions for each element controlling the shape gives differential perturbations of the envelope.

5. Results and discussion

These extensions of ODSIM have been implemented as a plugin of the GOCAD geomodelling software[4] and written in C++. It should be noted that this work can be developed in another modelling software, in a numerical computing environment such as MATLAB or Scilab as well as in a stand-alone application. The methodology has been tested on two synthetic cases. By using synthetic cases, we can easily demonstrate the new possibilities (cylinder, lens, keyholes, …) offered by the method in a few examples, without falling into a controversial context. To better illustrate the independence between the skeleton simulation and the three-dimensional envelop modelling, the same karstic skeleton is used

[4] http://www.pdgm.com/products/GOCAD.

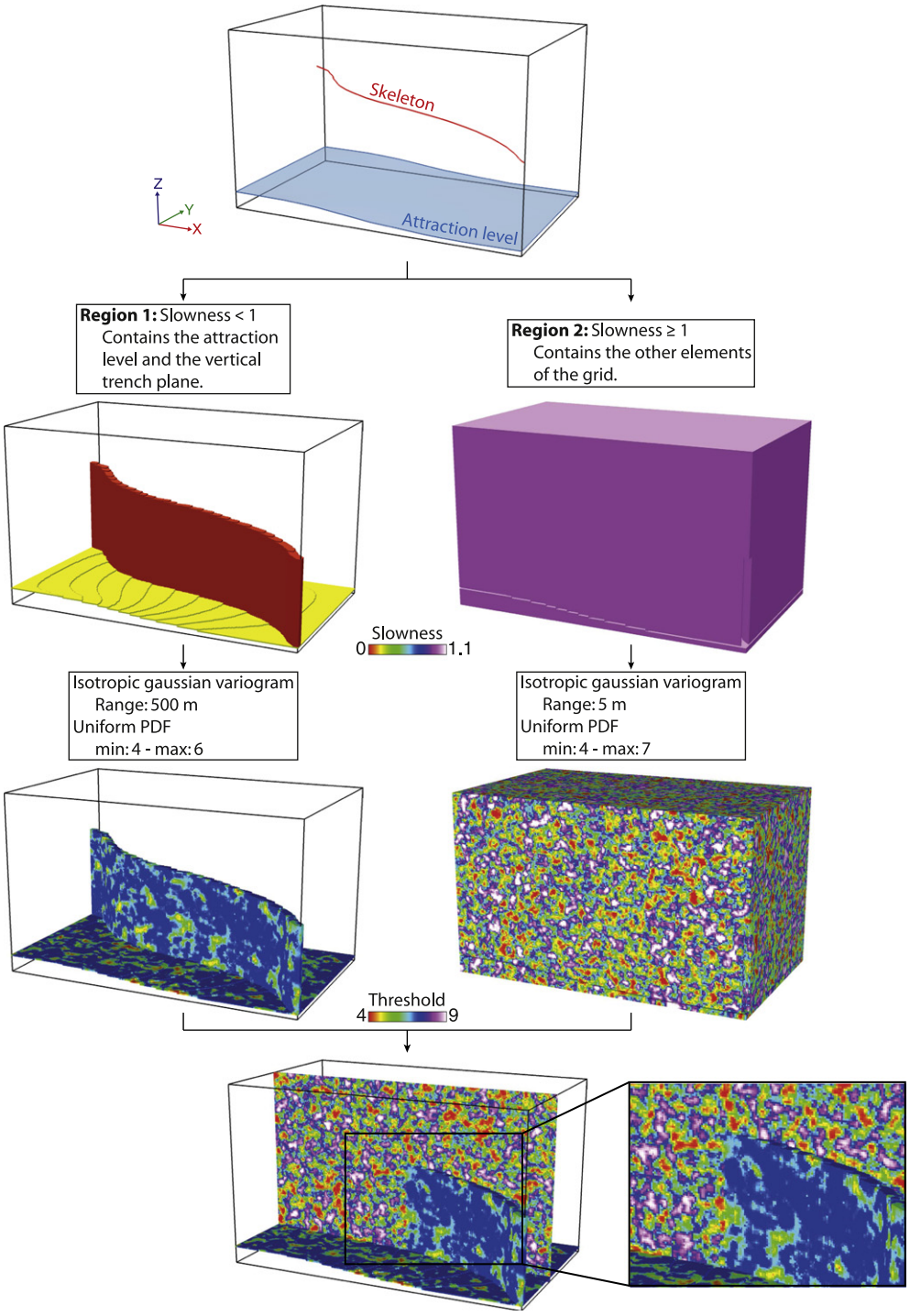

Fig. 12. Threshold generation example: the principle is to separate the structures with different perturbation types using their values in the slowness field. Here only two areas are created: the last screenshot shows the region 1 together with a section along the whole *x* axis, showing elements of the region 2. The enlargement on the right shows the continuity between the features of the two areas despite the two different distributions and variograms. This continuity is essential for obtaining good quality envelopes.

in the following examples. Inception features, water table and attraction level are modelled with triangulated surfaces. For the threshold simulations, a regular structural grid has been used. Both examples are supposed to be the expression of two genetic phases: i) an initial phreatic phase that is visible on the final shapes through an elongation along inception features; ii) and a second phase that results from a lowering of the water table. In the first example, to illustrate trench modelling capacities, an attraction level has been introduced at the water table level. The distance d_{max} has been chosen to limit entrenchments to the lowest conduit (Fig. 14). The various parameters used in this simulation are presented in Table 1 (Example 1). In the second example, we wanted to test the capacity of the method to reproduce notches (Fig. 15). A water table is thus introduced at the same altitude as the lowest conduits. It is duplicated into an attraction level to simultaneously develop trenches on the upper conduit, superposed to the inception elongation features. Detailed parameters are presented in Table 1 (Example 2).

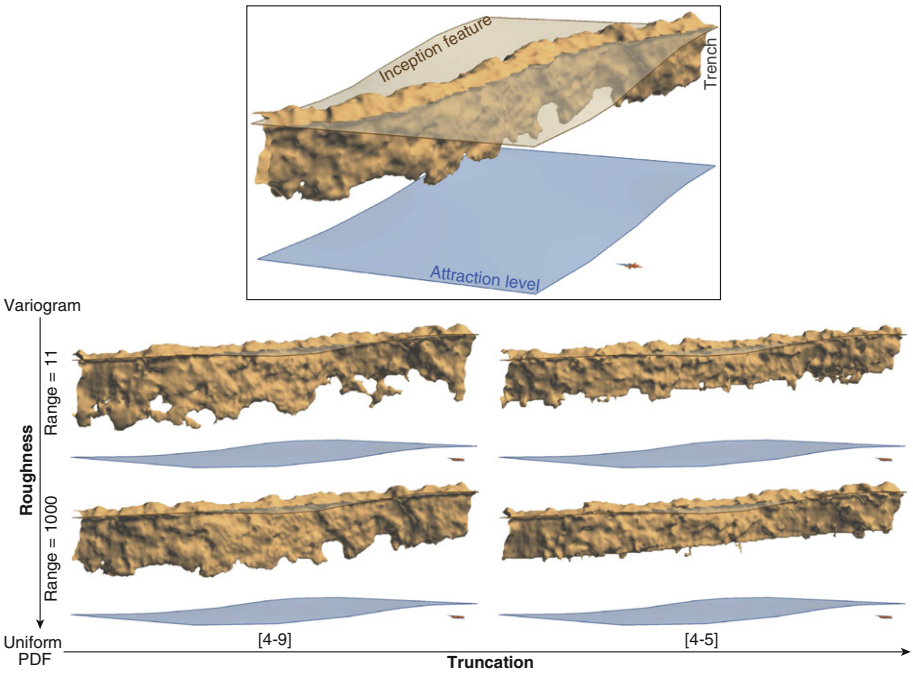

Fig. 13. Impact of the variogram and distribution used to generate the threshold: side view of the resulting envelopes. The given parameters are those of the weakness planes and the trench plane, the rest of the grid having a variogram range of 11 m and a uniform PDF of [4–9]. The velocity field values are 5 for the previous planes and 1 in the rest of the grid.

The resulting envelopes reflect the various coarse-scale karstic shapes that are now possible to model with this new methodology: i) lengthening and sharp incision along inception features (stratigraphical and tectonic); ii) realistic symmetric round shapes for the vertical conduits; iii) trenches superposed on a cylindrical or lens shape for keyhole passages; and iv) longitudinal notches. All these features can be combined. What trenches concern, depth variations follow the position of the conduits relatively to the attraction level: the further from the attraction level the conduits are, the lower is the trench depth. Their bottom is smoother than the shapes linked to the inception features thanks to the combined use of different variograms and distributions in the random threshold generation. Notch representations are more like a rounding of the lateral carving although they can be more "marked" in the caves. The result remains useful in representing large notches. Generally, the proposed methodology offers an interesting list of solutions to simulate or reconstruct realistic three-dimensional karstic conduits. In this dual-scale geostatistical simulation method, the coarse-scale features can be modelled by an adapted and modular combination of a skeleton representation of the studied object and geological/speleological constraints defined by the user.

This results in a custom velocity field representing the coarse-scale geometries. A solution is proposed for managing the different fine-scale features depending on the same geological/speleological constraints. The Gibbs sampler with inequality constraints algorithm — which is

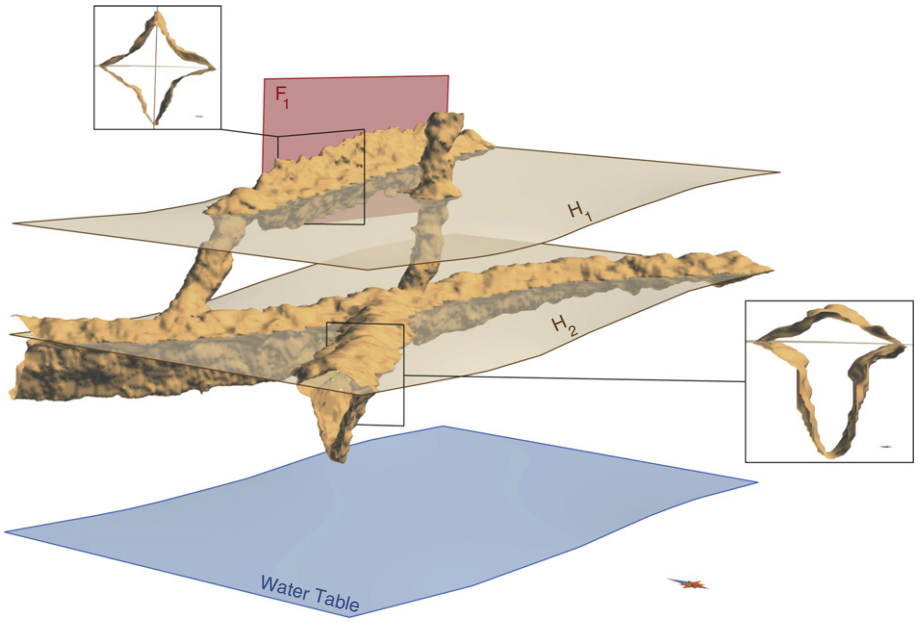

Fig. 14. Simulated envelope obtained by using two stratigraphic inception features (H_1 and H_2), one tectonic inception feature (fault F_1) and an attraction level. Complex three-dimensional karst features such as trenches or elongated shapes are successfully reproduced.

Table 1
Summary of parameters used to create the two synthetic models.

	Example 1	Example 2
GRID PARAMETERS		
Grid size (in cell)	250 × 150 × 150	250 × 150 × 150
Cell size (in m)	1 × 1 × 1	1 × 1 × 1
FAST MARCHING PARAMETERS		
Initial slowness field		
H_1 slowness value	0.2	0.2
H_2 slowness value	0.2	–
F_1 slowness value	0.2	0.2
Water table slowness value	0.2	0.2
Matrix slowness value	1	1
Trench parameters		
d_{max} (in m)	70	70
d_b (in cell)	4	4
w (in cell)	1	1
Notch parameters		
n (in cell)	–	1
THRESHOLD PARAMETERS		
Low slowness region (*Slowness* < 1)		
Variogram		
Type	Gaussian	Gaussian
Range (in m)	500	500
Distribution		
Type	Uniform	Uniform
Min–Max	4–6	4–6
High slowness region (*Slowness = 1*)		
Variogram		
Type	Gaussian	Gaussian
Range (in m)	7	7
Distribution		
Type	Uniform	Uniform
Min–Max	4–7	4–7

already available in the method (Henrion et al., 2010) — complements this toolbox by allowing hard data conditioning. Some further work is required to quantitatively validate the method capacity to reproduce realistic shapes. Several solutions could be explored:

- Compare a cave already modelled using a LiDAR survey or 2D sections and maps with several simulated conduits. Due to the stochastic nature of the process, the direct assessment of the real and simulated passage fit is worthless: a simulated conduit can be geomorphologically consistent even if it does not fit the real conduit. Some indicators have to be developed to capture the entire three-dimensional characteristics of a conduit, such as, for instance, the conduit volume or the ratio of conduit surface area to conduit volume. Those indicators are then used to compare the real conduit and the simulated ones.
- Compare the simulated shapes for the unknown parts of a network with the conditioned shapes in the known parts based on statistical or fractal-based principles such as introduced by Curl (1986) (e.g., Pardo-Iguzquiza et al., 2011).

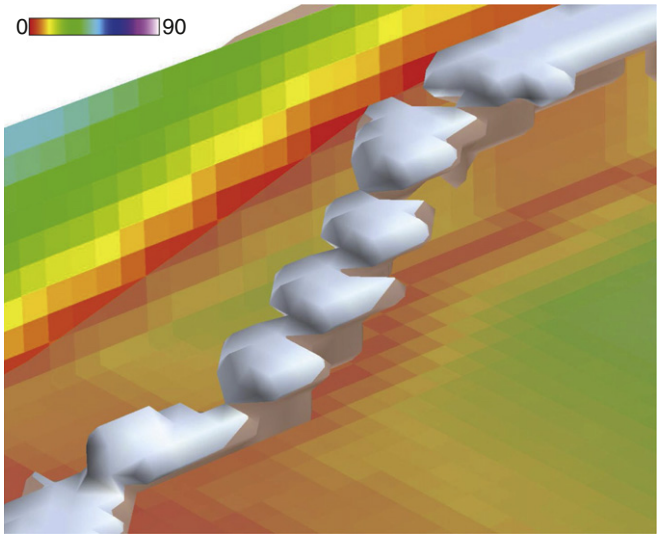

Fig. 16. Insufficient grid resolution leading to a non-continuous karstic conduit simulation. The colours correspond to the custom distance field and the transparent surface represents the weakness plane.

Despite these encouraging results, some limitations appear. First, the grid resolution can have a significant impact on the results. Indeed the introduction of the inception features in a velocity property corresponds to their rasterization in the grid. Stratigraphic inception horizons have a thickness of some centimetres to some decimetres (Filipponi, 2009), and conduits may be very stretched along them. Moreover, tectonic inception features induce very thin shapes at the intersection with the conduit. This means that shape modelling requires high grid resolutions,

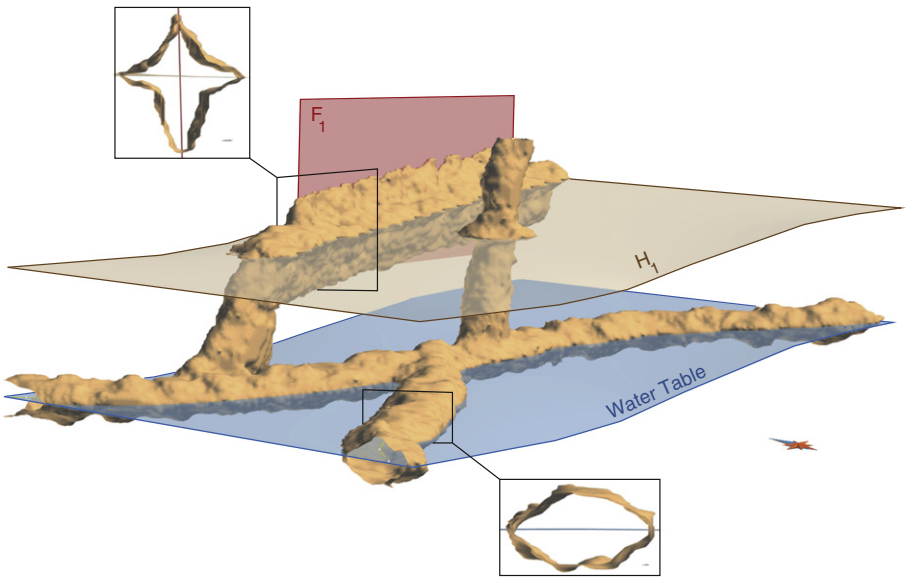

Fig. 15. Simulated envelope obtained by using one stratigraphic inception feature (H_1), one tectonic inception feature (fault F_1) and an attraction level superimposed on a water table at the same level as the lowest conduits. Complex three-dimensional karst features such as notches, trenches or elongated shapes are successfully reproduced.

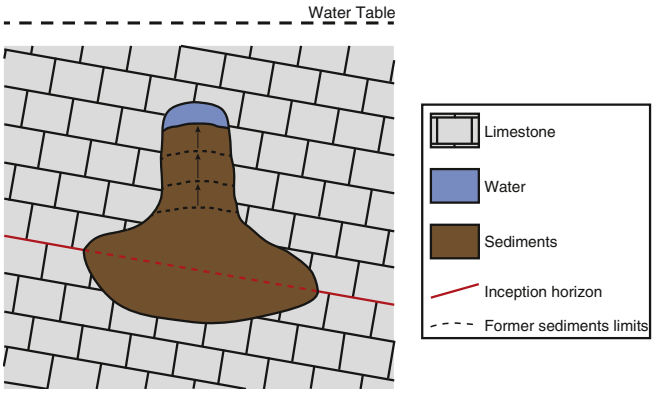

Fig. 17. Principle of the development of the paragenetic conduits: sediments progressively fill the cavity and block the downward dissolution, which favours an upward dissolution propagation.

at least to represent the global shape of the conduits in an acceptable way (Fig. 16). Another solution would be to have a non-regular grid organized along inception features. Second, the increase of the degrees of freedom in the process has a direct consequence on the increase of user choices and parameters, even if many features can be integrated directly in the custom distance field. But this last limitation is directly linked to the complexity of the studied case and difficult to avoid. Nevertheless, perhaps a new alternative could be found that avoids the use of the d_b and w parameters in the trench modelling process.

As for perspectives, a modelling method for other shapes could be studied. For instance paragenetic caves are made of conduits developed in the phreatic zone shaped like upside-down trenches, displaying an upward entrenchment of conduits (Fig. 17) (Renault, 1958; Pasini, 1967; Renault, 1968). They could probably be modelled with the same principle as trenches, but upturned. Another common geometry, partially linked to breakdowns, is strike-oriented passages (e.g., Palmer, 2012) that have a polygonal shape following horizons, with many perpendicular angles (Fig. 18). Even if various scales of variability are introduced in the simulated conduits through the threshold field, small-scale features such as scallops can still not be clearly and deliberately represented. On the other hand, larger scale features, such as conduit loops, are not linked to the conduit shape but to the network and should be introduced by the skeleton.

In a broader perspective, tests are required to assess the impact of these shapes on flow simulations. Modelling sediments could also be interesting considering their impact on fluid flows and on speleogenesis (Farrant & Smart, 2011). Finally, the entire methodology could be adapted to other underground processes, such as hydrothermal alteration, or be used to study the usefulness and applicability of the method in sinkhole prevention.

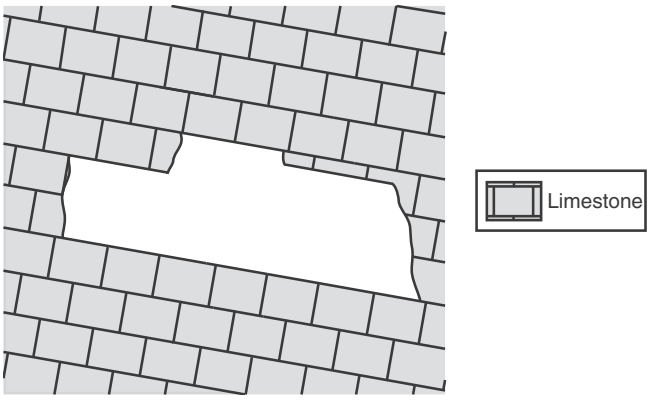

Fig. 18. A strike-oriented passage: the conduit shape follows lithostratigraphic horizons.

6. Conclusions

These improvements of ODSIM allow the stochastic generation of karst conduit envelopes around a skeleton by taking into account local geological information, especially inception features and (paleo)water table. It consequently contributes to the global workflow of stochastic karst generation, complementing the methods that stochastically generate skeletons representing the general network by introducing geomorphologically consistent conduit shapes. Various classic conduit shapes can be simulated, such as elongated or keyhole passages, while preserving the original capacities of ODSIM. Some other particular shapes still need to be taken into account to allow their simulation. Applying this method on synthetic cases gives quite satisfying results. The simulated shapes finely reproduce the most common conduit geometries while controlling the different scales and areas of shape perturbations. However, a confrontation to real data still needs to be carried out; first to validate the application to the reconstruction of explored and monitored conduits, then to validate more objectively the method's capacity to generate realistic conduits.

Acknowledgements

We would like to thank the industrial and academic members of the GOCAD Consortium,[5] especially Paradigm for providing the GOCAD Software and API, ASGA (Association Scientifique pour la Géologie et ses Applications) and the French National Scientific Research Center CNRS - GeoRessources for their support. We would also like to thank the reviewers, including Ph. Häuselmann, for constructive comments which helped improve this paper. This work was performed in the framework of the "Investissements d'avenir" Labex RESSOURCES21 (ANR-10-LABX-21).

References

Boggus, M., Crawfis, R., 2009. Explicit generation of 3D models of solution caves for virtual environments. Proceedings of the 2009 International Conference on Computer Graphics and, Virtual Reality, pp. 85–90.
Borghi, A., Renard, P., Jenni, S., 2012. A pseudo-genetic stochastic model to generate karstic networks. J. Hydrol. 414–415, 516–529.
Brinkmann, R., Parise, M., Dye, D., 2008. Sinkhole distribution in a rapidly developing urban environment: Hillsborough County, Tampa Bay area, Florida. Eng. Geol. 99, 169–184.
Chaojun, Z., Chengzao, J., Benliang, L., Xiuyu, L., Yunxiang, L., 2010. Ancient karsts and hydrocarbon accumulation in the middle and western parts of the North Tarim uplift, NW China. Pet. Explor. Dev. 37, 263–269.
Collon-Drouaillet, P., Henrion, V., Pellerin, J., 2012. An algorithm for 3D simulation of branchwork karst networks using Horton parameters and A-star. Application to a synthetic case. Geol. Soc. Lond. Spec. Publ. 370, 12. http://dx.doi.org/10.1144/SP370.3.
Curl, R.L., 1986. Fractal dimensions and geometries of caves. Math. Geol. 18, 765–783.
Deutsch, C.V., Journel, A.G., 1997. GSLIB: Geostatistical Software Library and User's Guide (Applied Geostatistics). Oxford University Press, USA.
De Waele, J., Gutiérrez, F., Parise, M., Plan, L., 2011. Geomorphology and natural hazards in karst areas: a review. Geomorphology 134, 1–8.
De Waele, J., Plan, L., Audra, P., 2009. Recent developments in surface and subsurface karst geomorphology: an introduction. Geomorphology 106, 1–8. http://dx.doi.org/10.1016/j.geomorph.2008.09.023.
Farrant, A.R., Smart, P.L., 2011. Role of sediment in speleogenesis; sedimentation and paragenesis. Geomorphology 134, 79–93.
Faulkner, T., 2006. Tectonic inception in Caledonide marbles. Acta Cardiol. 35, 7–21.
Field, M.S., 2002. A lexicon of cave and karst terminology with special reference to environmental karst hydrology. National Center for Environmental Assessment, Washington Office, Office of Research and Development, US Environmental Protection Agency.
Field, M.S., Pinsky, P.F., 2000. A two-region nonequilibrium model for solute transport in solution conduits in karstic aquifers. J. Contam. Hydrol. 44, 329–351.
Filipponi, M., 2009. Spatial Analysis of Karst Conduit Networks and Determination of Parameters Controlling the Speleogenesis along Preferential Lithostratigraphic Horizons. Ph.D. Thesis École Polytechnique Fédérale de Lausanne, Suisse.
Filipponi, M., Jeannin, P.Y., Tacher, L., 2009. Evidence of inception horizons in karst conduit networks. Geomorphology 106, 86–99.
Filipponi, M., Jeannin, P.Y., Tacher, L., 2010. Understanding cave genesis along favourable bedding planes. The role of the primary rock permeability. Z. Geomorphol. Suppl. 54, 91–114.

[5] http://www.gocad.org.

Ford, D., Williams, P., 2007. Karst Hydrogeology and Geomorphology. John Wiley and Sons, Ltd.
Freulon, X., de Fouquet, C., 1993. Conditioning a Gaussian model with inequalities. In: Soares, A. (Ed.), Geostatistics Tróia '92. Springer Netherlands. Number 5 in Quantitative Geology and Geostatistics, pp. 201–212.
Frumkin, A., Karkanas, P., Bar-Matthews, M., Barkai, R., Gopher, A., Shahack-Gross, R., Vaks, A., 2009. Gravitational deformations and fillings of aging caves: the example of Qesem karst system, Israel. Geomorphology 106, 154–164.
Geman, S., Geman, D., 1984. Stochastic relaxation, Gibbs distributions, and the Bayesian restoration of images. IEEE Transactions on Pattern Analysis and Machine Intelligence pp. 721–741.
Goldscheider, N., 2008. A new quantitative interpretation of the long-tail and plateau-like breakthrough curves from tracer tests in the artesian karst aquifer of Stuttgart, Germany. Hydrogeol. J. 16, 1311–1317.
Goovaerts, P., 1997. Geostatistics for natural resources evaluation. Applied GeostatisticsOxford University Press, New York.
Hartmann, A., Lange, J., Aguado, A.V., Mizyed, N., Smiatek, G., Kunstmann, H., 2012. A multi-model approach for improved simulations of future water availability at a large Eastern Mediterranean karst spring. J. Hydrol. 468–469, 130–138.
Hauns, M., Jeannin, P.Y., Atteia, O., 2001. Dispersion, retardation and scale effect in tracer breakthrough curves in karst conduits. J. Hydrol. 241, 177–193.
Henrion, V., Caumon, G., Cherpeau, N., 2010. ODSIM: an object-distance simulation method for conditioning complex natural structures. Math. Geosci. 42 (8), 911–924.
Horvatinčić, N., Krajcar Bronić, I., Obelić, B., 2003. Differences in the ^{14}C age, $\delta^{13}C$ and $\delta^{18}O$ of Holocene tufa and speleothem in the Dinaric karst. Palaeogeogr. Palaeoclimatol. Palaeoecol. 193, 139–157.
Jaillet, S., Sadier, B., Arnaud, J., Azéma, M., Boche, E., Cailhol, D., Filipponi, M., Roux, P.L., Varrel, E., 2011. Topographie, représentation et analyse morphologique 3D de drains, de conduits et de parois du karst. Images et modèles 3D en milieux naturels. pp. 119–130.
James, J.M., Contos, A.K., Barnes, C.M., 2012. Nullarbor caves, Australia, In: White, William B., Culver, David C. (Eds.), Encyclopedia of Caves, second edition. Elsevier Science, pp. 568–576.
Jameson, R.A., 1985. Structural segments and the analysis of flow paths in the North Canyon of Snedegar Cave, Friars Hole Cave System. Master's Thesis West Virginia University, Morgantown.
Kuo, T.S., Liu, Z.Q., Li, H.C., Wan, N.J., Shen, C.C., Ku, T.L., 2011. Climate and environmental changes during the past millennium in central western Guizhou, China as recorded by Stalagmite ZJD-21. J. Asian Earth Sci. 40, 1111–1120.
Labourdette, R., Lascu, I., Mylroie, J., Roth, M., 2007. Process-like modeling of flank-margin caves: from genesis to burial evolution. J. Sediment. Res. 77, 965–979.
Lauritzen, S.E., Lundberg, J., 2000. Solutional and erosional morphology. Speleogenesis: Evolution of Karst Aquifers: Huntsville, AlaNational Speleological Society pp. 408–426.
Lowe, D.J., 1992. The Origin of Limestone Caverns: An Inception Horizon Hypothesis. Ph.D. Thesis Manchester Polytechnic, United Kingdom.
Lü, X., Yang, N., Zhou, X., Yang, H., Li, J., 2008. Influence of Ordovician carbonate reservoir beds in Tarim Basin by faulting. Sci. China Ser. D Earth Sci. 51, 53–60.
Mongelli, G., 2002. Growth of hematite and boehmite in concretions from ancient karst bauxite: clue for past climate. Catena 50, 43–51.
Morales, T., Uriarte, J.A., Olazar, M., Antigüedad, I., Angulo, B., 2010. Solute transport modelling in karst conduits with slow zones during different hydrologic conditions. J. Hydrol. 390, 182–189.
Onac, B.P., Constantin, S. (Eds.), 2008. Archives of climate and environmental change in karst. Quaternary International, 187.
Palmer, A.N., 2012. Solution caves in regions of moderate relief, In: White, William B., Culver, David C. (Eds.), Encyclopedia of Caves, second edition. Elsevier Science, pp. 733–743.
Pardo-Igúzquiza, E., Dowd, P.A., Chaoshui, X., Durán-Valsero, J.J., 2012. Stochastic simulation of karst conduit networks. Adv. Water Resour. 35, 141–150. http://dx.doi.org/10.1016/j.advwatres.2011.09.014.
Pardo-Igúzquiza, E., Durán-Valsero, J.J., Rodríguez-Galiano, V., 2011. Morphometric analysis of three-dimensional networks of karst conduits. Geomorphology 132, 17–28.
Parise, M., De Waele, J., Gutiérrez, F., 2009. Current perspectives on the environmental impacts and hazards in karst. Environ. Geol. 58, 235–237.
Pasini, G., 1967. Nota preliminare sul ruolo speleogenetico dell'erosione “antigravitativa”. Le Grotte d'Italia., 4 pp. 75–90.
Renault, P., 1958. Eléments de spéléomorphologie karstique. Ann. Spéliol. 13, 23–48.
Renault, P., 1968. Contribution à l'étude des actions mécaniques et sédimentologiques dans la spéléogenèse. 3e partie: les facteurs sédimentologiques. Ann. Spéliol. 23, 529–596.
Sethian, J., 1996. A fast marching level set method for monotonically advancing fronts. Proc. Natl. Acad. Sci. 93, 1591–1595.
Sethian, J., 1999a. Fast marching methods. SIAM Rev. 41, 199–235.
Sethian, J., 1999b. Level Set Methods and Fast Marching Method. Cambridge University Press, Cambridge, United Kingdom.
Viles, H.A., 2003. Conceptual modeling of the impacts of climate change on karst geomorphology in the UK and Ireland. J. Nat. Conserv. 11, 59–66.

An algorithm for 3D simulation of branchwork karst networks using Horton parameters and ? Application to a synthetic case

Pauline Collon-Drouaillet, Vincent Henrion and Jeanne Pellerin

Geological Society, London, Special Publications v.370, first published June 27, 2012; doi 10.1144/SP370.3

Notes

Geological Society, London, Special Publications published online June 27, 2012 as doi: 10.1144/SP370.3

An algorithm for 3D simulation of branchwork karst networks using Horton parameters and $\mathcal{A}\star$ Application to a synthetic case

PAULINE COLLON-DROUAILLET*, VINCENT HENRION[1] & JEANNE PELLERIN

CRPG-CNRS, ENSG, Université de Lorraine, rue du doyen Marcel Roubault, BP 40, 54501 Vandoeuvre-lès-Nancy, France

[1]*Present address: Total EP, CSTJF, avenue Larribau, Pau, France.*

**Corresponding author (e-mail: pauline.collon@ensg.inpl-nancy.fr)*

Abstract: This paper presents a method to stochastically simulate 3D karstic networks and more specifically branchwork pattern cave systems. Considering that they can be compared with 3D fluvial networks, the topological classification of Strahler and the corresponding ratios of Horton are used to define three morphometric parameters. These parameters are integrated in an algorithm that computes branches hierarchically to obtain a final network organized around the main observed inlet and outlet with a branching complexity controlled by the user. Each branch corresponds to a low-cost path between two points calculated with the $\mathcal{A}\star$ graph search algorithm. Speleogenetic information on inception horizons, palaeo-water tables and fractures is accounted for by adapted definitions of the searching functions of $\mathcal{A}\star$. The method is demonstrated on a 3D synthetic case with discrete fractures networks, inception horizons and a palaeo-water table. The simulated karsts have a realistic geometry and are geologically consistent.

Simulation of 3D karstic networks is often required to build consistent geomodels in carbonate reservoir environments for various applications, such as water supply management, complex carbonate petroleum reservoirs studies and civil engineering. Genetic approaches try to reproduce the physical processes leading to karst formation (Dreybrodt *et al.* 2005; Ford & Williams 2007). Because of their extreme computational heaviness, they are essentially operating in 2D (e.g. Kaufman & Braun 2000; Kaufman & Romanov 2008). Moreover they are based on various parameters (e.g. palaeoclimate, boundary conditions) that are not always available (Dreybrodt & Gabrovsek 2003).

Static approaches directly simulate the result of the karstification process, but to our knowledge only a few attempts have been made in this direction. Jaquet *et al.* (2004) used a modified lattice-gas automaton for the discrete simulation of karstic networks. As it uses a random-walk technique, this method would be difficult to constrain exactly with field data. Karst networks are computed independently in several 2D horizontal layers and the addition of vertical conduits where karst were observed at surface provides a 2.5D image. The orientation of the lattice has a significant impact on the results since its segments determine the distribution of faults and fractures considered and impose their orthogonal orientations. The different approach of Labourdette *et al.* (2007) focuses on flank-margin cave modelling with an object-based method. Providing realistic geometries and volumes with a limited number of parameters, the main drawback of this method is that it needs a 3D model of surveyed caves. Indeed, it relies on an iterative procedure that stops when differences in volume and shape between simulated and observed caves become small enough. It also uses a dissolution probability cube based on a hypothesis specific to flank margin caves. Particularly adapted in the case of flank-margin caves, the method is not directly applicable to other karst types. Moreover, neither of these two methods considers the global shape of the networks.

According to Palmer (2003), karst patterns can be qualitatively separated into three main families related to speleogenetical context (Fig. 1): (i) branchwork patterns (curvilinear or rectilinear); (ii) maze patterns (anastomotic, network, spongework); and (iii) ramiform patterns. In this article, we focus on branchwork karsts and present a method to constrain their simulation by specific parameters.

The global workflow, first introduced by Henrion *et al.* (2007), consists of the four main steps described in the first section. The basic idea is to compute a skeleton of the karstic network and to simulate stochastically the karst envelope around it. The specific algorithm developed to build branchwork skeletons with control of the branching complexity is presented in the second section. It is based on a hierarchical computation

From: Garland, J., Neilson, J. E., Laubach, S. E. & Whidden, K. J. (eds) 2012. *Advances in Carbonate Exploration and Reservoir Analysis*. Geological Society, London, Special Publications, **370**,
http://dx.doi.org/10.1144/SP370.3

Geological Society, London, Special Publications published online June 27, 2012 as doi: 10.1144/SP370.3

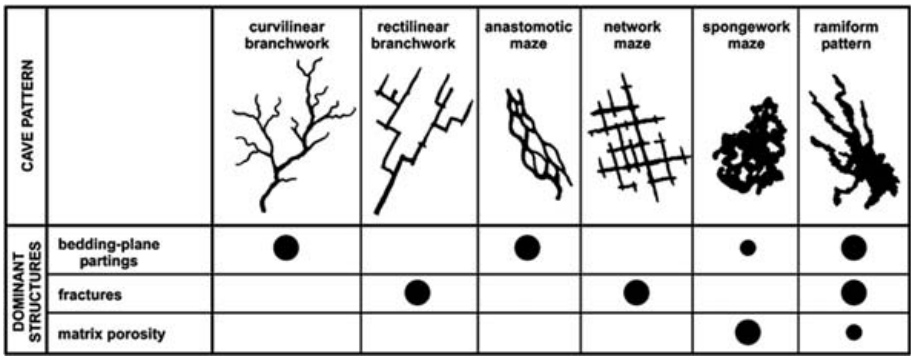

Fig. 1. Cave pattern classification after Palmer (2003): 'Common patterns of solutional caves. Dot sizes show the relative abundance of cave types in each of the listed categories. Single-passage caves are rudimentary or fragmentary versions of those shown here'.

of elementary branches, each branch being the lowest-cost path between two points computed with the $\mathcal{A}\star$ graph search algorithm. The searching functions of $\mathcal{A}\star$ are defined to account for speleogenetic information. The last section, which can be read independently, demonstrates the method on a 3D synthetic case with inception horizons and fractures showing the potential of the approach.

General workflow for karst simulation

Figure 2 summarizes the four main steps of the global workflow.

Geological model building

The capacity of the geomodel to synthesize geological data and knowledge of the studied zone impacts the complete workflow: surfaces that favour karstogenesis have to be integrated at this step. Following the basic principles of 3D geomodelling (Caumon *et al.* 2009) ensures the consistency of the model. The petrophysical properties, permeability and porosity, can be defined equally with kriging or sequential gaussian simulation (e.g. Goovaerts 1997). Discrete fracture networks can be simulated with the stochastic method developed by Macé (2006).

Discretization of the geomodel into a graph of connectivities

The graph used here is a *Pipe Network*, an unstructured connectivity graph designed to perform flow simulations (Vitel 2007). It consists of a set of pipes connecting a set of nodes, which respectively correspond to the facets of the control volumes and the grid points of a reservoir simulation grid. From a geometrical point of view, it corresponds to the partial topological dual of a corner-point grid (Fig. 3). The *Pipe Network* provides a unified structure for various types of geomodels: structured grids combined or not with fracture networks or unstructured grids with faults and horizons. Various properties simulated in the geomodel can be transferred on the graph (e.g. permeability) and some others may be computed during the discretization process (e.g. volumes). A specificity of the *Pipe Network* is storage of the properties of the media on nodes (e.g. permeability, volume), while properties concerning flow transmission are stored on pipes (e.g. transmissibility, permeability per length). Inlets and outlets can be imposed by field observation or stochastically simulated.

Karst skeleton computation

The skeleton of the karst is extracted from the previous graph as preferential flow paths between inlets and oulets points. This step controls the high-scale geometry of the karst. Thus, it is the key part for a process dedicated to the modelling of branchwork patterns and it is fully detailed in the next section of this paper.

Computation of realistic 3D karst envelopes

This final step relies on the object-distance simulation method (*ODSIM*) proposed by Henrion *et al.* (2010). It computes for each point $\mathbf{p} = [p_x\ p_y\ p_z]^{\mathrm{T}}$ of a grid G the euclidean distance to a geological body skeleton providing a 3D distance field $D(\mathbf{p})$ (Fig. 2, 4.1). This distance field is then truncated by a spatially correlated random threshold $\varphi(\mathbf{p})$, which may be generated using sequential Gaussian simulation or another stochastic simulation method (e.g. Deutsch & Journel 1997; Goovaerts 1997; Fig. 2, 4.2). The resulting object is identified in the grid by a binary categorical property I_{B} (Fig. 2, 4.3) defined by

$$I_{\mathrm{B}}(\mathbf{p}) = \begin{cases} 1 & \text{if } D(\mathbf{p}) \leq \varphi(\mathbf{p}) \\ 0 & \text{if not} \end{cases} \quad (1)$$

Geological Society, London, Special Publications published online June 27, 2012 as doi: 10.1144/SP370.3

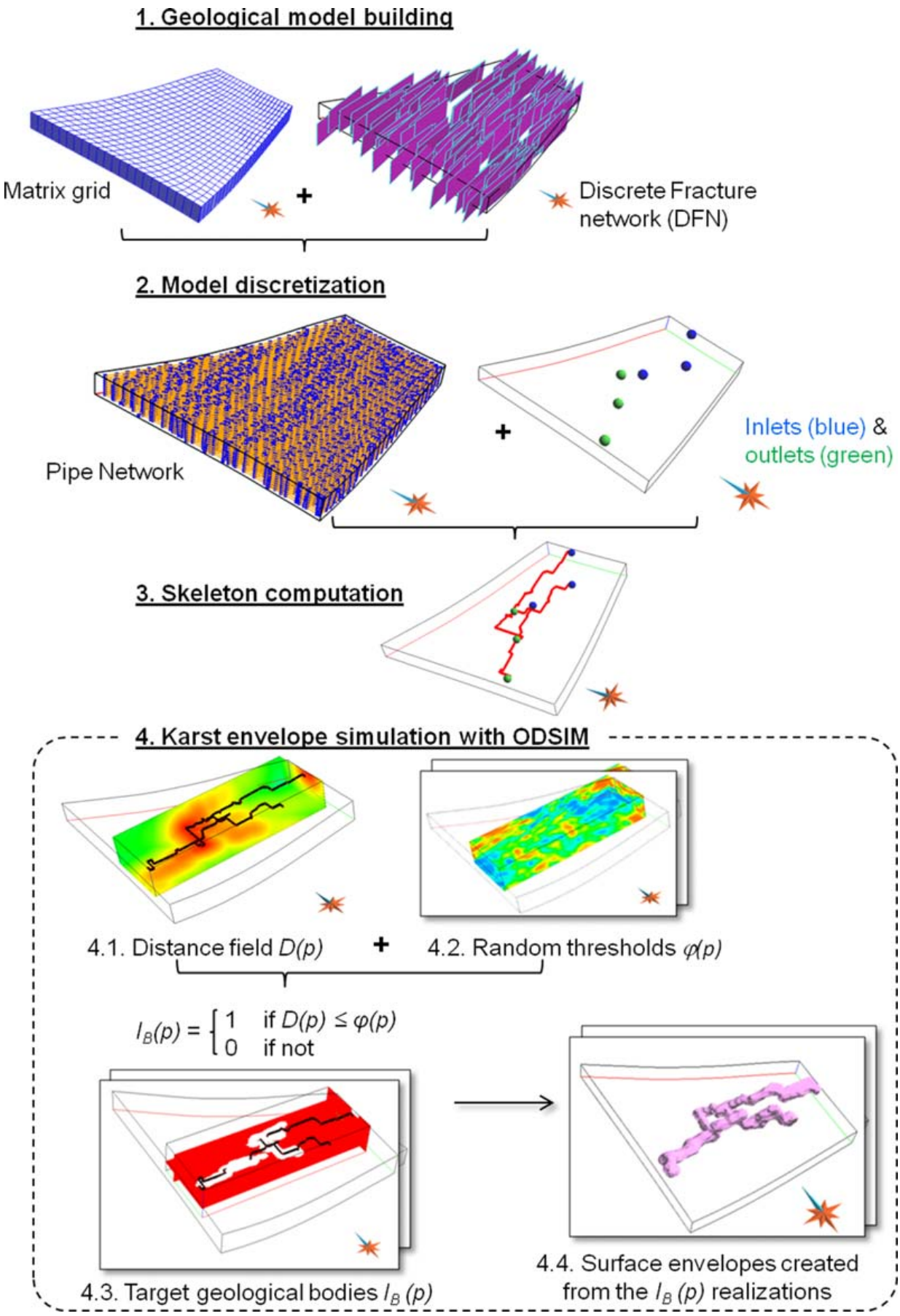

Fig. 2. General workflow for stochastic 3D karst simulation.

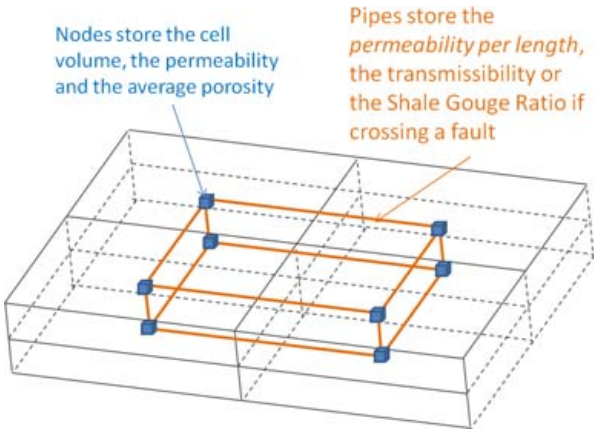

Fig. 3. *Pipe Network* as partial topological dual of a block-centred corner-point grid (blue cubes, nodes; orange lines, pipes; modified from Vitel 2007).

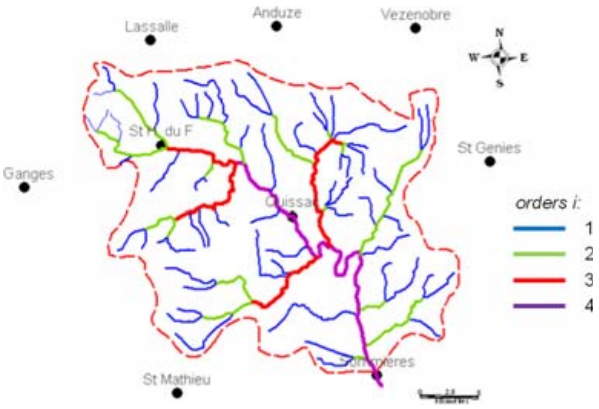

Fig. 4. Example of Strahler classification on a hydrological network (South France) where the Horton–Strahler number is equal to 4.

During this process, the extension of karst conduits is controlled by the distribution (PDF) of the threshold while the parameters of the variogram control the roughness and anistropy of karst conduits. Indeed, higher variogram ranges involve smaller changes of the threshold values, providing a smoother envelope. If the ranges vary with the directions, this will be reflected in the geometrical evolution of karst conduits, which will be smoother along the mean directions. An iterative Gibbs sampler (Geman & Geman 1984) with inequality constraints allows conditioning of the threshold simulation to well data while preserving its spatial structure and histogram (Henrion *et al.* 2010).

Methodology for branchwork karst pattern generation

An algorithm to control the branching complexity of karst networks

Branchwork patterns have a typical topology, characterized by a hierarchical organization excluding cycles (only one path between two points). A solution to reproduce this hierarchy is to extract a main path and compute secondary paths connected to it (Bonneau *et al.* 2010). However, none of the previously developed techniques integrates a possibility to control the branching complexity of the networks.

Developed for hydrological applications, the topological classification of Strahler (1952) can be applied on any directed graph tree. Each segment of the tree is assigned an order i with the followings rules (Fig. 4):

- each segment with no parent (that is, with no affluent for a stream) has an order equal to 1;
- a segment formed from the confluence of two segments of order i, has an order equal to $i + 1$;
- a segment formed from the confluence of two segments of order m and n, has an order equal to $max(m, n)$.

The Horton–Strahler number of a tree is defined as the order of its outlet. It is denoted K_o in this work.

The branching complexity of a network can be described by the Horton bifurcation ratio R_B, based on the law of stream numbers (Horton 1945) that states that the ratio N_{Ki}/N_{Ki+1}, where N_{Ki} is the number of paths of order i, converges to a constant when order increases. Moreover, the Horton law of stream lengths states that a geometric relationship exists between the cumulated length of streams of a given order L_i and the corresponding order i, that is, the ratio L_i/L_{i+1} converges to a constant called the Length Ratio, R_L.

From a geometrical point of view, a branchwork pattern is an oriented graph tree. Therefore, Strahler classification can be applied to it. The geostatistical and fractal studies of length caves made by Curl (1986) demonstrate that the lengths of caves in a given region and the size of modular elements constituting them are distributed hyperbolically. This indicates that a self-similarity appears in these complex systems. Despite the fact that Horton laws on stream numbers and stream lengths have not been proved for karstic systems, the Horton ratios may help to reproduce this self-similarity. Thus, the three parameters K_o, R_B and R_L are integrated in a new algorithm to simulate branchwork karsts controlled by the user.

The algorithm (Fig. 5) first computes a main path between the given input and output. Then, for each order i from $(K_o - 1)$ to 1, the following three steps are performed:

(1) Compute one path connected to each path of order 1 to increase its order. This is done using a *length smooth constraint*, described below.

Geological Society, London, Special Publications published online June 27, 2012 as doi: 10.1144/SP370.3

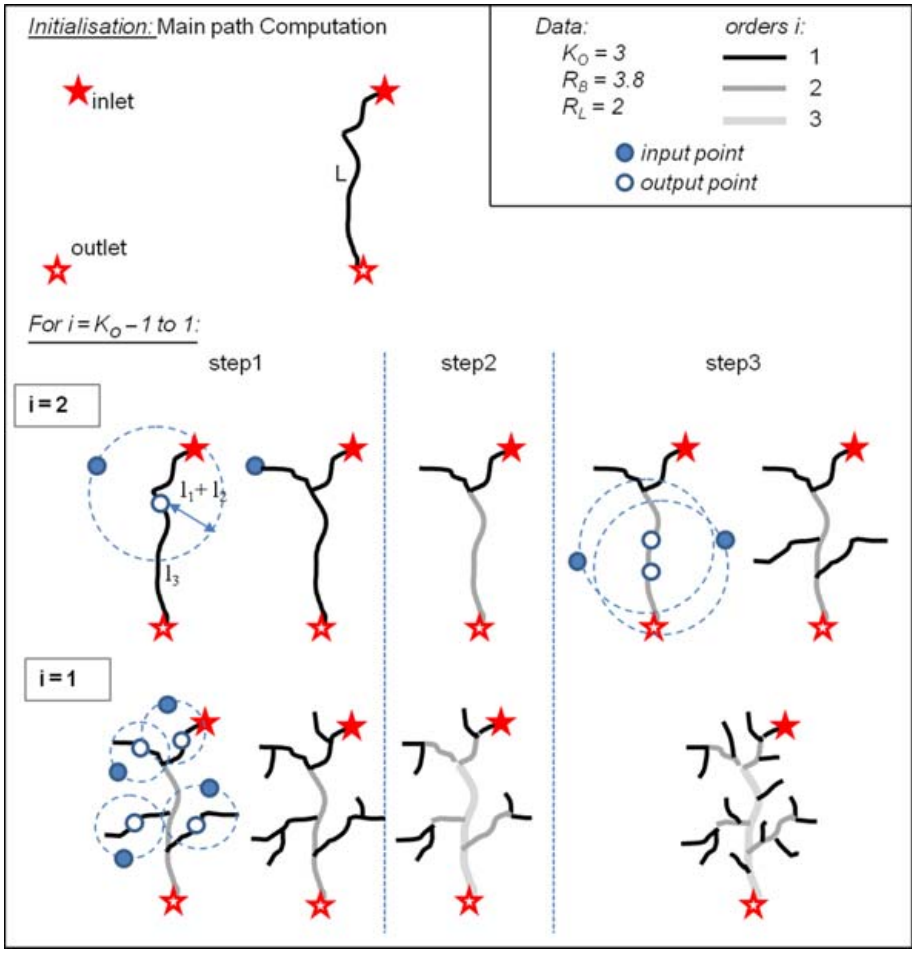

Fig. 5. The different steps of the branchwork network algorithm. The initialization consists of the extraction of a main path linking inlet and outlet. Then, for each order i from $(K_o - 1)$ to 1, step 1 computes one path connected to each path of order 1, the second step updates Horton orders and the third step generates the remaining paths on segments of order >1 to honour the bifurcation ratio R_B. The input points definition in steps 1 and 3 and the output points choice in step 1 are guided by the values of the length ratio R_B.

(2) Update Horton orders.
(3) Generate the $(N_{Ki} - 2N_{Ki+1})$ remaining paths with output points randomly chosen on paths of order >1, guaranteeing that Horton orders i are preserved.

The *length smooth constraint* enforces the use of the R_L ratio. Considering l_i as the average length of a segment of order i and L as the curvilinear length of the main path linking inlet and outlet, we have the following equations:

$$\begin{cases} L_i = N_i \times l_i \\ L = \sum_{i=1}^{K_o} l_i \end{cases} \quad (2)$$

Thus:

$$\frac{l_i}{l_{i+1}} = \frac{R_L}{R_B} = r \quad (3)$$

which leads to

$$l_i = r^{K_o - i} \times l_{K_o} \quad (4)$$

and

$$l_{K_o} = \frac{L}{\sum_{j=0}^{K_o - 1} r^j} \quad (5)$$

To perform the first step of the previous algorithm for a current order i, we impose the output point $\mathbf{p}_{out_i}$ of the new path to be located at a distance l_{i+1} from the downstream segment extremity. Then, the new input point $\mathbf{p}_{in_i}$ is randomly chosen on the upper half-sphere of radius $l = \text{rand}_{[0.5;1]} * \sum_{j=1}^{i-1} l_j$ where $\text{rand}_{[0.5;1]}$ is a random number chosen between 0.5 and 1. As karsts form from surface infiltration, the input point is vertically projected on the upper part of the *Pipe Network*. The new pair of

points [$\mathbf{p}_{\text{in}_i}$; $\mathbf{p}_{\text{out}_i}$] is then used to compute the connected path. The third step is quite similar to the first one, except that the output point is randomly chosen on an existing path of order 1. As the computed paths between two points are not straight lines (see the detailed method below) and as the path extraction ends when crossing an existing segment, the length of the resulting path is different from the used radius l (often superior to l, explaining the use of the random multiplier).

Thus, the R_{L} ratio guides the simulation but is not strictly honoured justifying the notion of *soft constraint*. The R_{B} ratio is more constraining but the use of non-integers permits a network to be obtained with different values. In contrast, the Horton–Strahler number K_{o} is always strictly respected and can be considered as a *hard constraint*.

Using $\mathcal{A}\star$ for single path computation

The $\mathcal{A}\star$ algorithm allows easy computation of single karst branches honouring given input and output points. These points might be the actual inlet and/or outlet of the network or location computing by the branchwork karst simulation algorithm as described in the previous section. $\mathcal{A}\star$ is a graph search algorithm that aims to find the least cost path between two given nodes (Hart *et al.* 1968). It uses a best-first search, that is, it first explores the most promising node chosen according to a specified rule, and derives from the algorithm of Edsger Dijkstra (1959). A better performance (with respect to time) is obtained thanks to the use of a heuristic function $f(x)$. f is the sum of (1) a *cost* function $g(x)$, which is the cumulated cost from the starting node to the current node, and (2) an admissible *heuristic estimate* $h(x)$ of the distance to the goal. Two rules have to be respected:

- The cost has to be strictly positive: $g(x) > 0$.
- The *heuristic estimate* has to be admissible, that is, it must not overestimate the distance to the goal, $h(x) < g(x, \text{goal})$, where $g(x, \text{goal})$ is the minimal cost from x to the goal.

To use $\mathcal{A}\star$ for karst skeleton computation, these two functions must be defined consistently. Despite the complexity of the phenomena involved, speleologists agree that, knowing two connected points, karstic conduits develop preferentially along paths with high hydraulic conductivity and short length (Ford & Williams 2007, chap. 7). Thus, we define the cost on a pipe as a function of the inverse of the *permeability per length* K_{Lij} [Eq. (6)]. The *permeability per length* is a weighted average permeability calculated on a pipe linking two nodes i and j using the node hydraulic conductivities and volumes and divided by the pipe length [Eq. (7)]. The resulting *cost*, proportional to $1/K_{Lij}$, is homogeneous to a time and thus it can be summed and is independent of mesh resolution.

$$\text{cost}_{ij} = \frac{1}{K_{Lij}} \times \text{grav}_{ij} \tag{6}$$

$$K_{Lij} = \frac{1}{d_{ij}} \times \frac{k_i \times \text{vol}_i + k_j \times \text{vol}_j}{\text{vol}_i + \text{vol}_j} \tag{7}$$

with k_i the permeability at point i; vol_i the volume of the cell represented by node i; *and* d_{ij} the distance between the points i and j.

The gravity, grav_{ij}, is included in the cost computation as a multiplier coefficient [Eq. (6)] to avoid vertically oscillating paths [Eq. (8)]:

$$\text{grav}_{ij} = \begin{cases} 1 & \text{if } \Delta z_{ij} \geq 0 \\ 1 - \dfrac{\Delta z_{ij}}{d_{ij}} & \text{if } \Delta z_{ij} < 0 \end{cases} \tag{8}$$

The admissible heuristic is a function of the distance from the current node to the output node [Eq. (9)]. Unit homogeneity and $\mathcal{A}\star$ requirements are guaranteed by the use of a multiplier coefficient equal to the maximal cost *Mcp* encountered on the *Pipe Network* multiplied by the length of this maximal cost pipe *Lmp* [Eq. (9)]:

$$\text{heur}_j = \frac{d_{j,\text{output}}}{\max(K_L \times d)} \tag{9}$$

where $d_{j,\text{output}}$ is the distance between the point j and the output.

With these definitions of the cost and the heuristic, the $\mathcal{A}\star$ algorithm extracts paths between two points of a *Pipe Network* using hydraulic conductivity information. Speleogenetical concepts and geological information might be included at the geomodel building step and will then be taken into account when the skeleton is computed. Different kinds of surfaces have been identified as preferential surfaces for karst development: inception horizons are the restricted numbers of bedding planes within the limestone series along which a karstic network tends to develop (Lowe 1992); palaeo-water tables and fractures have also been proved to favour karst development (Dreybrodt & Gabrovsek 2003). For inception horizons and palaeo-water tables, an adapted building of the geomodel using a grid conformable to the considered surfaces with a local mesh refinement along these levels allows their integration in the *Pipe Network*. Giving these surfaces higher values of hydraulic conductivity promotes the simulation of paths along them. The object-based method

developed by Macé (2006) stochastically simulates a discrete fracture networks (DFN) from data on their orientation, extension and density. These fractures can be jointly discretized with the geomodel (Vitel 2007), allowing the generation of karst skeletons strongly influenced by their presence.

Application to a synthetic case

The method was applied on a 3D synthetic case. The fractured geological system was made up of a succession of three stratigraphic units, from base to top: one layer of shale overhung by two layers of limestone. Two inception horizons separated these units and a palaeo-water table was located inside the bottom limestone unit (Fig. 6a). Two fracture families were considered. All of these surfaces favour karstogenesis.

A stratigraphic grid (cell numbers $30 \times 37 \times 21$) was built from these data, with thinner cells (2 m high) centred on the inception horizons and the palaeo-water table (Fig. 6b). The hydraulic conductivities and porosities of the different units (Table 1) were simulated using an unconditional sequential gaussian simulation (Goovaerts 1997) with a uniform law and a spherical variogram (with ranges 200, 200 and 50 m). The two DFNs were simulated (Fig. 6a) according to the workflow proposed by Macé *et al.* (2004), with a higher density of fracturation along the fold axis. Their

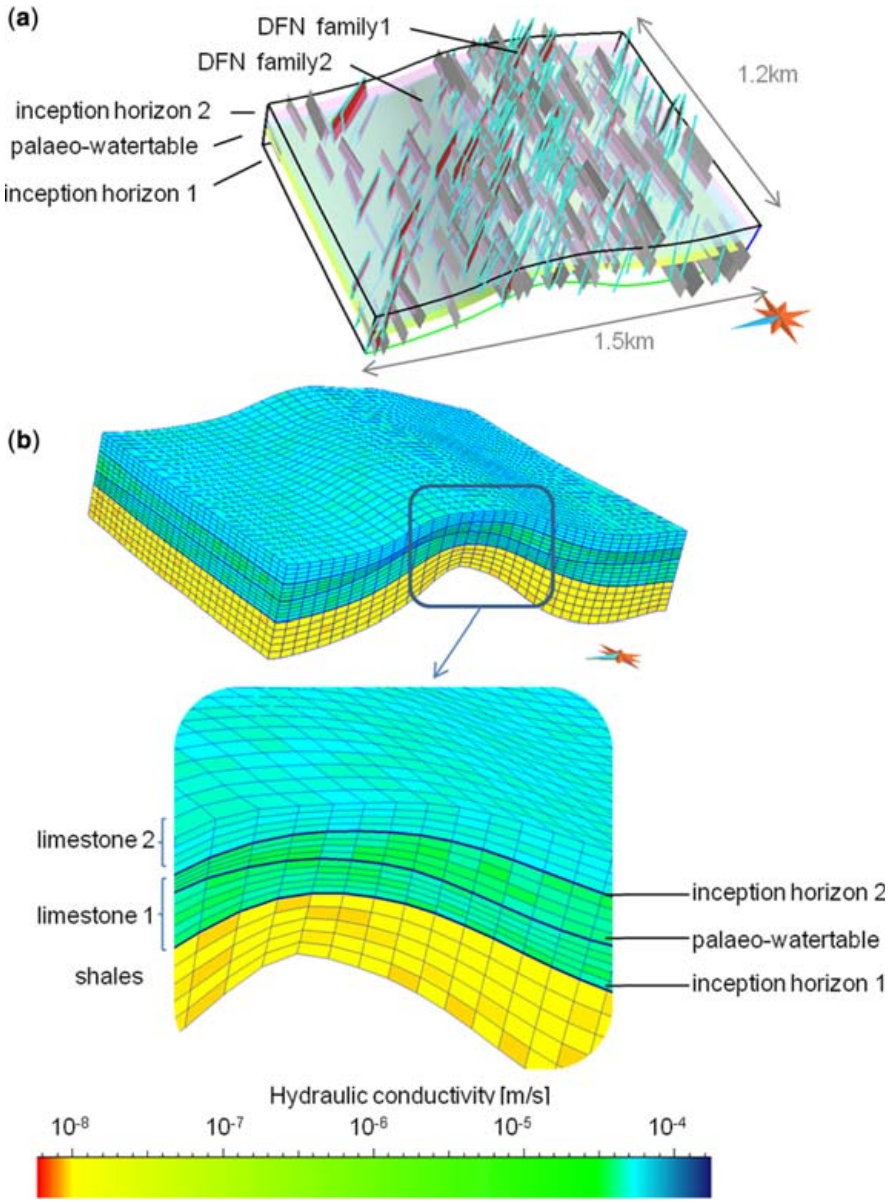

Fig. 6. Three dimensional geological synthetic model of the area in which karstic network is generated: (**a**) the three surfaces favouring karstogenesis and the two discrete fracture networks; (**b**) the corresponding stratigraphic grid with simulated hydraulic property values.

Geological Society, London, Special Publications published online June 27, 2012 as doi: 10.1144/SP370.3

Table 1. *Stratigraphic grid specifications*

Stratigraphic unit	Number of layers	Mean hydraulic conductivity (m s^{-1})	Mean porosity (%)	Mean thickness (m)
Limestone 2	5	5×10^{-5}	20	32.5
Inception horizon 2	1	1×10^{-3}	24	2
Limestone 1	4	4×10^{-5}	19	35
Water level	1	1×10^{-3}	24	2
Limestone 1	5	4×10^{-5}	19	50
Inception horizon 1	1	1×10^{-3}	24	2
Shale	5	1×10^{-8}	7.5	80

Table 2. *Discrete fracture networks properties*

DFN	Hydraulic conductivity (m s^{-1})	aperture (m)	Dip (deg) min–mode–max	Direction (deg) min–mode–max	Length (m) min–mode–max	Width (m) min–mode–max
1	1.2×10^{-3}	0.003	85–90–100	85–90–100	150–210–250	70–100–120
2	0.8×10^{-3}	0.002	75–85–100	120–130–135	160–230–260	80–120–140

DFN, discrete fracture networks.

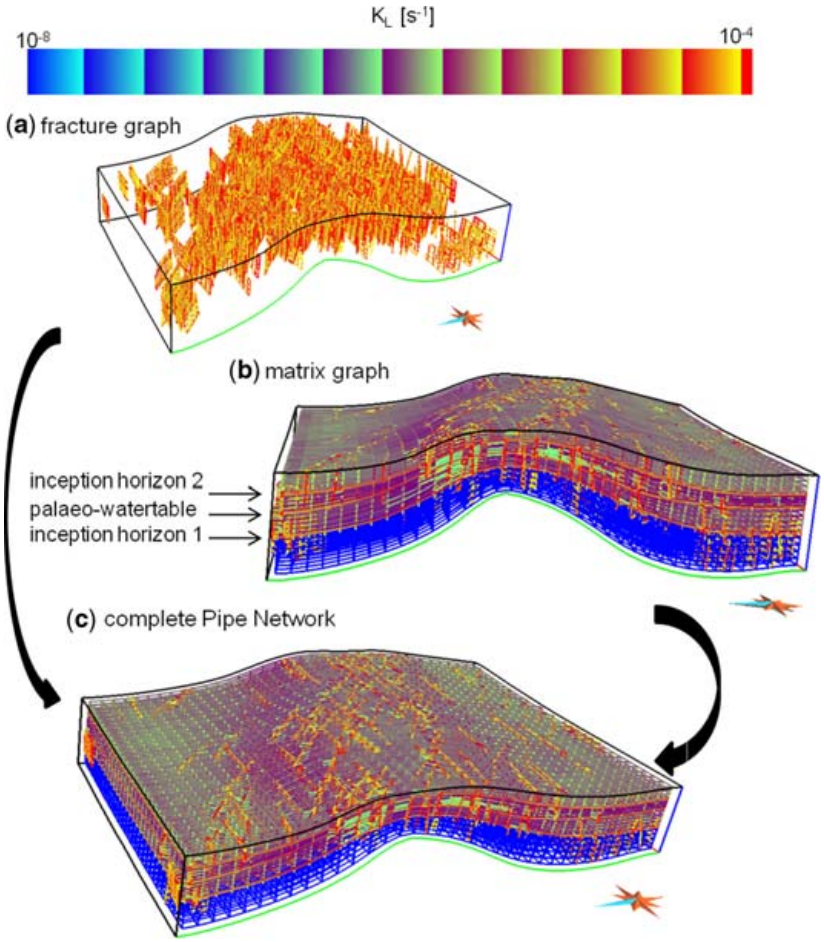

Fig. 7. *Pipe Network* resulting from the joined discretization of the stratigraphic grid and the two discrete fracture networks (**c**). Preferential surfaces for karst development, (**a**) fractures, and (**b**) inception horizons and palaeo-water table, have a higher *permeability per length* (orange) than the layers.

properties, following triangular laws, are indicated in Table 2.

The model was discretized into a *Pipe Network* composed of 50 605 nodes, including 27 300 nodes for the fractures (Fig. 7). The *permeability per length* values ranged from 1.7×10^{-11} s^{-1} in the lower shale to around 10^{-2} s^{-1} in short pipes of fractures, inception horizons and the palaeo- water table.

A network simulation was performed between inlet and outlet (Fig. 8) with the following values: $K_o = 3$, $R_B = 2.8$ and $R_L = 3.5$. The obtained branchwork skeleton honoured its input parameters K_o and R_B and the skeleton paths were located preferentially along the fractures, the inception horizons and the water table owing to their higher permeability (Fig. 8).

To illustrate the influence of the three morphometric parameters, several simulations were performed, each time with the same random seed for the search for input points (Fig. 9). Consistently with their definitions, the K_o value controlled the hierarchical organization, that is, the branching complexity of the network, and imposed an order on the outlet of the karst. Increasing the bifurcation ratio R_B produced denser networks without changing the global order, that is, for the same K_o value it generated a higher number of paths. Finally, the length ratio R_L influenced the lengths of secondary paths.

As presented in the global workflow, the object-distance simulation method (*ODSIM*) was applied on the resulting skeletons to generate stochastically several 3D envelopes of the network (Henrion *et al.* 2010). Figure 10 illustrates this method on the reference skeleton computed in the synthetic case. In karstic systems the geometry of the voids is perceptible on a local scale (dimensions from metres to ten of metres or so), whereas the previous studied skeletons were computed at a regional scale (a kilometre or so). The thresholds were simulated using a triangular distribution (PDF; minimum = 1, mode = 2, maximum = 15) and a gaussian variogram with an azimuth = 60, a dip = 0, range = [30 25 15], no nugget effect and a cumulative sill = 1. The distance field was then truncated by these thresholds to produce three binary categorical properties. To make the visualization of the results easier, envelope surfaces were extracted from grid isovalues.

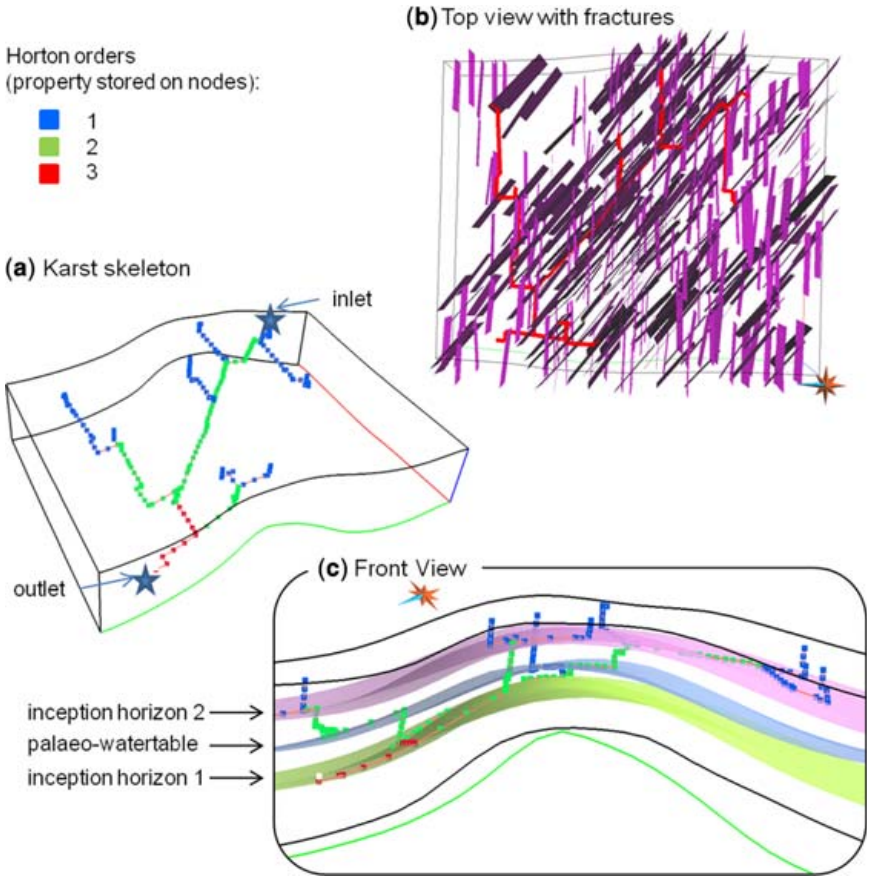

Fig. 8. Branchwork skeleton obtained with $K_o = 3$, $R_B = 2.8$ and $R_L = 3.5$ and given inlet and outlet. (**a**) The branching connectivity respects the input parameters; (**b**) top view – the skeleton paths are located preferentially along the fractures; (**c**) vertical cross-section – the paths are also preferentially located around the inception horizons and the water table owing to their higher permeability.

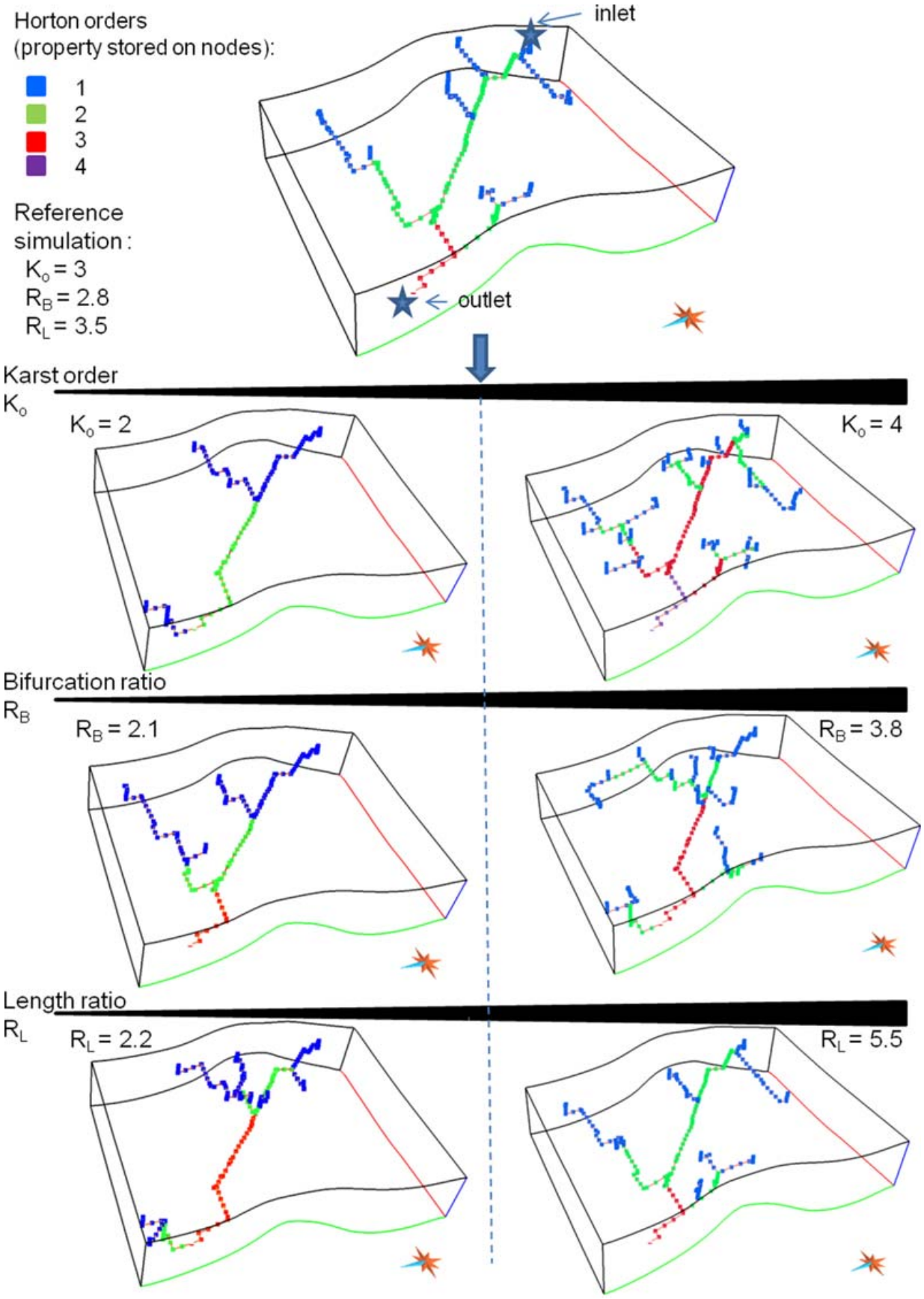

Fig. 9. Branchwork skeletons obtained by changing the values of the three morphometric parameters K_o, R_B and R_L. (**a**) The K_o value controls the hierarchical organization, that is, the branching complexity; (**b**) the global number of paths increases with the R_B parameter; (**c**) a higher value of R_L involves higher lengths of secondary paths.

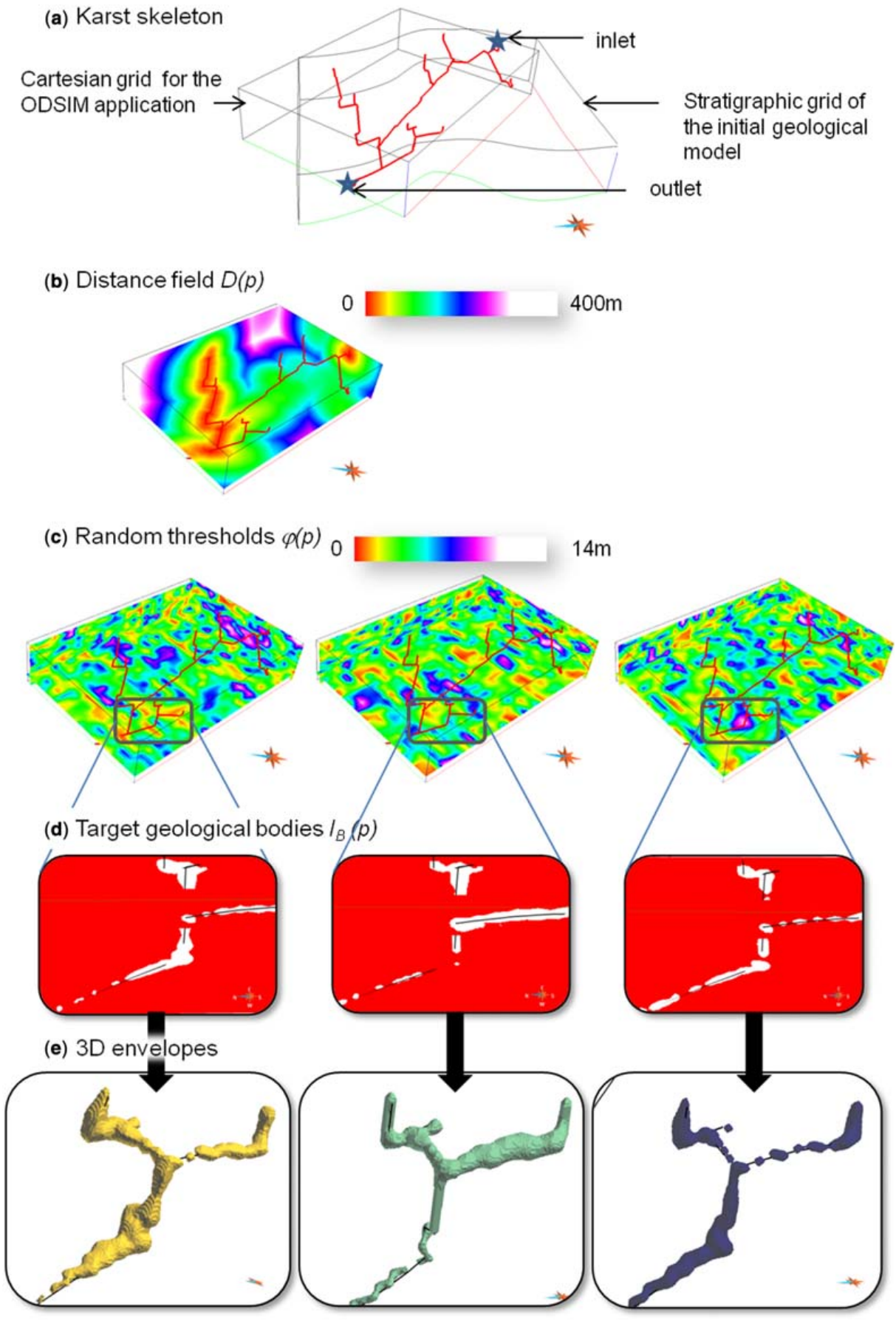

Fig. 10. Application of the ODSIM method to the reference skeleton.

Conclusions and perspectives

The developed methodology generates branchwork karstic networks with a user control on branching complexity and gives promising results. However, the choice of using Horton–Strahler parameters should be discussed. Indeed these parameters have been proven relevant in the case of fluvial networks, but not yet in the case of natural karstic systems. The main differences are that karsts are not organized along a unique horizon, and that often some multiple interconnections appear. preliminary work is underway on to test the relevance of the Strahler orders to natural karsts. The few multiple interconnections could be reproduced by additional path computations. However, formalism and automation steps are required to obtain an effective tool.

Further work will aim to provide tools to simulate the other karst patterns. The network maze is easy to simulate by the direct application of the ODSIM method on an adequate selection of DFN fractures, but improvements could be made concerning their automation and calibration by the user. Anastomotic mazes, spongework mazes and ramiform patterns require specific developments to be deliberately simulated.

Regarding the karst envelope, the ODSIM method generates various shapes, but could still be improved to integrate field data like seismic information, a library of natural karstic shapes and their geological environment.

We would like to thank the industrial and academic members of the Gocad Consortium, ASGA, for their support, Paradigm Geophysical for providing the Gocad Software, and API and the French National Scientific Research Center CNRS-CRPG for their support.

References

Bonneau, F., Henrion, V. & Collon-Drouaillet, P. 2010. Genetic-like modeling of karst network. *In*: *Proceedings of 30th Gocad Meeting*. Nancy, France.

Caumon, G., Collon-Drouaillet, P., Le Carlier de Veslud, C., Viseur, S. & Sausse, J. 2009. Surface-based 3d modeling of geological structures. *Mathematical Geosciences*, **41**, 927–945.

Curl, L. R. 1986. Fractal dimensions and geometries of caves. *Mathematical Geology*, **18**, 765–783.

Deutsch, C. V. & Journel, A. G. 1997. *GSLIB: Geostatistical Software Library and User's Guide (Applied Geostatistics)*. Oxford University Press, New York.

Dijkstra, E. W. 1959. A note on two problems in connexion with graphs. *Numerische Mathematik*, **1**, 269–271, doi: 10.1007/BF01386390.

Dreybrodt, W. & Gabrovsek, F. 2003. Basic processes and mechanisms governing the evolution of karst. *Speleogenesis and Evolution of Karst Aquifers, The Virtual Scientific Journal*, **1**, 26.

Dreybrodt, W., Gabrovsek, F. & Romanov, D. 2005. *Processes of Speleogenesis: a Modeling Approach*. Karst Research Institut, ZRC SAZU.

Ford, D. & Williams, P. 2007. *Karst Hydrogeology and Geomorphology*. John Wiley and Sons, Chichester.

Geman, S. & Geman, D. 1984. Stochastic relaxation, Gibbs distribution and the Bayesian restoration of images. *IEEE Transactions Pattern Analysis and Machine Intelligence*, **6**, 721–741.

Goovaerts, P. 1997. *Geostatistics for Natural Resources Evaluation*. Applied Geostatistics series, Oxford University Press, New York.

Hart, P. E., Nilsson, N. J. & Raphael, B. 1968. A formal basis for the heuristic determination of minimum cost paths in graphs. *IEEE Transactions on Systems Science and Cybernetics*, **SSC-4**, 100–107.

Henrion, V., Caumon, G. & Cherpeau, N. 2010. Odsim: an object-distance simulation method for conditioning complex natural structures. *Mathematical Geosciences*, **42**, 911–924.

Henrion, V., Caumon, G., Vitel, S. & Kedzierski, P. 2007. Stochastic simulation of cave systems in reservoir modeling. *Proceedings of the 27th Gocad Meeting*. Nancy, France, 11.

Horton, R. E. 1945. Erosional development of streams and their drainage basins; hydrophysical approach to quantitative morphology. *Bulletin Geological Society of America*, **56**, 275–370.

Jaquet, O., Siegel, P., Klubertanz, G. & Benabderrhamane, H. 2004. Stochastic discrete model of karstic networks. *Advances in Water Resources*, **27**, 751–760.

Kaufman, G. & Braun, J. 2000. Karst aquifer evolution in fractured, porous rocks. *Water Resources Research*, **36**, 1381–1391.

Kaufman, G. & Romanov, D. 2008. Cave development in the swabian alb, south-west Germany: a numerical perspective. *Journal of Hydrology*, **349**, 302–317.

Labourdette, R., Lascu, I., Mylroie, J. & Roth, M. 2007. Process-like modeling of flank-magin caves: from genesis to burial evolution. *Journal of Sedimentary Research*, **77**, 965–979.

Lowe, D. 1992. *The origin of limestone caverns: an inception horizon hypothesis*. PhD thesis, Manchester Polytechnic.

Macé, L. 2006. *Caractérisation et modélisation numérique tridimensionnelle des réseaux de fractures naturelles*. PhD thesis, INPL, Nancy.

Macé, L., Souche, L. & Mallet, J.-L. 2004. 3d fratures characterization based on geomechanics and geologic data uncertainties. *Proceedings of the 24th Gocad Meeting*. Nancy, France.

Palmer, A. N. 2003. Speleogenesis in carbonate rocks. *Speleogenesis and Evolution of Karst Aquifer, The Virtual Scientific Journal*, **1**, 11.

Strahler, A. 1952. Hypsometric (area-altitude) analysis of erosional topography. *Bulletin Geological Society of America*, **63**, 1117–1142.

Vitel, S. 2007. *Méthodes de discrétisation et de changement d' échelle pour les réservoirs fracturés 3D*. PhD thesis, INPL, Nancy, France.

Available online at www.sciencedirect.com
ScienceDirect
Journal of Contaminant Hydrology 96 (2008) 97–112
JOURNAL OF Contaminant Hydrology
www.elsevier.com/locate/jconhyd

Two modelling approaches to water-quality simulation in a flooded iron-ore mine (Saizerais, Lorraine, France): A semi-distributed chemical reactor model and a physically based distributed reactive transport pipe network model

V. Hamm [a,*], P. Collon-Drouaillet [b], R. Fabriol [a]

[a] BRGM, 1 Av. du parc de Brabois, 54500 Vandoeuvre-lès-Nancy, France
[b] Nancy Université, CRPG, rue du doyen Marcel Roubault, 54501 Vandoeuvre-lès-Nancy cedex, France

Received 29 August 2006; received in revised form 28 September 2007; accepted 11 October 2007
Available online 24 October 2007

Abstract

The flooding of abandoned mines in the Lorraine Iron Basin (LIB) over the past 25 years has degraded the quality of the groundwater tapped for drinking water. High concentrations of dissolved sulphate have made the water unsuitable for human consumption. This problematic issue has led to the development of numerical tools to support water-resource management in mining contexts. Here we examine two modelling approaches using different numerical tools that we tested on the Saizerais flooded iron-ore mine (Lorraine, France). A first approach considers the Saizerais Mine as a network of two chemical reactors (NCR). The second approach is based on a physically distributed pipe network model (PNM) built with EPANET 2 software. This approach considers the mine as a network of pipes defined by their geometric and chemical parameters. Each reactor in the NCR model includes a detailed chemical model built to simulate quality evolution in the flooded mine water. However, in order to obtain a robust PNM, we simplified the detailed chemical model into a specific sulphate dissolution–precipitation model that is included as sulphate source/sink in both a NCR model and a pipe network model. Both the NCR model and the PNM, based on different numerical techniques, give good post-calibration agreement between the simulated and measured sulphate concentrations in the drinking-water well and overflow drift. The NCR model incorporating the detailed chemical model is useful when a detailed chemical behaviour at the overflow is needed. The PNM incorporating the simplified sulphate dissolution–precipitation model provides better information of the physics controlling the effect of flow and low flow zones, and the time of solid sulphate removal whereas the NCR model will underestimate clean-up time due to the complete mixing assumption. In conclusion, the detailed NCR model will give a first assessment of chemical processes at overflow, and in a second time, the PNM model will provide more detailed information on flow and chemical behaviour (dissolved sulphate concentrations, remaining mass of solid sulphate) in the network. Nevertheless, both modelling methods require hydrological and chemical parameters (recharge flow rate, outflows, volume of mine voids, mass of solids, kinetic constants of the dissolution–precipitation reactions), which are commonly not available for a mine and therefore call for calibration data.

Keywords: Flooded mine; Network of chemical reactors (NCR); Pipe network model (PNM); Reactive transport modelling; Dissolution–precipitation reaction; Sulphate concentrations

* Corresponding author. Tel.: +33 3 83 59 63 27; fax: +33 3 83 44 15 18.
E-mail addresses: v.hamm@brgm.fr (V. Hamm), pauline.collon@ensg.inpl-nancy.fr (P. Collon-Drouaillet), r.fabriol@brgm.fr (R. Fabriol).

0169-7722/$ - see front matter © 2007 Elsevier B.V. All rights reserved.
doi:10.1016/j.jconhyd.2007.10.004

1. Introduction

The end of mining operations, and consequently of mine dewatering, in the Lorraine Iron Basin (LIB) of northeastern France at the end of the 20th century resulted in hydrological and hydrochemical changes. The water pumped from the mine workings to keep them dry during exploitation usually had a chemical composition suitable for human consumption and so represented an important supply used directly for drinking water. Once mining ceased, the mine water remained in contact with the gallery walls and pillars and became enriched with dissolved elements that degraded its initial quality and made it unsuitable for human consumption. Consequently, questions are being raised about the future evolution of the water quality and how long it can be expected to conform again drinking-water standards.

The chemical reactions that occur with flooding are mainly the dissolution of secondary minerals formed in the surrounding rock during mining, but modelling multi-component reactive transport in an entire mine is a very complex topic that calls for specific tools. Many approaches for predicting the impact of mining activities on groundwater quality use semi-distributed lumped-parameter models, also known as "box" models, because of the complexity of the mine structure and the lack of information on its hydrodynamic parameters. The method consists in dividing the complex mine workings into hydraulically connected homogeneous hydrological units or "reservoirs" (Brown and Lowson, 1997; Collon et al., 2005; Collon et al., 2006; Heller et al., 2005). Other approaches use physically-based distributed flow and solute-transport models originally studied for fractured rocks or karst-conduit genesis. The method uses the concept of channel or pipe networks (Moreno and Neretnieks, 1993; Gylling et al., 1998; Bauer et al., 2003; Birk et al., 2003; Moreno et al., 2006) or models of two-dimensional rectangular planes for fractures (Therrien and Sudicky, 1996; Graf and Therrien, 2007), along with different formulations for the flow and solute-transport processes. Still other approaches consider interactions between the porous media and the flooded mine workings through coupling continuum porous media with a box model (Babot et al., 2005; Veschkens et al., 2005) or a pipe-network model (Adams and Younger, 2001; Spiessl et al., 2002; Hamm et al., 2005) used for mine conduits, in order to simulate flow processes or coupled flow and transport processes. Veschkens et al. (2005) and Babot et al. (2005) combined a classical porous medium model of the upper aquifer with a box model of the underground coal mining reservoir (Liège and Ruhr coal basins, Saar-Lorraine coal basin) in order to predict flooding processes and interactions between shallow aquifers and flooded coal mines. Adams and Younger (2001) coupled a pipe network model (PNM) to a variably saturated porous medium model (VSS–NET) for modelling groundwater rebound and applied this to abandoned coalfields in the United Kingdom. Hamm et al. (2005) used a PNM to study the impact of back-filling material on water quality evolution in a flooded iron-ore mine in Lorraine.

The codes used for porous media, however, are not designed for resolving flow and reactive transport in a network of fractures or mine galleries. They are based on the concept of representative elementary volumes (REV) within which variables are averaged. The REV concept becomes invalid in underground mines where two distinct transport regimes coexist: a high-velocity regime in the network of highly conductive galleries, and a low-velocity regime in the considerably less permeable porous rock material. Consequently, flow and reactive transport in a network of discrete gallery conduits implies that each gallery has to be taken into account individually. A reactive hybrid transport model (RUMT3D) has recently been developed that combines a standard transport model for porous media with a conduit transport model and a standard geochemical model (Spiessl, 2004). Nevertheless, compared to box models, few pipe network models consider reactive chemical transport.

The aim of this paper is to describe and compare the results of two modelling approaches to the evolution of water quality in flooded mines; the one is a semi-distributed chemical reactor model and the other is a distributed reactive transport pipe network model. Both models consider flow and advective transport in the flooded galleries associated with precipitation–dissolution reactions of minerals present in the surrounding rock. Because of the complexity of the chemical reactions and the strategy adopted to compare box models with spatially distributed reactive transport models, our approach consisted in simplifying a detailed chemical model so as to obtain a specific, but efficient, sulphate dissolution–precipitation model to simulate the behaviour of the sulphate content in a flooded mine of the LIB. Such predictive simulation is important in that the reservoir is used as a drinking-water resource in the LIB. The first model represents the mine as two chemical reactors in a "box" model approach, whereas the second model represents the mine as a network of connected pipes with advective transport and a dissolution–precipitation reaction occurring inside each pipe. The Saizerais Mine of the LIB was modelled because of its small size and well-known structure. Furthermore, our knowledge of its boundary data, such as recharge flow and withdrawal rate,

and its calibration data, such as measurements of sulphate concentrations at the supply well and overflow point, has enabled the two models to be constructed and calibrated with a high degree of accuracy.

2. Description of the Saizerais Mine

2.1. Site location and mining techniques

The Lorraine Iron Basin (LIB), located along the eastern edge of the Paris Basin from the Luxembourg border to Nancy (Fig. 1), is separated into two unequal basins by the Pont-à-Mousson anticline: the Longwy–Briey Basin to the north and the Nancy Basin to the south. The Saizerais Mine, with an area of about 6 km^2, lies in the Nancy Basin. Its iron-bearing formation, no thicker than 5 m and known as "minette" because of its low iron content (30 to 35%), is overlain by about 5 m of micaceous marl, followed by a Dogger limestone succession, some 50 m thick, which constitutes a karstic aquifer. The iron ore comprises two layers: an upper calcareous layer about 2.7 m thick, and a lower siliceous layer about 1.2 m thick. Being separated by only a thin (0 to 0.4 m) marly intercalation, they were worked together and not individually. Mining began in 1957 using the room and pillar method, except that, because of roof instability and considerable water ingress at the beginning of the exploitation, the pillars were left standing. This has resulted in a dense network of galleries (8 10^6 m^3 of voids; Fig. 1) from which the ore was extracted between the 80 m level (northeast end of the mine) and the 140 m level (southwest end of the mine) with a slope of about 2%. When mining ceased in June 1981, 21 million tons of ore had been excavated.

2.2. Hydrological and hydrochemical behaviour during and after mining

Excavation of the mine galleries resulted in an ingress of groundwater from the Dogger aquifer, turning the Saizerais Mine into an artificial drain. The water inflow was not diffuse throughout the rock mass, but appeared to follow preferential flow paths along karstic conduits and fractures induced by the exploitation in specific areas.

Because of its good quality, the water pumped from the Saizerais Mine has been used directly as a drinking-water supply for Pont-à-Mousson since 1972. Dewatering ceased, however, when the mine was closed in June 1981. The mine galleries were then progressively flooded from the deeper northeastern part (gallery roofs at the 80 m level) to the shallower southwestern part (gallery roofs at the 140 m level), and by December 1982 the mine water had risen to the overflow point at 200 m in Drift 2 (Fig. 1), northeast of the mine, from where it flows directly into the Moselle river. Chemical monitoring (Cl, SO_4, Na, Mg, NO_3 and Fe) of the water as the mine flooded showed that the flooding was accompanied by a sharp increase in the sulphate content; 42 mg/l before flooding to a maxima of 1200 mg/l at the overflow point and 595 mg/l at the pumping well. The difference between the maximum concentrations at these two points can be explained by a stratification of the water quality inside the mine due to the presence of a dead storage zone in the deepest part of the reservoir connected by Drift 2 (Collon et al., 2002); this dead zone probably has different physical and chemical properties compared to the main mine conduits. A water over-pumping system was added to Drift 2 in September 1987 in order to increase the renewal rate of the mine water and consequently decrease the sulphate concentrations.

3. Hydrological and chemical modelling parameters

3.1. Hydrological parameters

The hydrological parameters needed for both the models are inflow and outflow rates and volume of the mine voids. The inflow rate was calculated using the TEMPO® computer code based on signal-processing methods (Pinault et al., 2001a; Pinault et al., 2001b). The principle is to calculate impulse responses relating effective rainfall data with dewatering discharge records over the mining period when such data were measured (1971–1981). From this it was possible to establish the mine's outflow discharge rate and its post-flooding recharge rate over the 1981–2000 period when the effective rainfall could be calculated. The outflow rates correspond to a) withdrawals from the supply well and b) the post-flooding overflow rate. The total volume of the mine reservoir was calculated by integrating the difference between the inflows and withdrawals from the end of dewatering in June 1981 until the first overflow in December 1982. This gives an estimate of 8.85 10^6 m^3, which is in accordance with the 8 10^6 m^3 estimated by the mining company and thus validates the hydrological data.

3.2. Chemical models and parameters

In a first step, we used the detailed chemical model (Collon et al., 2006) built to simulate the evolution of water quality of the flooded iron-ore mines in the Lorraine region. This model includes 10 chemical elements, 25 aqueous species, 19 minerals, 2 gases and 4 ion-exchange reactions. All the reactions of the detailed

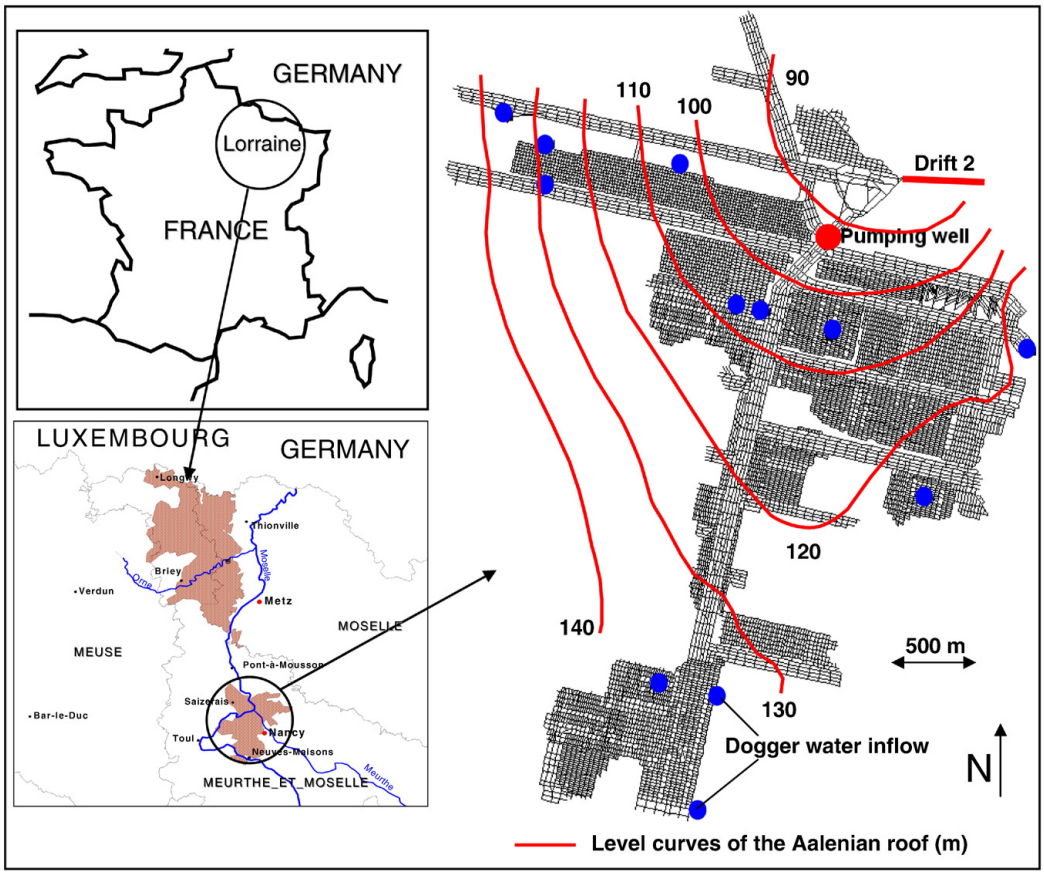

Fig. 1. Site location and network of the Saizerais flooded iron-ore mine.

chemical model are kinetic, Table 1 gives some examples of those reactions. The general precipitation–dissolution reaction rate $r(t)$ is written as:

$$r(t) = F_g[m_{A_nB}(t)]^{2/3} k'_{\text{pcp}} \left[K(A_nB) - (A^+)^n (B^{n-})\right] \quad (1)$$

where K is the equilibrium constant of a reaction $A_nB \leftrightarrow nA^+ + B^{n-}$; (A^+) and (B^{n-}) are the activity of aqueous species A and B (in mol/L); (A_nB) is the activity of the solid phase A_nB (considered equal to 1); k'_{pcp} is the apparent kinetic precipitation constant (in mol/s); $m_{AnB}(t)$ is the mass of A_nB at time t (in mol/L), with $[m_{AnB}(t)]^{2/3}$ taking into account the variation of mineral surface with the available mineral quantity; and F_g expresses the influence of the specific surface of a block of rock (in m^2) on the global reaction rate (Collon et al., 2006).

The equilibrium constants (Table 2) are those from PHREEQC thermodynamic data base (Parkhurst and Appelo, 1999). The Debye–Hückel relation is used for aqueous species activity calculation.

The initial mass m_{AnB} ($t=0$) is defined by the mineral quantity per kilogram of rock, M_{AnB}, multiplied by the mass of rock per litre of water, M_R:

$$m_{AnB}(t=0) = M_{AnB} M_R \quad (2)$$

The mineral quantity per kilogram of rock (defining the rock composition, Table 3) and the apparent kinetic precipitation constant (Table 2) were adapted from Collon et al. (2006), considering the particular geometry of the Saizerais Mine. The mineralogical composition and the apparent kinetic constant of the three groups of rocks observed in the mine (*crassin*, marly hanging walls, and marly intercalations) were evaluated from laboratory experiments (Collon et al., 2004; Collon et al., 2005). Based on the Saizerais Mine maps, we evaluated a mean gallery width of 5.25 m and height of 4.1 m, and a mean pillar width of 7.5 m and length of 20 m. This allowed us to define an average unit cell around each pillar (Fig. 2) and to estimate a "mixed rock" surface in contact with the water; i.e. 2% marly intercalations, 29.5% marly hanging wall and 68.5% *crassin*. Thus, the mineralogical composition and the apparent kinetic constant for each mineral of the "Saizerais mixed rock" are obtained by using the relative proportions of the above rock types. The kinetic constants for aqueous speciation and complexation reactions are set arbitrarily to account for their rapid rates compared to those of mineral dissolution and precipitation.

The reference rock mass M_R (on the basis of 1 l of associated water) and the F_g factor are unknown at the mine scale, being two parameters independent of the nature of the rock and depending only on the mining method used (Collon et al., 2006). They were determined by fitting the simulated SO_4 concentration to the Saizerais field data during the first 3 years (Table 4) (see Section 4.3).

This detailed chemical model is included as a source/sink in each reactor of a network of chemical reactors (NCR) as described in Section 4.2. Due to the amount of computer time required for each run, the number of reactors in the NCR with the detailed chemical model is limited. Thus, in order to build a large NCR able to simulate the sulphate evolution in the water of each sector of the flooded mine, we simplified the detailed chemical model to obtain a specific sulphate dissolution–precipitation model that could also be easily included as sulphate source/sink in a pipe network model (PNM).

In this second step, we only consider the sulphate from minerals, SO_4c, and the sulphate from aqueous species, SO_4aq. We assume a global sulphate dissolution–precipitation reaction written as:

$$SO_4c \leftrightarrow SO_4aq \quad (3)$$

The rate of this reaction $r(t)$, based on the general formulation (1) is defined as:

$$r(t) = k^*_{\text{pcp}}[m(t)]^{2/3}[K^* - C(t)] \quad (4)$$

where $C(t)$ is the SO_4aq concentration; K^* is the apparent equilibrium constant of reaction (3), defined as equal to $C(t)$ when the rate is nil; $m(t)$ is the available mass of SO_4c at time t; and k^*_{pcp} is the apparent kinetic precipitation constant of reaction (3), including both

Table 1
Kinetic model of five chemical reactions

Type of Reaction	Reaction	Rate
Dissolution/precipitation	$CaSO_4$, $2H_2O \leftrightarrow Ca^{++} + SO_4^{2-} + 2\ H_2O$	$r(t)=F_g(m_{AnB})^{2/3}\ k'_{\text{pcp-gyps}}[K-(Ca^{++})(SO_4^{2-})]$
Dissolution/precipitation	$FeS_2 + 3.75\ O_2 + 3.5\ H_2O \leftrightarrow 4\ H^+ + Fe(OH)_{3aq} + 2\ SO_4^{2-}$	$r(t)=F_g(m_{AnB})^{2/3}\ k'_{\text{pcp-pyr}}[K(O_2)^{3.75}-(H^+)^4(SO_4^{2-})^2\ (Fe(OH)_{3aq})]$
Aqueous complexation	$H_2O \leftrightarrow H^+ + OH^-$	$r(t)=k'_{H2O}[K-(H^+)\ (OH^-)]$
Dissolution/degassing	$CO_{2(g)} \leftrightarrow CO_2$	$r(t)=k'_{CO2}\ [K\ P_{CO2}-(CO_2)]$*
Cationic exchange	$X\_Na + 0.5\ Ca^{++} \leftrightarrow Na^+ + X\_Ca_{0.5}$	$r(t)=k'_{XNa}[K\ (X\_Na)(Ca^{++})^{0.5}-(X\_Ca_{0.5})(Na^+)]$

* P_{CO2} is the partial pressure of $CO_{2(g)}$.

Table 2
Reactions of the detailed chemical model and their constants

	Log K(T) T=25 °C*	k'_{pcp}** (mol/s)
Mineral dissolution and precipitation reactions		
$Al(OH)_{3\ (am)} \leftrightarrow Al(OH)_3$	−6.1	8.30 10−^{4}
$NaAlSi_3O_8 + 4\ H_2O \leftrightarrow Na^+ + Al(OH)_4^- + 3\ H_4SiO_4$	−18.002	1.76 10^{+3}
$SiO_{2\ (Chalcedony)} + 2\ H_2O \leftrightarrow H_4SiO_4$	−3.55	3.82 10^{-4}
$CaCO_3 + H^+ \leftrightarrow Ca^{++} + HCO_3^-$	1.849	5.41 10^{-4}
$SrSO_4 \leftrightarrow Sr^{++} + SO_4^{2-}$	−6.63	1.7518
$Mg_5Al_2Si_3O_{10}(OH)_8 + 10\ H^+ \leftrightarrow 5\ Mg^{++} + 2\ Al(OH)_3 + 3\ H_4SiO_4$	34.58	3.90 10^{+7}
$CaMg(CO_3)_2 + 2\ H^+ \leftrightarrow Ca^{++} + 2\ HCO_3^- + Mg^{++}$	3.568	6.55 10^{-3}
$Fe(OH)_{3\ (am)} \leftrightarrow Fe(OH)_3$	−7.669	9.75 10^{-6}
$Al(OH)_{3\ (am)} \leftrightarrow Al(OH)_3$	−8.79	23.7
$FeOOH + H_2O \leftrightarrow Fe(OH)_3$	−13.56	3.02 10^{-10}
$CaSO_4{,}2H_2O \leftrightarrow Ca^{++} + SO_4^{2-} + 2\ H_2O$	−4.58	4.82 10^{-2}
$Fe_2O_3 + 3\ H_2O \leftrightarrow 2\ Fe(OH)_3$	−29.128	5.13 10^{-4}
$KAlSi_3O_8 + 8\ H_2O \leftrightarrow K^+ + Al(OH)_4^- + 3\ H_4SiO_4$	−20.573	3.08 10^{-3}
$KAl_3Si_3O_{10}(OH)_2 + 1H^+ + 9\ H_2O \leftrightarrow K^+ + 3\ Al(OH)_3 + 3\ H_4SiO_4$	−37.997	7.39 10^{+6}
$Al_2Si_2O_5(OH)_4 + 7\ H_2O \leftrightarrow 2\ H_4SiO_4 + 2\ H^+ + 2\ Al(OH)_4^-$	−37.965	8.00 10^{+31}
$FeS_2 + 3.75\ O_2 + 3.5\ H_2O \leftrightarrow 4\ H^+ + Fe(OH)_3 + 2\ SO_4^{2-}$	211.441	1.64 10^{-203}
$SiO_{2\ (Quartz)} + 2\ H_2O \leftrightarrow H_4SiO_4$	−3.98	1.89 10^{-6}
$FeCO_3 + 2.5\ H_2O + 0.25\ O_2 \leftrightarrow H^+ + Fe(OH) + HCO_3^-$	−4.621	9.13 10^{-6}
$SrCO_3 + H^+ \leftrightarrow Sr^{++} + HCO_3^-$	1.058	9.25 10^{-8}
Aqueous speciation reactions		k' (mol/s)
$H_2O \leftrightarrow H^+ + OH^-$	14	10^{+18}
$Al(OH)_3 + H^+ \leftrightarrow Al(OH)_2^+ + H_2O$	6.8	10^{+4}
$Al(OH)_3 + H_2O \leftrightarrow Al(OH)_4^- + H^+$	−5.8	6.3 10^{+9}
$HCO_3^- \leftrightarrow H^+ + CO_3^{2-}$	−10.329	2.1 10^{+14}
$Ca^{++} + HCO_3^- \leftrightarrow CaCO_3 + H^+$	−7.105	1.27 10^{+11}
$Ca^{++} + HCO_3^- \leftrightarrow CaHCO_3^+$	1.106	10^{+4}
$Ca^{++} + H_2O \leftrightarrow CaOH^+ + H^+$	−12.78	6 10^{+16}
$Ca^{++} + SO_4^{2-} \leftrightarrow CaSO_4$	2.3	10^{+4}
$Fe(OH)_3 + H^+ \leftrightarrow Fe(OH)_2^+ + H_2O$	6.89	10^{+4}
$Fe(OH)_3 + H_2O \leftrightarrow Fe(OH)_4^- + H^+$	−9.04	10^{+13}
$H_2O + O_2 \leftrightarrow H_2$	−92.38	10^{+50}
$CO_2 + H_2O = H^+ + HCO_3^-$	−6.352	5 10^{+10}
$H_4SiO_4 \leftrightarrow H^+ + H_3SiO_4^-$	−9.83	6.8 10^{+13}
$H^+ + SO_4^{2-} \leftrightarrow HSO_4^-$	1.988	10^{+4}
$K^+ + SO_4^{2-} \leftrightarrow KSO_4^-$	0.85	10^{+4}
$Mg^{++} + CO_3^{2-} \leftrightarrow MgCO_3$	2.98	10^{+4}
$Mg^{++} + HCO_3^- \leftrightarrow MgHCO_3^+$	1.07	10^{+4}
$Mg^{++} + H_2O \leftrightarrow MgOH^+ + H^+$	−11.4	2.5 10^{+15}
$Mg^{++} + SO_4^{2-} \leftrightarrow MgSO_4$	2.37	10^{+4}
$Na^+ + CO_3^{2-} \leftrightarrow NaCO_3^-$	1.27	10^{+4}
$Na^+ + HCO_3^- \leftrightarrow NaHCO_3$	−0.25	1.8 10^{+4}
$Na^+ + SO_4^- \leftrightarrow NaSO_4^-$	0.7	10^{+4}
$Sr^{++} + CO_3^{2-} \leftrightarrow SrCO_3$	2.81	10^{+4}
$Sr^{++} + HCO_3^- \leftrightarrow SrHCO_3^+$	1.18	10^{+4}
$Sr^{++} + SO_4^{2-} \leftrightarrow SrSO_4$	2.29	10^{+4}
Dissolution and degassing of O_2 and CO_2		
$CO_{2(g)} \leftrightarrow CO_2$	−1.468	3 10^{-6}
$O_{2(g)} \leftrightarrow O_2$	−2.96	1.97 10^{-7}
"Cationic exchange reactions" (representation of sorption/desorption/surface reactions phenomena)		
$X\_Na + 0.5\ Ca^{++} \leftrightarrow Na^+ + X\_Ca_{0.5}$	1.439	8.55 10^{-3}
$X\_K + 0.5\ Ca^{++} \leftrightarrow K^+ + X\_Ca_{0.5}$	0.548	0.44
$X\_Mg_{0.5} + 0.5\ Ca^{++} \leftrightarrow 0.5\ Mg^{++} + X\_Ca_{0.5}$	1.349	3.93 10^{-2}
$X\_H + 0.5\ Ca^{++} \leftrightarrow H^+ + X\_Ca_{0.5}$	−5.492	30.4

Table 3
Mineralogical composition (mol/kg of rock): M_{AnB}

Mining conditions	Galleries with marly hanging walls
Corresponding rock	Saizerais Mixed rock
$Al(OH)_3$	$4.66\ 10^{-1}$
Albite	$2.01\ 10^{-2}$
Chalcedony	$7.80\ 10^{-2}$
Calcite	3.53
Celestite	$3.79\ 10^{-5}$
Chlorite	$6.83\ 10^{-2}$
Dolomite	$2.85\ 10^{-2}$
$Fe(OH)_3$	$4.19\ 10^{-1}$
Gibbsite	$1.17\ 10^{-1}$
Goethite	3.56
Gypsum	$4.42\ 10^{-3}$
Hematite	$1.05\ 10^{-1}$
K-mica	$5.00\ 10^{-2}$
K-feldspar	$3.33\ 10^{-2}$
Pyrite	$2.23\ 10^{-2}$
Quartz	1.48
Siderite	$1.86\ 10^{-1}$
Strontianite	$3.10\ 10^{-3}$
X_Na	$3.95\ 10^{-3}$
X_K	$5.74\ 10^{-4}$
X_Ca0.5	$5.79\ 10^{-1}$
X_Mg0.5	$1.77\ 10^{-2}$
X_H	$7.16\ 10^{-8}$

elementary mechanisms and geometric parameters — this parameter can thus differ according to local specificities.

4. Water-quality simulation with a network of chemical reactors (NCR) model

4.1. Conceptual model of the mine

The conceptual model of the mine, according the NCR approach (Barranger and Kervévan, 1998; Collon et al., 2002; Collon et al., 2005; Collon et al., 2006), is a superposition of two perfectly mixed chemical reactors representing two reservoirs. The lower reservoir (reactor 2 of Fig. 3A) with the smaller volume represents the deepest part of the mine workings that is connected to the overflow drift (northeastern part). The upper reservoir (reactor 1 of Fig. 3A) represents the upper part of the mine workings. During the flooding, it is the deepest part of the mine (reactor 2) that is first filled with Dogger water recharge (Table 5). Once this reservoir is full, then the upper reservoir (reactor 1) is filled up to the overflow. From this moment the mine water overflows through Drift 2, which is linked directly to the lower reservoir. Equilibrium between the two reservoirs is established once the mine is filled; they are recharged by Dogger groundwater in proportions related to their volume, with the lower reservoir also being recharged by the upper reservoir when overflow and overpumping occur.

4.2. The chemical reactor

The chemical reactor is described by the following mass-balance equation (Villermaux, 1993):

$$Q_{\text{out}}C_{\text{out}} = Q_{\text{in}}C_{\text{in}} + V(t)r(t) - \frac{d(V(t)C(t))}{dt} \qquad (5)$$

where Q_{out} is the total outflow rate (volume/time); Q_{in} is the total inflow rate (volume/time); C_{out} is the outflow concentration (mass/volume); C_{in} is the inflow concentration (mass/volume); $C(t)$ is the concentration (mass/volume) in the reactor equal to the outflow concentration for a perfectly mixed reactor; $V(t)$ is the volume of water in the reactor; $r(t)$ is the rate of the dissolution–precipitation reaction (mass/time).

The perfectly mixed reactor assumes that all water entering the reservoir is instantaneously and completely mixed with the water already in the reactor. With the detailed chemical model reactor, C_{out}, C_{in} and $C(t)$ concern each aqueous species, and $r(t)$ is the rate of each dissolution–precipitation reaction (Eq. (1)). With the simplified chemical model reactor, C_{out}, C_{in} and $C(t)$ only concern the sulphate content of the water, and $r(t)$ the rate of Eq. (3). A schematic single reactor is represented in Fig. 3B.

4.3. Building the NCR

The Saizerais Mine NCR was built using the Matlab® and Simulink® software package. The volume of reactor 2, connected to the overflow point through Drift 2 and corresponding to voids below the 90 m level, is estimated at $0.5\ 10^6\ m^3$ by the mining company, and that of reactor 1 at $8.35\ 10^6\ m^3$ (Collon et al., 2002).

The parameters M_R and F_g of the NCR with the detailed chemical model were obtained using the constants from the LIB south basin as an initial guess (Collon et al.,

Notes to Table 2:
*For each reaction, except the "exchange" reactions, K(T) is extracted from the PHREEQC database (Parkhurst and Appelo, 1999). The equilibrium constant of the exchange reactions are extracted from the experimental workings of Collon (Collon, 2003).
**k'_{pcp} varies from one rock to another. These fluctuations have influence only if the reactions don't reach the thermodynamic equilibrium but are closed to it (Collon, 2003; Collon et al., 2006). For these reactions, the value of k'_{pcp} indicated here, is specific for Saizerais Mine.

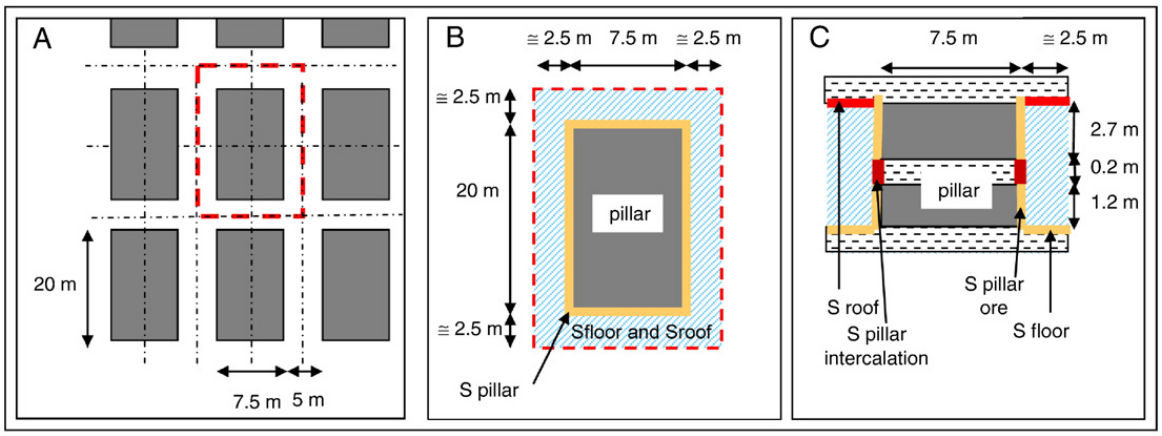

S pillar intercalation = [(7.5 + 20) x 2)] x 0.2 = 11 m²
S pillar ore = [(7.5 + 20) x 2] x (2.7 + 1.2) = 214.5 m²
S floor = S roof = [(7.5 + 2.5) x 2.5 + (20 + 2.5) x 2.5] x 2 = 162.5 m²
S total = 550.5 m²

Then:
S intercalation = 11 / 550.5 = 2%
S ore (floor + pillar) = (214.5 + 162.5) / 550.5 = 68.5%
S roof = 162.5 / 550.5 = 29.5%

Fig. 2. Average unit cell around a pillar.

2006), and by fitting the calculated sulphate with the measured sulphate over the first 3 years of overflow (Fig. 4 and Table 4). The parameters of the NCR with the simplified chemical model were obtained by fitting the calculated sulphate to the results obtained with the detailed chemical model (Fig. 4 and Table 6). This fitting was constrained with initial masses of sulphate $m(t=0)$, as close as possible with those of the detailed chemical model (0.046 mol/l and 0.088 mol/l for the upper and lower reactor respectively).

5. Reactive-transport simulation with a pipe network model (PNM)

5.1. Conceptual model of the mine

In this second model, the mine galleries are represented by a network of connected pipes. This approach considers that the volume of water is contained mainly in the empty galleries, which can be compared to highly conductive pipes (with sections between 15 and 20 m^2) as against the very small porosity of the rock matrix. The large difference in hydraulic conductivity between the rock and the open galleries allows only a small part of the water to penetrate into the rock surrounding these galleries. Likewise, the water flow from the surrounding rock towards the galleries is also limited. For this reason, pore space of the rock matrix is neglected in the pipe network model.

Table 4
M_R and F_g parameters for the NCR with the detailed chemical model

	Upper reservoir Reactor 1	Lower reservoir Reactor 2
M_R (kg/L)	10.5	20
F_g (m^2)	$9.21\ 10^{-4}$	$1.36\ 10^{-3}$

The software used for simulating the flows and reactive transport in the mine is the EPANET 2 code (Rossman, 2000) which was initially designed for modelling flow and simulating water quality in water-supply networks. The governing equations of the EPANET code for flow modelling appear suitable for simulating flow in flooded mine galleries. For the reactive-transport simulations, however, the EPANET code had to be enhanced in order to simulate the possibility of a dissolution–precipitation reaction at the pipe wall. The physical and hydraulic characteristics of such a network include the pipe lengths, inside diameters and roughness coefficients. Furthermore, for the water-quality simulation, each pipe is characterised by kinetic dissolution and precipitation constants and by an initial solid sulphate mass in the pipe wall. The model considers that all the pipes are saturated with water at the beginning of the simulation; this implies that the simulation begins at the post-filling phase when overflow begins, and does not include the filling process itself.

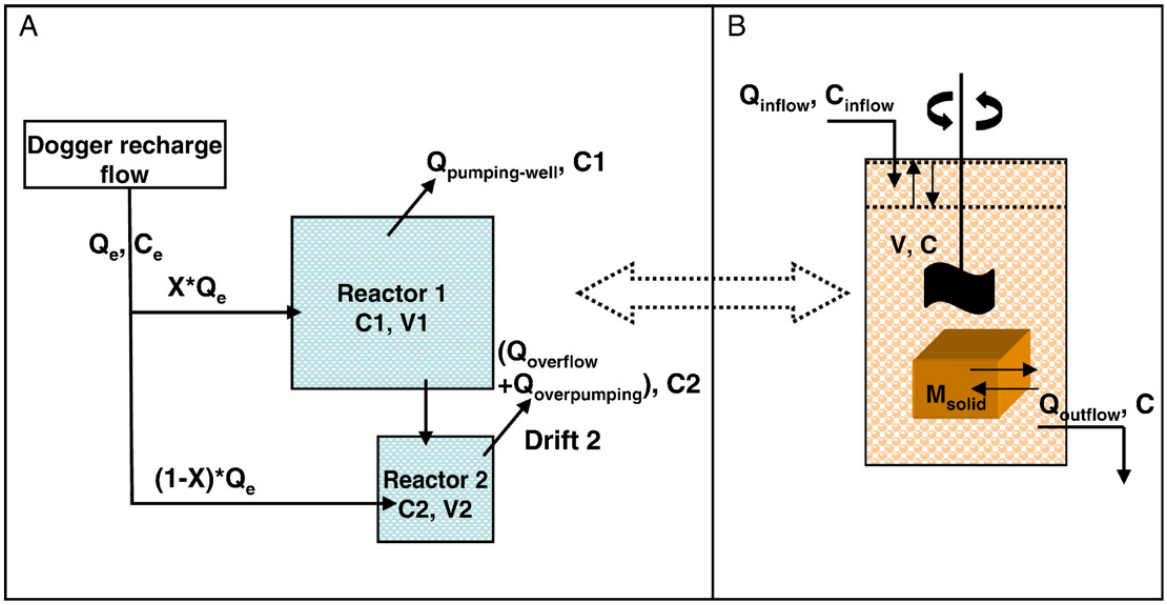

Fig. 3. Schematic representation of the Saizerais Mine (A) and perfectly mixed chemical reactor (B).

5.2. Hydraulic assumptions

The hydraulic state of the pipe network at a given time is characterised by head-loss and flow-continuity equations. The flow–head loss relationship in a pipe between nodes i and j is expressed by the Darcy–Weisbach equation in the EPANET code:

$$H_i - H_j = h_{ij} = 0.0252 f(\varepsilon, d, q) d^{-5} L \cdot q_{ij}^2 \quad (6)$$

where H is the nodal head; h is the head loss; q_{ij} is the flow rate in the pipe ij; L *is* the pipe length; d is the hydraulic diameter; and f is the friction factor dependent on the roughness coefficient, pipe diameter and flow rate with different expressions according to the flow's Reynolds Number.

Eq. (6) expresses the loss of energy due to the friction between the moving water process and the stationary pipe surface.

The second set of equations that must be satisfied is the flow continuity at each pipe junction i:

$$\sum_j q_{ij} - D_i = 0 \quad (7)$$

where D_i is the flow demand at node i (positive for outflow and negative for inflow).

5.3. Water-quality simulation

The governing equations for water quality in the EPANET code include advective transport in the pipes coupled with kinetic reactions and mixing processes at the pipe junctions. To take the earlier described solid-sulphate dissolution–precipitation reaction into account, certain specific developments had to be made to the EPANET water-quality solver.

Advective transport within a pipe is represented by the equation:

$$\frac{\partial C_p}{\partial t} = -v\frac{\partial C_p}{\partial x} + r(C_p, m) \quad (8)$$

where C_p is the concentration (mass/volume) of sulphate in a pipe as a function of distance x and time t; v is the velocity of fluid in the pipe (length/time); and r is the rate of the reaction (mass/volume/time) as a function of the sulphate concentration in water and the available mass of solid sulphate (see Eq. (4)).

The equation for advective transport (Eq. (8)) is solved in the EPANET solver using a Lagrangian time-based method (Liou and Kroon, 1987) to track the fate of discrete parcels of water as they move along the pipes

Table 5
Average composition of inflow to the mine workings (water seepage through the galleries roof)

Element	pH	Cond mS/cm	Al µg/l	B µg/l	Ca mg/l	Cl mg/l	HCO_3 mg/l	Fe µg/l	K mg/l	Mg mg/l	Na mg/l	SO_4 mg/l	SiO_2 mg/l	Sr µg/l
Concentration	7.6	0.55	<30	131	83	23	236	<20	1.3	11	14	42	8	502

and mix together at junctions. Fig. 5 gives an example of parcels or segments of water moving in the pipes, reacting with the pipe walls and then mixing at the nodes. The volume of a segment equals the product of the pipe flow rate and the time step.

The water quality in each segment is updated by introducing a reactive term in the EPANET solution in order to reflect a dissolution–precipitation reaction occurring over each time step *dt*. The change in water concentration is given by:

$$C_{seg}^{n+1} = C_{seg}^{n} + k_{pcp}^{*}(m^{n})^{2/3}\left(K^{*} - C_{seg}^{n+1}\right)dt \qquad (9)$$

where C_{seg}^{n} is the concentration of sulphate at time t in a segment of water (mass/volume segment); C_{seg}^{n+1} is the updated concentration of sulphate at time $t+\mathrm{dt}$; m^{n} is

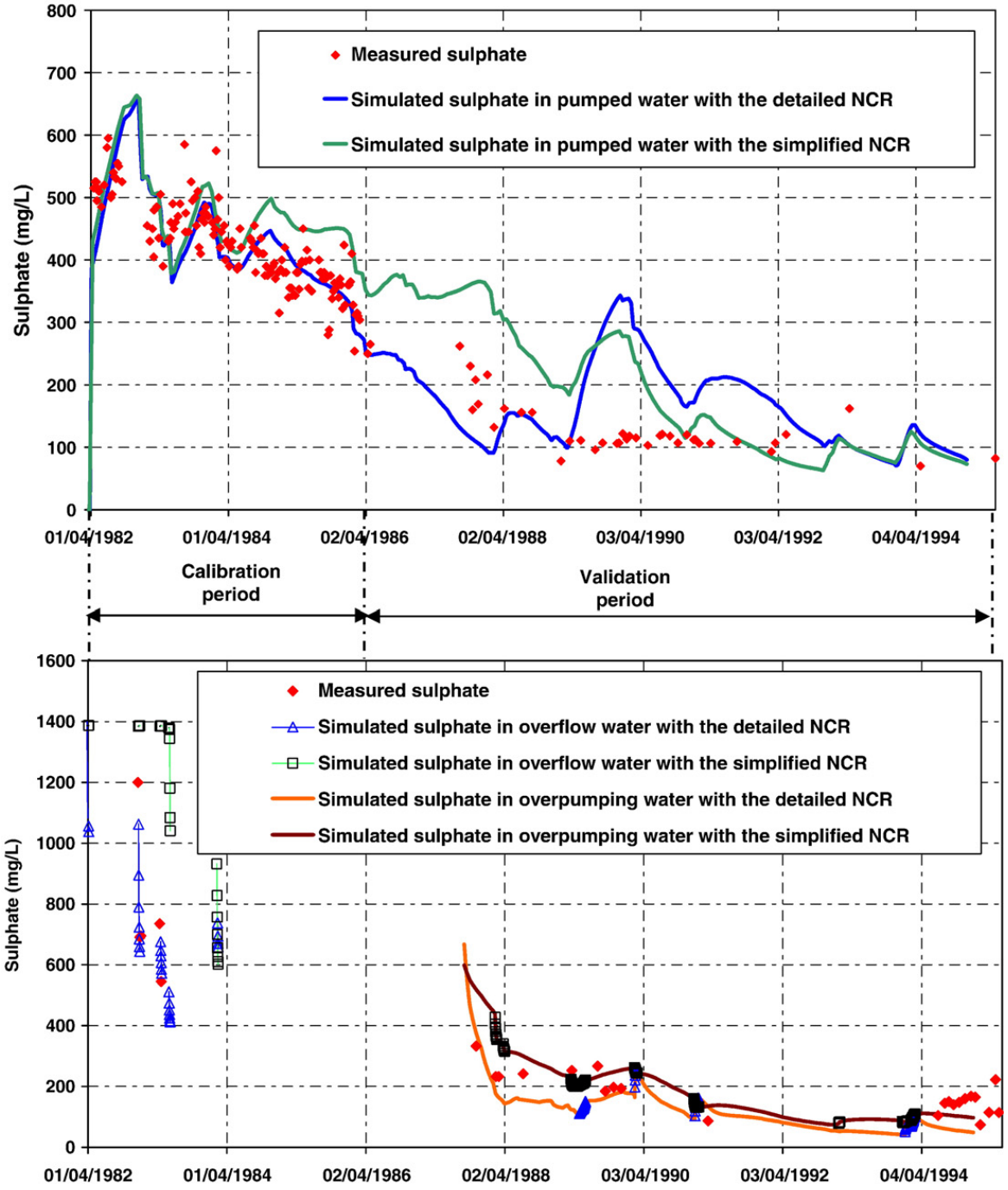

Fig. 4. Simulated sulphate for the detailed and simplified chemical models.

Table 6
Parameters of the NCR and PNM with the simplified chemical model

	Log K^*	Log k^*_{pcp}	$m(t=0)$ (mol/L)
Upper reservoir (Reactor 1 in the NCR or Pipes above 90 m level in the PNM)	−1.84	−6.5	0.05
Lower reservoir (Reactor 2 in the NCR or Pipes below 90 m level in the PNM)	−1.84	−2	0.07

the mass of solid sulphate available per volume of water at time t; k^*_{pcp} is the apparent kinetic constant of precipitation; and K^* is the equilibrium constant of the solid sulphate dissolution and precipitation reaction (see Section 3.2).

We then introduced the mass m of solid sulphate for each pipe in the EPANET code through the equation:

$$m^{n+1} = m^n - \frac{\sum_{\text{segment}} \left(C^{n+1}_{\text{seg}} - C^{n}_{\text{seg}} \right) \cdot V_{\text{seg}}}{\sum_{\text{segment}} V_{\text{seg}}} \tag{10}$$

where m^{n+1} is the updated solid sulphate mass in the pipe wall after dissolution or precipitation has occurred; m^n is the mass at the previous time; and V_{seg} is the water segment volume.

After the dissolution–precipitation reaction has occurred in a pipe (Eqs. (9) and (10)), the water quality and flow from the leading segments of the pipes are blended together to compute a new water quality at the downstream junction. This is expressed in the EPANET code by:

$$C_{\text{dstrnode}} = \frac{\sum_{\text{upstrlink}} C_{\text{seg1}} \min\left(Qdt, V_{\text{seg1}}\right)}{\sum_{\text{upstrlink}} \min\left(Qdt, V_{\text{seg1}}\right)} \tag{11}$$

where C_{seg1} is the concentration of the leading segment in a pipe; and $\min(Qdt, V_{\text{seg1}})$ is the minimum between the flow volume and the leading segment volume.

If the flow volume exceeds the leading segment volume, then the next segment behind begins to contribute part of its volume and water quality. The new quality at a node is then obtained by summing the quality value at a junction calculated by Eq. (11) with the outside source contribution. New segments are created in the pipes with the segment volume equal to the product of the pipe flow and the time step, and with the segment water quality equal to the new computed quality for the upstream node.

5.4. Building the PNM

The pipe network model (PNM) was built using both Mapinfo® and EPANET interfaces. The junctions were first digitized, using Mapinfo®, from the map of the Saizerais Mine workings with their Lambert coordinates. The junctions file was then imported into EPANET and links between junctions traced and set automatically with their real lengths. The Saizerais Mine network (Fig. 1) is composed of 10 470 nodes (junctions) and 19 075 pipes

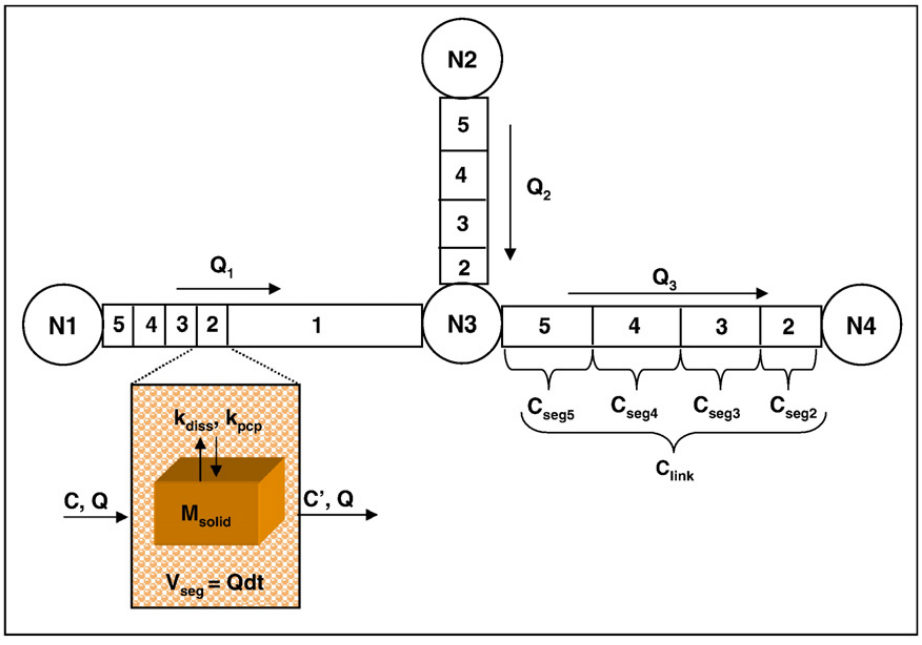

Fig. 5. Advective and reactive transport in pipes.

(galleries). The network was built in its entirety, including each individual gallery, and is therefore a precise representation of the mine workings. The pipe diameter was fixed so that the total volume of the mine corresponds to 8.85 10^6 m^3; this gave a hydraulic diameter of about 5.1 m, which represents an average mine gallery width of 5.25 m and height of 3.9 m; the gallery width corresponding roughly to that of the heavy equipment and the height to an average thickness of the two ore layers. Hydraulic connections to the Dogger aquifer were located approximately on the mine workings map based on water inflows observed by the miners. They are represented in the model with recharge flow rates estimated by TEMPO® (see hydrological parameters Section 3.1), are equally distributed for each potential inflow, and are connected to outside reservoirs with a unique level corresponding to that of the aquifer. The Pont-à-Mousson supply well, the Drift 2 overflow and the overpumping are represented by their flow rates calculated with a daily step.

6. Simulation results and comparison between the two methods

6.1. Simulation results

The sulphate concentrations simulated with both the detailed and the simplified NCR models, present the same general behaviour (Fig. 4). The curve superposition due to the fitting process during the first 2 years is no longer maintained beyond 1984. The hydrological model being the same in both NCR, the divergence is the result of the differences between the chemical models. In the detailed chemical model, the sulphate concentration is the result of interactions between a set of precipitation–dissolution, aqueous speciation and ion-exchange reactions. Conversely, the sulphate of the simplified model is controlled by only one single reaction. When compared with the observed sulphate concentration at the pumping well and overflow drift, the results from both NCR models are similar, except during the 1989–1990 period (Fig. 4). This discrepancy is mainly linked with errors on the calculated inflow (Q_{in}) during this period due to the lack of reliable hydrological data.

The sulphate concentrations simulated with the simplified NCR model and the PNM are compared against measurements at the pumping well and overflow drift. Values of their chemical parameters are given in Table 6 and are identical for both models. Fig. 6 compares the simulated sulphate concentrations obtained for each model against the chemical analyses.

The sulphate concentrations simulated at the supply well by each model are similar to the observations. Those simulated by the PNM are more jagged than those of the NCR model. The difference is due to the way the mine is modelled; flows in the NCR model are homogeneously shared throughout the entire reservoir, whereas in the PNM they are divided between the individual pipes and are very low in zones with only a slight connection to the main galleries. Spreading of the flows in the network explains the retardation of sulphate concentration arrivals at the supply well. Roughly 7 years after the mine was fully flooded, the measured sulphate concentrations stabilized at around 100 mg/l. The concentrations calculated by the PNM at this point are slightly overestimated, oscillating around 150 mg/l. This difference makes us think that Dogger water inflow sites are probably more numerous than the observed locations used for the model, and that consequently the modelled network of pipes takes longer to be washed. The sulphate concentrations calculated by the NCR model at the pumping well are smoothed, but nevertheless render a good description of the average sulphate concentrations during flooding.

The simulated sulphate concentrations at the overflow point and for the overpumping system are expressed differently by the two approaches. With the NCR model, the concentrations at the overflow and overpumping points are calculated separately. With the PNM, the overflow and overpumping are considered together, whereupon an absence of sulphate concentration values indicates that there is no overflow and no overpumping and changes in sulphate concentrations indicate that there is overflow or overpumping after September 1987. Comparison between the two models shows that simulated concentration values in the overflow water are similar. Nevertheless, concentrations in the overflow water with the NCR model are a little higher than those with the PNM, and are a little overestimated the first years compared to measured sulphate concentrations. Overflow in the PNM occurs more often than in the NCR model (see January and April 1986). This difference could be explained by the fact that the overflow rates are imposed in the pipe network model and thus correspond to observed flows, whereas in the NCR model the overflow depends on the volume of the reactors, which appear to be slightly overestimated (bear in mind that the total volume of mine water was estimated at 8.85 10^6 m^3 from hydraulic data, compared to 8 10^6 m^3 estimated by the mining company). With the start of overpumping in September 1987, the simulated concentrations in the NCR model are higher than those in the PNM during the initial years, but then both decrease and stabilize between 50 and 100 mg/l.

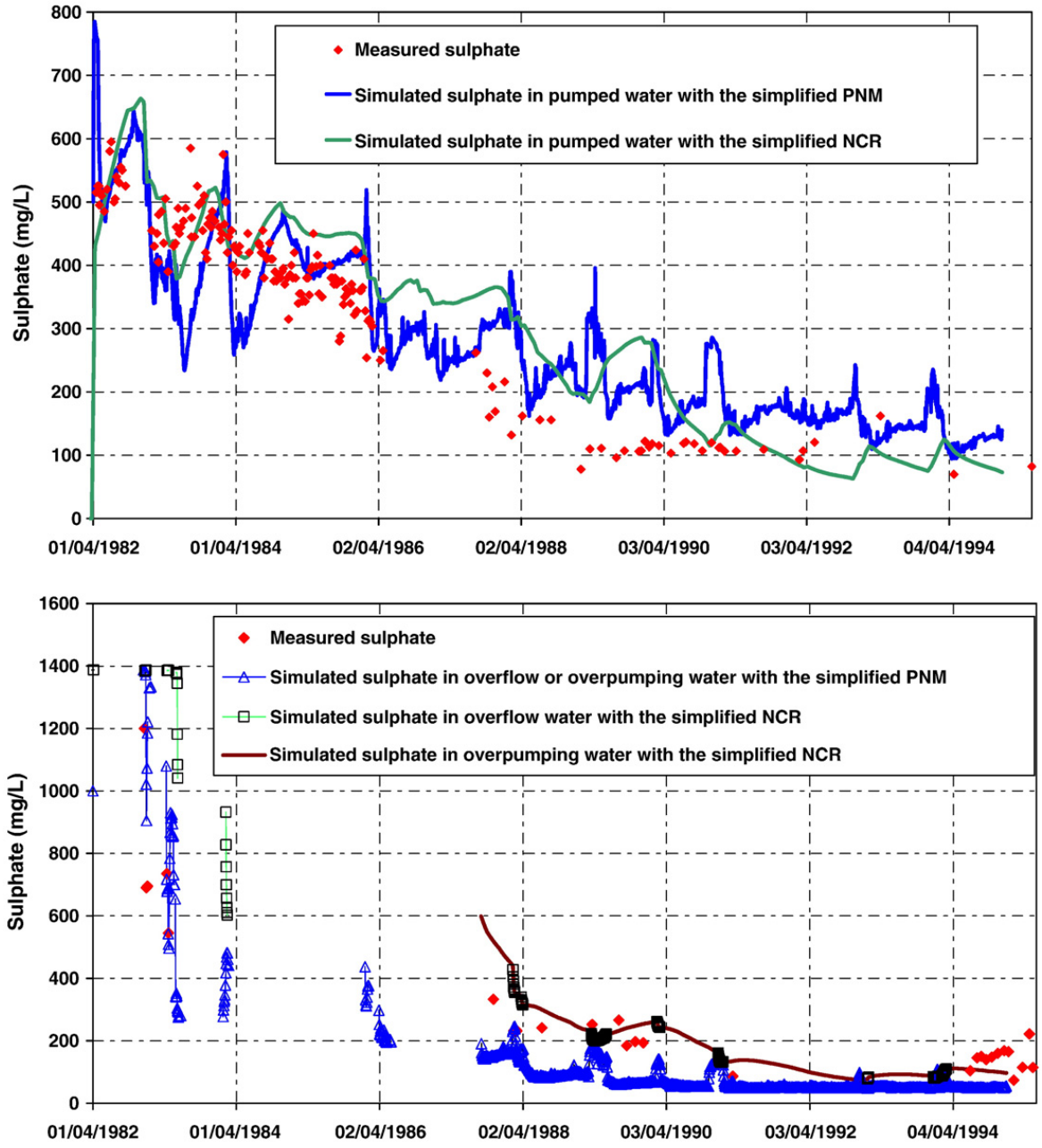

Fig. 6. Results and comparison of simulated sulphate concentrations at the pumping well and at the overflow point for the simplified NCR model and the PNM.

The chemical parameters for each model (Table 6) were fixed similar with regard to their chemical equilibrium and kinetic constants, and in the available initial mass of solid sulphate per volume water. The total mass of initial solid sulphate in each model amounts to 4.5 10^8 mol. Nevertheless, this mass is spatially distributed in the network of pipes and proportionally to the pipe lengths, whereas in the NCR model it is uniformly distributed in each reactor according to its volume of water. Results show that more than 12 years after the mine flooding, the mass of solid sulphate remaining in the PNM is 1.2 10^8 mol, meaning that around 75% of the introduced mass has been dissolved, as opposed to the full 4.5 10^8 mol of introduced solid sulphate being dissolved in the NCR model. The PNM clearly gives a better description of the physics controlling outflow and clean-up time compared to the simplified NCR model that underestimates time of solid sulphate removal due to the complete mixing assumption used. Moreover, the last measured concentration of sulphate at the supply well in March 2005 indicated a concentration of 83 mg/l (compared to 42 mg/l for

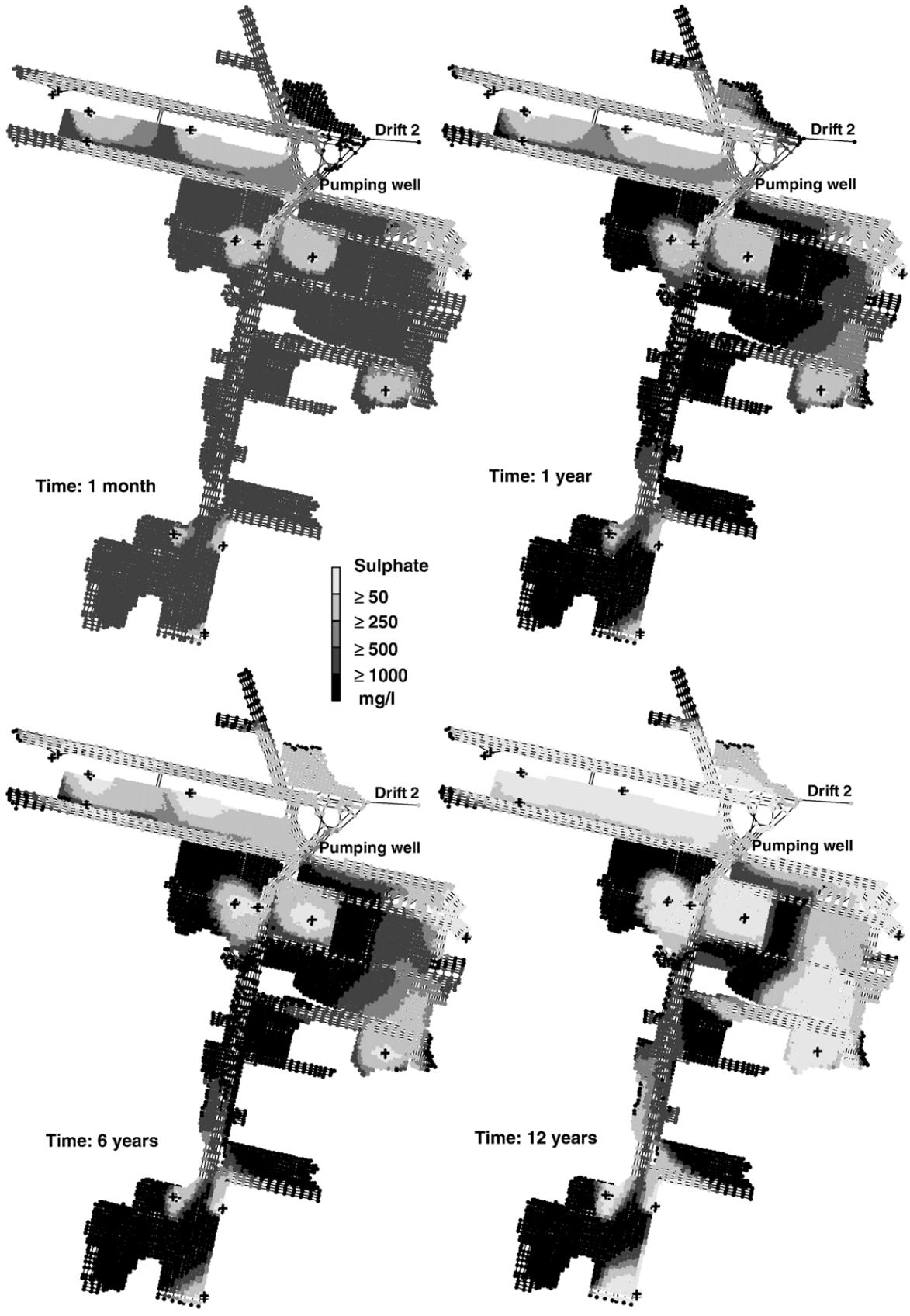

Fig. 7. Evolution of sulphate concentrations in the PNM.

Dogger water); this is close to that measured in 1995 and indicates that there is still available solid sulphate or that a stock of dissolved sulphate remains in the mine water.

6.2. Evolution of sulphate concentrations in the reactive transport pipe network model

The characteristics of the PNM with reactive transport include a spatially elaborated model of the mine and an estimate of the flow and sulphate concentrations at every mine node and pipe. This method needs to know the inflow and outflow locations for the model, which is not necessary with a NCR model. The last important point is the pipe filling process, which is not modelled because of the hydraulic assumptions used in EPANET (see Sections 5.1 and 5.2).

Fig. 7 shows the evolution of sulphate concentrations in the mine water after the mine had completely flooded, at this time sulphate concentrations are next to 500 mg/l in pipes above 90 m level (upper reservoir) and next to 1000 mg/l in pipes below 90 m level (lower reservoir). The concentrations of the water entering the mine reservoir equal those measured for Dogger aquifer water (around 42 mg/l). The simulated concentrations are shown in Fig. 7 at 1 month, 1 year, 6 years and 12 years after the mine had been filled. They indicate that the process of dissolution lasts for a very long time, and that more than 12 years after the beginning of mine flooding, concentrations in the reservoir are higher than those of the Dogger aquifer (except where surrounding the hydraulic inflows) with 25% of the initial mass of solid sulphate still remaining. Furthermore, concentrations in the galleries with low flow rates, located at the extremities or outside of the main flow paths, evolve very slowly and remain close to equilibrium with regard to the solid sulphate.

7. Conclusions

We have described two approaches to modelling the chemical aspects of mine flooding after closure of the Saizerais iron-ore mine in Lorraine (NE France). Both models make it possible, after calibrating their chemical parameters, to predict the evolution of sulphate concentration in the mine water. The first approach, based on a semi-distributed model represented by a network of chemical reactors (NCR), conceptualizes the mine as interconnected reservoirs with homogeneous properties. The method is efficient especially for large mine areas, but is limited by the concept of grouping mine workings with a subsequent loss of local information. The major advantage of this approach, however, is the possibility of modelling the evolution of water quality during the mine filling process and of being able to include a detailed chemical model that allows the detailed water chemistry to be simulated. The second approach, based on a distributed pipe network model (PNM), was developed with a modified version of the EPANET code in order to simulate a simplified sulphate dissolution–precipitation reaction. In this approach, each mine gallery is taken individually into account as a network of connected pipes. The major advantage of this method compared to the NCR model, is that the PNM allows a better description of the physics controlling flow and time of solid sulphate removal due to the effect of low flow zones. Nevertheless, the method could be less efficient for large mine areas; first, the time needed to build the network of pipes increases proportionally to the size of the mine which is not necessary the case for a NCR approach, and second, the computer time and allocated memory size increase proportionally to the number of pipes. Consequently, it would appear that the NCR method which is much quicker (except for NCR with a large number of reactors with detailed chemistry) could be used in preliminary assessments and secondary the PNM method that provides more detailed information on flow and clean-up effect.

The two modelling approaches (NCR and the PNM) are not limited to flooded iron-ore mines. They can equally be applied to other kinds of mines for predicting the evolution of water quality after flooding as long as their hydrological and chemical parameters are adapted to each studied case.

Acknowledgments

This work forms part of the research program carried out by the GISOS Research Group for the Impact and Safety of Underground Works.

References

Adams, R., Younger, P.L., 2001. A strategy for modelling groundwater rebound in abandoned deep mine systems. Groundwater 39 (2), 249–261.

Babot, Y., Duzan, A., Eckart, M., Kories, H., Metz, M., Rengers, R., 2005. Flooding of the Saar-Lorraine coal mines: coupling of the regional model of the lower Triassic sandstones aquifer with a “box” model of the mining reservoir. Post-Mining 2005. France, Nancy. November 16-17, CD, 7 pp.

Barranger, P., Kervévan, C., 1998. SCS: Specific Chemical Simulators dedicated to chemistry–transport coupled modelling part II — a simplified coupled modelling approach based on Networks of Chemical Reactors, Goldschmidt conference 1998, Toulouse. Mineralogical magazine 62A, 114–115.

Bauer, S., Liedl, R., Sauter, M., 2003. Modeling of karst aquifer genesis: influence of exchange flow. Water Resources Research 39 (10), 1285. doi:10.1029/2003WR002218, 2003.

Birk, S., Liedl, R., Sauter, M., Teutsch, G., 2003. Hydraulic boundary conditions as a controlling factor in karst genesis: a numerical modelling study on artesian conduit development in gypsum. Water Resources Research 39 (1), 1004. doi:10.1029/2002WR001308, 2003.

Brown, P.L., Lowson, R.T., 1997. The use of kinetic modelling as a tool in the assessment of contaminant release during rehabilitation of a uranium mine. Journal of Contaminant Hydrology 26, 27–34.

Collon, P. (2003) - Evolution de la qualité de l'eau des mines abandonnées du bassin ferrifère lorrain. De l'expérimentation en laboratoire à la modélisation in situ. Thesis INPL, October 2003, 247 pp.

Collon, P., Fabriol, R., Buès, M., 2004. Ennoyage des mines de fer lorraines: impact sur la qualité de l'eau — flooding of the iron mines of Lorraine: impact on the water quality. Comptes Rendus Géoscience, Géochimie 336, 889–899.

Collon, P., Fabriol, R., Buès, M., 2005. Evolution of water quality in the abandoned iron mines of Lorraine towards a semi-distributed modelling approach. C.R. Geoscience 337, 1492–1499.

Collon, P., Fabriol, R., Buès, M., 2006. Modelling the evolution of water quality in abandoned mines of the Lorraine Iron Basin. Journal of Hydrology 328, 620–634.

Collon, P., Fabriol, R., Vaute, L., Pinault, J.L., Buès, M., 2002. Modelling changes in sulphate concentrations in discharge water from the abandoned iron mine of Saizerais. Proceedings SWEMP 917–924,, 2002.

Graf, T., Therrien, R., 2007. Variable-density groundwater flow and solute transport in irregular 2D fracture networks. Advances in Water Resources 30, 455–468.

Gylling, B., Birgersson, L., Moreno, L., Neretnieks, I., 1998. Analysis of a long-term pumping and tracer test using the channel network model. Journal of Contaminant Hydrology 32, 203–222.

Hamm, V., Fabriol, R., Vaute, L., Fourniguet, G., Baubron, J.C., 2005. Modelling the impact of back-filling material on the water quality of flooded iron mines (Lorraine, France). Post-Mining 2005, Nancy, France, November 16-17. CD, 12 pp.

Heller, M., Poppei, J., Schlickenrieder, L., Förster, B., 2005. Natural processes and system evolution during mine closure: numerical simulation and visualization. Post-Mining 2005, Nancy, France, November 16-17. CD, 8 pp.

Liou, C.P., Kroon, J.R., 1987. Modelling the propagation of waterborne substances in distribution networks. J. AWWA 79 (11), 54–58.

Moreno, L., Crawford, J., Neretnieks, I., 2006. Modelling radionuclide transport for time varying flow in a channel of network. Journal of Contaminant Hydrology 86, 215–238.

Moreno, L., Neretnieks, I., 1993. Fluid flow and solute transport in a network of channels. Journal of Contaminant Hydrology 14, 163–192.

Parkhurst, D.L., Appelo, C.A.J., 1999. User Guide to PHREEQC (Version 2): a computer program for speciation, batch-reaction, one-dimensional transport, and inverse geochemical calculations. U.S. Geological Survey Water-Resources Investigations. Report 99–4259,, 312 pp.

Pinault, J.L., Pauwels, H., Cann, C., 2001a. Inverse modelling of the hydrological and the hydrochemical behaviour of hydrosystems: application to nitrate transport and denitrification. Water Resources Research 37 (8), 2179–2190.

Pinault, J.L., Plagnes, V., Aquilina, L., Bakalowicz, M., 2001b. Inverse modelling of the hydrological and the hydrochemical behaviour of hydrosystems: characterisation of karst system functioning. Water Resources Research 37 (8), 2191–2204.

Rossman, L.A., 2000. EPANET 2 users manual. Water Supply and Water Resources Division. National Risk Management Research Laboratory, Cincinnati, OH, p. 45268.

Spiessl, S.M., , 2004. Development, evaluation and demonstration of a reactive hybrid transport model (RUMT3D) for coupled discrete-continuum systems. PhD Thesis, June 2004, 149 pp.

Spiessl, S.M., Sauter, M., Zheng, C., Liu, G., 2002. Simulation of contaminant transport in flooded underground mines using a coupled continuum-conduit transport model: comparison of two numerical methods for advection in the pipe network, Model-CARE 2002. In: Kovar, K., Hrkal, Z. (Eds.), Acta Universitatis Carolinae. Geologica, vol. 46 (2/3), pp. 37–41.

Therrien, R., Sudicky, E.A., 1996. Three-dimensional analysis of variably-saturated flow and solute transport in discretely-fractured porous media. Journal of Contaminant Hydrology 23, 1–44.

Veschkens, M., Unland, W., Kories, H., 2005. Development of tools for managing the impacts on surface due to changing hydrological regimes surrounding closed underground coal mines (ECSC coal RDT program, contract 7220-PR-136). Post-Mining 2005, Nancy, France, November 16-17. CD, 13 pp.

Villermaux, J., 1993. Génie de la réaction chimique, conception et fonctionnement des réacteurs. Lavoisier, p. 448.

Modélisation géologique et hydrogéochimique de réservoirs souterrains à géométrie complexe

Résumé : La modélisation numérique des réservoirs souterrains est un outil essentiel à la compréhension de leur organisation, de leur fonctionnement et à la prévision des impacts des activités anthropiques sur leur évolution. Certains réservoirs se caractérisent par des géométries complexes qui vont directement influencer la connectivité hydrodynamique en leur sein, et plus largement l'hétérogénéité des propriétés du milieu et tous les processus physiques qui s'y déroulent. C'est le cas des bassins miniers ennoyés, des karsts, des chenaux, ou des dépôts salifères. L'objectif de mes travaux est de définir de nouvelles méthodologies de modélisation numérique adaptées à ces réservoirs à géométrie complexe et ce, en fonction de l'échelle spatiale et du processus physique d'intérêt.

Dans une première partie, l'accent est mis sur le lien entre la stratégie de modélisation retenue et le phénomène étudié lorsque deux processus principaux, ou plus, entrent en jeu. Ceci est principalement illustré à travers des travaux menés sur la gestion de l'après-mine lorrain. La deuxième partie est consacrée à l'analyse et à la caractérisation des objets géologiques à géométrie complexe, et notamment des systèmes karstiques et chenalisés. La troisième partie s'intéresse aux méthodes de simulation stochastiques de ces milieux : l'objectif n'est pas de trouver *la* solution unique, mais d'identifier *une/des* solutions honorant les données disponibles et rendant compte de la réalité, de sa complexité et des incertitudes qui lui sont associées. Le dernier chapitre dresse enfin une rapide conclusion et présente les perspectives de ces travaux à court et moyen termes.

Geological and Hydrogeochemical modelling of reservoirs characterised by complex geometries

Summary : Numerical modelling of subsurface reservoirs is crucial to better understand their organization, their response and to improve our capacity in forecasting the impacts of human activity on their becoming. Some reservoirs are characterized by complex geometries that directly control their hydrodynamic connectivity, and more globally their petrophysical heterogeneity and the physical processes that occur in them. It is particularly the case of flooded mines, karsts, channelized systems and salt deposits. The goal of my works is to find new methodologies dedicated to the modelling of reservoirs characterized by a complex geometry, and this, depending on the spatial scale and the main physical process of interest.

In a first part, I focus on the link between the adopted modelling strategy and the main phenomena of interest when two processes, or more, are involved. It is mainly illustrated with works made on the post-mining management. The second part is dedicated to the analysis and characterization of geological objects with a complex geometry, notably karstic and channelized systems. The third part deals with stochastic simulations of these reservoirs : the aim is not to find *the* exact theoretical solution but to find *a set of* solutions that account for the observed reality, its complexity and the associated uncertainties. The last chapter presents a brief conclusion and proposes some short and long term perspectives of these works.